Modeling of Hot Electron Driven Reactions Over Localized Surface Plasmon Resonance-Active Nanoparticles

by

Matthew Patrick Morabito

A dissertation submitted in partial fulfillment
of the requirements for the degree of
Doctor of Philosophy
(Chemical Engineering)
in the University of Michigan
2016

Doctoral Committee:

Professor Suljo Linic, Chair
Professor Mark A. Barteau
Professor Johannes W. Schwank
Associate Professor Max Shtein

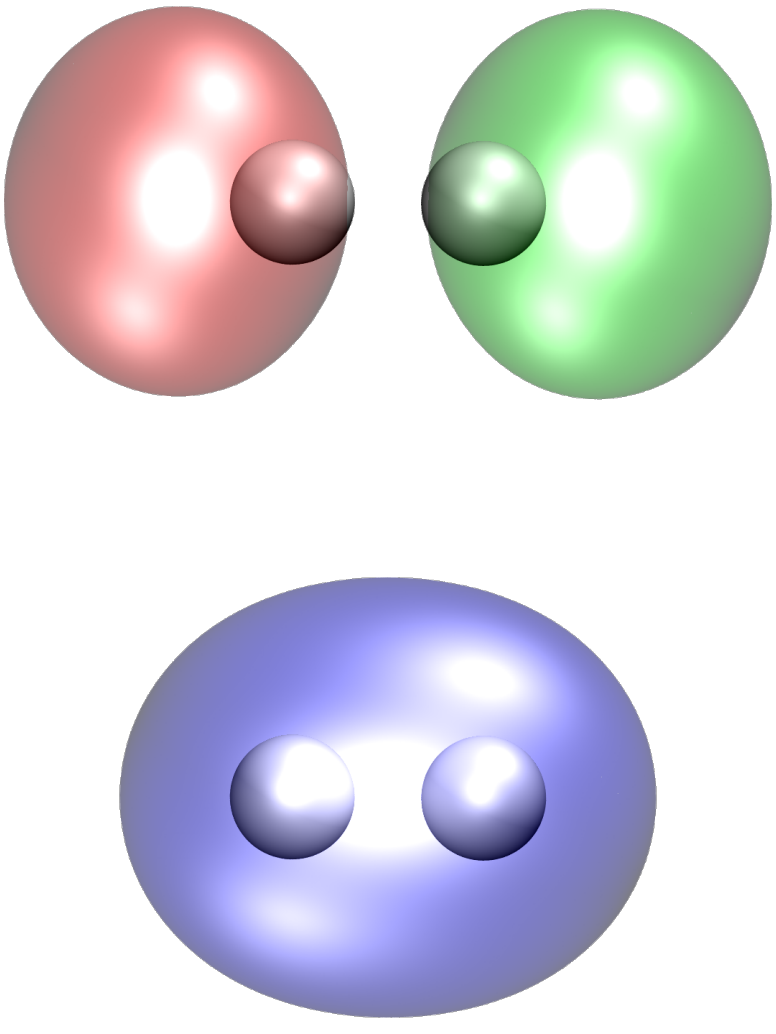

DEDICATION

I dedicate this to my parents for the amazing amount of love and support they've given me over the years.

ACKNOWLEDGMENTS

I would like to acknowledge all the people that have helped me along this journey. I would like to thank Professor Suljo Linic for his guidance and support throughout both my undergraduate and graduate studies at the University of Michigan. I would like to thank the rest of my committee for their input and direction: Professor Mark Barteau, Professor Johannes Schwank, and Professor Max Shtein.

I'd like to thank everyone in the Linic group, especially Hongliang Xin for mentoring me in quantum chemical calculations, David Ingram for teaching me all about BASH programming and cluster administration, and Eranda Nikolla for helping me get started in the lab. I'd also like to thank Paul Hernley for helping out with the cluster, Phil Christopher, Thomas Yeh, Umar Aslam, Neil Schweitzer, Robert Campana, and Tim van Cleve.

I'd like to thank my backpacking buddy, Huanan Zhang for helping me discover the wonderful meal that is Italian Wedding Soup.

I'd like to thank the rest of my Engineering/Science friends: Lilian Hsiao, Alex Bryan and Anne Jaskot, Aaron Shinkle, Chad Huelsman, Youngri Kim, Julia Faeth, Elizabeth Stewart, and Min Kim.

I'd also like to thank some of my fellow Kendoka for their support throughout my time at Michigan: Tabia Chui, Alex Nitz, and Ken Wakabayashi.

I am grateful to the love and support given by everyone. I could not have done it without you.

TABLE OF CONTENTS

LIST OF FIGURES

LIST OF TABLES

LIST OF APPENDICES

LIST OF ABBREVIATIONS

c.c. complex conjugate

DDA Discrete Dipole Approximation

DFT Density Functional Theory

DIET Dissociation or Desorption Induced by Electronic Transitions

DIMET Dissociation or Desorption Induced by Multiple Electronic Transitions

DOS density of states

EELS electron energy loss spectra

fcc face-centered cubic

FEM finite-element method

FDTD finite-difference time-domain

H-K Hohenberg-Kohn

hcp hexagonal close-packed

KIE kinetic isotope effect

LCAO linear combination of atomic orbitals

LDA Local Density Approximation

LrTDDFT Linear-response time-dependent density functional theory

LSPR Localized Surface Plasmon Resonance

PES potential energy surface

RPBE Revised Perdew Burke Ernzerhof

SERS surface-enhanced Raman spectroscopy

TTM two-temperature model

UV-Vis Ultraviolet/visible light

ABSTRACT

Modeling of Hot Electron Driven Reactions Over Localized Surface Plasmon Resonance-Active Nanoparticles

by

Matthew Patrick Morabito

Chair: Dr. Suljo Linic

In this dissertation, we have used a number of different approaches including simple quantum mechanical models, quantum chemical calculations, electron dynamics, and molecular dynamics to explore the underlying phenomena of photon-mediated chemical reactions over nanostructured catalysts exhibiting strong localized surface plasmon resonance. These reactions could occur either from formation of energetic electrons directly on or to the adsorbate molecule, or formation of energetic electrons on the substrate that are subsequently transferred to the adsorbate. The work presented models portions of both mechanisms. The first portion of this work investigated the properties and characteristics of the interaction between surface plasmons and adsorbate states. Our studies suggest that surface plasmons can enhance the promotion of energetic electrons into empty adsorbate states through strong electric fields at the surface. The surface plasmon increases the interaction

of a light molecule with the nanostructure, which can transfer energy into empty adsorbate states if the energy is correct.

We also studied the characteristic time scales for relaxation of energetic electrons and formation of a thermalized hot electron gas. These time scales lay the groundwork for modeling the interaction of the hot electron gas with adsorbate molecules through molecular dynamics simulations within the electronic friction model.

We used position-dependent electronic friction in molecular dynamics simulations employing the Langevin equation to show what type of experimental signatures (e.g. kinetic isotope effect) are expected from this type of interaction. We found that the expected experimental signatures for our model O_2 dissociation over Ag were similar to and consistent with the experimental results for the same. These discoveries help illuminate some of the underlying physical processes for photon-driven chemical transformations over nanostructured catalysts and suggest areas for future study in the discovery and design of these catalysts.

CHAPTER 1

General Introduction

This chapter provides an introduction to both the wide field of traditional heterogeneous catalysts as well as the new emerging field of photocatalysts that utilize the phenomenon of Localized Surface Plasmon Resonance (LSPR) to affect chemical transformations. These LSPR-mediated reactions offer two advantages over existing thermal and (high-intensity) photon-driven processes: first, they allow usage of lower intensity light (on the order of solar intensity) and second, they offer an opportunity to tune the selectivity of competing reaction mechanisms. A large body of work has been done on metallic photocatalysis but much of the underlying physics of LSPR-driven chemistry remains in the dark.

1.1 Heterogeneous Catalysis

A catalyst is a substance that enhances a reaction by participating, while not being consumed, in the process. Metal nanoparticles are used as heterogeneous catalysts for many chemical reactions including ammonia synthesis, hydrocarbon reforming, oxidation and hydrogenation reactions [1]. These chemical transformations

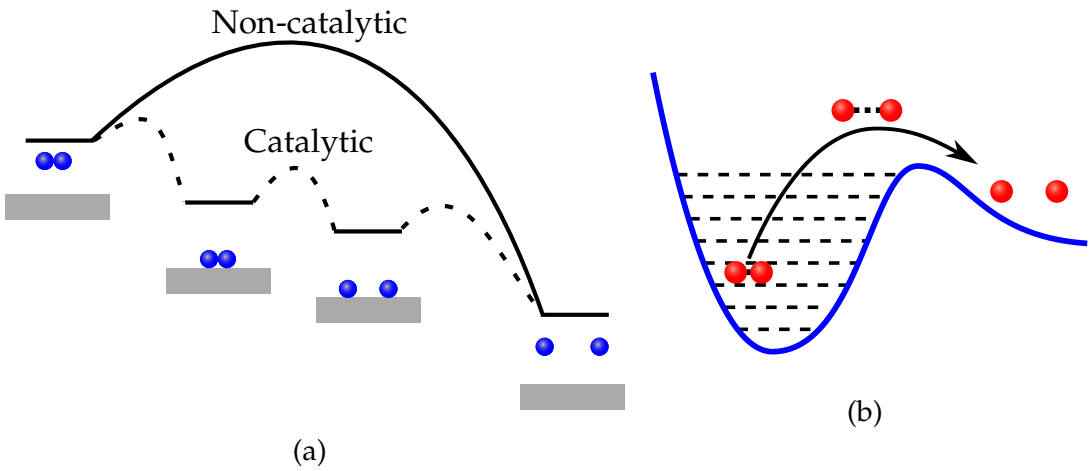

Figure 1.1: **a.** Potential energy surface comparing the energetics of a non-catalytic process (top) and a catalytic process (bottom). **b.** Potential energy surface of a dissociating diatom; in a thermal process, thermal energy drives a molecule up the vibrational ladder leading to dissociation.

typically occur through a series of elementary steps in which the reactants adsorb to the surface, undergo surface reactions (i.e. bond breaking and formation), and the resulting products desorb from the surface. For a molecule undergoing catalytic dissociation (see Figure 1.1a), the resulting series of incremental changes – adsorption, reaction, desorption – lower the activation barrier compared to a single step without a catalyst.

1.1.1 Thermally-Driven Catalysis

Chemical transformations are typically driven by thermal excitation of the system, activating phonons (i.e. vibrational modes) of adsorbed species through thermal heating of the substrate. The energetic substrate phonon modes couple to adsorbate vibrational modes, pushing the species along the ground-state PES up the vibrational ladder and over the reaction barrier, shown in Figure 1.1b. This process

can lead to dissociation – if the vibration is along the axis of a diatomic molecule – or desorption – if the vibration is between a molecule and the surface [2, 3, 4]. These thermal excitations will preferentially activate reaction pathways with the lowest activation barrier.

1.1.2 Electron-Mediated Reactions

Alternatively, reactions can be triggered by energetic charge carriers such as holes or electrons, generated from absorption of photons by photocatalysts [5]. On metals this phenomenon has been observed in experiments using short-duration high-intensity femtosecond lasers, illuminating single crystal metal catalysts [6, 7, 8, 9, 10, 11, 12]. Recently, a new class of metallic nanoparticles that enhances reactions under low-intensity visible light – on the order of solar intensity – has been discovered [13, 14]. These electron-mediated reactions exhibit two distinguishing experimental characteristics [15]. The first is a transition from a linear to superlinear dependence of the reaction rate on photon flux (intensity) from low to high intensity (flux). This transition suggests that the linear dependence at low intensities is caused by single-photon events while the power law dependence at high intensities is caused by multiple-photon events. The second is an elevated kinetic isotope effect – a stronger change than expected for a thermal process in the ratio between reaction rates involving heavier and lighter isotopes.

1.2 Localized Surface Plasmon Resonance (LSPR)

Electromagnetic waves (i.e. light) that come into contact with matter set electric charges (i.e. electrons) in motion [16]. This process can result in absorption of the photon to generate energetic charge-carriers (i.e. electron-hole pairs) or emission of a new photon in a process called scattering. The energetic electrons can dissipate their energy to substrate phonon modes, causing thermal heating of the nanoparticle. The nanostructured low-intensity catalysts mentioned in the previous section interact very strongly with light through the phenomenon of LSPR in the Ultraviolet/visible light (UV-Vis) region and are characterized by a high ratio of surface states to bulk states which limits bulk dissipation (to thermal heat) of energetic charge-carriers [5].

The phenomenon of LSPR is a collective resonant oscillation of valence electrons in a metal forming a standing wave on the surface of the metal in response to an external electromagnetic stimulus. An external electromagnetic stimulus (i.e. photon or impinging electron) polarizes the electron cloud of a metal particle displacing it away from the positively charged metal nuclei. This displaced electron cloud experiences a restoring force in the direction of the electron-deficient core. When the frequency of the incident electromagnetic field matches the natural frequency of this restoring force, LSPR is established [17, 18]; a diagram of this process can be found in Figure 1.2. LSPR is characterized by intense electric fields on the surface; a simulation of these is shown in Figure 1.3a.[1]

[1] For simulation details please see Appendix A.

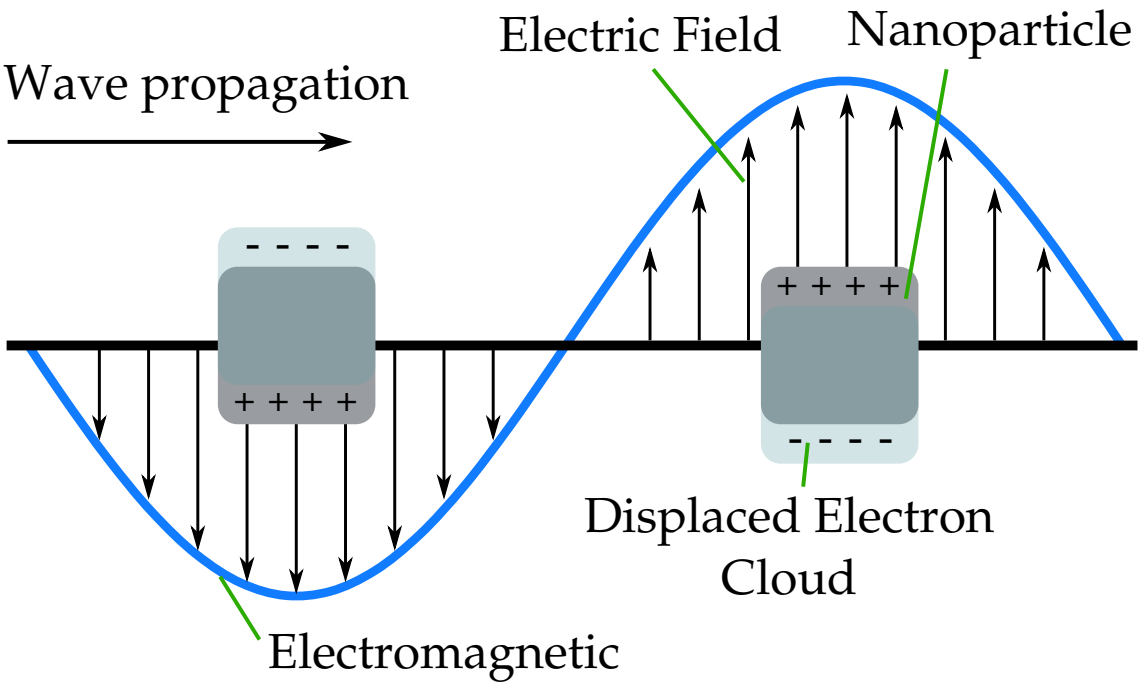

Figure 1.2: Schematic of a resonant surface plasmon oscillation.

Copper, silver, and gold nanostructures exhibit LSPR under (UV-Vis) illumination. These nanostructures are of particular interest for solar applications, interacting strongly with wavelengths within the solar spectrum (Figure 1.3b) [19, 20, 21, 22]. The frequency – and consequently the photon energy and wavelength – of the plasmon peak is determined not only by the constituent element (Figure 1.3b) but also the nanoparticle shape (Figure 1.3c) and size (Figure 1.3d) [23, 24, 25, 26, 27, 28]. Silver nanostructures exhibit a redshift (toward longer wavelengths and lower energies) as the shape changes from wires to spheres to cubes. Ag nanostructures also exhibit a redshift as the particle size increases. Tuning nanostructures to interact more strongly with the solar spectrum and/or specific wavelengths is possible by manipulating the composition, size, and shape [19, 20, 21, 22].

The strong surface-localized electromagnetic fields generated by LSPR-active

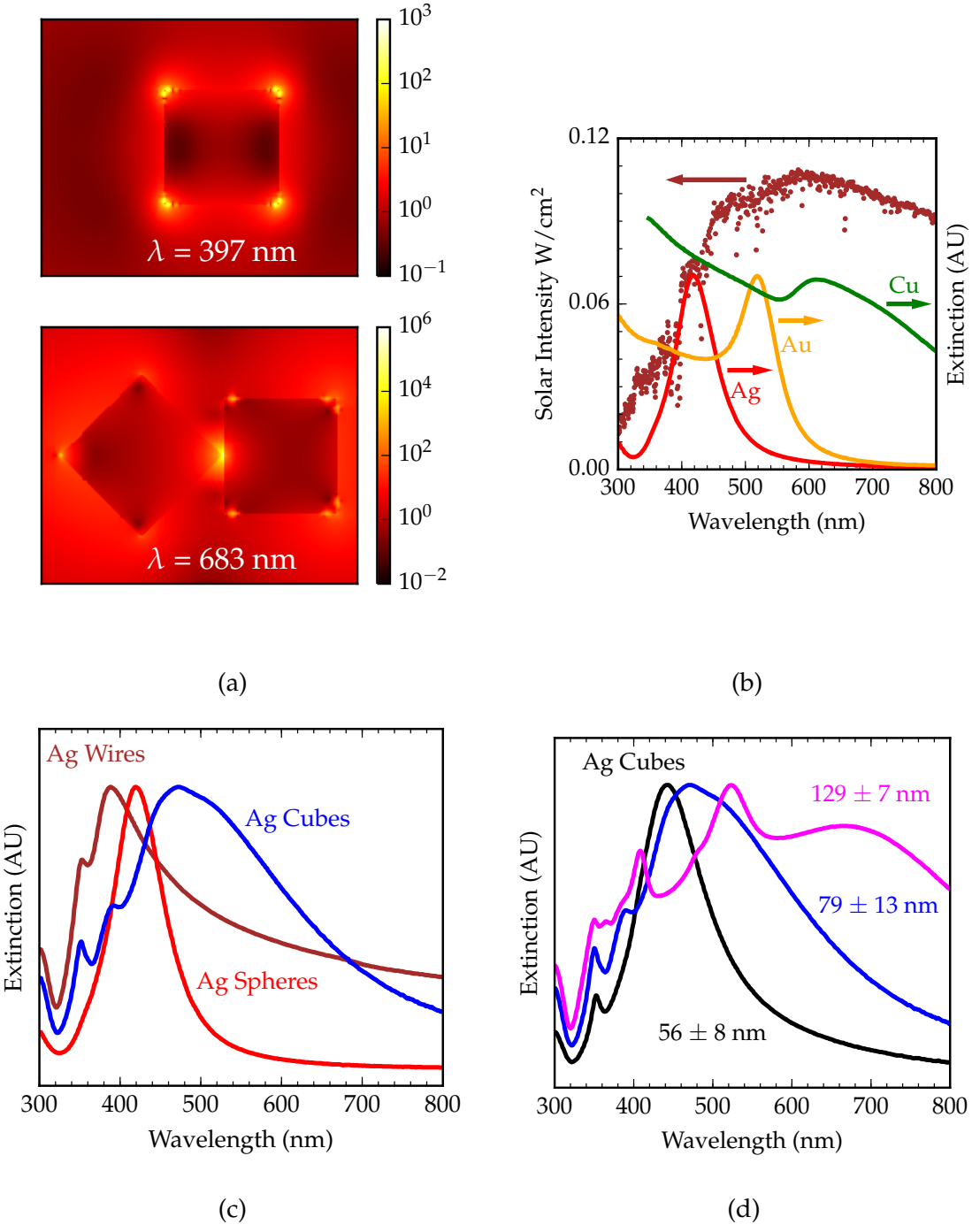

Figure 1.3: **a.** Simulation showing intense electric fields on the surface of LSPR-active nanoparticles in response to light at the resonant wavelength. **b.–d.** LSPR wavelength can be tuned by modifying nanostructure composition, shape, and size. Solar spectrum data from: http://rredc.nrel.gov/solar/spectra/am1.5/, Spectral data from [21].

nanoparticles have been used in many applications ranging from single-molecule spectroscopy [26, 29, 30, 31], surface-enhanced Raman spectroscopy (SERS) [32], molecular sensing and detection [33], solar cells [34], among many others [26, 29, 34, 35, 36]. These strong electric fields and scattered light could also amplify HOMO-LUMO excitations in photoactive molecules adsorbed to the surface [29, 37].

LSPR is characterized by a strong extinction peak. The interface between metal and external media show electric field enhancements over the strength of the incident electromagnetic field $\left(|E|^2\right)$ on the order of $10^2 - 10^3$ for single particles [23, 24, 25, 38]. Clusters of particles in close proximity ($\sim$1 nm apart) see even stronger localized enhancements up to 10^5 [26, 29, 38, 39, 40]. These areas between particles are referred to as hot spots; due to the very intense electric field strength, these hot spots could be very important in plasmon-mediated photocatalysis. It is suggested that the strong electric fields at these hot spots can facilitate the tunneling of charge-carriers between nanoparticles, resulting in the formation of energetic charge-carriers [41, 42, 43]. The effect of a reactive environment (i.e. surface-adsorbed species) on the optical spectra and charge-carrier formation is discussed in chapter 2 and chapter 3.

1.2.1 LSPR Decay

The electronic oscillation comprises a number of metal electrons oscillating from filled states just below the Fermi level to unfilled states just above. Relaxation of

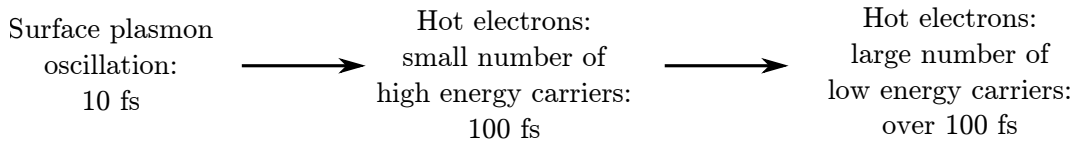

Figure 1.4: The time scale of the initial surface plasmon oscillation is around 10 fs. This oscillation decays to form a small number of high energy states

this photon/plasmon oscillation takes place on the order of tens of femtoseconds (see Figure 1.4) [44, 45, 46]. The decay can either emit a new photon (scattering) or to excite electron-hole pairs (energetic charge-carriers) in the nanoparticle (absorption). Photon re-emission (scattering) is the primary mode of plasmon decay in unreactive environments for large isolated nanostructures [47]. Surface plasmons on larger particles (e.g. Ag nanoparticles larger than 50 nm) in a reactive environment can also decay through chemical interface damping – exciting a hot electron on surface-adsorbed species. This process occurs on a slightly longer time scale – around 10 fs to 100 fs.

Plasmon relaxation in smaller particles (e.g. Ag nanoparticles smaller than 30 nm) is dominated by absorption: the formation of electron-hole pairs on the surface that typically dissipate through recombination, releasing thermal energy. The absorption process can occur through different pathways; the photon can excite surface-adsorbed species through chemical interface damping or excite single electron-hole pairs in the substrate through a process called Landau damping [25, 48, 49]. Landau damping forms a single hot electron with a corresponding hole; the energy difference between the electron and hole being equal to the photon

energy [44, 45].

Hot electrons formed on the surface will scatter off of other electrons in the nanoparticle over time, dispersing energy from a single electron to a larger number of low-energy excited electrons. These low-energy electrons will couple to substrate phonon modes over a longer time scale ($\sim$ 1 ps) and cool back towards thermal equilibrium with the substrate ($\sim$ 10 ps). The formation of the small number of high-energy states on the surface, the electron scattering to form a resulting hot electron distribution, and the cooling of this collection of low-energy excited charge-carriers through coupling to phonons in the substrate is discussed in chapter 4. The collection of low-energy excited charge carriers can also couple to adsorbate phonons, potentially triggering chemical transformations. This thesis discussed modeling this process through the electronic friction model in chapter 5.

1.2.2 Electron-Mediated Chemical Transformations

There are a number of more recent examples of charge-carrier mediated photochemistry under illumination by low-intensity light. The Linic Lab has first reported this phenomenon in studies of photo-activated oxygen dissociation over $\sim$50 nm Ag nanocubes [13, 14]. Quantum efficiencies ranged from $\sim$1% to $\sim$30%, with efficiency increasing as thermal temperature increases. This quantum efficiency is calculated as the ratio of photocatalytic reaction rate divided by the number of photons impinging on the catalyst bed. This efficiency suggests that energy can be applied to selectively heat the adsorbate; a light intensity low enough to

give a negligible increase the thermal temperature of the system can increase the reaction rate by a factor of four.

Halas and co-workers have demonstrated similar photo-activation of H_2 dissociation on 5 nm – 20 nm Au nanostructures using a light intensity of around 2 W/cm^2 [50, 51]. Studies have also focused on more complex molecules such as reduction of nitroaromatic compounds on 6 nm Au nanostructures, formation of hydrogen from ammonia borane on <10 nm Au nanoparticles, and esterification of benzaldehyde over <10 nm Au nanoparticles; all occurring under illumination from visible or UV-Vis light sources operating on a few hundred mW/cm^2 [52, 53, 54]. Bimetallic nanostructured particles combining plasmonic properties of one metal (e.g. Ag and Au) with catalytic properties of another (e.g. Pt and Pd) have also been reported. One such study reported hydrogen evolution over Pt-tipped Au nanorods at room temperature under very low intensity light – on the order of a few mW/cm^2 [55]. Other studies reported hydrocarbon oxidation and coupling reactions on Au-Pd and Au-Cu nanostructures [56, 57, 58, 59, 60].

Electron-mediated reactions offer a promising possibility for tuning selectivity: favoring one reaction pathway (e.g. dissociation) over another (e.g. desorption). For example, low pressure experiments of CO oxidation on Ru(0001) in the presence of a small amount of oxygen show only CO desorption under light-off conditions. In the presence of high-intensity laser illumination, light activates a second reaction pathway leading to CO oxidation [4]. This suggests the possibility exists to use photocatalysts to tune selectivity and drive specific surface reactions.

Hot electron excitation on adsorbate molecules can occur through two mecha-

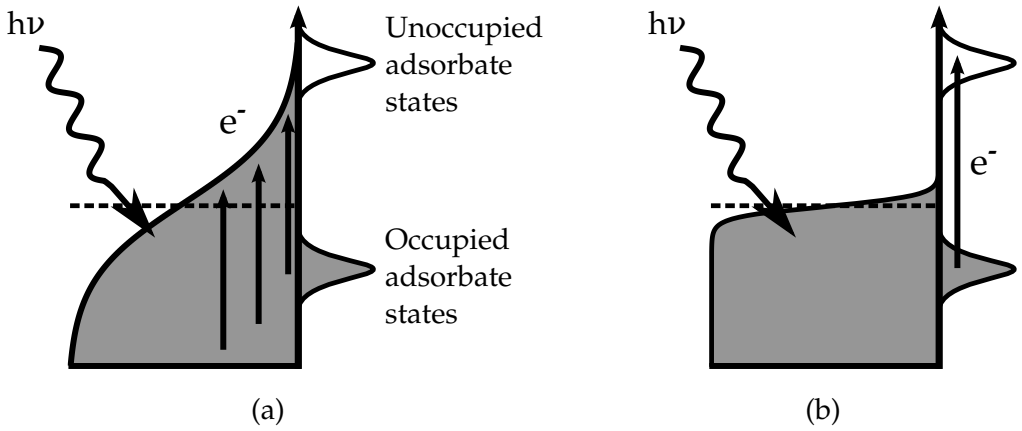

Figure 1.5: **a.** Indirect charge-transfer mechanism. A photon excites substrate electrons which are transferred to empty adsorbate states. **b.** Direct charge-transfer mechanism; an electron is promoted to empty adsorbate states directly from plasmon decay.

nisms; the first is an indirect charge transfer, depicted in Figure 1.5a where metal electrons are excited in the nanoparticle and those energetic electrons scatter across empty adsorbate states. This mechanism is typically associated with high-intensity laser studies where a large number of photons generate a large number of energetic charge-carriers in the nanoparticles.

The second mechanism is an alternative pathway suggested by some experiments, including photocatalytic CO oxidation on platinum nanoparticles under a high-intensity laser which show enhanced reaction rates at a particular frequency, with the reaction rate increasing to a maximum and then decreasing as photon energy is increased [61]. This direct charge-transfer process, also known as chemical interface damping, is initiated by the interaction of surface plasmons with accessible adsorbate electronic states, promoting an energetic charge carrier across these states (see Figure 1.5b). This direct excitation shows an increased reaction rate when the incoming photon energy matches the energy difference between the

bonding/antibonding states of the adsorbate. The charge transfer to the adsorbate could be enhanced or caused by the electric fields generated on the surface of a nanoparticle – it is critical to gain a better fundamental understanding of the generation of energetic charge-carriers (either electrons or holes) on the adsorbate molecules through interaction between a surface plasmon and adsorbed species.

One interesting direction suggested by the direct charge-transfer mechanism is the possibility of changing selectivity by targeting electronic excitation between specific adsorbate orbitals, potentially through engineering plasmonic photocatalysts with optical properties that support the preferential attachment of charge to a specific orbital over other orbitals in the adsorbate. This could be accomplished by matching the optical properties of the nanostructure (e.g., the LSPR energy) to target the gap between occupied and unoccupied states localized on the adsorbate. The direct charge-transfer process allows for this; however, the indirect charge-transfer mechanism discussed above does not support this possibility. Under the indirect mechanism the large number of charge-carriers excited on the metal surface will have energies relatively close to the Fermi level and will typically scatter preferentially across states close to the Fermi level.

The ability of a surface plasmon to dump energy directly into empty adsorbate electronic states is not well understood; chapter 2 and chapter 3 focus on the interaction between a surface plasmon with empty adsorbate states through quantum mechanical methods.

1.2.3 Electron-Mediated Thermal Heating

Another application of LSPR-active catalysts is to take advantage of efficient light absorption to increase thermal temperature at targeted areas. This phenomenon has been used to drive reactions such as catalytic steam reforming of ethanol over 10–20 nm Au nanospheres [62], decomposition of dicumyl peroxide over 13 nm Au nanoparticles [63], and chemical vapor deposition onto Au nanostructures [64, 65, 66]. Adleman and coworkers reported in ethanol steam reforming the formation of vapor pockets around the catalytic particles with the reaction likely occurring at the solid-vapor interface; this localized phase change potentially improves mixing of reactants or separation of products [67, 68]. Fasciani and coworkers estimated the surface temperature for dicumyl peroxide decomposition at around 500 °C. Steam reforming of ethanol and decomposition of dicumyl peroxide both occurred at light intensities upwards of 10^7 times solar flux; this localized heating is important under very intense light irradiation.

Another application for localized heating has been discovered in the field of medicine. Localized heating of around 25 °C has been demonstrated using SiO_2-Au core–shell particles to treat epithelial carcinoma [69]. Similar results were also reported in the photothermal destruction of malignant squamous cells and the treatment of drug-resistant breast cancer cells, among others [70, 71, 72, 73]. While these reactions are triggered by photons, they are ultimately driven by thermal excitation of substrate phonon modes; not directly by energetic charge-carriers. At high light intensities, it is important to be aware of the possibility of driving chem-

ical transformations through thermal heating of the substrate.

1.3 Surface Chemistry and Electronic Structure

Catalytic activity and optical properties are tied very closely to the electronic structure of catalyst/adsorbate complexes. The interplay of bonding within adsorbates, the surface, and between are of critical importance to plasmon-mediated catalysis.

1.3.1 Bonding

We start with a simple discussion of bonding and band formation using the tight binding approximation and molecular orbital theory to give a better understanding of the basic properties of electronic structure. When two atoms are brought together, the electrons in each can interact in both favorable (lower energy) and unfavorable (higher energy) combinations. A simple quantum-chemical calculation (numerical solution for electronic wavefunctions) for molecular hydrogen is found in Figure 1.6. Having properties of waves, two electrons can either combine in constructive (Figure 1.6a) or destructive interference (Figure 1.6b, top). Constructive interference is a positive interaction between electrons that is favorable toward bond formation (bonding); destructive interference is unfavorable toward bond formation (antibonding).

A graphical depiction of this is shown in Figure 1.6c which is a molecular orbital diagram of molecular hydrogen constructed using molecular orbital theory. When two hydrogen atoms bond, the two s-orbitals combine to form in-phase

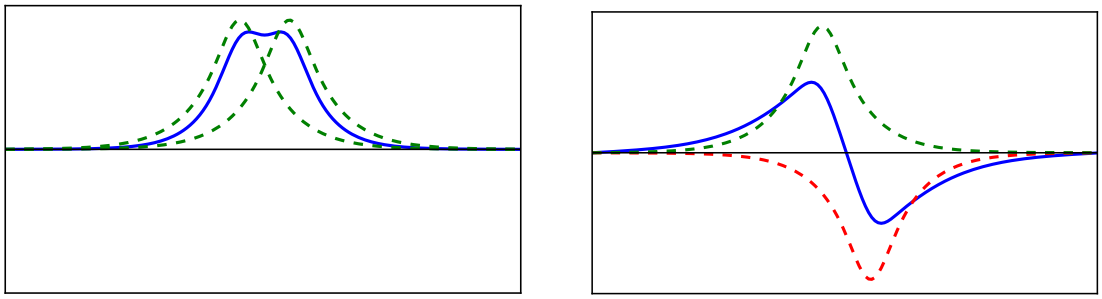

(a) (b)

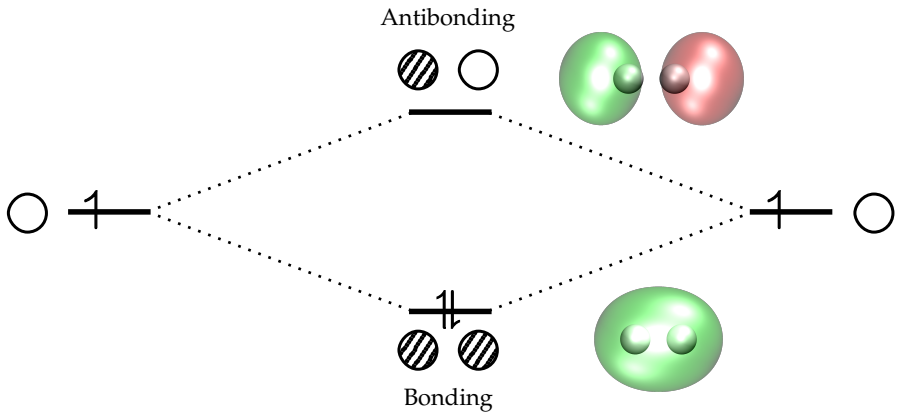

(c)

Figure 1.6: **a.** Plot of the in-phase combination (solid line) of individual wavefunctions (dashed lines). **b.** Plot of the out-of-phase combination (solid line) of individual wavefunctions (dashed lines). Green and red colors correspond to different phases. **c.** Diagram of bonding between two hydrogen atoms forming bonding (in-phase) and antibonding (out-of-phase) states. Visualization of bonding and antibonding states are shown.

(bonding) and out-of-phase (antibonding) combinations. The new bonding state localized in between the two hydrogens contributes to bonding behavior. If the two electrons are out-of-phase, the interaction creates an antibonding state that is higher in energy; this change of phase between neighboring atoms is called a node. More nodes (areas where two neighboring orbitals are out-of-phase – destructive interference) contributes to unfavorable, high-energy states. Electrons in favorable 'bonding states' will contribute to bond formation; antibonding states will detract from bond formation. In order for a bond to form, the number of electrons in bonding states must be larger than the number of electrons in antibonding states; this is the concept of 'bond order':

$$B.O. = \frac{1}{2}\left(N_{electrons,bonding} - N_{electrons,antibonding}\right) \tag{1.1}$$

A bond is favorable if the bond order is greater than zero and unfavorable if the bond order is zero. Each hydrogen brings an s-orbital with a capacity of two electrons but only containing one electron; these interact to form two orbitals (σ, bonding, and σ^*, antibonding) that can each hold two electrons. When filling the states, electrons will always fill the lowest available states – in this case the bonding state will hold 2 electrons and the antibonding state will hold zero. Therefore the final molecular orbital diagram for molecular hydrogen is shown in Figure 1.6c – the bond order is $\frac{1}{2}(2-0) = 1$. Helium's molecular orbital diagram looks almost identical to hydrogen but with one critical difference: each atom contributes 2 electrons each – there will be two electrons in both bonding and antibonding

states resulting in a bond order of zero.

Either injection of energetic electrons to antibonding states or excitation of electrons from bonding states (either to antibonding states or even nonbonding states, states not participating in bonding) can both reduce the bond order, weakening the chemical bond and potentially triggering chemical transformations.

1.3.2 Band Formation

In more complicated systems, bonding will comprise interactions of more than two electronic orbitals – such as in a metallic solid, which contains a large number of atoms (on the order of Avogadro's number, 6.022×10^{23}) all interacting with each other. Within the linear combination of atomic orbitals (LCAO) approximation, each atom owns its atomic orbitals with each combined molecular orbital (bonding, antibonding) being a linear combination of atomic orbitals: $\psi_{molecular} = C_1\psi_{H1} + C_2\psi_{H2}$.

The simplest case is of two atoms, discussed above, depicted in the first pane of Figure 1.7 showing the in-phase bonding and out-of-phase antibonding states. For three atoms, the interaction is more complicated but the in-phase bonding (bottom of the second pane of Figure 1.7) and out-of-phase antibonding (top of the second pane) combinations are still present. For four constituent atoms (third pane of Figure 1.7) we still see the in-phase and out-of-phase behavior but we also see the formation of intermediate energy combinations – these each contain both two pairs of bonding and two pairs of antibonding interactions. As the chain gets

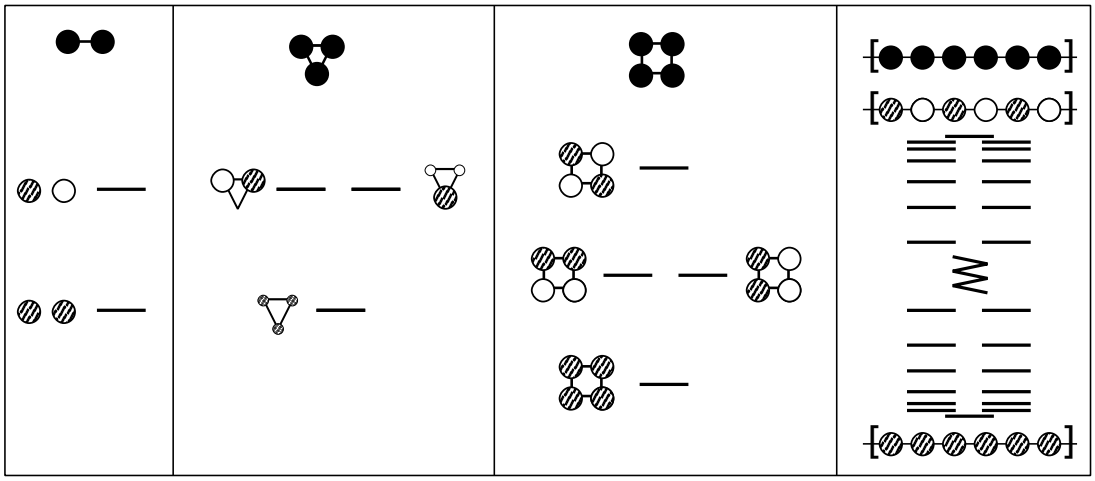

Figure 1.7: Schematic diagram of bonding for a dimer, trimer, quadmer, and infinite chain. Adapted from [74]

longer, the number of these intermediate states increases: as the number of constituent orbitals increases, so does the number of final states. The rightmost pane of Figure 1.7 shows an infinitely long chain of atoms – the lowest energy state comprises all wavefunctions in-phase with its neighbors; the highest energy is every wavefunction out-of phase with its neighbors.

These representations can be rewritten by the parameter 'k', which describes translational symmetry in inverse space (the first Brillouin zone).For this linear chain of s orbitals (Figure 1.8, top), the bottom representation (all in-phase) corresponds to k = 0. Moving along this k-space the orbitals become more out-of-phase; at k = $\frac{\pi}{a}$ all orbitals are out-of-phase and there are nodes between all neighboring orbitals. This gives a band structure – a plot of energy (E) vs. k that shows the energy of electronic states through k-space.

The slope of the band structure in k-space is inversely proportional to the number of states; a more flat band structure means more states present at this energy.

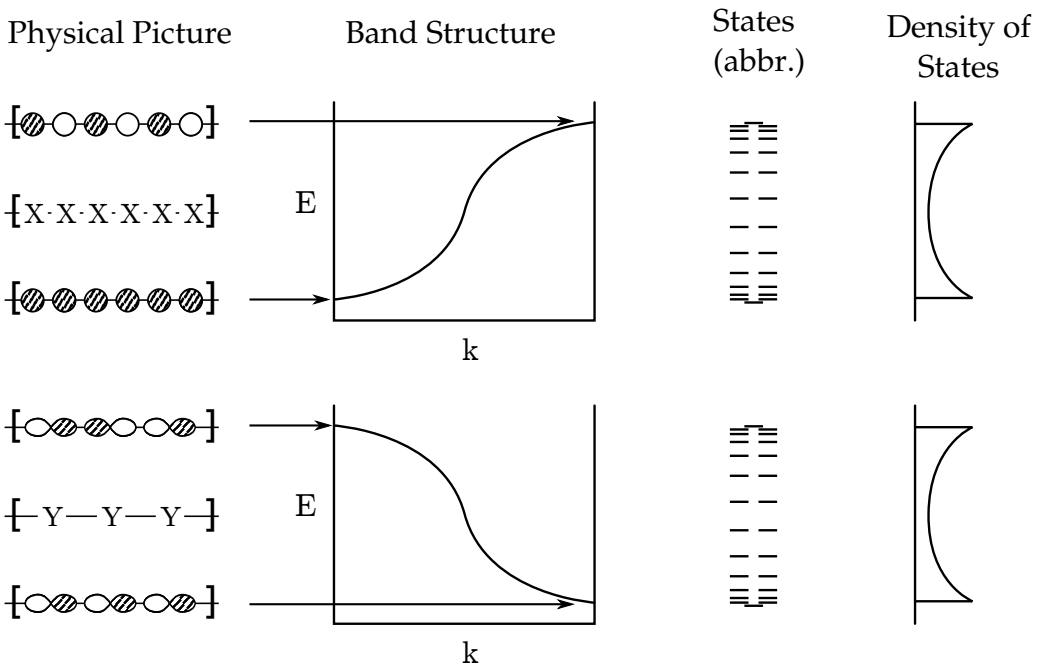

Figure 1.8: Schematic diagram of the fomation of a band structure and density of states for an infinite chain. Adapted from [74]

The DOS can be constructed from the band structure; it is a measure of the number of states, $\rho(E)$ in an energy interval between E and $E + \Delta E$.

The cases mentioned above all comprise 's' electrons – one type of electronic orbital. S-bands have certain characteristics – they will increase in energy through k-space and will have a DOS diagram similar to Figure 1.8. A second type of orbital that can bond is a p-orbital. P-orbitals have two lobes – each out-of-phase with each other. When neighboring p-orbitals form bonding pairs is when the orbitals are all out-of-phase (conversely, antibonding is when all orbitals are in-phase) – these bands will exhibit the opposite energy dependence on k-space, as shown in Figure 1.8, bottom.

The characteristics of the band structure also give other useful information: orbitals that are delocalized – that is those that interact with many of their neighbors

– will show a large dependence on k. A broad metal sp band corresponds to the strongly delocalized metallic states. Highly localized orbitals (that is, electrons that do not participate in much bonding with many orbitals) will have energy relatively independent of k and have very narrow bands (and very narrow DOS). There are other types of orbitals (d, etc.) and bonding (π,δ) that we will not discuss in detail here, for a full discussion see [74] and [75].

Of importance to this dissertation is the idea of k-space. Electronic transitions can occur at any point in k-space and detailed electronic structure information is necessary for probing electronic excitations. This idea is critical to chapter 3.

1.4 Scope of Dissertation

This dissertation covers elements of every aspect of LSPR from the initial photon interaction with the collective oscillation, through the formation of a small number of highly-energetic charge-carriers and subsequent decay to form a large number of lower energy excited charge-carriers (see Figure 1.9). Chapter 2 and Chapter 3 both explore the characteristics of the initial photon/electron oscillation interaction through a simple quantum-mechanical model and a more robust Density Functional Theory (DFT) treatment. Chapter 4 covers the decay of a small number of high-energy to a large number of lower-energy charge-carriers using the Boltzmann transport equation and the two-temperature model (TTM). Chapter 5 details one mechanism through which this large number of low-energy charge-carriers can trigger chemical transformations

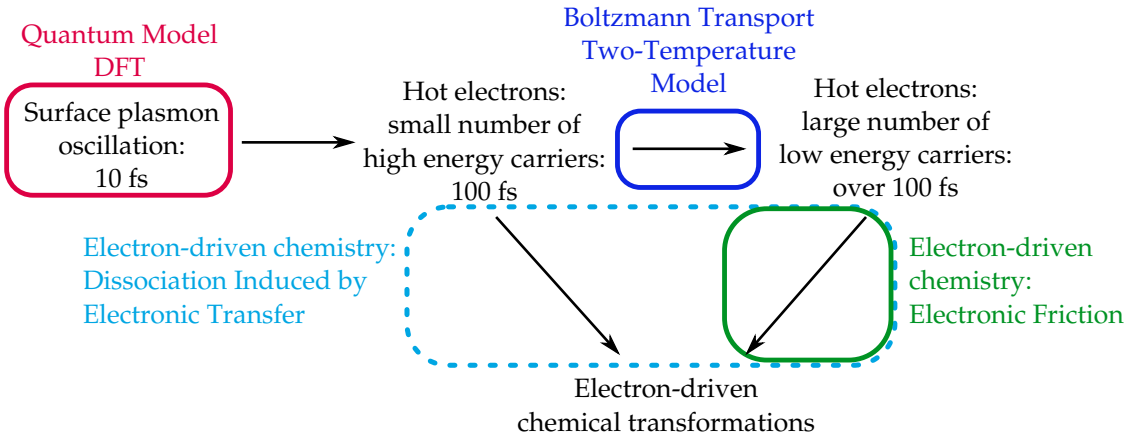

Figure 1.9: Outline of the concepts covered in this dissertation.

1.5 Summary

In this chapter we introduced the concepts of energetic charge-carrier catalysis; how it differs from traditional thermally driven processes. We dicussed what LSPR is and its importance in strengthening the light-matter interaction, localizing hot electron formation on the surface, and its ability to facilitate charge-carrier formation at relatively low light intensities. We discussed the decay paths for these surface plasmons – through photon re-emission or through production of electron-hole pairs in either the metal substrate or adsorbate molecules. Last, we introduced some concepts in bonding and band formation that are topical throughout this dissertation.

CHAPTER 2

Quantum Mechanical Model for Surface Plasmons

Localized Surface Plasmon Resonance (LSPR) is a collective resonant oscillation of electrons in a metal in response to an external electromagnetic stimulus. The stimulus – a photon or electron – displaces the negatively charged electron cloud of a metal particle away from the positively charged metal nuclei. This displaced electron cloud experiences a restoring force back toward the electron-deficient core. When the frequency of the incident electromagnetic field matches the natural frequency of this restoring force, LSPR is established. This resonance condition is characterized by intense electric fields at the surface and strong extinction.

2.1 Optical Properties

The polarization of the electron cloud is described by the dielectric function, which comprises real (ε_1) and imaginary (ε_2) parts:

$$\varepsilon(\omega) = \varepsilon_1(\omega) + i\varepsilon_2(\omega) \tag{2.1}$$

For metals the frequency dependence of the dielectric function is often approximated using the Drude model, which models the intraband (sp band to sp band) contribution to the dielectric function [16, 76]:

$$\varepsilon(\omega) = 1 - \frac{\omega_p^2}{\omega(\omega + i\gamma)} \tag{2.2}$$

where ω_p is the plasmon frequency and γ is the damping factor, equal to the inverse of the relaxation time, τ. Below 3.8 eV, the Drude model (green line, Figure 2.1) fits the intraband contribution of the experimentally determined dielectric function (blue line) well. Above 3.9–4.0 eV, however, excitation of electrons from the metal d band to empty sp states is possible. This interband transition is not accounted for in the Drude model, but can be included through the introduction of a Lorentzian term or terms to the above model, fit to experimental data:

$$\varepsilon(\omega) = 1 - \frac{\omega_p^2}{\omega(\omega + i\gamma)} + \sum_N \frac{\Delta\varepsilon_N \omega_N^2}{\omega_N^2 + \gamma_N \omega i - \omega^2} \tag{2.3}$$

where N are added Lorentzian poles; ω_N is the pole-specific resonant frequency of each Lorentzian, $\Delta\varepsilon_N$ is the permittivity at $\omega = 0$ multiplied by an oscillator strength term, and γ is the dipole damping of the transition; all are empirically fit to data. The results from one-term and six-term Lorentzian fits to the experimental data are found as the red line and black line (respectively) in Figure 2.1. The many-

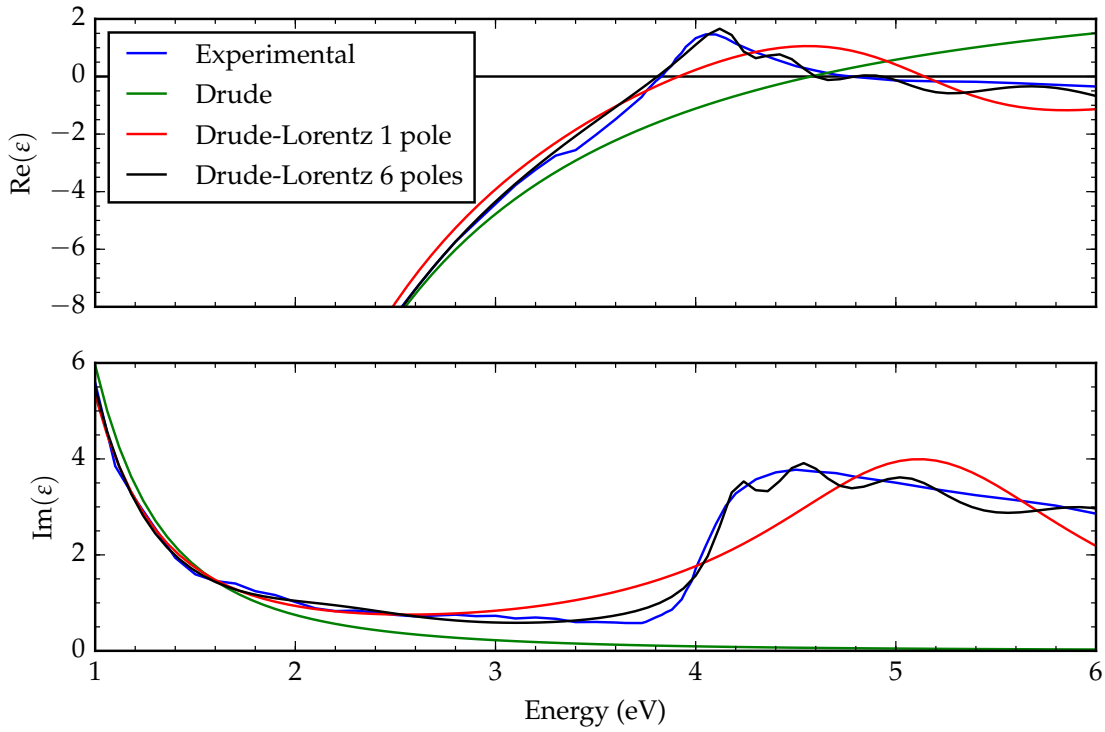

Figure 2.1: Comparison of empirical extinction models compared to literature data from [77]. The Drude model captures lower-energy behavior but cannot handle the interband transition. Introduction of Lorentzian poles can empirically capture this behavior. These poles are characterized by a peak in the imaginary part of the dielectric function and a corresponding wiggle in the real part of the dielectric function.

term fit captures the qualitative behavior of the dielectric function much better than the simple Drude model, but it is empirical, not from first-principles, and lacks any predictive power.

Solutions giving us extinction and other characteristic information (e.g. electric field strength, etc.) can be obtained several ways from this dielectric function. Using the Discrete Dipole Approximation (DDA) to calculate extinction properties, the system is treated as a finite mesh of polarizable points that couple with the applied electromagnetic field and other dipoles – this system can be solved algebraically [24, 38, 78]. Macroscopic treatments for electrodynamics (i.e. Maxwell's equations) can describe surface plasmons when the electron mean free path in the metal is small compared to the plasmon wavelength; numeric solutions can be obtained using finite-difference time-domain (FDTD) and finite-element method (FEM) solutions [79, 80, 81, 82]. A rich literature of work on this subject exists, for more information see Refs. [16, 76, 83, 84]

Models such as DDA, FDTD, and FEM using Drude or Drude-Lorentz models use empirical dielectric functions which do not contain detailed electronic structure information. For instance, they cannot predict the electronic structure of a nanoparticle in the presence of chemisorbed adsorbates. When particles decrease in size to the nanoscale (on the order of 10 - 100 nm) the continuous metal band (discussed in § 1.3) breaks down into discrete states and a quantum description of the optical response is necessary [85].

For particles much smaller than the wavelength of incoming light ($D_p/\lambda << 1$), the particle can be treated as an ideal dipole interacting with a surrounding

dielectric. This dielectric function is related to the extinction cross-section (in units of cross-sectional area) of a nanoparticle (σ_{ext}) through the following equation [86, 87, 88]:

$$\sigma_{ext} = \frac{18\pi V_{np}\varepsilon_m^{3/2}}{\lambda}\frac{\varepsilon_2}{[\varepsilon_1 + 2\varepsilon_m]^2 + \varepsilon_2^2} \tag{2.4}$$

where a is the particle radius, λ is the wavelength of the electromagnetic stimulus, V_{np} is the volume of the nanoparticle, ε_1 and ε_2 are the real and imaginary parts of the dielectric function of the particle, and ε_m is the dielectric constant of the medium surrounding the particle. From this equation there are two cases where the extinction cross-section should increase. The first is when the numerator, ε_2, is large; this contribution correlates to the number of individual electric charges oscillating in response to the electromagnetic field. We refer to this term hereafter as the single-particle term. The second is when the denominator is small; this occurs when ε_2 is relatively small and $(\varepsilon_1 + 2\varepsilon_m)$ is close to zero, i.e. when $\varepsilon_1 \sim -2\varepsilon_m$. We refer to this as the plasmon effect, as it corresponds to the optical response due to the formation of LSPR and strong electric fields at the surface.

2.2 Particle in a Box Model

A simple quantum mechanical model has been used in the past to study quantum effects on the dielectric function of small metal nanoparticles from first principles [89, 90, 91, 92, 93]. This simple, physically transparent model treats the optical response from a quantum standpoint; treating the metal s and p states in a

nanoparticle as comprising a sea of non-interacting electrons, in an infinite potential well. Inside the cubic potential well – the particle – of length L, the background potential is zero (V = 0). Outside the particle the potential is infinity – the electrons are restricted to the inside of the infinite potential well, and the wavefunctions at the edges of the box must be zero. The expression for calculating potential and the boundary conditions are:

$$V\left(0 < x < L\right) = 0 \tag{2.5}$$

$$V\left(x < 0 \text{ or } x > K\right) \to \infty \tag{2.6}$$

$$\psi\left(x = 0\right) = 0 \tag{2.7}$$

$$\psi\left(x = L\right) = 0 \tag{2.8}$$

The nanoparticle has three spatial dimensions; however, each spatial dimension is independent. We begin by obtaining solutions to the 1-dimensional time-independent Schrödinger equation:

$$-\frac{\hbar^2}{2m}\frac{\partial^2\Psi\left(x,t\right)}{\partial x^2} + V\left(x\right)\psi\left(x\right) = E\psi\left(x\right) \tag{2.9}$$

where V is the potential, E is the energy, m is the mass, x is position, and Ψ are the wavefunctions. We are looking at solutions inside the potential well; $V\left(x\right) = 0$. Rearranging gives:

$$\frac{\partial^2\Psi\left(x\right)}{\partial x^2} = -\frac{2mE}{\hbar^2}\psi\left(x\right) = -k^2\psi\left(x\right) \tag{2.10}$$

substituting in the wavenumber, k:

$$k_{wn} = \sqrt{\frac{2mE}{\hbar^2}} = \frac{p}{\hbar} \tag{2.11}$$

The general solution to differential equations of the same form as Equation 2.10 is a linear combination of sine and cosine functions:

$$\psi(x) = C_1 \sin(kx) + C_2 \cos(kx) \tag{2.12}$$

with integration constants C_1 and C_2. Since the wavefunction must not be discontinuous at the edges of the well, (where $V \to \infty$) the wavefunction must go to zero at the edges. The cosine term must drop out, i.e. $C_2 = 0$. Applying the second boundary condition gives:

$$\psi(L) = 0 = C_1 \sin(kL) \tag{2.13}$$

This equation has an infinite number of solutions corresponding to every integer n (the quantum number):

$$k_{wn} = \frac{n\pi}{L} \qquad n = 1, 2, 3, \ldots \tag{2.14}$$

where each n corresponds to a non-trivial wavefunction that is exactly zero at the edges. The constant of integration C_1 must satisfy the normalization condition –

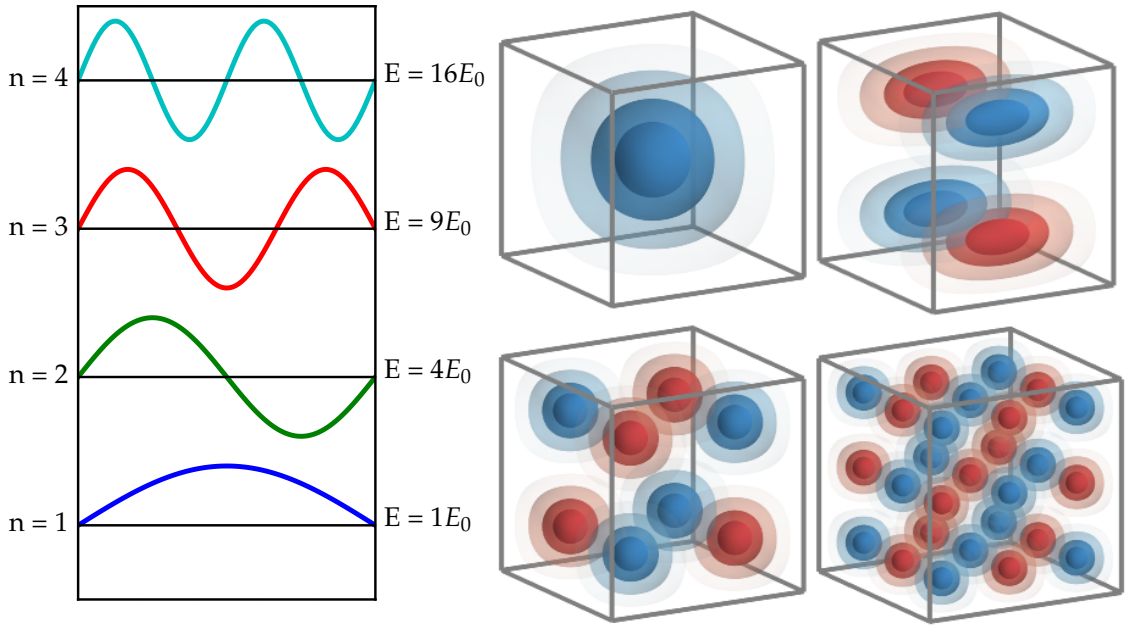

Figure 2.2: **a.** Solutions to 1-d Schrödinger equation for n = 1 to n = 4. **b.** Clockwise from top left, 3-D solutions for (n_x,n_y,n_z) = (1,1,1), (1,2,2), (2,2,2), (3,3,3).

the total density of each wave function in the box must be one electron:

$$\int_0^L \psi_n^* \psi_n dx = \int_0^L = A_n^2 \sin\left(\frac{n\pi x}{L}\right)^2 = 1 \tag{2.15}$$

The first four of these solutions are shown in Figure 2.2a. Waves with a higher frequency (higher wavenumber, shorter wavelength) have by nature, a higher energy. As the number of waves in each box increases, the amount of energy in each wave goes up proportional to n^2 – see Equation 2.11. The energy of each wave function is:

$$E = \frac{\hbar^2 k_{wn}^2}{2m} = \frac{n^2 \hbar^2 \pi^2}{2mL^2} = n^2 E_0 \tag{2.16}$$

Particular electrons (wave functions) are free in a 3-dimensional box. Each di-

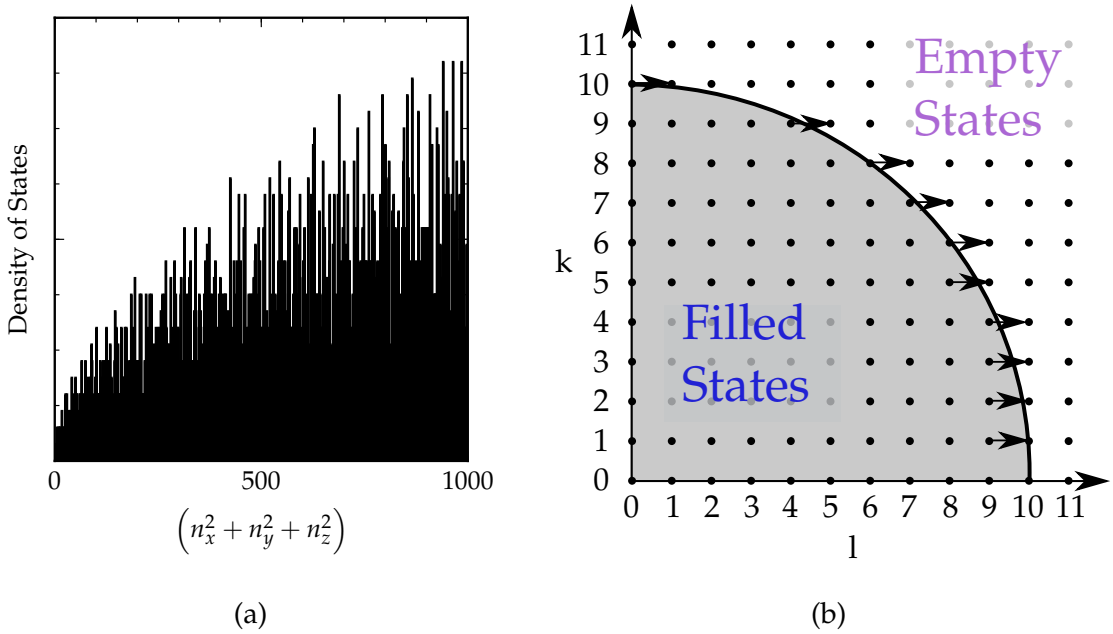

Figure 2.3: **a.** Density of states for 3-dimensional particle in a box; follows a square root dependence. **b.** Schematic diagram showing $\Delta l = 1$ transitions for a cubic nanoparticle where $l_F = 10$. Shaded areas correspond to filled states. Adapted from [89] (**b.** only)

mension is an independent degree of freedom – an electron will have one wave-function in each of x, y, and z directions:

$$\psi_{n_x,n_y,n_z} = \sqrt{\left(\frac{8}{L^3}\right)} \sin\left(\frac{n_x \pi x}{L}\right) \sin\left(\frac{n_y \pi y}{L}\right) \sin\left(\frac{n_z \pi z}{L}\right) \tag{2.17}$$

$$E_{n_x,n_y,n_z} = \frac{\pi^2 \hbar^2}{2mL^2}\left(n_x^2+n_y^2+n_z^2\right) \tag{2.18}$$

This leads to a square-root density of states, shown in Figure 2.3a, which is a reasonable analogue for the sp band of a real metal (see § 1.3). In a collective oscillation, such as a plasmon/metal nanoparticle interaction, electrons are transitioning around the Fermi level; from filled states just below the Fermi level to unfilled states above. The oscillator strength (transition probability) is dependent

on the energy difference between the initial and final states. For electrons in a box, simplifications can be made for symmetry and spin, giving an oscillator strength (S) dependent on initial 1-dimensional energy level (referred to as l):

$$S_{l,\Delta l} = \frac{32}{\pi l_F^3} \frac{l^2 \left(l + \Delta l\right)^2}{\Delta l^2 \left(2l + \Delta l\right)^2} \tag{2.19}$$

where l_F is the highest occupied quantum number and Δl is the number of levels between the initial and final states of the transition. A graphical depiction showing a sampling of allowed transitions for $\Delta l = 1$ is seen in Figure 2.3b for $l_F = 10$. The symmetry reduction is illuminated here; with the transitions originating at l = 9, corresponding to initial k levels of 1, 2, 3, and 4 all have identical oscillator strengths and are lumped together by symmetry. l_F is calculated as the cubed root of the total number of electrons in the nanoparticle (N), which is in turn calculated as:

$$l_F = N^{\frac{1}{3}} = \frac{V_{np}\rho}{M.W.N_A}. \tag{2.20}$$

where ρ is the density of silver, V_{np} is the volume of the nanoparticle, $M.W.$ is the molecular weight of silver, and N_A is Avogadro's constant.

2.3 Dielectric Function

The dielectric function can be written as a sum of these oscillator strengths, $S_{l,\Delta l}$ over symmetry allowed transitions ($\Delta l = 1, 3, \ldots$) from filled states ($l \leq l_F$) to

unfilled states ($l + \Delta l > l_F$):[89]

$$\varepsilon(\omega) = \varepsilon_\infty(\omega) + \omega_p^2 \sum_{\Delta l}^{1,3,\ldots} \sum_{l}^{l_F} \frac{S_{l,\Delta l}}{\omega_{l,\Delta l}^2 - \omega^2 - i\omega\gamma_{l,\Delta l}} \tag{2.21}$$

where the sum of all oscillator strengths has been normalized to one, ω_p is the bulk plasmon frequency, $\varepsilon_\infty(\omega)$ is the interband contribution – accounting for transitions from d-states to the sea of s and p electrons not explicitly handled with the quantum treatment above – to the dielectric function (below 3.8 eV, this value is relatively constant around 4), and γ is the damping for the dipole transition (related to the Drude lifetime: 0.016 eV for bulk Ag [89]), $\omega_{l,l+\Delta l}$ is the frequency of the transition $l \to l + \Delta l$. The frequency of transition is the difference between the initial and final frequencies:

$$\omega_{l,l+\Delta l} = \omega_{l+\Delta l} - \omega_l = \frac{E_0}{\hbar}\left[(l+\Delta l)^2 - (l)^2\right] \tag{2.22}$$

which simplifies to:

$$\omega_{l,\Delta l} = \frac{E_0}{\hbar}\Delta l\,(2l + \Delta l) \tag{2.23}$$

All relevant parameters are shown in Table 2.1. The dielectric function can be rearranged to give the real and imaginary parts:

$$Re(\omega) = \varepsilon_1(\omega) = \varepsilon_{1,IB}(\omega) + \omega_p^2 \sum_{\Delta l}^{1,3,\ldots} \sum_{l}^{l_F} \frac{S_{l,\Delta l}\left(\omega_{l,\Delta l}^2 - \omega^2\right)}{\left(\omega_{l,\Delta l}^2 - \omega^2\right)^2 - \omega^2\gamma_{l,\Delta l}^2} \tag{2.24}$$

Table 2.1: Summary of Parameters for Quantum Mechanical Model

Lattice constant q	4.08	Å
Fermi energy, E_F	5.52	eV
Plasma frequency, ω_p	$1.59 \times \omega_F$	
Dipole damping, γ	0.016	eV
Density	5.856×10^{28}	atoms/m^3
Interband term, ε_{IB}	4	
Medium dielectric constant	2.25	

$$Im\left(\omega\right) = \varepsilon_2\left(\omega\right) = \varepsilon_{2,IB}\left(\omega\right) + \omega_p^2 \sum_{\Delta l}^{1,3,\ldots} \sum_{l}^{l_F} \frac{S_{l,\Delta l}\omega\gamma_{l,\Delta l}}{\left(\omega_{l,\Delta l}^2 - \omega^2\right)^2 - \omega^2\gamma_{l,\Delta l}^2} \tag{2.25}$$

This dielectric function is related to the extinction cross-section (in units of cross-sectional area) of a nanoparticle (σ_{ext}) through the following equation [86, 87, 88]:

$$\sigma_{ext} = \frac{18\pi V_{np}\varepsilon_m^{3/2}}{\lambda} \frac{\varepsilon_2}{\left[\varepsilon_1 + 2\varepsilon_m\right]^2 + \varepsilon_2^2} \tag{2.26}$$

where V_{np} is the volume of the nanoparticle, ε_m is the dielectric constant of the surrounding medium, and λ is the wavelength of incoming light. Equation 2.26 gives some insight for properties of ε_1 and ε_2 that will cause an increase in the extinction cross-section. As discussed in § 2.1, the first condition is when the numerator increases; this is met when the imaginary part of the dielectric function, ε_2, is large, corresponding to a large number of electron oscillations generated in response to the optical perturbation. The second condition is where the denominator is very small; this happens when $(\varepsilon - 2\varepsilon_m) \sim 0$, or more specifically, when the real part of the dielectric function, ε_1 is roughly equal to $-2\varepsilon_m$. This condition characterizes an increase in extinction driven by electric fields generated from a collective oscillation.

To maximize extinction, the denominator, $[\varepsilon_1 + 2\varepsilon_m]^2 + \varepsilon_2^2$, must be as small as possible; ε_2, the transitions of individual electrons must not be too large. In metals such as Pt, transitions from the d-band to the sp band increase ε_2, and a strong, clear LSPR extinction peak is not observed. For Ag particles these transitions are approximated as a constant; the addition of a frequency-dependent interband term (similar to Ref. [18]) did not significantly affect the results. In Ag, the interband transition occurs mainly above 3.8 eV ($\sim$ 325 nm), in the ultraviolet region. Depending on nanoparticle size and shape, the Ag plasmon peak occurs around 2 – 3 eV, well below the interband region.

The scattering cross-section, that is, the portion of light that is not absorbed, but is re-emitted as photons is calculated in Equation 2.27:

$$\sigma_{sc} = \frac{24\pi^3 V_{np}^2 \varepsilon_m^2}{\lambda^4} \left| \frac{\varepsilon - \varepsilon_m}{\varepsilon + 2\varepsilon_m} \right|^2 \tag{2.27}$$

2.4 Results

2.4.1 Comparison of Model to Experiment

Calculated dielectric function and simulated extinction spectrum from a 75 nm silver nanocube can be found in Figure 2.4. Imaginary (top) and real (middle) parts of the dielectric function are plotted as a function of photon energy. The inset zooms in on the real part of the dielectric; the horizontal line in the inset corresponds to the resonance condition, $-2\varepsilon_m = -2 \times 2.25$. The predicted plasmon peak appears at

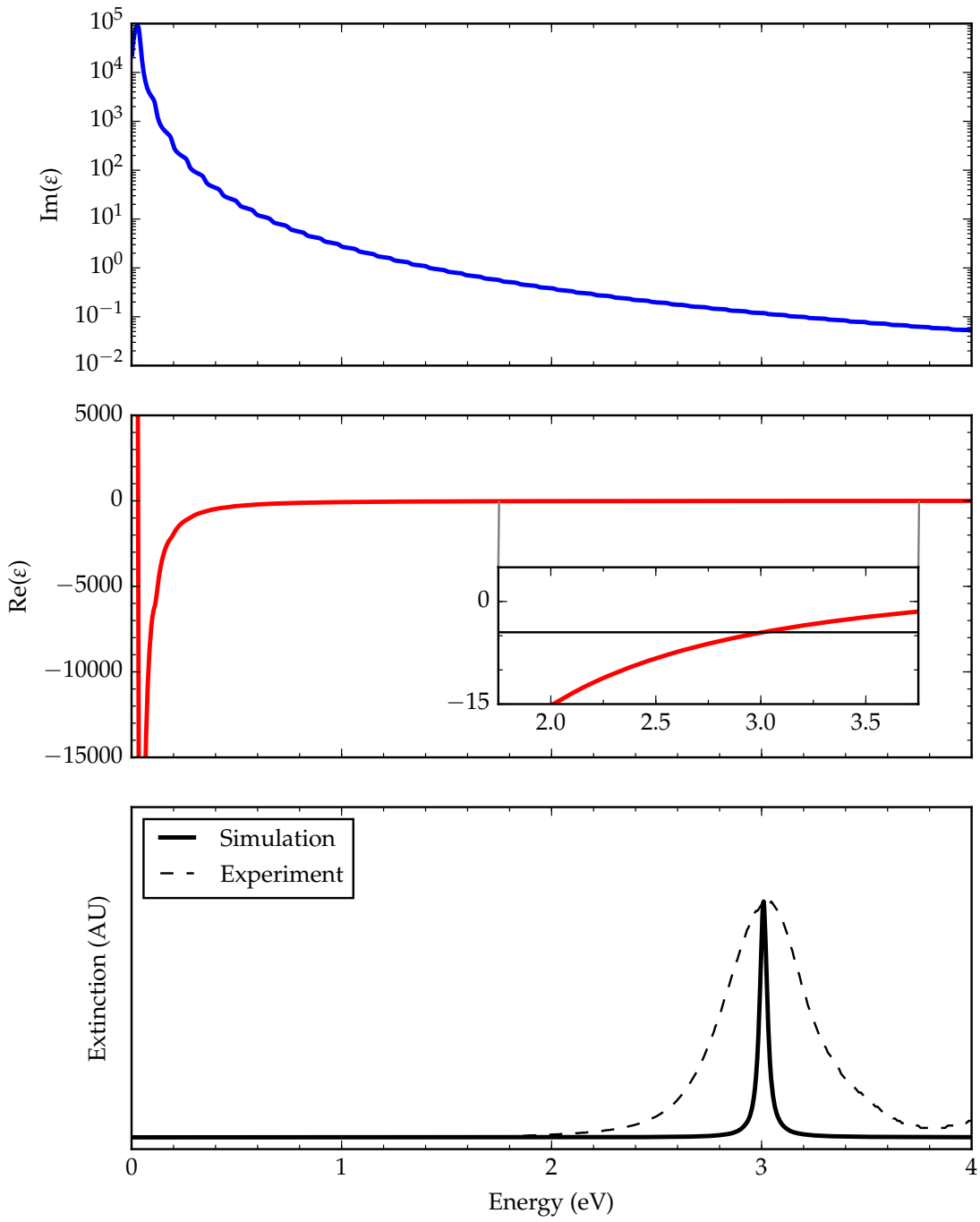

Figure 2.4: (Top) Imaginary part of the dielectric. (Middle) Real part of the dielectric. Inset, zoom in to the plasmon resonance condition, $\varepsilon_1 \sim -2\varepsilon_m$. (Bottom) simulated extinction spectrum compared to experimental solution of 70 nm.

the energy where this condition is met; at 3 eV. The peak location is well-matched to experiment; the width of the experimental results will have extra broadening due to dispersion and other factors. Of note from the experimental results is the interband transition – the increase in the experimental extinction above 3.8 eV.

2.4.2 Particle Size Effects

2.4.2.1 Electron-Hole Pair Energies

The effect of discrete states leads to different electron-hole pair energies for different particle sizes. Histograms of electron-hole pair formation, weighted by the oscillator strength, are found in Figure 2.5. Smaller particles show more quantum effects – more discrete states with less continuous behavior. The 5 nm particle shows distinct states; the only available transitions are above 0.5 eV (corresponding to $\Delta l = 1$) in energy with another cluster around 1.8 eV ($\Delta l = 3$) and again above 2.5 eV ($\Delta l = 5$). As the particle size increases, the difference between filled and empty states decreases to under 0.1 eV, with 75 nm particles showing no apparent discrete behavior.

2.4.2.2 Dielectric Function and Extinction

Calculated dielectric functions for 5 nm – 75 nm cubes can be found in Figure 2.6. The plasmon resonance condition of $\varepsilon_1 \sim -4.5$ for particles embedded in a dielectric medium where $\varepsilon_m = 2.25$ is shown as a dashed horizontal line in Figure 2.6. The peaks in the histograms from Figure 2.5 help identify features in the calcu-

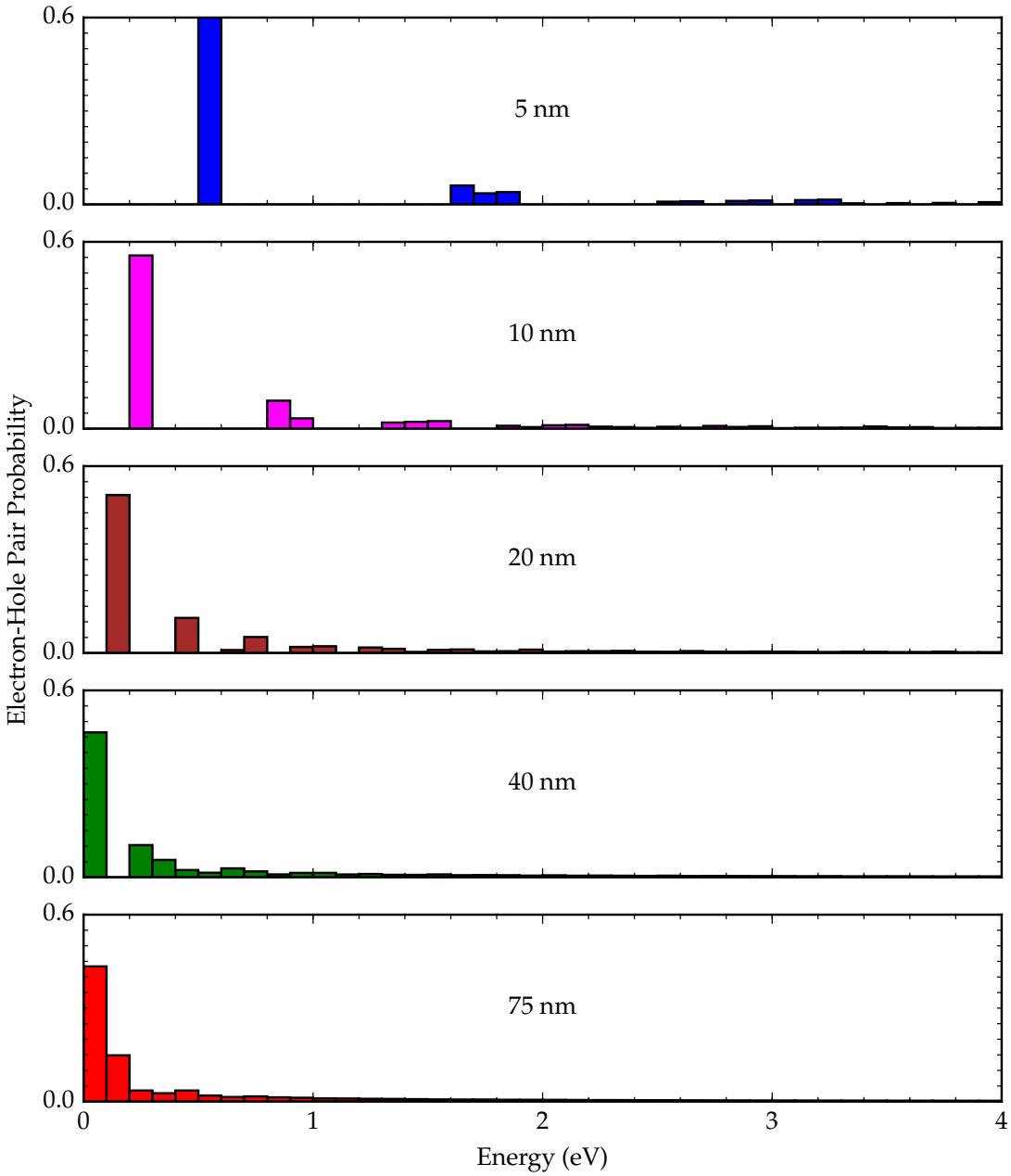

Figure 2.5: Histogram of electron-hole pair formation for nanoparticles ranging in size from 5 nm – 75 nm. Smaller particles show fewer available states and more discrete state behavior. Larger nanoparticles have more continuous band structure and have more low-energy states available for electrons to dump into just above the Fermi level.

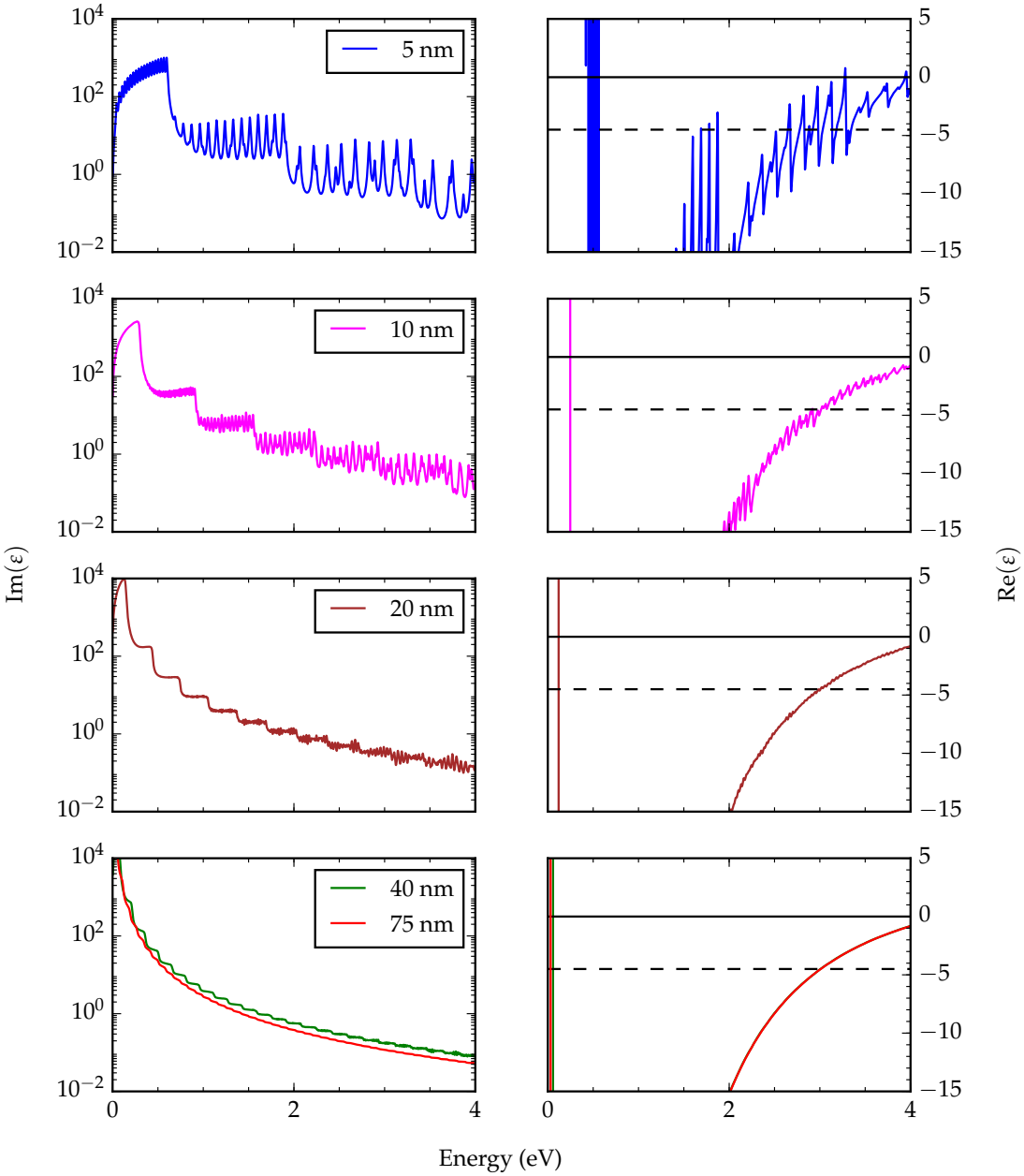

Figure 2.6: Dielectric functions for nanoparticles from 5 nm – 75 nm. Fine structure in the dielectric functions correspond to discrete transitions; plateaus in imaginary part of dielectric correspond to different Δl values. The dashed lines correspond to $Re\,(\varepsilon) = -2\varepsilon_m$, the resonance condition.

lated imaginary and real parts of the dielectric function. The peak in the imaginary part tracks with the first lowest available state, shifting to lower energy at larger particles. Each plateau in the imaginary parts – clearest for the 10 nm particle – correspond to a different $\Delta l = 1, 3, 5, \ldots$. The smallest particle shows very distinct discrete transitions; each of the peaks in the imaginary part of the dielectric correspond to different initial energies. As the particle size increases, the discrete set of states begins to act more like a continuum – by 40 nm the small peaks in the imaginary part are almost gone; by 75 nm they are negligible.

2.4.2.3 Absorption and Scattering

Smaller particles are dominated by absorption of electrons – that is, the formation of electron/hole pairs on the surface that dissipate to heat. Larger particles scatter light more effectively – plasmon decay typically results in re-emission of a photon. These size effects are captured using Equation 2.27 – the scattering term increases as the square of the nanoparticle size, rapidly dominating the extinction. The results for absorption and scattering calculated from the quantum mechanical model for nanoparticles from 5 nm – 75 nm is found in Figure 2.7. The small particles (5 nm, 10 nm) are almost completely dominated by absorption (dot-dash lines); larger particles (40 nm, 75 nm) are completely dominated by scattering (dashed lines). Both effects could be contributing to photon-driven chemical transformations. Absorption of light to form electron-hole pairs on the nanoparticle is how the process is typically understood using high-intensity laser experiments, however lower intensity processes typically do not form a large number of electron-hole pairs on the

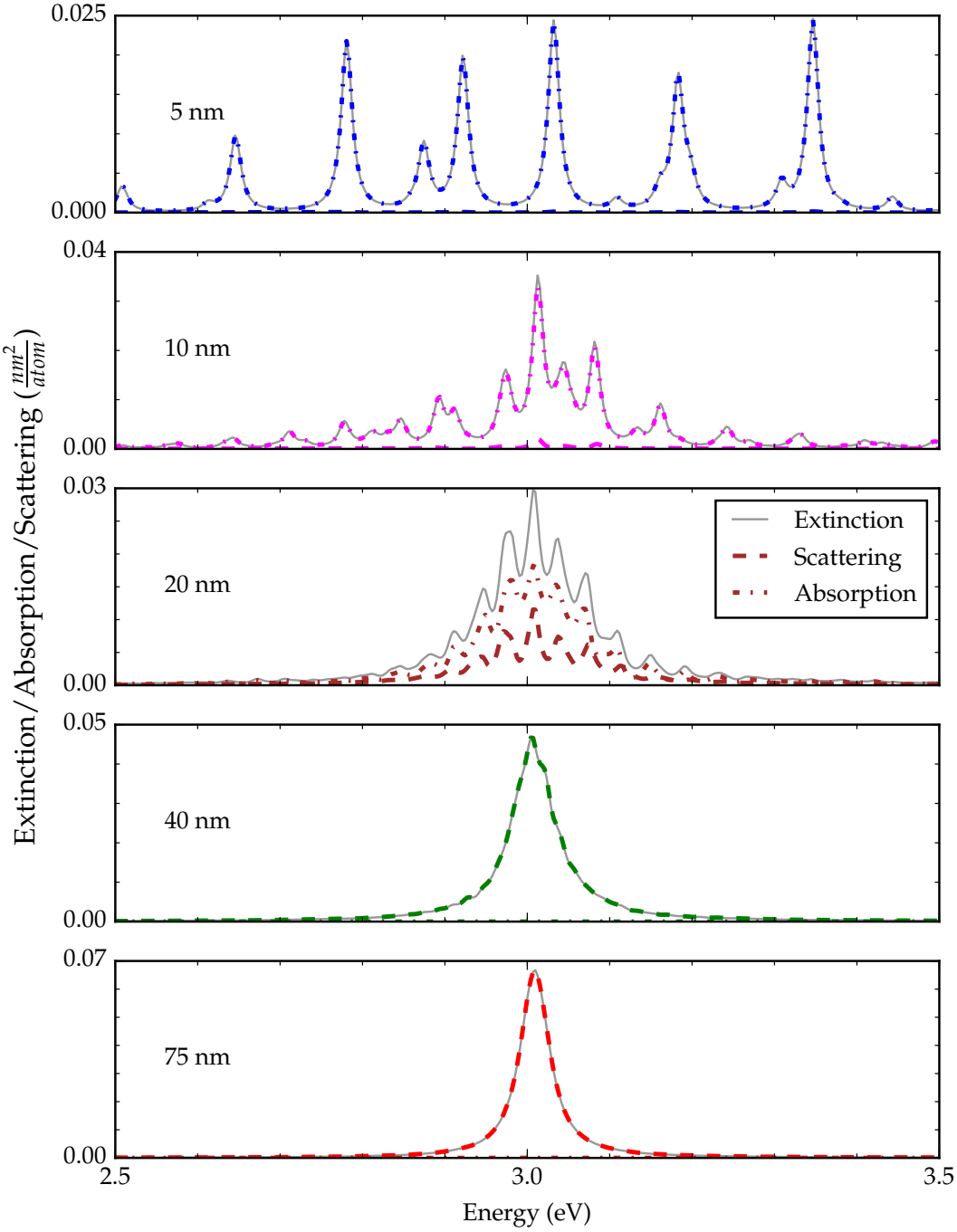

Figure 2.7: As the particle size increases (top to bottom) scattering becomes more important. Small particles are dominated by absorption of electrons to form electron/hole pairs which dissipate to heat; large particles are dominated by scattering and re-emission of photons.

surface; the electronic temperature of nanoparticles above 10 nm does not change appreciably under single-photon illumination. For larger particles, scattering of light could be important in increasing the interaction of light with nanoparticles by focusing light, using nanoparticles as antennae [31]. Another pathway exists: a surface plasmon could decay to form a hot electron directly on a species adsorbed to the surface. This process, called chemical interface damping, could operate in parallel or serial with absorption and scattering, driving chemical transformations on the surface.

2.4.3 Single-Particle and Plasmonic Effects

As discussed in § 2.3, the extinction cross-section will be large under two conditions. The first is where ε_2 is large; this indicates the presence of a large number of electronic oscillations not associated with the collective oscillations (e.g. d-band to sp-band transitions). The portion of Equation 2.26 responsible for describing this process we label the single-particle term (with units of area or length squared):

$$\text{Single-particle term} = \frac{18\pi V_{np}\varepsilon_2}{\lambda} \tag{2.28}$$

The second condition where the extinction cross-section will be large is when the electrons in the surface oscillate at the same frequency as the incoming electromagnetic field. The portion of the extinction equation responsible for this effect we

denote the plasmonic term (a unitless quantity):

$$\text{Electric field term} = \frac{\varepsilon_m^{\frac{3}{2}}}{|\varepsilon_1 + 2\varepsilon_m|^2} = \frac{\varepsilon_m^{\frac{3}{2}}}{[\varepsilon + 2\varepsilon_m]^2 + \varepsilon_2^2} \tag{2.29}$$

The extinction is the product of these two terms. These parts allow us to review how changes in the electronic structure of the nanoparticle (e.g. size effects, adding adsorbates) will change the extinction properties. Figure 2.8 shows extinction, single-particle effect, and electric field effect for 5 nm and 10 nm nanocubes. These small particles show discrete transitions. Both single-particle and electric field effects are important; the electric field (i.e. ultimately the real part of the dielectric function) is responsible for the location of the plasmon peak while the single-particle (i.e. the imaginary part of the dielectric function) is reponsible for determining the fine structure and width. This is especially apparent in the 10 nm results where the electric field effect is centered mostly around 2.8 to 3.3 eV while the single-particle transitions below and above this energy broaden the extinction spectrum.

The data in Figure 2.9 shows the same information for larger particles – 20 nm up to 75 nm. There are still noticeable discrete transitions for 20 and 40 nm particles; the transition should be somewhere around 50 nm. The effect of broadening from the single-particle transitions is largely negligible above 20 nm. The single-particle effect decreases by at least a factor of 10 compared to the 5 nm particles; this is offset by an increase in the corresponding electric field effect, which dominates larger particles.

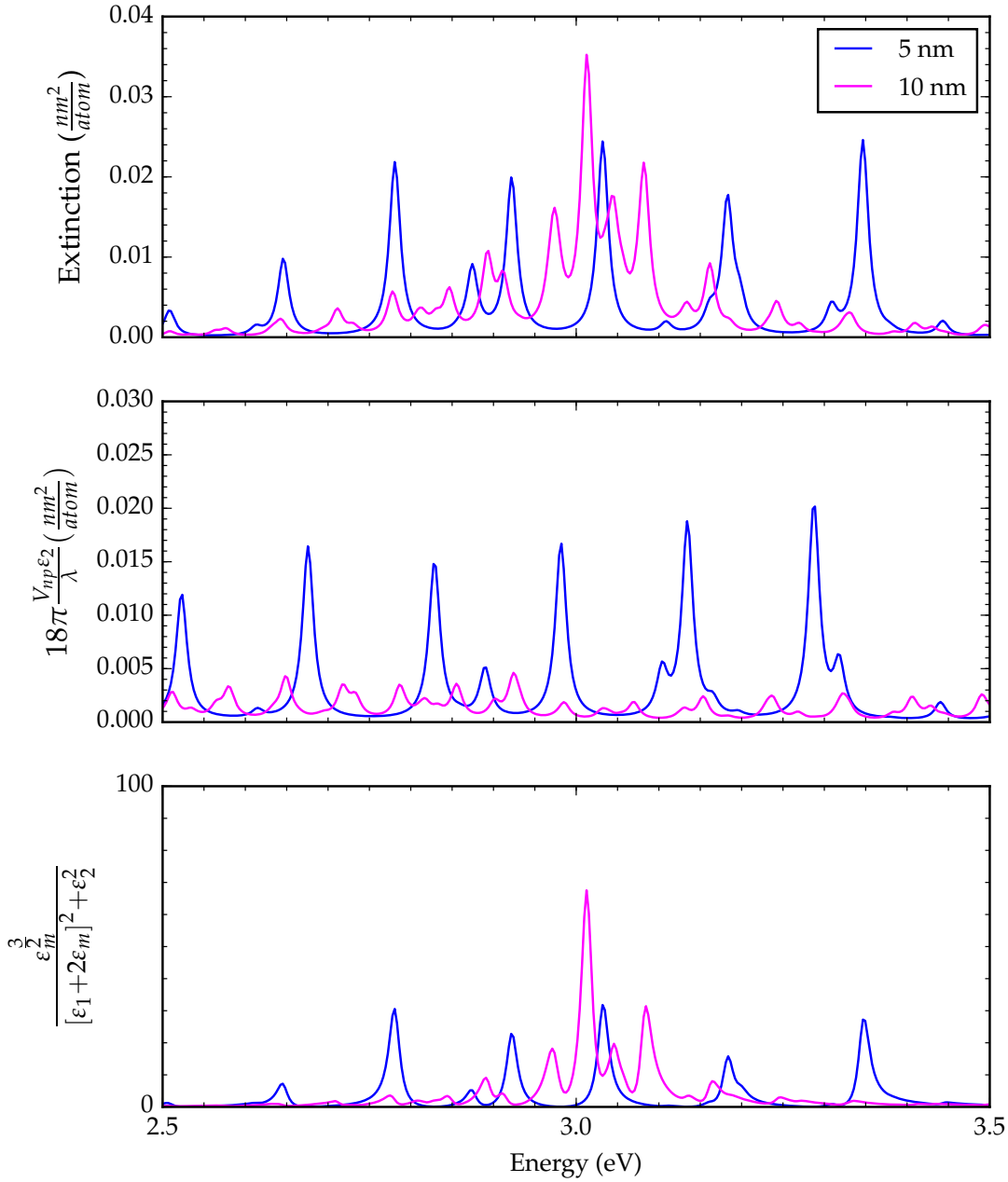

Figure 2.8: Extinction spectra with single-particle and and electric field contributions for nanoparticles from 5 nm – 10 nm

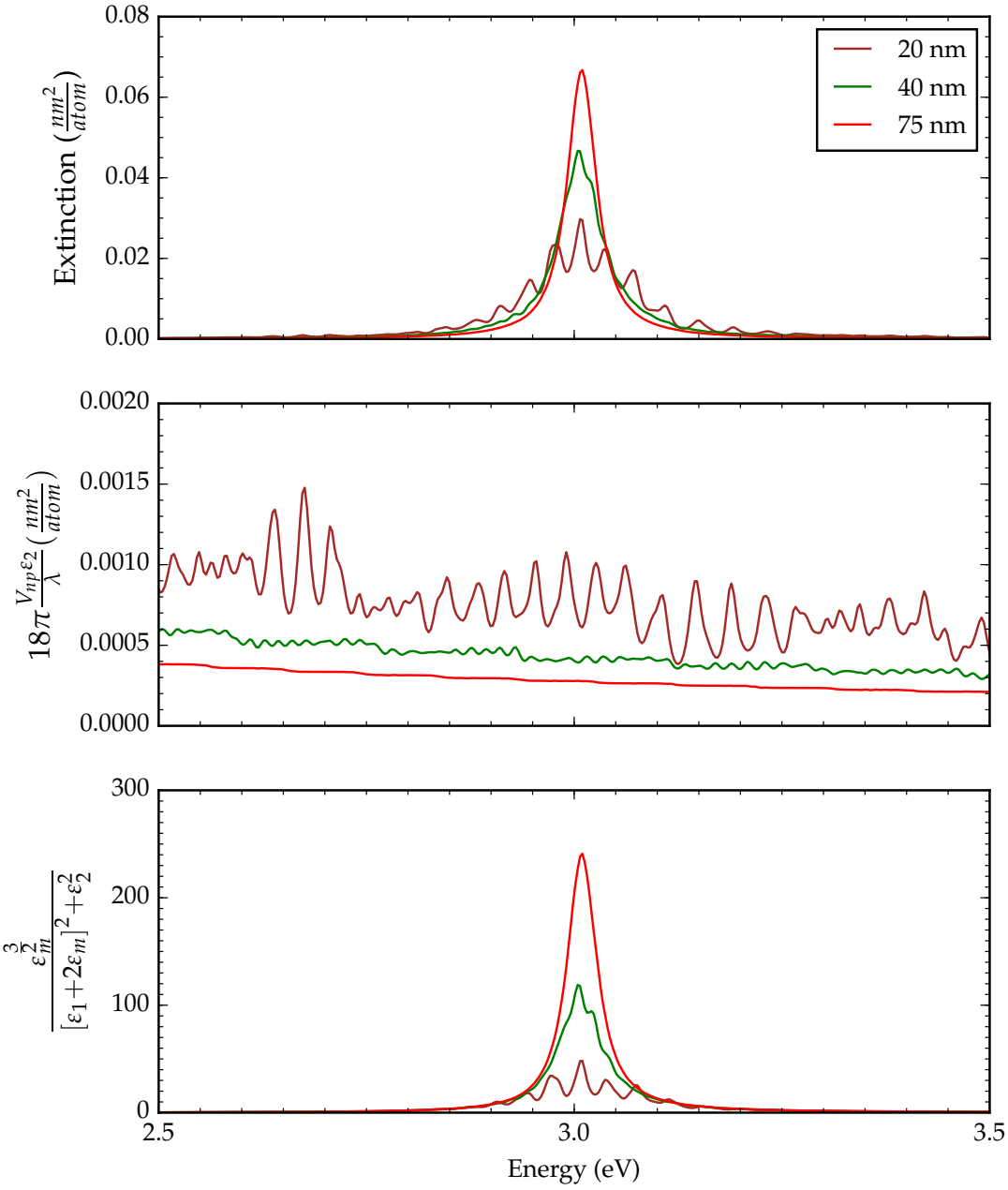

Figure 2.9: Extinction spectra with single-particle and and electric field contributions for nanoparticles from 20 nm – 75 nm

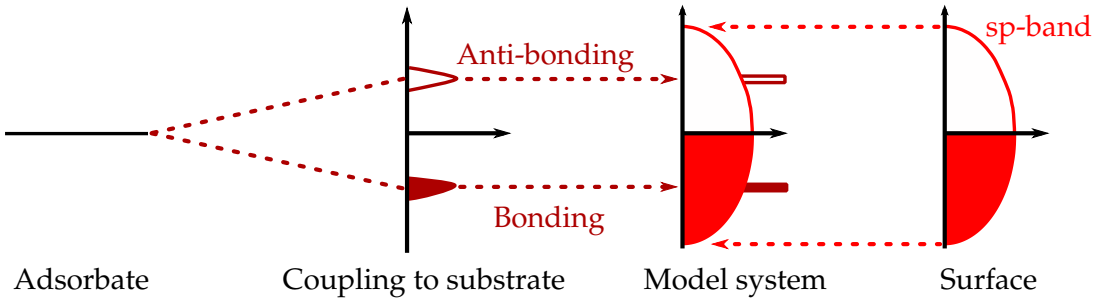

Figure 2.10: Illustration of adsorbate-substrate coupling. An adsorbate far from the surface (left) has discrete states. As the adsorbate interacts with the surface, it forms bonding and anti-bonding states (left center). These states combined with the metal surface (right) gives a combined system which we model as shown here (right center.

2.4.4 Impact of Adsorbates

We developed a natural extension of this quantum mechanical model to give a physically transparent description for the photon-driven HOMO-LUMO type excitations within adsorbate molecules. The quantum mechanical model assumes that the density of states follows a square root energy dependence, as shown in the right-most portion of Figure 2.10. When a generic adsorbate interacts with the surface the electronic structure changes, forming filled bonding states below the Fermi level and unfilled states above, shown in the left half of Figure 2.10. We model these as additional states below and above the Fermi level. The oscillator strengths are modified according to the following rules:

$$\text{Metal-metal:} \qquad S'_{l\to l+\Delta l} = S_0 \times N_{l\to l+\Delta l} \tag{2.30}$$

$$\text{Adsorbate-adsorbate:} \qquad S'_{l\to l+\Delta l} = S_0 \times \left(N_{l\to l+\Delta l} + N_{B\to AB}\right) \tag{2.31}$$

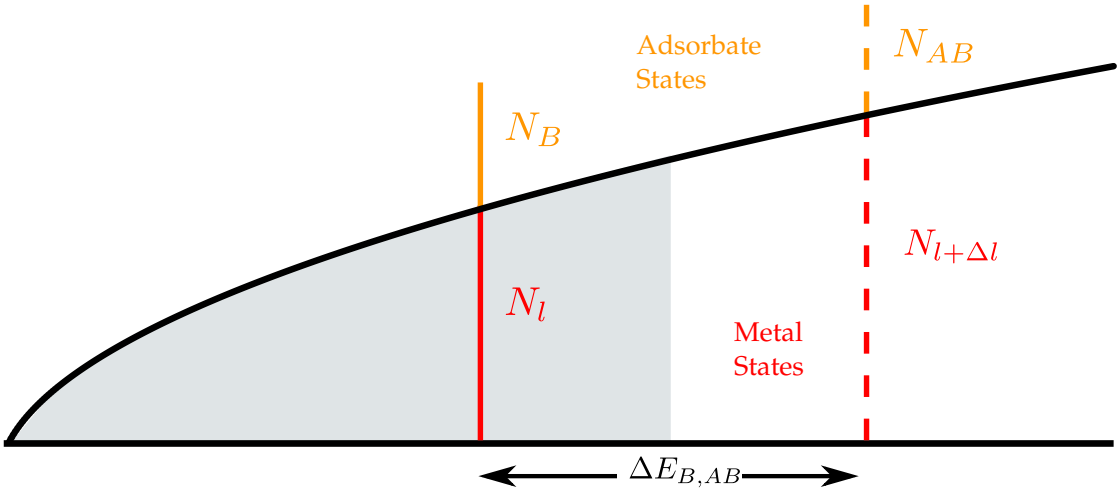

Figure 2.11: Schematic diagram of quantum model with added states. Shaded area depicts filled electronic states. Orange lines correspond to adsorbate bonding and antibonding states.

where $S_{l\to l+\Delta l}$ is the oscillator strength, $N_{l\to l+\Delta l}$ is the number of transitions from l to Δl, and $N_{B\to AB}$ is the number of transitions from adsorbate bonding to antibonding states. The oscillator strengths are normalized to one:

$$\sum_{l}\sum_{l+\Delta l} S'_{l\to l+\Delta l} = 1 \tag{2.32}$$

The result of this model is adding in intra-molecular electronic transitions from filled adsorbate states to unfilled adsorbate states. The energy of the bonding states, energy of the antibonding states, and the difference in energy between states can all be changed relative to each other and relative to the energy which exhibits plasmon resonance to understand the effects on the optical properties.

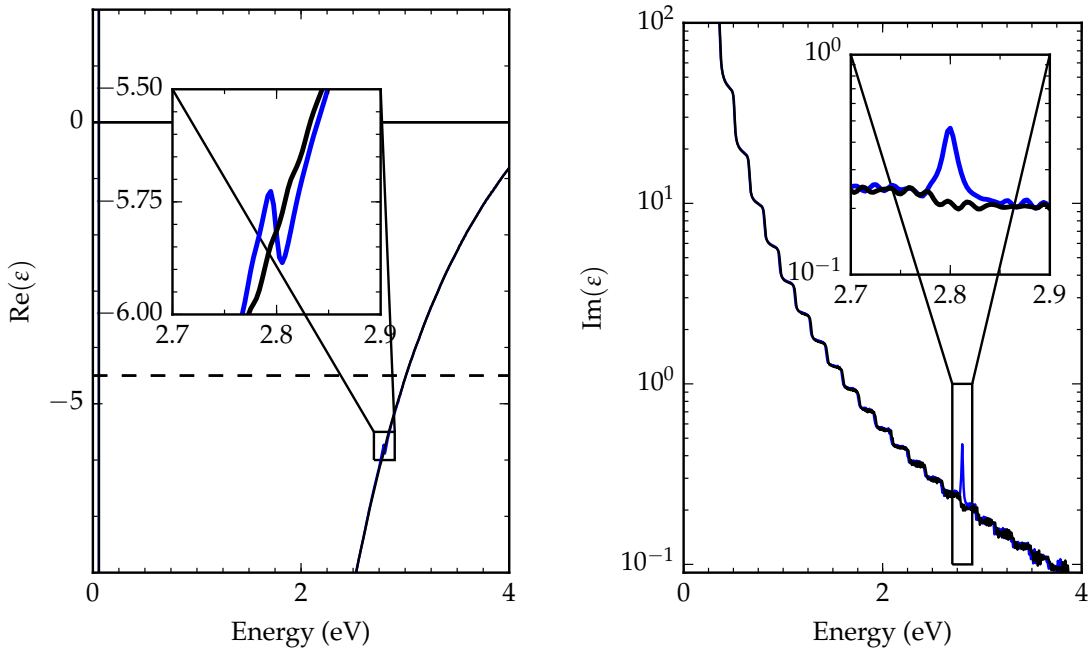

(a) (b)

Figure 2.12: Adsorbate-induced changes to the real (**a.**) and imaginary (**b.**) parts of the dielectric function for a 40nm silver nanocube. Adsorbate-adsorbate oscillator strength has been increased by a factor of five for illustrative purposes.

2.4.4.1 Impact on Dielectric Function

Using the updates to the quantum model through adding adsorbate states (see subsection 2.4.4) we simulated optical properties of a generic adsorbate on a metal nanoparticle to probe how the adsorbate transition energy changes the extinction through electric field enhancement. Changes to the dielectric function due to an inclusion of adsorbate states can be found in Figure 2.12. The adsorbate-adsorbate transition brings a peak in ε_2 and a wiggle in ε_1. This result is similar to the addition of Lorentz poles to the Drude model to account for interband (non sp-band to sp-band transitions) contributions, discussed in § 2.1. This implementation, however, is from first-principles and is directly dependent on the electronic structure

of the system.

The peak in the imaginary part of the dielectric corresponds to a larger number of single-electron transitions at that frequency – in addition to the metal-metal transitions, there are additional adsorbate-adsorbate transitions occurring. The wiggles in the real part of the dielectric function correspond to changes to the collective oscillation through changes in the response of the electron cloud due to the additional transitions – a phenomenon called chemical interface damping.[94]

2.4.5 Impact on Optical Properties

The results for adding states with a corresponding HOMO-LUMO excitation are found in Figure 2.13 for a 40 nm Ag nanocube. The three cases presented are (i) adsorbate states added with an excitation energy far from the plasmon resonance energy, (ii) adsorbate states added with some overlap between the intra-adsorbate transition and the plasmon peak, and (iii) adsorbate states added with an excitation energy very close to the plasmon peak. The top plot shows single-electron transitions, the middle plot shows the collective oscillation plasmon effect, and the bottom plot shows the extinction. The increase in the single-particle term (Figure 2.13, top) is similar between the three cases; an identical number of adsorbate bonding/antibonding states are added. The change in the plasmon effect (Figure 2.13, middle) is near negligible for the 2.8 eV HOMO-LUMO gap (blue), small for the 2.96 eV gap (green) and both increasing and decreasing for the 2.92 eV gap case (red) that lies around 0.01 eV of the plasmon peak. The calculations show that

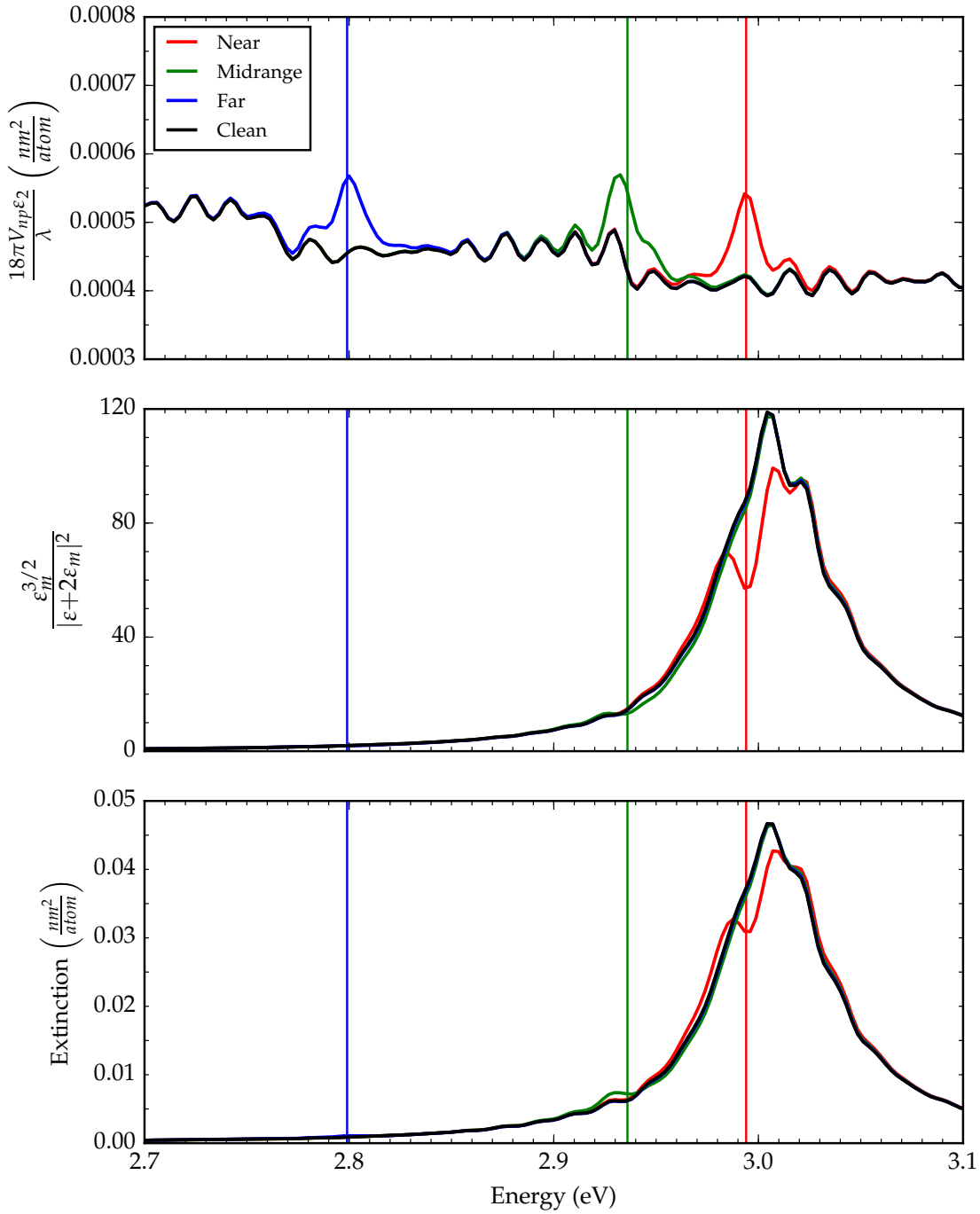

Figure 2.13: Changes to extinction for a 40 nm particle from adding bonding/antibonding states. The intra-state transition energy is sampled near to the plasmon energy (red), far away from the plasmon energy (blue) and midrange in between those two (green). Vertical lines depict the bonding/antibonding state excitation energy.

an adsorbate electron excitation energy located far from the plasmon peak (blue) only generates a minimal increase in the extinction. When the excitation energy lies closer to the peak, a slightly larger change in the extinction is shown, manifested as a peak in the extinction (Figure 2.13, bottom, green). Interestingly, the electric field effect is slightly decreased at the HOMO-LUMO energy. The added states increase the extinction below the transition energy and decrease the extinction above. The decrease in extinction is primarily due to a suppressed collective oscillation (larger ε_2, leading to a smaller denominator). When the adsorbate transition energy is moved even closer to the plasmon peak (red) this peak splitting becomes more evident with a larger suppression of the plasmon. In all cases, the changes result in roughly the same increase to the imaginary part of the dielectric – see the third plot. Despite a similar increase, the change in extinction – both increase and decrease – is magnified when the transition energy matches up well with the plasmon energy.

Extinction only captures one portion of the story: it measures how strong photon absorption is. Which transitions participate at energies (i.e. frequencies) near the plasmon peak is important in processes such as chemical interface damping, where the electron oscillation imparts a force (and thus, energy) into adsorbates through scattering an energetic electron across empty adsorbate states. Individual oscillator strengths in the summation in Equation 2.24 and Equation 2.25 can account for metal-metal or adsorbate-adsorbate transitions (neglecting transitions from the metal to the adsorbate and from the adsorbate to the metal). These two

transition types are separated:

$$\varepsilon(\omega) = \varepsilon_{\infty}(\omega) + \omega_p^2 \sum_{\Delta l}^{1,3,\ldots} \sum_{l}^{l_F} \frac{S_{l,\Delta l}}{\omega_{l,\Delta l}^2 - \omega^2 - i\omega\gamma_{l,\Delta l}} + \omega_p^2 \left(\frac{S_{B,AB}}{\omega_{l,\Delta l}^2 - \omega^2 - i\omega\gamma_{l,\Delta l}} \right) \tag{2.33}$$

assuming that all parameters such as the dipole damping constant, γ, remain the same. The oscillator strengths are again normalized to one. This separates the extinction into two terms; one is the interaction with metal electrons, one is interaction with adsorbate electrons Equation 2.34:

$$\sigma_{ext} = \frac{9\omega V_{np} \varepsilon_m^{3/2}}{c|\varepsilon + 2\varepsilon_m|^2} \left(\varepsilon_{2,metal} + \varepsilon_{2,adsorbate}\right) \tag{2.34}$$

The data in Figure 2.14a and Figure 2.14b show the contributions to the extinction cross-section from adsorbate-adsorbate and metal-metal transitions using Equation 2.34 for 20 nm and 40 nm particles, respectively, as a function of adsorbate-adsorbate transition energy: $\hbar\omega = E_{A,B\rightarrow A,AB}$ When this transition energy overlaps with the plasmon peak (just above 3 eV), there are more adsorbate-adsorbate transitions occurring.

This participation of an adsorbate-adsorbate transition is related to chemical interface damping where the collective oscillation decays to form a single energetic electron on an adsorbate.

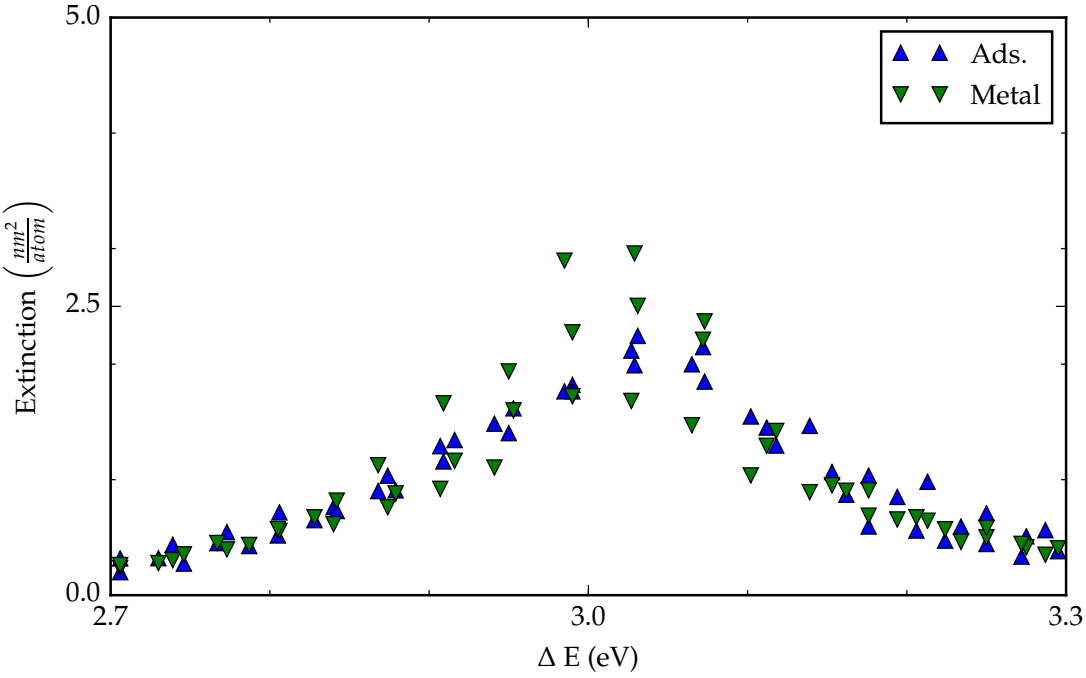

(a)

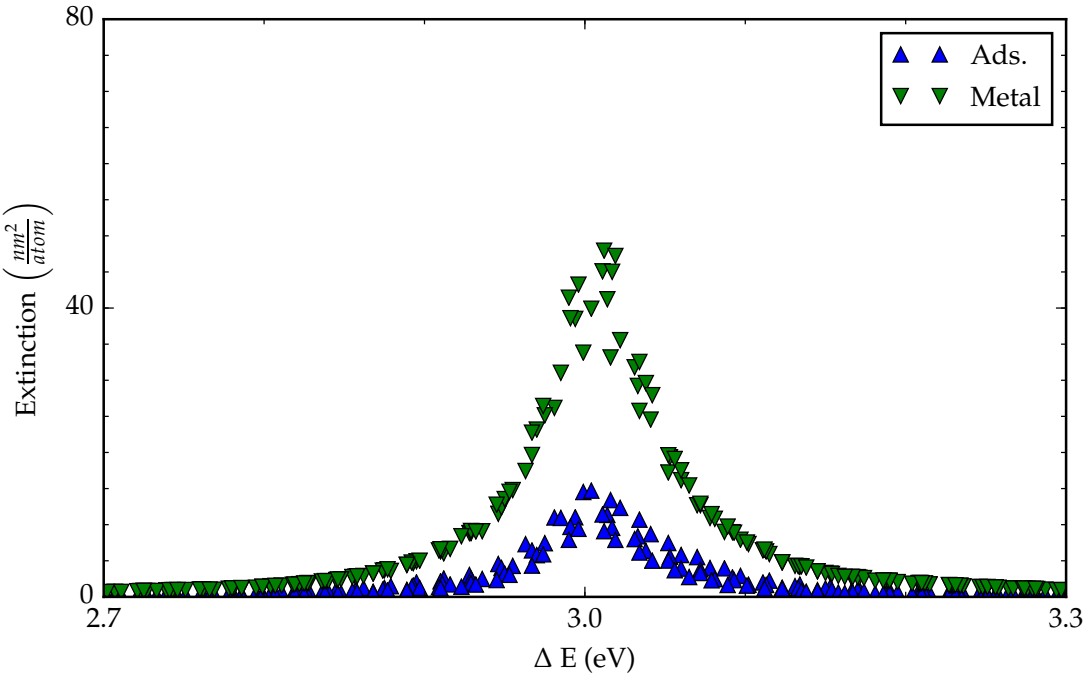

(b)

Figure 2.14: Separation of extinction into metal-metal and adsorbate-adsorbate contributions from the quantum mechanical added states model for a large number of initial (l) and final ($l + \Delta l$) states.

2.5 Energetic Charge-Carrier Formation

Adsorbate-induced changes to the extinction are observable from changes in the UV-Vis spectra. Changes to the formation of energetic electrons and holes (charge-carriers) are much more difficult to analyze. Using Fermi's golden rule and a charge-carrier lifetime (τ), the steady-state charge-carrier distribution can be calculated from the oscillator strengths [91]. This treatment includes contributions from the electric field – strong electric fields such as those triggered by a localized surface plasmon oscillation can drive the formation of charge-carriers. Using the oscillator strengths from the quantum model, we can calculate the energetic charge-carrier formation rate, Γ. The equation (adapted from Ref. [91]) is:

$$\Gamma = \frac{2}{\tau}\left(\frac{\hbar}{\tau}\frac{\varphi_{l,l+\Delta l} \times S_{l,l+\Delta l}}{(\hbar\omega - E_{l+\Delta l} - E_l) + \hbar^2\tau^{-2}}\right) \tag{2.35}$$

where $\varphi_{l,l+\Delta l}$ is the electric field enhancement of the oscillator strength, S; $\hbar\omega$ is the energy of the impinging electromagnetic disturbance, $E_{l+\Delta l}$ and E_l are the final and initial state energies, respectively, and τ is the electronic lifetime of 1 ps (taken from [91]). The electric field enhancement is calculated as:

$$\varphi_{l,l+\Delta l} = Z \times E \times \frac{2}{\pi^2}\frac{1}{(\Delta l)^2} \tag{2.36}$$

where Z is the particle thickness, E is the electric field, and Δl is the difference in initial and final quantum number. The frequency-dependent electric field contribution was was taken from finite-difference time domain simulations of Ag cubes

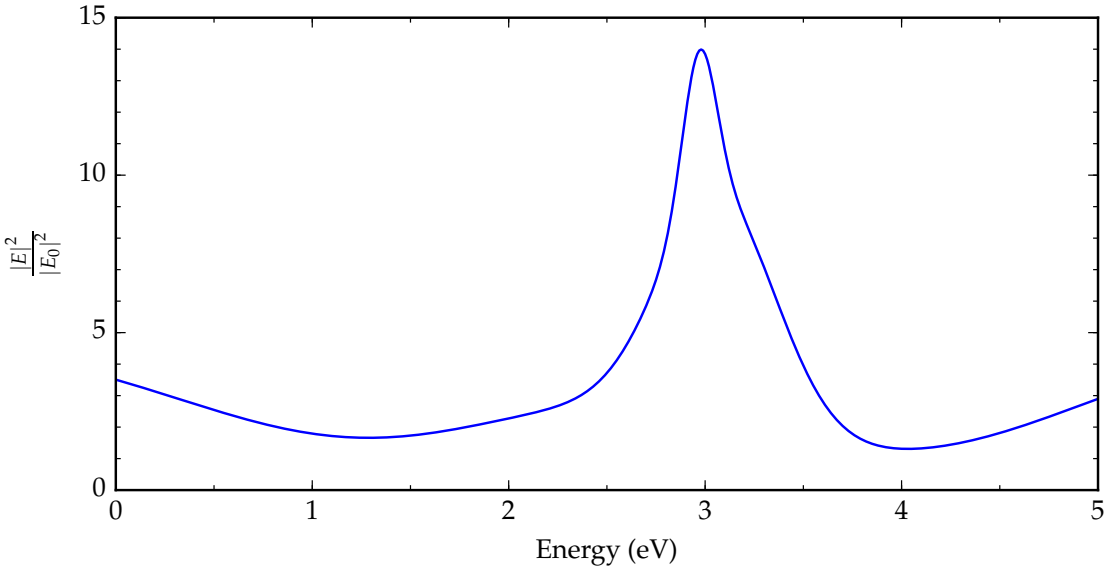

Figure 2.15: FDTD simulation results showing the surface-averaged electric field enhancement, $\frac{|E|^2}{|E_0|^2}$.

(see Appendix A). These electric fields are shown in Figure 2.15.

The electric field calculated for these simulations of 40 nm particles is strongest at the plasmon peak of 3.0 eV. The results for steady state electron distribution for both clean (green lines) and adsorbate-covered (blue lines) Ag are found in Figure 2.16. Solid lines represent the formation of energetic electrons; dashed lines represent the formation of holes. The clean nanoparticle shows the formation of large numbers of low energy electrons and holes near the Fermi level, with the formation rate decreasing for energies far away from the Fermi level. The addition of bonding and antibonding states leads to a corresponding increase in the formation of holes – at the bonding state energy – and energetic electrons – at the antibonding state energy. This increase corresponds to electronic excitation within the adsorbate between bonding and antibonding states, at 3.0 eV above the bond-

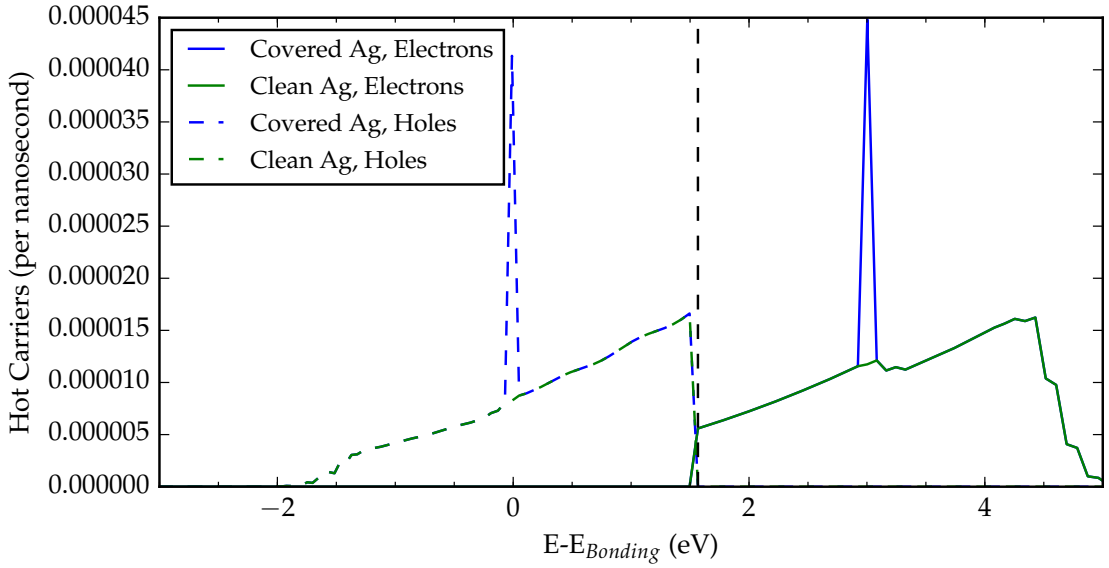

Figure 2.16: Steady-state electron distribution of clean and adsorbate-covered 40 nm Ag nanocubes. Energetic holes are formed at the location of added bonding states; energetic electrons are formed at the location of added antibonding states. The Fermi level is the vertical dashed line.

ing states – these bonding and antibonding state locations were chosen to match the plasmon energy.

To study the effects of relative LSPR energy and adsorbate excitation energy, the bonding orbital was held constant and a number of simulations run for antibonding states varying from 0.2 eV above the Fermi level to 3.2 eV above the Fermi level; the steady-state electron distributions are found in Figure 2.17. On one hand, a larger gap between bonding and antibonding states means a lower oscillator strength. On the other hand, if the energy (i.e. frequency) of the transition matches the energy (i.e. frequency) of the LSPR, the electric field enhances the formation of hot electrons by roughly a factor of 4. These results are in agreement with the previous sections: matching the energy of the transition with the plasmon

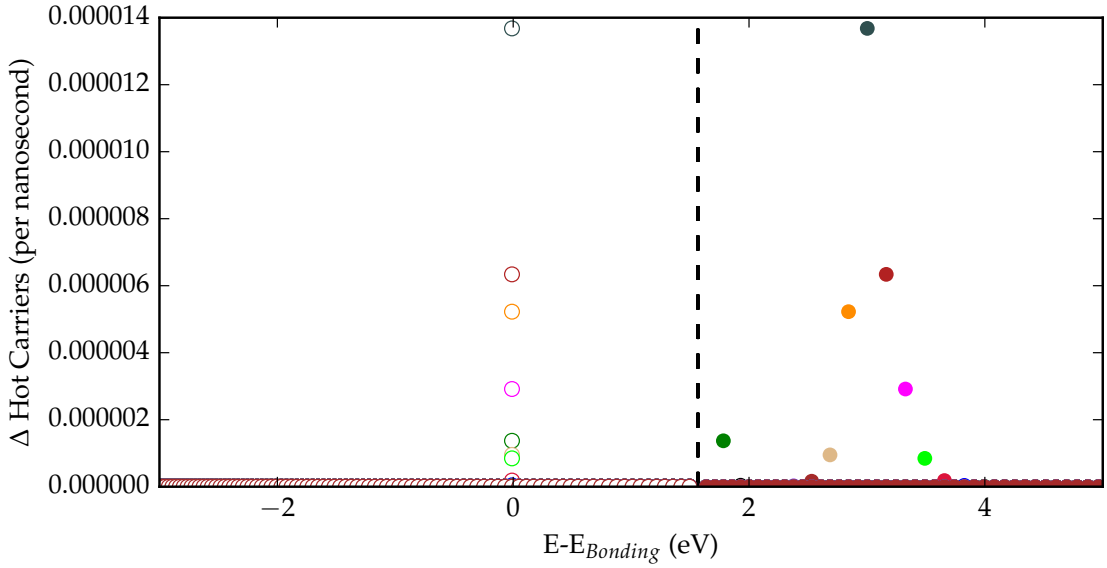

Figure 2.17: Change in charge-carrier formation rate plotted as a function of energy. Each color corresponds to a different anti-bonding state energy. Plasmon resonance energy is 3.0 eV, corresponding to maximum charge-carrier formation rate. Energetic charge-carrier formation is at a maximum when the frequency of electronic transition matches this plasmon resonance energy.

frequency gives the greatest channeling of energy between incoming photons and the formation of energetic charge carriers on the adsorbate.

2.6 Limitations

LSPR should preferentially operate on states on or near the surface; the delocalized nature of this model does not capture this effect. As such, a limitation of this model includes the electric field effects and plasmon resonance scaling with volume instead of surface area; the trends for adsorbate participation with respect to particle size are likely only qualitatively captured. The extinctions of large particles are likely overestimated relative to small particles, the effects scale with the volume of

the particle instead of surface area.

2.7 Summary

We have used a physically transparent quantum mechanical model to identify important descriptors in the properties of a plasmonic nanoparticle and developed an extension to review the effects of species adsorbed to the surface. We have demonstrated how smaller particles are dominated by higher-energy oscillations – for adsorbates that create states well above the Fermi level, adsorbate participation might be increased in small particles which show a greater affinity for the creation of higher-energy electron-hole pairs. We evaluated how this model changes in the presence of adsorbates on the surface – adding a monolayer of adsorbates increases the single-particle effect but dampens the collective oscillation. The overall combination of single-particle and electric field effects are critical to the optical response. Weak single-particle transition at the energy corresponding to LSPR is necessary for the plasmon condition but the overlap between adsorbate excitation energy and plasmon energy was shown to be the greatest factor in enhancing the extinction due to channeling energy into electrons scattering across adsorbate states. This framework also shows how to separate contributions to the extinction into single-particle and electric field (collective oscillation) contributions.

CHAPTER 3

Density Functional Theory

In this chapter we discuss a more rigorous model for the optical response of a metal nanoparticle using DFT. The simple quantum mechanical model discussed in chapter 2 treats electrons as non-interacting particles in an infinite potential well, with three independent spatial modes. With some simplifications, numeric solutions can be calculated for an electron density in a model system along with the response to an external optical stimulus.

DFT is a method for simplifying and obtaining numeric solutions for electronic wavefunctions for many-body systems, and is widely used to calculate geometries, adsorption energies, electronic structure, and optical spectra of various species (substrates, adsorbates, and complexes). We evaluate three case studies to study the plasmonic characteristics of metal nanoparticles, modeled as infinite slabs. The first case is to review the effect of metal substrate for Ag, Cu, and Pt to see the effects of the interband transition on optical properties. The second case is to add a simple adsorbate (H) to the surface to see how the optical properties change and the nature of electronic transitions. The third case is study the effects of introducing a more complex, strongly-bound adsorbate (O).

3.1 Schrödinger Equation

In any system of electrons, each electron has its own wavefunction that must satisfy the Schrödinger Equation (a more general form of Equation 2.9 [95]):

$$\hat{H}\Psi = E\Psi \tag{3.1}$$

where E is the electronic energy, Ψ are the wave functions, and $\bar{H}$ is the Hamiltonian operator. In practice, this is impossible to solve without making some approximations and simplifications. One approach is to gain analytical solutions, as seen in chapter 2. Another approach is to simplify the expression enough to allow for numeric solutions.

3.1.1 Born-Oppenheimer Approximation

Within the Born-Oppenheimer approximation atomic nuclei motion is separated from electronic motion and the electrons are approximated as moving through a static external potential, v:

$$E\Psi = \hat{H}\Psi = \left[\sum_{i=1}^{N}\left(-\frac{1}{2}\nabla_i^2\right) - \sum_{i=1}^{N} v\left(\mathbf{r_i}\right) + \sum_{i<j}^{N}\left(\frac{1}{r_{ij}}\right)\right]\Psi \tag{3.2}$$

where the Hamiltonian can also be written:

$$\hat{H} = T + V + U \tag{3.3}$$

where the first term is a kinetic energy operator, the second is an external potential operator including ion core-electron interactions, and the third is an electron-electron operator. Analytic solutions do not exist for most many-body systems, while numerical solutions – even to this simplified problem – are extremely computationally expensive due to the electron-electron term, scaling as $(3N)^3$.

3.1.2 Hohenberg-Kohn Theorems

Two theorems derived by Hohenberg and Kohn help reduce the computational difficulty of solving the many-body Schrödinger equation [96]. The first Hohenberg-Kohn (H-K) theorem states that the electron density, ρ, uniquely determines the external potential. It then follows that this electron density determines all properties of the system, including the many-body wave functions of the system and the ground state energy, E_v:

$$E_v[\rho] = T[\rho] + V[\rho] + U[\rho] \tag{3.4}$$

It follows that the system can be described as a density through 3-dimensional space instead of N particles in 3-dimensional space, shown in Figure 3.1.

The second theorem states that for an arbitrary density, the energy will always be greater than or equal to the real ground-state energy:

$$E_0 \leq E_v[\tilde{\rho}] \tag{3.5}$$

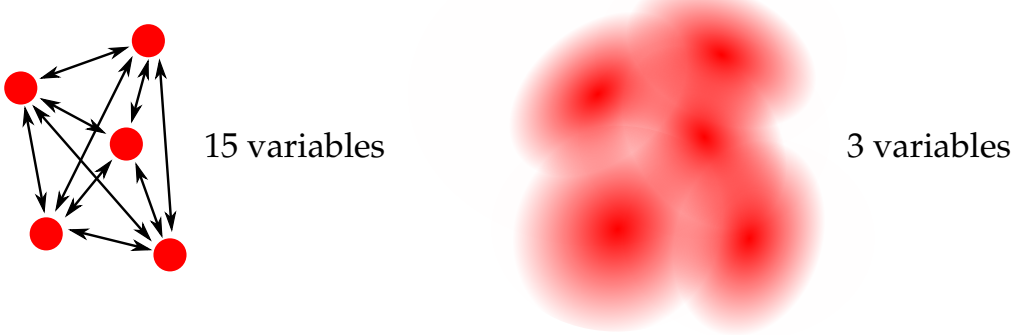

Figure 3.1: Schematic diagram showing a many-body problem (left) simplified to a density in 3-dimensions (right)

where $\tilde{\rho}(\mathbf{r})$ is any arbitrary non-negative density ($\tilde{\rho}(\mathbf{r}) \geq 0$) that comprises the correct number of electrons in the system $\int \tilde{\rho}(\mathbf{r})\, d\mathbf{r} = N$. Since the electron density uniquely defines the wave functions of the system, the arbitrary density is the exact ground-state density when the energy functional is minimized.

3.1.3 Kohn-Sham Equations

The Kohn-Sham approach is a way of transforming Equation 3.4 into something more easy to solve. It does this by separating terms into single-particle and correlation contributions. For example the kinetic and electron-electron operators are separated into:

$$T[\rho] = T_s[\rho] + T_c[\rho] \tag{3.6}$$

$$U[\rho] = U_H[\rho] + U_c[\rho] \tag{3.7}$$

where U_H is the Hartree potential; the potential operating on each electron with all others frozen. This gives the exact energy functional relationship:

$$E[n] = T[n] + U[n] + V[n] = T_s[n] + U_H[n] + E_{xc}[n] + V[n] \tag{3.8}$$

where the collective terms have been rolled in to a single 'exchange-correlation' term, E_{xc}. Numerous approaches exist to calculate this exchange-correlation term, each having strengths and weaknesses depending on the properties of the system. Some functionals work well for describing extended metallic systems while others work well for gas-phase isolated molecules; some functionals work well for calculating adsorption energies while others give better insight into electronic properties [97, 98, 99, 100, 101, 102]. Some further resources for the theory behind DFT include Density-Functional Theory of Atoms and Molecules [95], A Bird's-Eye View of Density-Functional Theory [103], and Solids and surfaces: A chemist's view of bonding in extended structures [74]. For a good resource on use and application of DFT, the reader is directed to Density Functional Theory: A Practical Introduction [104].

3.1.4 Dielectric Response

The electronic response of a system due to an external stimulus can be calculated using first-order perturbation theory in Linear-response time-dependent density functional theory (LrTDDFT). This section is drawn from numerous resources in literature [105, 106, 107, 108, 109, 110].

The polarizability of a many-body system, χ, is related to the independent single-body polarizabilities, χ_0 by Equation 3.9 [108]:

$$\chi = \left(1 - \chi_0 V_C - \chi_0 K_{xc}\right)^{-1} \chi_0 = \mathbf{A}^{-1} \chi_0 \tag{3.9}$$

where V_C is the Coulombic effect, K_{xc} is the change in the exchange correlation term for a perturbed electron density, and $\mathbf{A}$ is the combined matrix for inversion:

$$A_{\mathbf{G}\mathbf{G}'}\left(\mathbf{q}, \omega\right) = \delta_{\mathbf{G}\mathbf{G}'} - \chi^0_{\mathbf{G}\mathbf{G}'}\left(\mathbf{q}, \omega\right) \frac{4\pi e^2}{\left|\mathbf{q} + \mathbf{G}'\right|^2} - \sum_{\mathbf{G}''} \chi^0_{\mathbf{G}\mathbf{G}''}\left(\mathbf{q}, \omega\right) K_{xc}\left(\mathbf{G}'' - \mathbf{G}'\right) \tag{3.10}$$

K_{xc} is the derivative of the exchange-correlation contribution with respect to the electron density at the initial and final states:

$$K_{xc}\left(\mathbf{r}, \mathbf{r}'\right) = \frac{\delta^2 E_{xc}}{\delta\rho\left(\mathbf{r}\right) \delta\rho\left(\mathbf{r}'\right)} \tag{3.11}$$

The independent-particle polarizabilities are found using Equation 3.12:

$$\chi^0_{GG'}\left(\mathbf{q}, \omega\right) = \frac{2}{\Omega} \sum_{n,n',\mathbf{k}} \frac{f_{n,\mathbf{k}}\left(1 - f_{n',\mathbf{k}+\mathbf{q}}\right)}{\omega + \varepsilon_{n,\mathbf{k}} - \varepsilon_{n',\mathbf{k}+\mathbf{q}} + i\eta} \left(\langle n, \mathbf{k} | e^{-i(\mathbf{q}+\mathbf{G})\cdot r} | n', \mathbf{k}+\mathbf{q}\rangle \langle n', \mathbf{k} | e^{-i(\mathbf{q}+\mathbf{G}')\cdot r'} | n, \mathbf{k}\rangle + c.c.\right) \tag{3.12}$$

with complex conjugate (c.c.), $\mathbf{q}$ is the wave vector of the incident electromagnetic wave, $\mathbf{G}$ is reciprocal lattice vector, $\mathbf{k}$ is a wave vector of electronic states, f is occupation number, ω is the frequency of the incident electromagnetic wave (related

to the energy difference) and Ω is the crystal volume.

This expression bears similarities to the quantum mechanical dielectric function (see Equation 2.21); the sum is over transitions from filled states, n, to unfilled states, n', and the denominator gets very small (and the polarizability large) when the frequency of the incoming stimulus, ω, matches the transition frequency from electronic state with initial energy level, n, and momentum, $\mathbf{k}$, to $n', \mathbf{k}+\mathbf{q}$.

The response in electron density, $\chi_{\mathbf{GG'}}$ due to the polarization from incoming light, can be calculated from Equation 3.10 and Equation 3.12:

$$\chi_{\mathbf{GG'}}\left(\mathbf{q},\omega\right)=\sum_{\mathbf{G''}}\mathbf{A}^{-1}_{\mathbf{GG''}}\left(\mathbf{q},\omega\right)\chi^{0}_{\mathbf{G''G'}}\left(\mathbf{q},\omega\right) \tag{3.13}$$

The dielectric matrix is calculated from this density response function:

$$\epsilon^{-1}_{\mathbf{GG'}}\left(\mathbf{q},\omega\right)=\delta_{\mathbf{GG'}}+\frac{4\pi}{\left|\mathbf{q}+\mathbf{G}\right|^{2}}\chi_{\mathbf{GG'}}\left(\mathbf{q},\omega\right) \tag{3.14}$$

The macroscopic dielectric function is calculated from this [108]:

$$\epsilon_{M}\left(\mathbf{q},\omega\right)=\frac{1}{\epsilon^{-1}_{00}\left(\mathbf{q},\omega\right)} \tag{3.15}$$

The extinction spectrum with electric field effect is calculated in the optical limit ($\mathbf{q}\rightarrow 0$, as $\left|\mathbf{q}+\mathbf{G}\right|^{-2}$ diverges when $\mathbf{q}$,$\mathbf{G}$ are both zero):

$$\text{Extinction}=\text{Loss Function}=-Im\frac{1}{\epsilon_{M}\left(\mathbf{q}\rightarrow 0,\omega\right)}=\frac{\varepsilon_{2}}{\varepsilon_{1}^{2}+\varepsilon_{2}^{2}} \tag{3.16}$$

The absolute value of this loss function allows us to quantitatively compare results between different metals and different adsorbates. This equation is similar to Equation 2.26; DFT treatment explicitly handles the dielectric function of the vacuum; that is, it already includes the dielectric function of the surrounding medium (vacuum). The corresponding plasmon condition for DFT-calculated systems using Equation 3.16 is therefore $\varepsilon(\omega) = 0$ [111]. For DFT we define slightly different single-particle (Equation 3.17) and electric-field effects (Equation 3.18):

$$\text{Single-particle term} = \varepsilon_2 \tag{3.17}$$

$$\text{Electric field term} = \frac{1}{\varepsilon_1^2 + \varepsilon_2^2} \tag{3.18}$$

3.2 Computational Details

Three steps are needed to properly set up the model system and calculate optical properties. First, the system is allowed to relax (move) to minimize the interatomic forces between atoms to find the lowest energy geometry. During this step, the two innermost layers are set at the bulk lattice constant and not allowed to relax. Second, the model system is solved with a higher plane wave cutoff energy, finer k-point sampling, higher accuracy exchange-correlation functionals, etc. to obtain better electronic structure information for obtaining the electronic response. Third, the linear response calculation is performed on this ground state system to

calculate the electronic response and optical properties.

DFT calculations were performed using the grid-based projector augmented wavefunction code implemented in GPAW [111, 112]. Hydrogen was placed on surface face-centered cubic (fcc) sites (hexagonal close-packed (hcp)) sites and top sites were also tested and had a lower affinity for hydrogen) on both the bottom and top surfaces. With both surfaces covered, the optical properties resulting are only for an adsorbate-covered surface. If only one surface contains adsorbates, the resulting optical properties are a combination of two infinite surfaces: one fully clean surface and one covered surface.

Model systems were 1x1x6 slabs, shown in Figure 3.2. Systems were allowed to relax until the forces on each atom were below 0.05 eV. The middle two layers were fixed at bulk geometry; the top two layers on each side allowed to relax. A vacuum layer of 16 Å was inserted in the direction perpendicular to the surface to decrease communication between neighboring unit cells. A 8x8x1 Monkhorst-Pack grid was used for sampling k-points in the Brillouin zone for relaxation. The Local Density Approximation (LDA) functional was used to approximate exchange and correlation effects [113]. Fermi smearing was applied at an electronic temperature of 0.05 eV to aid convergence, and only occupied bands were converged. In plane wave mode, wave functions were expanded in plane waves with a cutoff energy of 500 eV; results were converged with respect to increasing plane wave cutoff energy.

After geometry optimization, the system was reconverged for more thorough electronic structure detail. The vacuum distance between parallel slabs was increased to 30 Å and a 100x100x1 Monkhorst-Pack grid was used for sampling k-

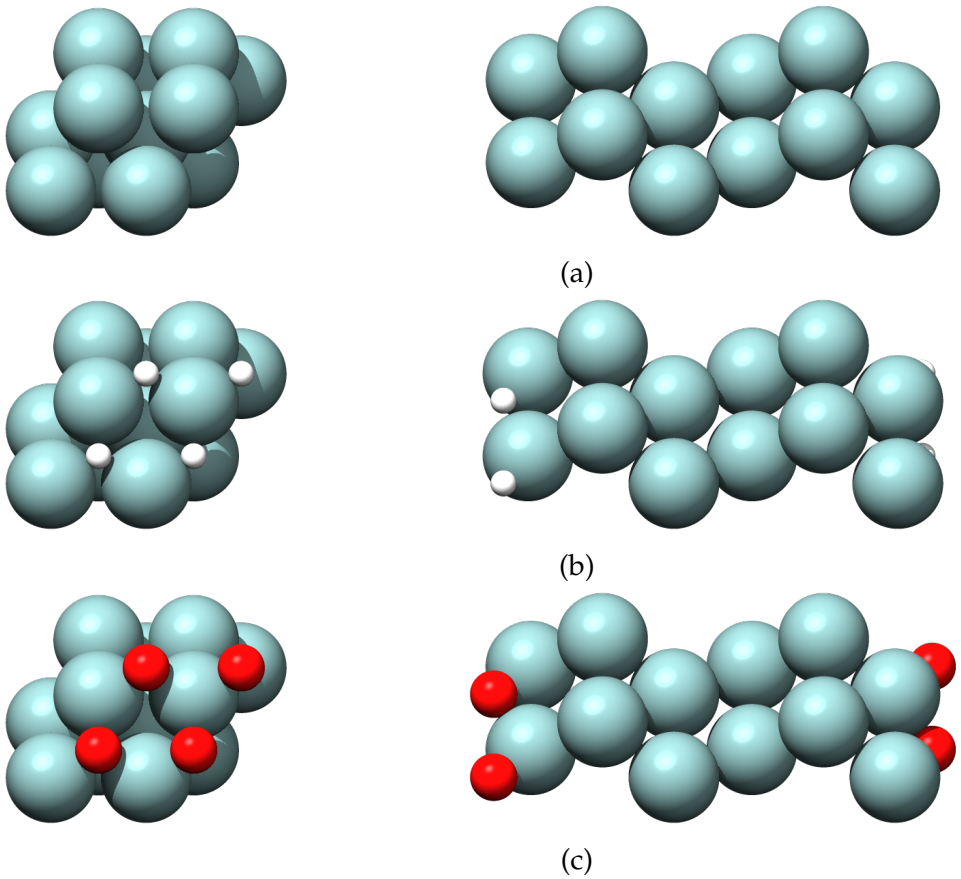

Figure 3.2: Density Functional Theory model system (left) top view and (right) side view. The model system visualization is repeated twice in x and y dimensions to show symmetry. **a.** 6 layer Ag slab. **b.** 6 layer Ag slab with a monolayer of H. **c.** 6 layer Ag slab with a monolayer of O.

points in the Brillouin zone. For optical simulations we use the LDA exchange-correlation functional [113] and the modified GLLB-SC functional for its improved treatment of Ag d bands [111, 114, 115]. Fermi smearing was applied at an electronic temperature of 0.05 eV. For Ag, 120 bands were included in the calculation; for Cu, 90 bands were included in the calculation; for Pt, 122 bands were included. These numbers included all bands up to 15 eV above the Fermi level. A diagonalization of the full Hamiltonian was performed after the system converged, giving a more robust approach for unoccupied states above the Fermi level.

3.2.1 Linear Response Time-Dependent DFT

Optical response DFT calculations were performed with the LrTDDFT code for extended surfaces in GPAW [111]. The EELS loss spectra was calculated by GPAW with an initial frequency grid spacing (at $\omega = 0$) of 0.01 eV and a broadening factor of 0.05 eV. For EELS calculations, the momentum was sampled in increments of q = 0.025 $Å^{-1}$ corresponding to the inverse distance between k-points. Both EELS and the dielectric function were performed with an energy cutoff of 500 eV – the calculations were converged with respect to cutoff energy.

3.3 Results

We analyze three different case studies; the first is to study the changes to optical properties by changing the metal element from Ag to Cu and Pt. The second case study probes the effect of adding an adsorbate, Hydrogen, to the surface that only

induces minor changes in the electronic structure. The third case is to introduce an adsorbate, Oxygen, that incudes much larger changes in the electronic structure.

3.3.1 Effect of Metal Element

The first case study is to look at the plasmon properties for Ag, Cu, and Pt slabs and comparing the effect between metals. These calculations were performed on 6 layer pure metal slabs using the modified GLLB-SC exchange correlation functional [114, 115].

3.3.1.1 Dielectric Function

Calculated dielectric functions for 6 layer slabs are found in Figure 3.3. The real dielectric functions for Ag and Cu are very similar, predicting a plasmon peak for both around 3.5 – 4.5 eV; for Pt, the real part of the dielectric does not reach zero and there is no well-defined peak below 5 eV. The similarities in the real part of the dielectric function for Ag and Cu suggest that differences in the imaginary part of the dielectric function will drive extinction differences.

The imaginary part of the dielectric function shows the presence of strong interband transition for platinum over the whole range, a somewhat weaker one for copper beginning at around 2.5 eV and an even weaker one for silver beginning at around 3.5 – 4.0 eV. The peak in Ag at 3.5 eV is due to an interband transition from Ag d states to the Ag sp band.

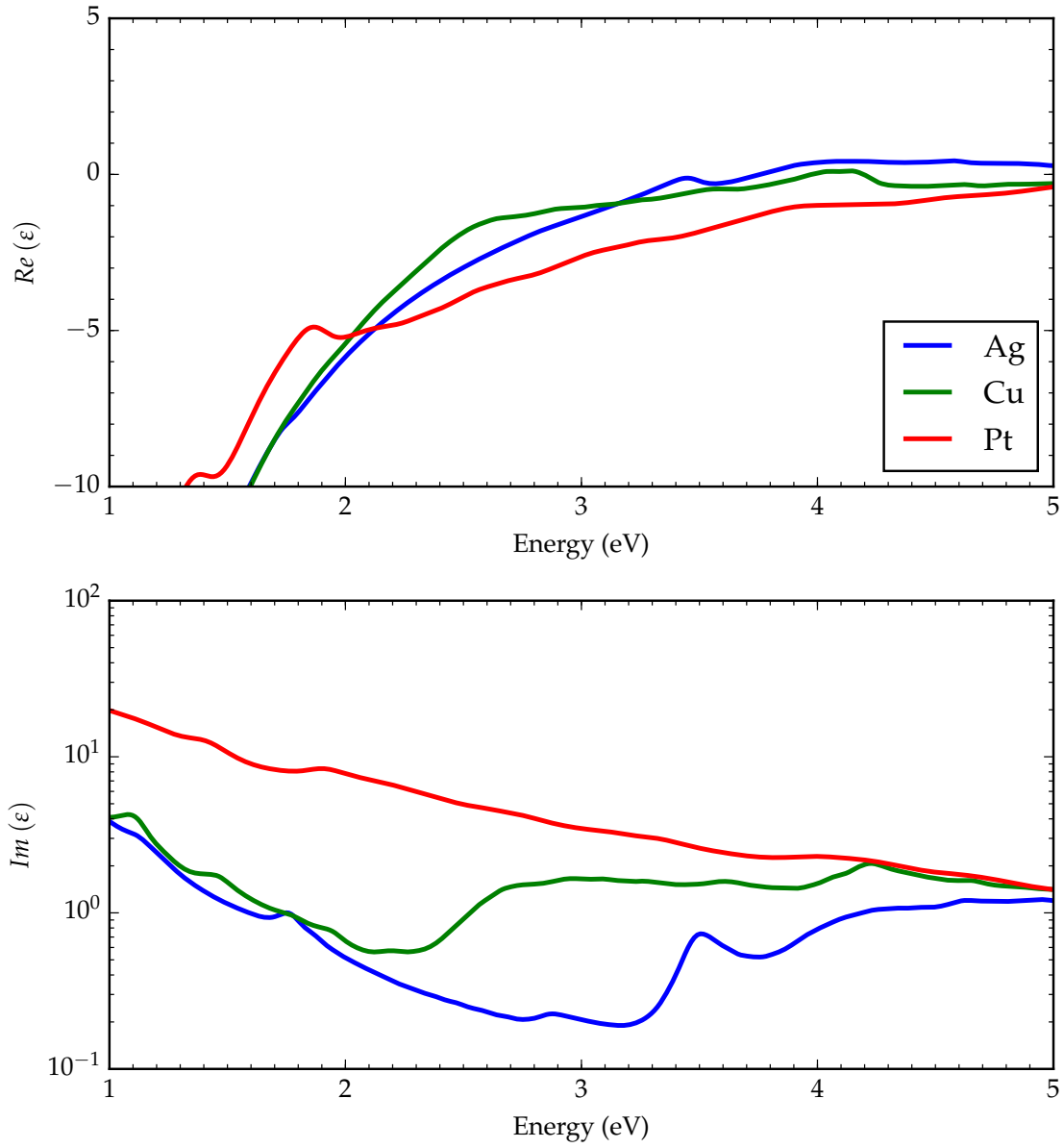

Figure 3.3: DFT-calculated real (top) and imaginary (bottom) dielectric functions for 6 layer clean Ag slab and H-covered Ag slab. Peaks in the imaginary part of the dielectric from 2.0 – 3.5 eV correspond to electronic transitions from H to Ag; the peak around 4.5 eV is an Ag d-band to Ag sp-band interband transition.

3.3.1.2 Optical Properties

Calculated extinction plots with electric field and single-particle effects for each of the three metals are found in Figure 3.4. The extinction for silver is roughly twice as large compared to copper and platinum. The driving force behind this is the electric field effect, plotted in the second pane of Figure 3.4. With the real part of the dielectric being largely similar between the two metals, the difference in Ag and Cu is primarily due to the larger interband transition suppressing the plasmon peak. There is no clear surface plasmon resonance for Pt, with it being suppressed by the presence of the interband transition.

The origin of the single-particle peaks in the bottom frame of Figure 3.4 is clear from the atomic projected density of states, found in Figure 3.5. The peak for Ag at around 3.5 eV is an intraband transition from Ag sp states at the Fermi level to Ag sp states well above the Fermi level. The peak for Cu at around 4.2 eV is the corresponding transition from filled sp states to unfilled sp states, with the band located slightly higher for Cu.

The electronic structures of Ag and Cu are quite similar; the largest difference is in the lower energy for onset of the interband transition for Cu; this leads to a much weaker plasmon resonance. Platinum's interband is much stronger and very broad compared to either Ag or Cu and causes no clear plasmon peak.

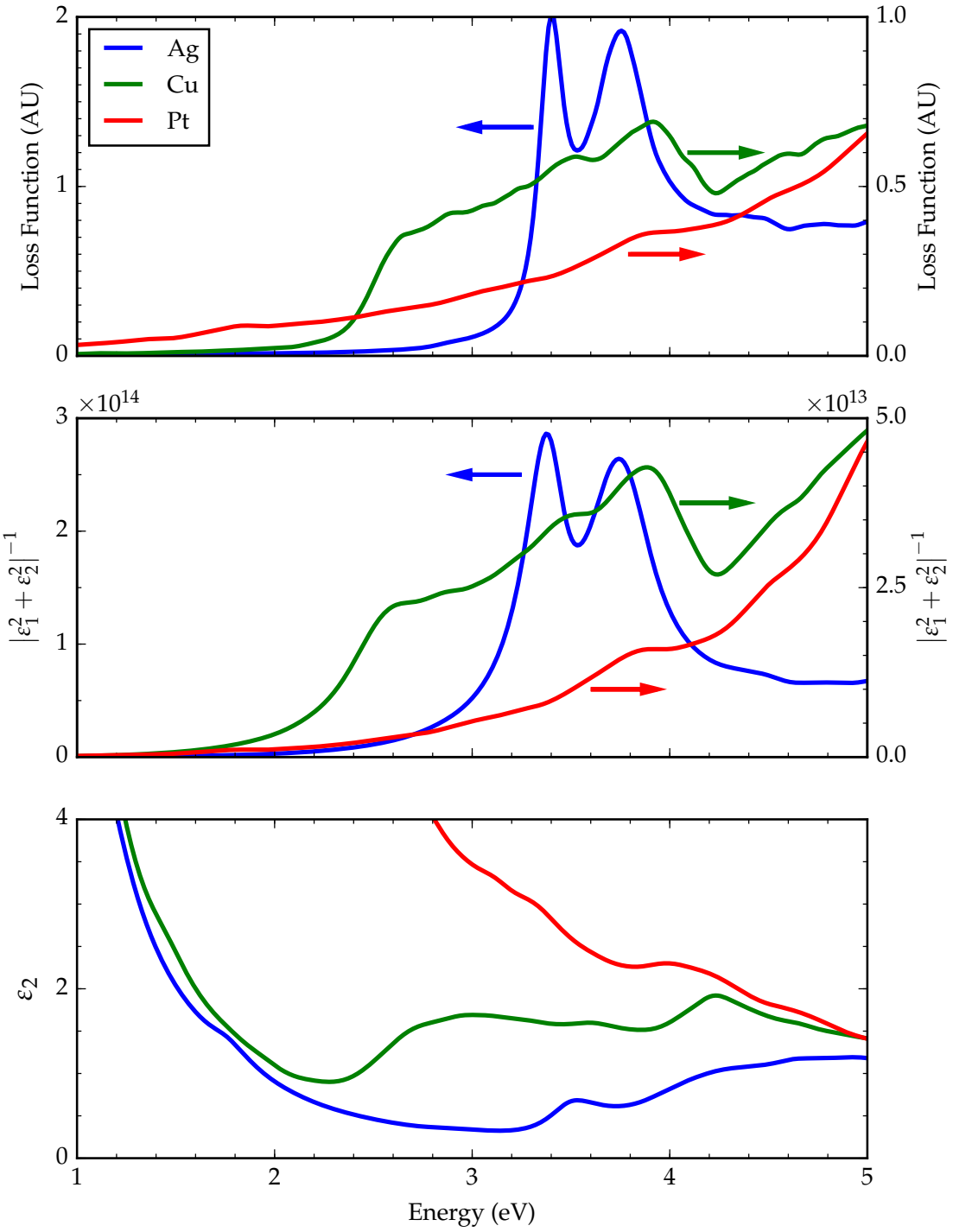

Figure 3.4: DFT-calculated spectrum (top) with electric field (middle) and single-particle (bottom) effects for Ag, Cu, and Pt. The Ag spectrum is larger than Cu and Pt by a factor of ~ 2, primarily due to the interband transition suppressing surface plasmon resonance.

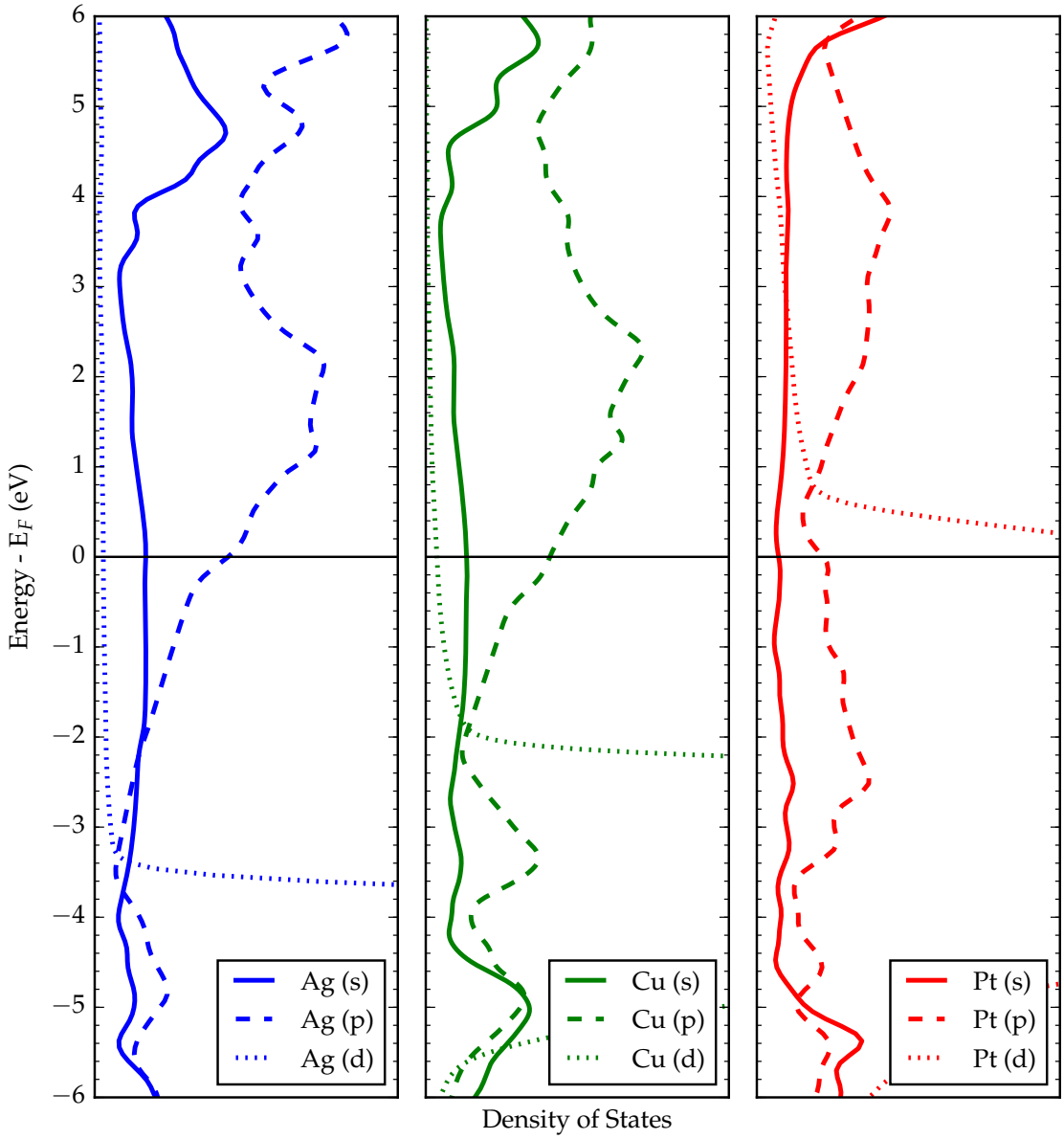

Figure 3.5: Ag (left), Cu (middle), and Pt (right) projected DOS for s orbitals (solid), p orbitals (dashed) and d orbitals (dotted). Ag and Cu are very similar below 4 eV except for d-band location; -2 eV for Cu, -3.8 eV for Ag. Pt d-band has states at E_F, these are responsible for the low interband transition energy.

3.3.1.3 Single-Particle Transitions: Electronic Structure Properties

Bands can run – that is, increase or decrease energy – through *k*-space (see Figure 1.8). The energy differences for vertical transitions (i.e. transitions go from one band to another without changing location in *k*-space – the optical stimulus imparts no momentum into the electronic excitation and an electron is promoted from a band in reciprocal space **k** to a different band at the same point in reciprocal space) as well as other transitions (i.e. where an electron is promoted from a band in reciprocal space **k** to a different band at $\mathbf{k} + \mathbf{q}$ by the electron momentum **q**) are dependent on the position in k-space, and can be investigated by evaluating the differences in eigenvalues (that is, differences in energy between states) at specific points in k-space (see subsection 1.3.2). As a result, the DOS plots above do not contain explicit information for these transitions.

To visualize this information, we use transition plots, as depicted in Figure 3.6, for a 6-layer Ag slab. The top half of each plot is a histogram of the relative energy differences between bands (normalized, arbitrary units), overlaid with the imaginary part of the dielectric function (single-electron transitions, depicted by the solid black line).

Peaks in the histogram have a possible link to peaks appearing in ε_2 at the same energy. The histograms are constructed by counting the number of points throughout the reducible Brillouin zone (k-space) where an electron can transition from a filled band below the Fermi level to unfilled bands above the Fermi level. To obtain results in the reducible Brillouin zone, the quantum-chemical calculation

results in the irreducible Brillouin zone are multiplied by the k-point weights (i.e. the number of places in k-space that have the same symmetry as the point in the irreducible Brillouin zone). Responsible bands are identified in the band structure in the bottom half of the transition plot; the solid black line is the initial state; colored lines indicate the final states.

Figure 3.6 shows a transition plot for transitions originating from the highest energy d-band. Counts for the histogram are only tallied where the initial states are empty and the final states are filled. The entire first Brillouin zone is counted; this includes many points not along the x-axis in Figure 3.6b. This analysis only tracks the energy differences between states, the propensity of each transition is not accounted for. As an initial study, we focus on vertical transitions; further studies could investigate the momentum dependence, where $\mathbf{q} \neq 0$.

Figure 3.6 comprises a transition plot for the interband transition; electronic excitation from the d band to unfilled sp states. The histograms in the top frame (colored lines) show the relative energy difference between filled and unfilled states throughout the first Brillouin zone. Overlaid on the transition plot is the imaginary part of the dielectric function overlaid for comparison between the transition energies and peaks in the extinction from single-particle transitions.

The imaginary part of the dielectric function (black line in Figure 3.6a) shows the interband transition taking off between 3.5 and 4 eV, as well as a small single peak at 3.5 eV. Transitions occurring for the broad interband transition are visualized in Figure 3.7. These transitions comprise electron donation from well below the Fermi level ($\sim$ 3.70 eV) to just above the Fermi level ($\sim$ 0.30 eV). One such in-

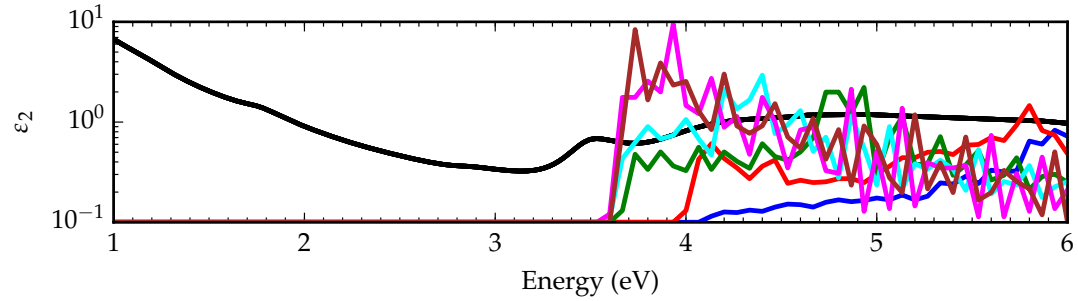

(a)

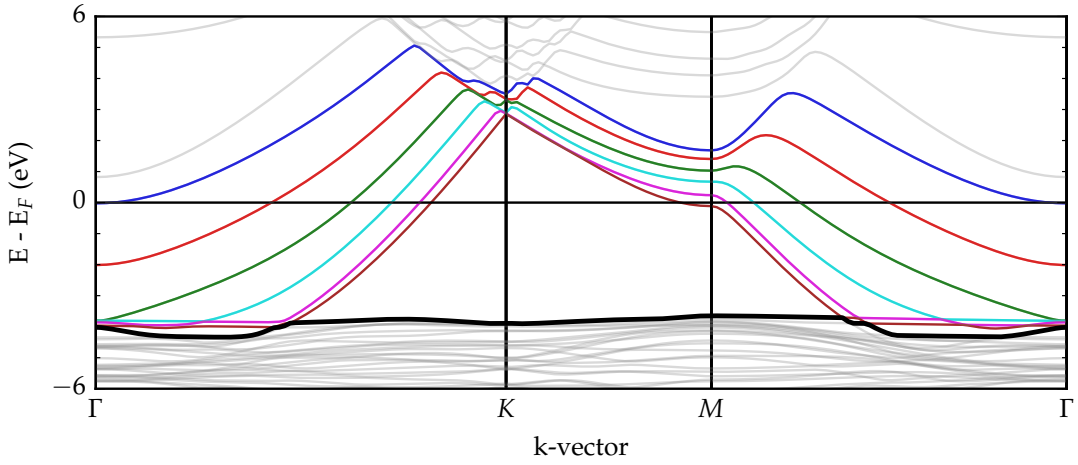

(b)

Figure 3.6: **a.** Transition plot shows energy difference between Ag d-states and Ag sp bands (colored lines) is over 3.6 eV. **b.** Band structure showing d states (thick black band around -4 eV) and silver sp states (purple, magenta, cyan, green, red, blue) – colors correspond to histograms in **a.**.

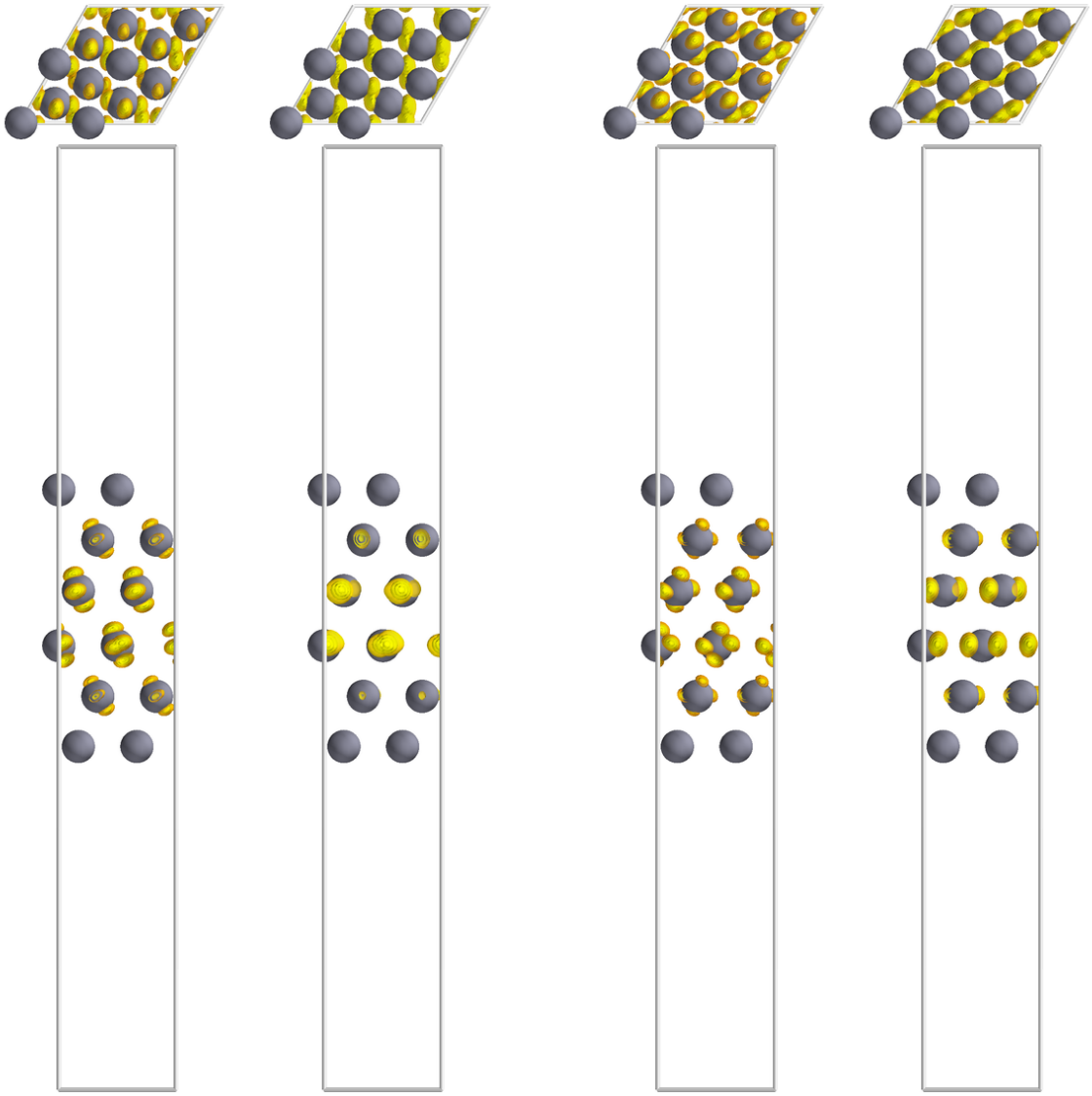

(a) Figure 3.6 Black -3.70 eV

(b) Figure 3.6 Maroon 0.30 eV

(c) Figure 3.6 Black -3.71 eV

(d) Figure 3.6 Maroon 0.29 eV

Figure 3.7: Wavefunction visualization: interband transition. These comprise excitations from Ag d-states (**a.**, **c.**) to delocalized Ag sp states (**b.**, **d.**). Wavefunctions visualized in k-space where the bands differ in energy by the transition energy of $\sim$ 4.0 eV. Wavefunctions output in k-space at an energy difference between filled and unfilled states where the interband transition appears in the imaginary part of the dielectric; $\sim$ 4.0 eV.

terband transition is an electronic excitation from states visualized in Figure 3.7a to states visualized in Figure 3.7b. This transition (and similarly, the transition from states in Figure 3.7c to Figure 3.7d and two more in Figure 3.8) has an energy of around 4 eV; this difference is energetic enough to satisfy the broad interband transition peak. From the band structure and the wavefunction visualizations, these transitions are from localized d-states to more delocalized bulk metal states.

There is also a small apparent peak at around 3.5 eV in the imaginary part of the dielectric; the transition plot identifying this transition is found in Figure 3.9. The localized visualization of the states show this peak is from two similar bands running in the same direction across k-space. Both electron-donating and electron-accepting states comprise primarily Ag states with sp-character; visualizations are found in Figure 3.10. The single-electron peaks seen on clean silver at energies above 2 eV are all interband transitions from either d-states to sp-states or intraband transitions between sp-states. Introducing new adsorbate states to the system will change the states available for electron donation and electron reception and open up more pathways for hot electron formation.

3.3.2 Effect of Weakly-Bound Adsorbate

The second case study we evaluated observed the effects of adding an adsorbate to the surface, inducing relatively small changes into the substrate – hydrogen. These calculations were performed on 6 layer pure metal slabs using the modified GLLB-SC exchange correlation functional [114, 115]. A single monolayer of Hydrogen

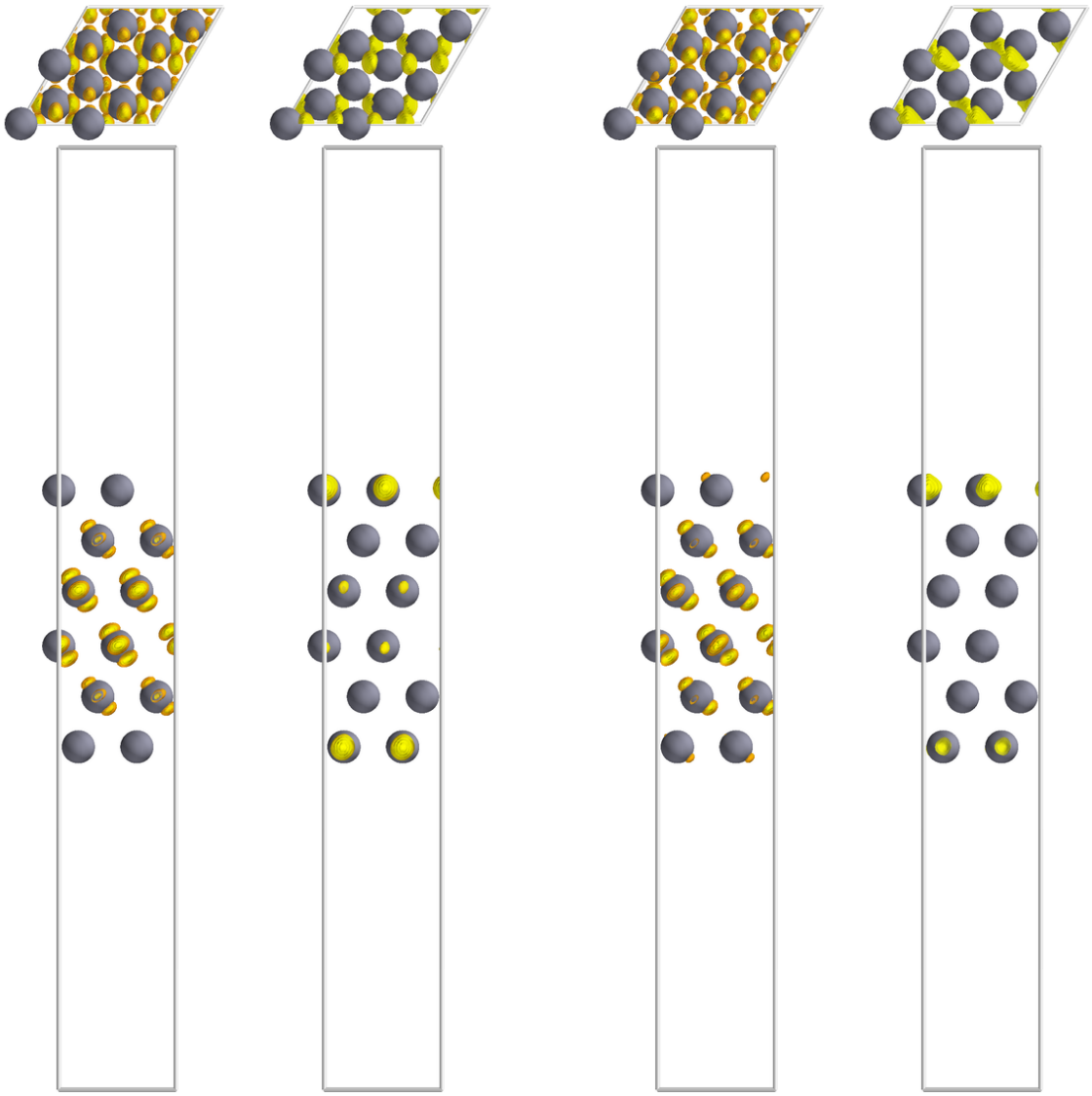

(a) Figure 3.6
Black
-3.68 eV

(b) Figure 3.6
Cyan
0.31 eV

(c) Figure 3.6
Black
-3.72 eV

(d) Figure 3.6
Green
0.28 eV

Figure 3.8: Wavefunction visualization: interband transition. These transitions are functionally similar to Figure 3.7; excitations from Ag d-states (**a.**, **c.**) to delocalized Ag sp states (**b.**, **d.**). Wavefunctions output where the bands differ in energy by the transition energy of ~ 4.0 eV.

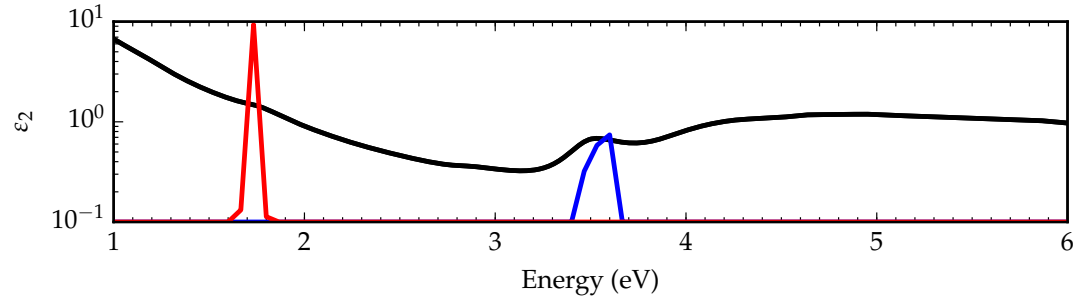

(a)

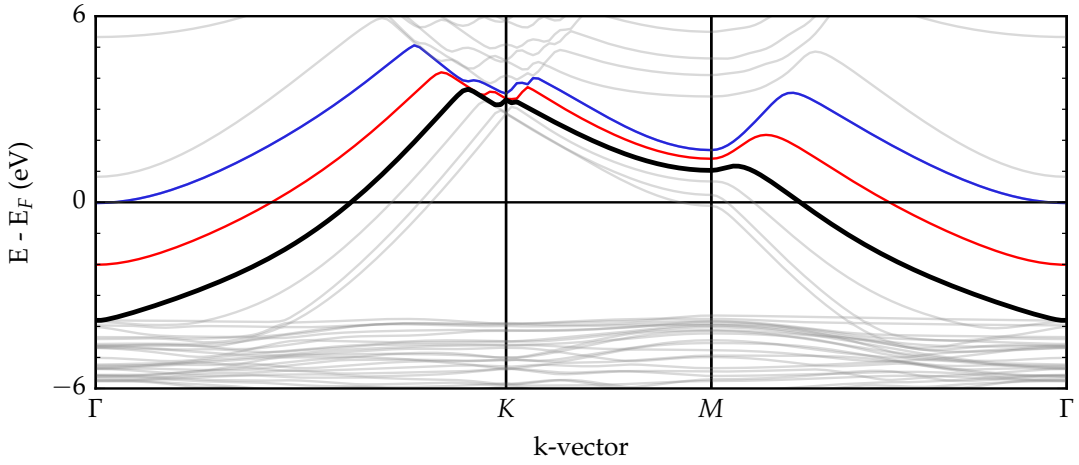

(b)

Figure 3.9: **a.** Transition plot shows energy difference between a lower-energy Ag sp-band **b.**, black line) and two higher energy sp-bands (**b.**, red and blue lines). Transitions from the lower-energy Ag sp-band to the blue band appear at around 3.5 eV, matching a peak in the imaginary part of the dielectric function. **b.** Band structure highlighting Ag sp states – colors correspond to histograms in **a.**

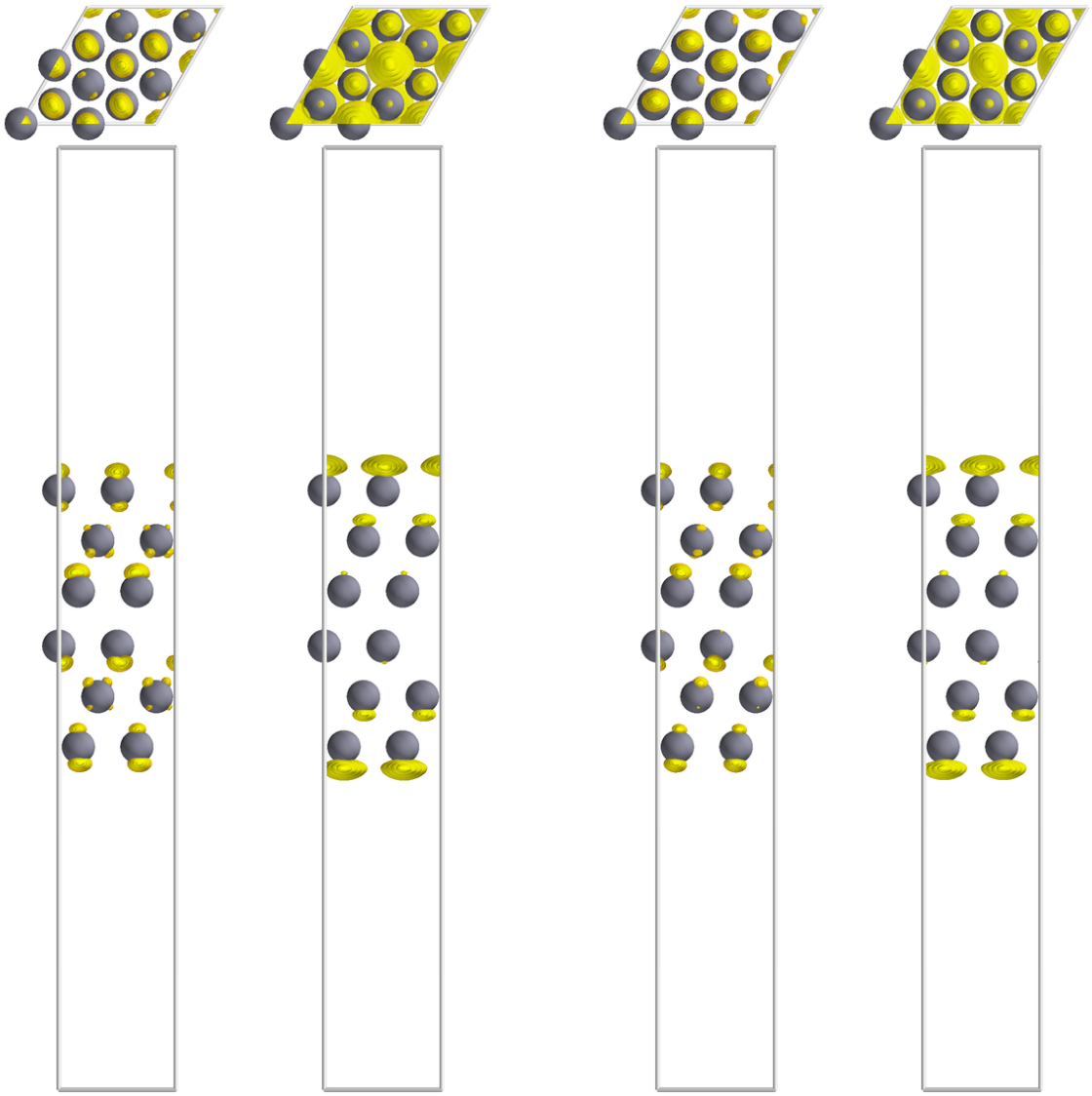

(a) Figure 3.9
Black
-2.86 eV

(b) Figure 3.9
Blue
0.64 eV

(c) Figure 3.9
Black
-3.70 eV

(d) Figure 3.9
Blue
0.30 eV

Figure 3.10: Wavefunction visualization: interband peak. The donating state (**a.**, **c.**) appears to have some Ag d character; the accepting state (**b.**, **d.**) has no apparent d-character. Wavefunctions output when the energy difference between filled donating and empty accepting states is ~ 3.5 eV.

was added at the three-fold high-symmetry fcc hollow site which relaxed to M-H bond distances of 1.861 Å, 1.690 Å, and 1.847 Å for Ag, Cu, and Pt, respectively. Electronic adsorption energy was calculated to be -0.20 eV, -0.50 eV, and -0.84 eV per hydrogen atom on each metal, respectively.

3.3.2.1 Impact on Dielectric Function

The calculated real and imaginary dielectric function contributions for H-covered single-monolayer slabs of 6 layers (Ag/H, Cu/H, Pt/H) are found in Figure 3.11. The real part of the dielectric function shows the emergence of wiggles introduced by new adsorbate states (e.g. just above 2 eV for both Ag and Cu) accompanied with corresponding peaks in the imaginary part of the dielectric function (same energies) - this is consistent with the results seen for the Quantum Model (see Figure 2.12). The plasmon peak for Ag (2.9 eV) and Cu (2.5 eV) has red-shifted to lower energies (longer wavelengths); this is consistent with changes in plasmon dispersion through introduction of a reactive environment through chemical interface damping[94]. As the polarized electron cloud oscillates through the metal nanoparticle, scattering of electrons across empty adsorbate states exerts a drag force on the electronic oscillation, dumping energy to adsorbates through chemical interface damping. These fluctuations serve to 'slow' the free electron oscillation – it will thus satisfy the resonance condition at lower frequencies.

The imaginary part of the dielectric shows several clear peaks for Ag near 1.8, 2.3, 2.8, 3.5, and 4.5 eV and similar peaks for Cu near 1.5, 2.1, 2.7, 3.2, and 4.6 eV. Compared to the clean surface case, the largest changes are manifested between

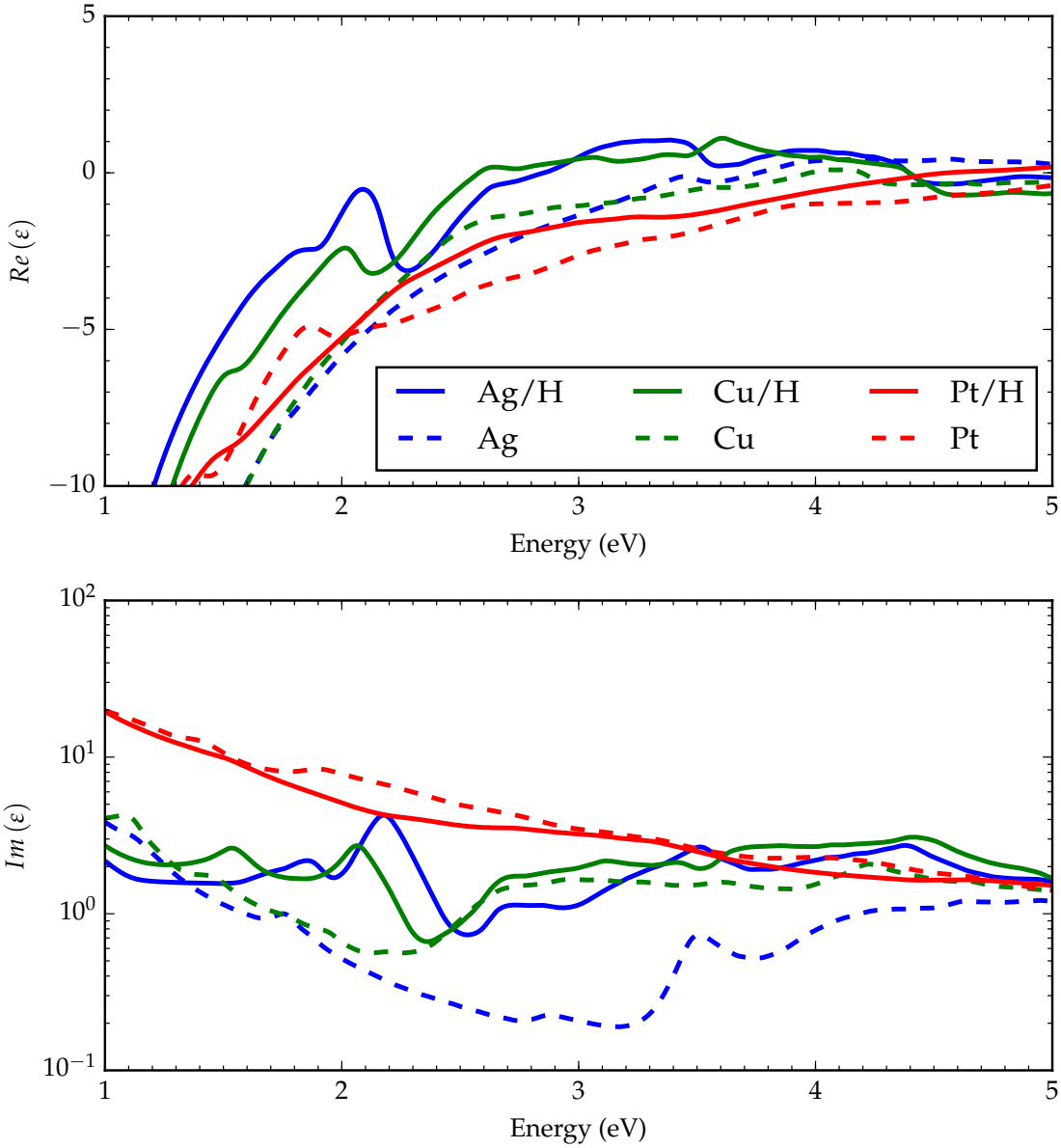

Figure 3.11: DFT-calculated real (top) and imaginary (bottom) dielectric functions for 6 layer clean and H-covered slabs. The appearence of wiggles in the real part of the dielectric function and corresponding peaks in the imaginary part of the dielectric function indicate the formation of new electronic transitions in the presence of adsorbates.

clean Ag and Ag/H. The imaginary part of the dielectric, ε_2, for clean Ag ranges from 0.2 to 1 between 2 and 4 eV; in the presence of a single monolayer of hydrogen the value is instead from 1 to 5 – a five-fold increase. New peaks are observed in Cu in the presence of a monolayer of hydrogen but the increase in magnitude is much smaller; there is only a small increase in ε_2 above 2.5 eV between Cu and Cu/H. The qualitative changes in Ag and Cu upon introduction of an adsorbate are consistent with the results from the quantum model – a peak in ε_2 coupled with a wiggle in ε_1. The imaginary part of the dielectric function for Pt is relatively featureless and decreases slightly across the energy range from 1 eV to 5 eV; there are only small changes with the introduction of hydrogen.

3.3.2.2 Impact on Extinction

The loss functions, electric field effects, and single-particle effects for Ag, Cu, and Pt slabs covered in a single monolayer of hydrogen are found in Figure 3.12. The loss function for the plasmon peak of clean Ag of 0.8 was slightly higher than the peak intensity of 0.75 for Cu. Pt still exhibits an absence of a strong LSPR peak at low energies. The new peaks appear at around 2 eV for Ag and Cu. This is from the increased single-particle transition shown in the third panel of Figure 3.12 lowering the electric field effect, shown in the second panel. The imaginary part of the dielectric is between 0 and 1.5 for most of the range from 1 to 5 eV for clean Ag and Cu; for hydrogen-covered it ranges from 1 to 3. This increased single-particle contribution comprises transitions from Ag/H combined states at the Fermi level to Ag sp states above the Fermi level; depicted in Figure 3.13. The presence of

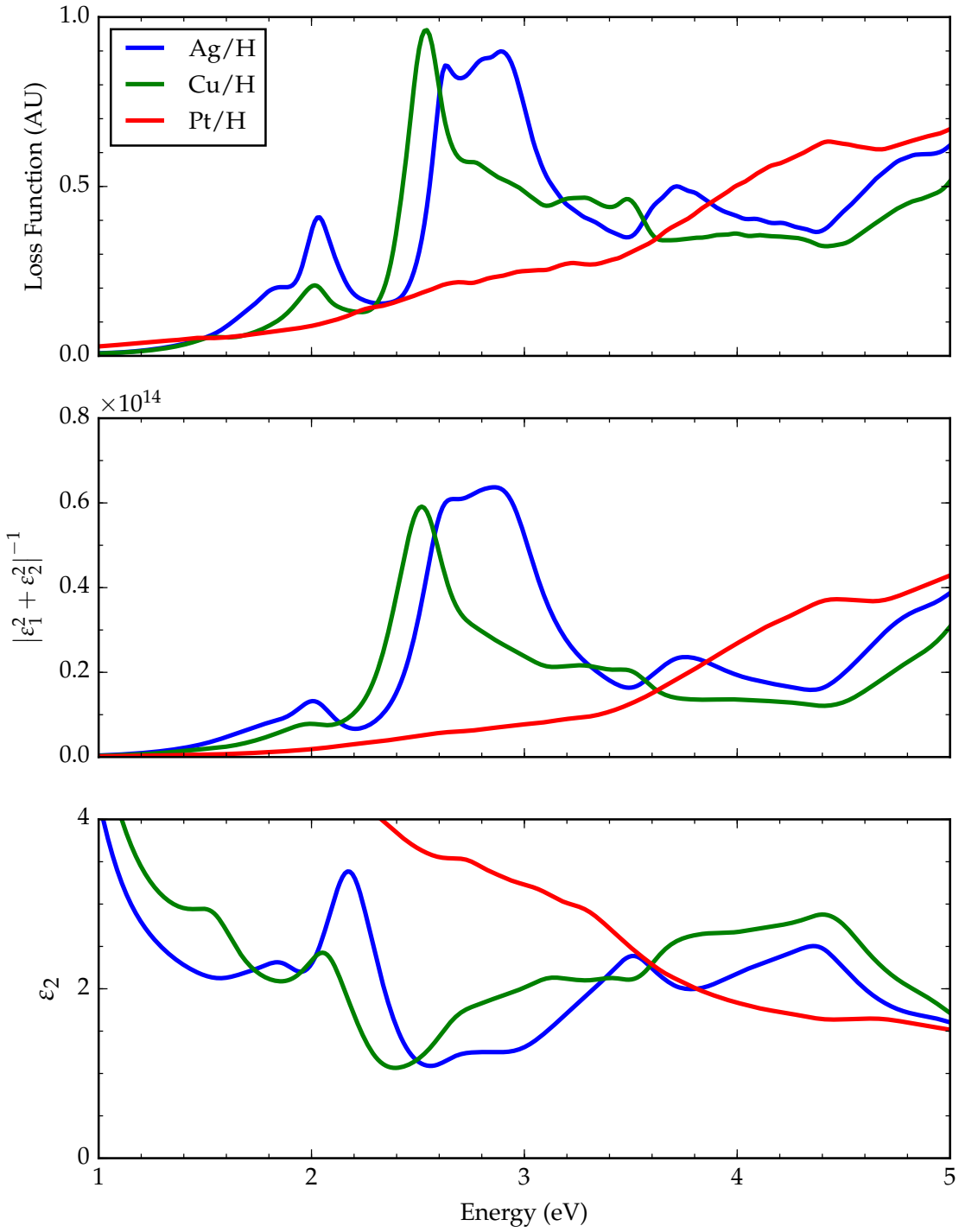

Figure 3.12: DFT-calculated spectrum (top) with electric field (middle) and single-particle (bottom) effects for Ag, Cu, and Pt. The Ag spectrum is larger than Cu and Pt by a factor of ~ 2, primarily due to the interband transition suppressing surface plasmon resonance.

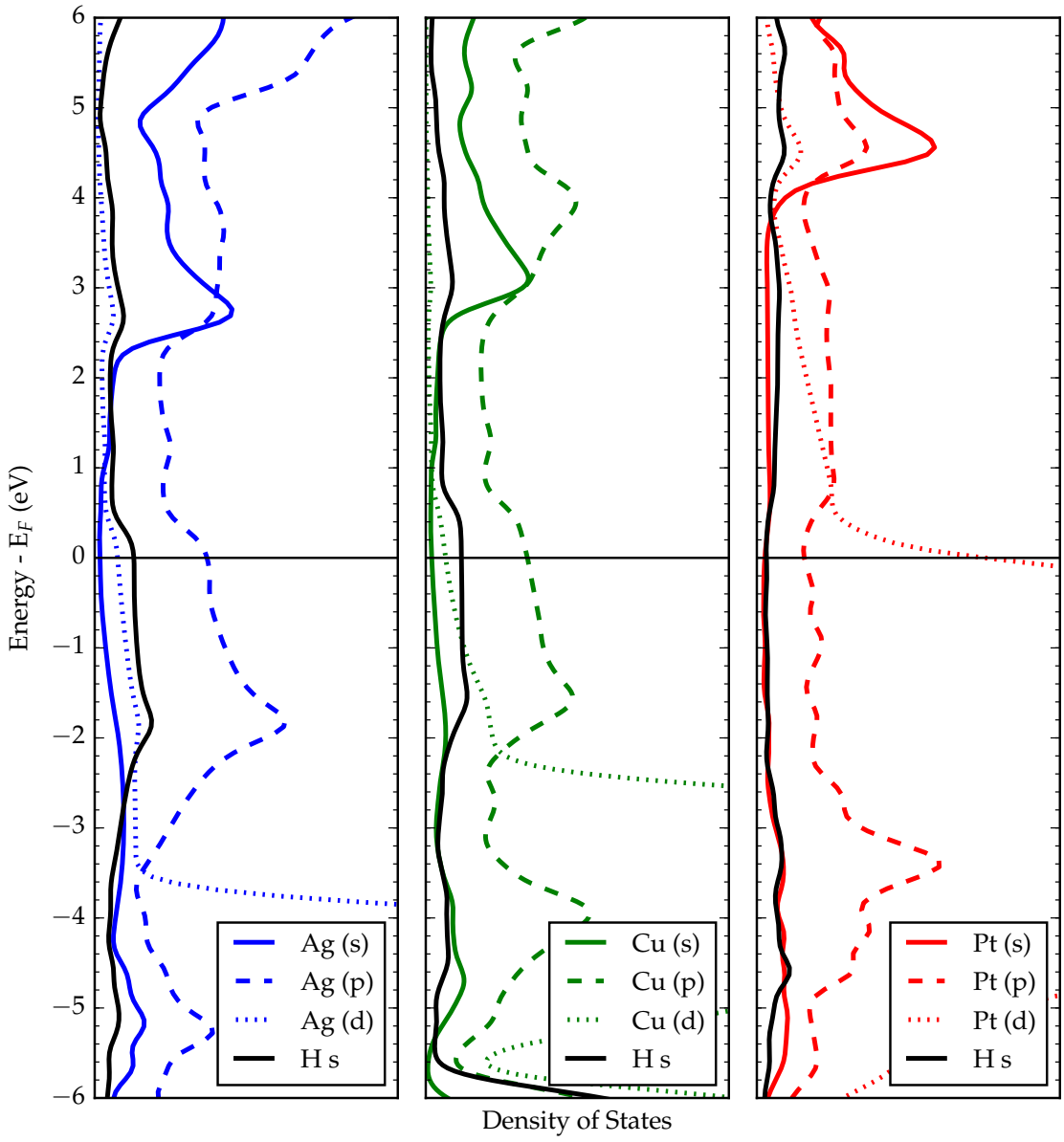

Figure 3.13: Ag/H (left), Cu/H (middle), and Pt/H (right) projected DOS for metal s orbitals (colored solid lines), metal p orbitals (colored dashed lines), metal d orbitals (colored dotted lines) and hydrogen s orbitals (solid black lines). Ag and Cu are very similar below 4 eV except for d-band location and the metal s peak around 3 eV. Pt d-band has states at E_F, these are responsible for the low interband transition energy.

hydrogen lowers the edge of the unoccupied sp band from 3.5 eV to 2.2 eV in Ag and from 4.2 eV to around 2.5 eV for Cu.

Effectively, the presence of hydrogen adsorbed to the surface lowers the onset energy of the interband transition such that it occurs well below the area where $\varepsilon_1 \sim 0$ for both Ag and Cu, exhibiting a much weaker extinction. Any strong interaction with the surface is likely to modify the electronic structure in such a manner; the strength of both Ag and Au as plasmonic nanocatalysts may rest in a combination of both LSPR energy and weak interaction with adsorbed species.

3.3.2.3 Changes to Electronic Structure

The transition plots for hydrogen-covered slabs need one additional piece of information; to assist in peak identification, the adsorbate is moved vertically above the surface to review how well changes in the histogram peaks correlate to changes in the peaks in the imaginary part of the dielectric function. The presence of many new transitions requires this more rigorous treatment for peak identification.

The transition plot in Figure 3.14a shows such a plot for a band in Ag/H with the hydrogen moved 0.4 Å up and down above the surface. The band corresponds to the highest-energy d-band, with the band structure shown in Figure 3.14b. This d-state is highly localized, and transitions from this state to bands above the Fermi level are shown to occur beginning at around 3.7 eV – this correlates with the onset of the typical interband transition in Ag. The transition histograms remain relatively unchanged with some broadening in the transitions at around 4.0 eV. Visualizations of the states participating in these transitions can be found in Fig-

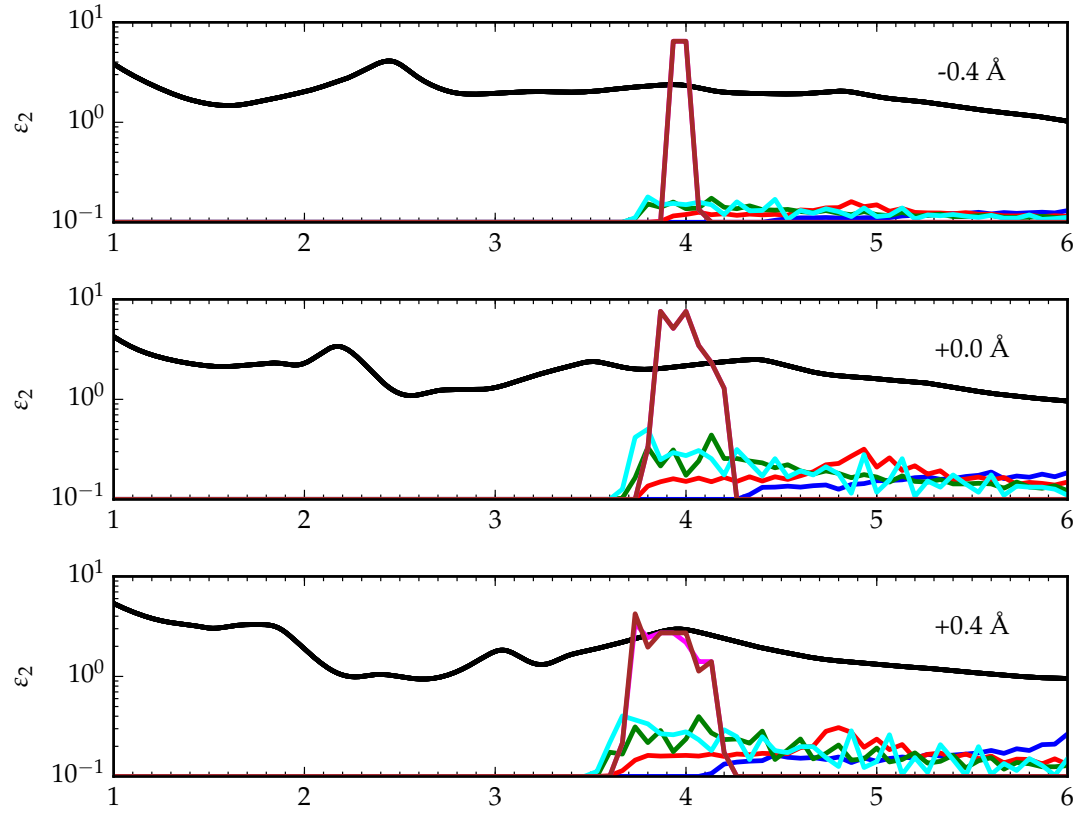

(a)

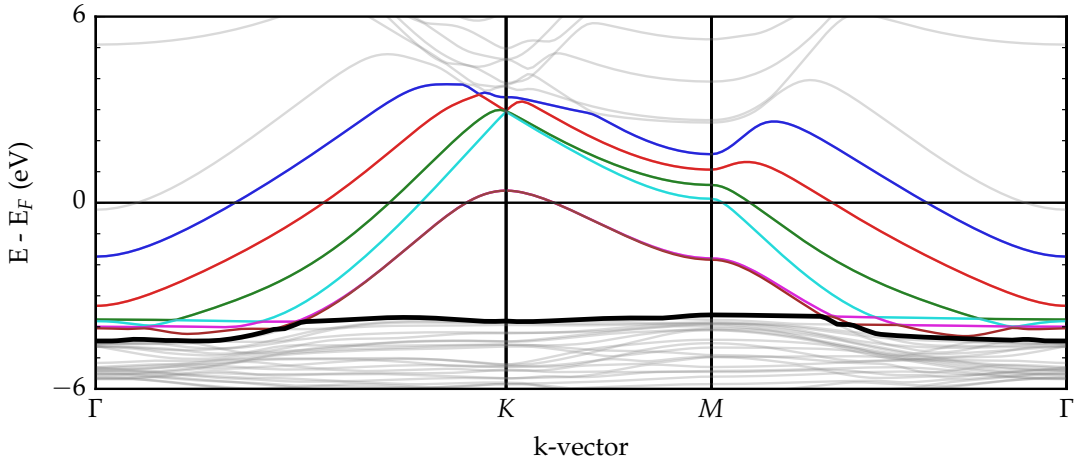

(b)

Figure 3.14: **a.** Transition plot shows interband transitions to silver s,p states (cyan, green, red, blue). **b.** Band structure showing d states (black band around -4 eV), Ag/H states (purple) and silver s,p states (cyan, green, red, blue)

ure 3.15; they are still transitions from localized bulk Ag d-states to delocalized Ag sp-states.

The bottom four transition peaks are all associated with the formation of the new 'hydrogen' states – the two degenerate bands shown as the black lines in Figure 3.16b. The lowest-energy peak tracks well with the energy difference between this band and the cyan band (see Figure 3.16a). The next peak is associated with transitions from this band to the green band. The next two peaks are attributed to transitions from this band to the red band.

The first peak corresponds to transitions of electrons from states localized on hydrogen adsorbed to the surface and the Ag sp-band (see Figure 3.17). The second peak is similar; transitions from these localized hydrogen states to a delocalized Ag sp-band (see Figure 3.18). The accepting state for the third (Figure 3.19) and fourth (Figure 3.20) peaks both correspond to the same band but slightly different behavior; the third peak is more delocalized whereas the fourth peak is more localized. The third peak (Figure 3.19 has more surface Ag/H behavior compared to the first two peaks. The fourth peak (Figure 3.20 includes a final state that comprises more localized hydrogen states. The fifth peak at 4 eV is an electronic excitation from the black band shown in Figure 3.21 to the blue band. This is either attributed to transitions from localized Ag d-states to localized hydrogen states (Figure 3.22) or delocalized Ag bulk sp-states (Figure 3.23); both occur at the correct energy.

Ultimately, the addition of hydrogen to the surface introduces a large number of pathways for electronic excitation between the adsorbate and the metal – both to and from the adsorbate. Most literature discusses the formation of a transient

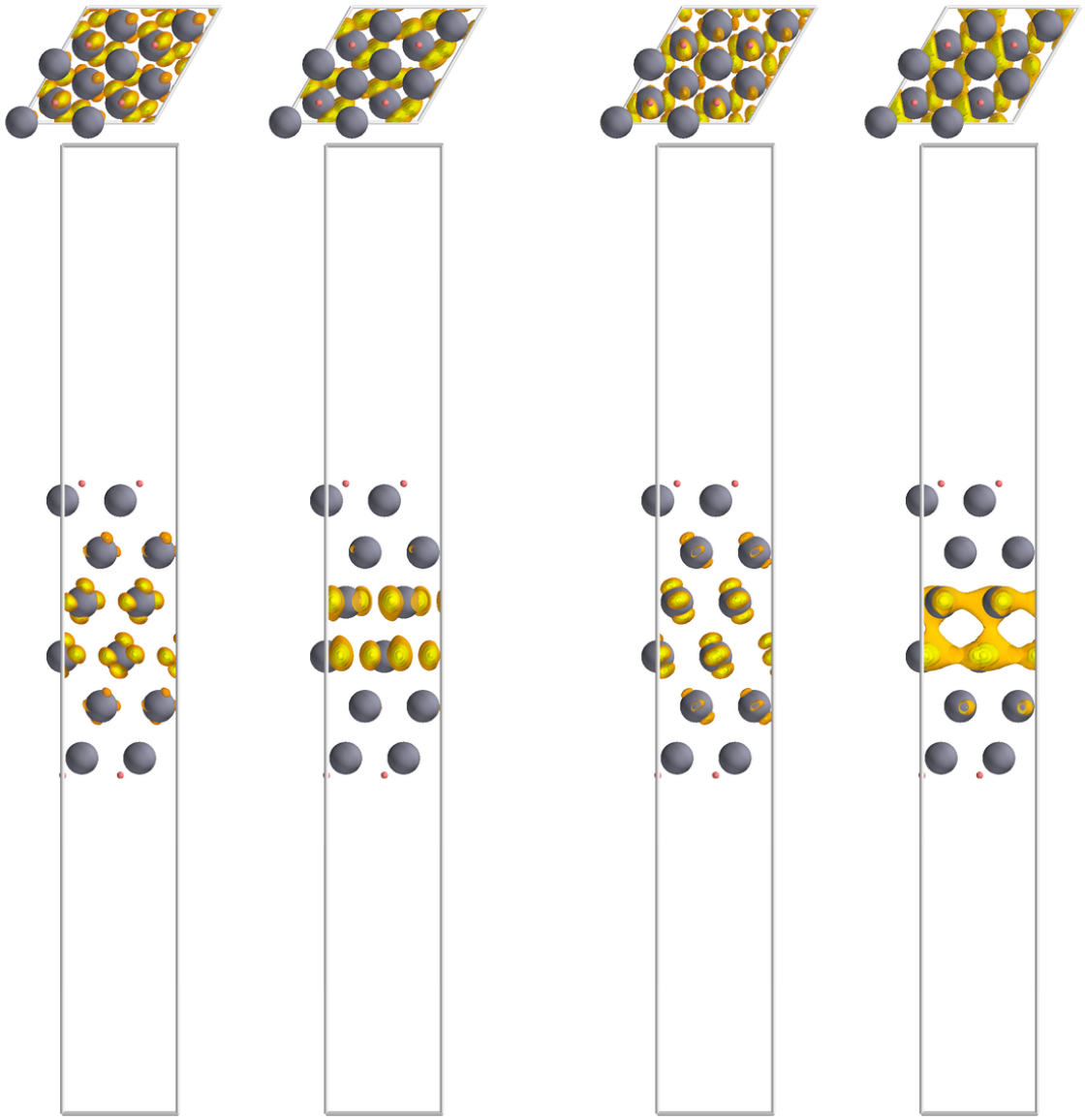

(a) Figure 3.14 Black -3.73 eV

(b) Figure 3.14 Cyan 0.07 eV

(c) Figure 3.14 Black -3.74 eV

(d) Figure 3.14 Cyan 0.06 eV

Figure 3.15: Wavefunction visualization: interband transition
Excitations from silver d-states to delocalized silver sp states. Wavefunctions output in k-space where the bands differ in energy by the transition energy of $\sim$ 3.8 eV.

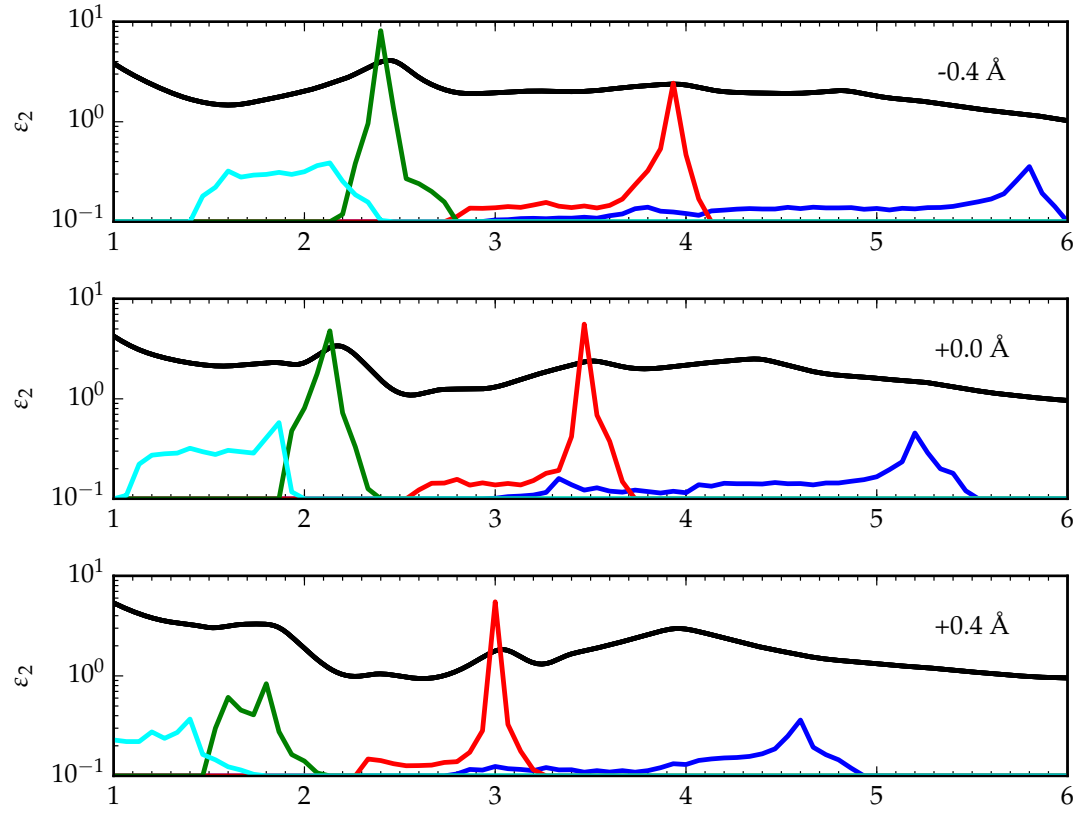

(a)

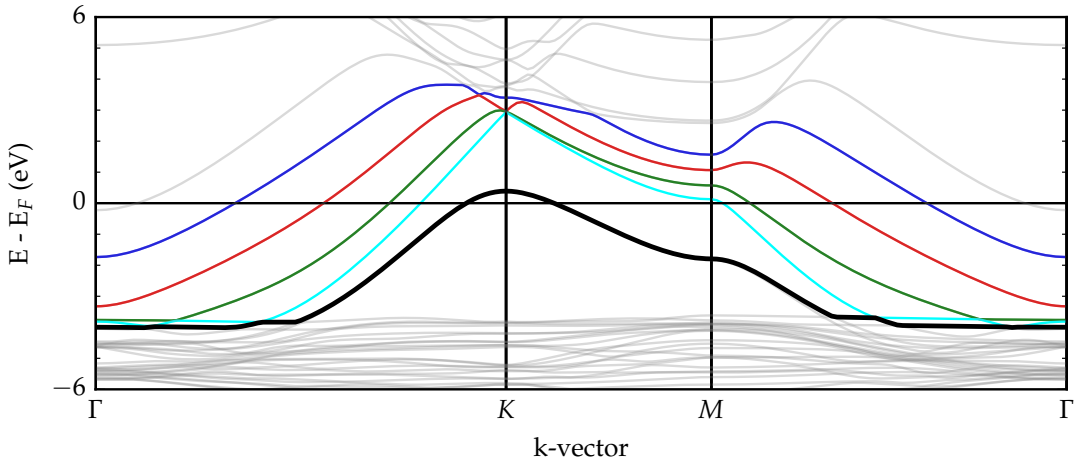

(b)

Figure 3.16: **a.** Transition plot showing this state can transition to a number of states above the Fermi level, associated with peaks in the extinction. **b.** Band structure showing this H-state (solid black line) and silver s,p states (colored lines) There are two degenerate hydrogen states; these results are functionally identical to the other band at the same energy.

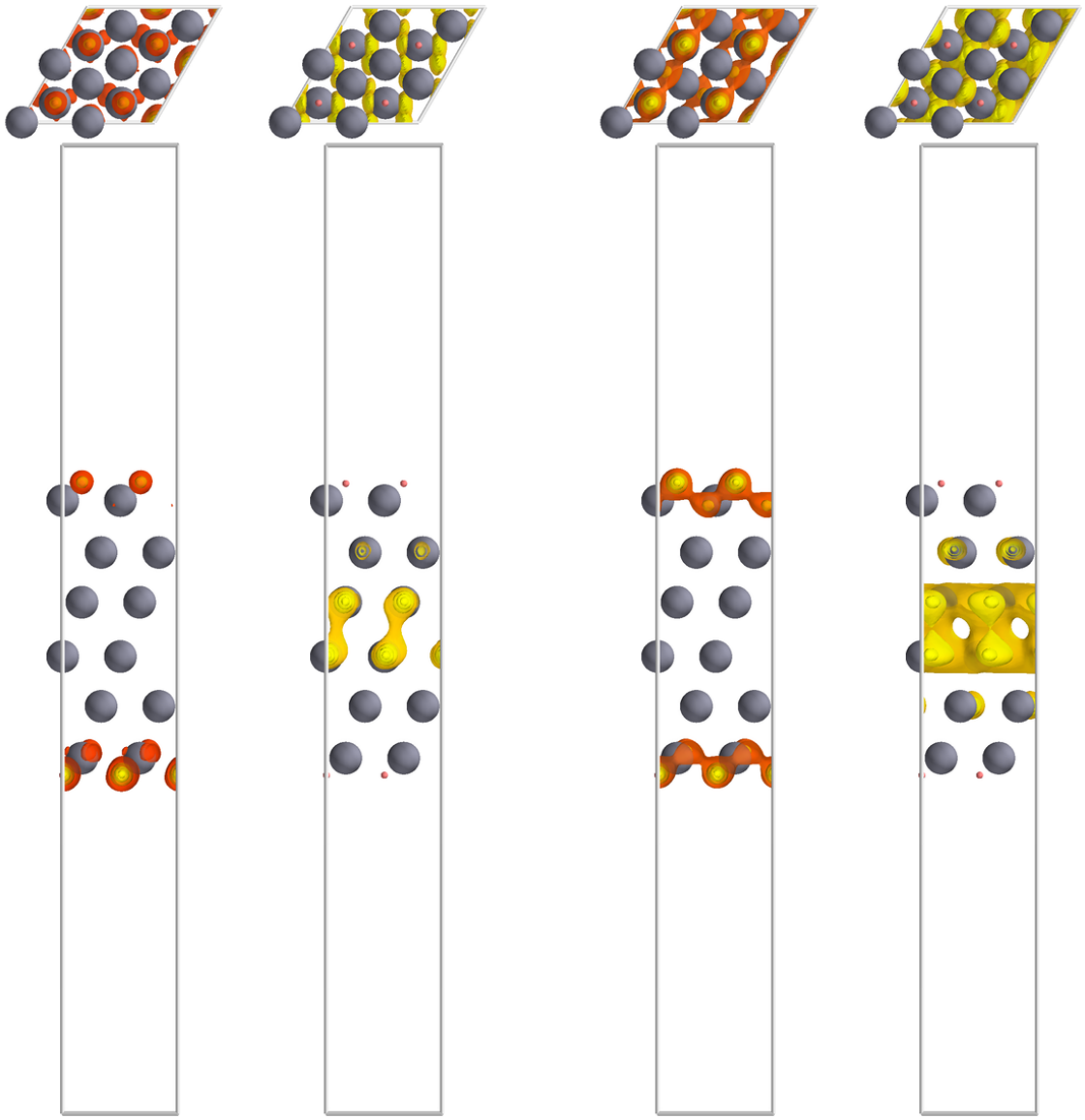

(a) Figure 3.16 Black -0.01 eV

(b) Figure 3.16 Cyan 1.79 eV

(c) Figure 3.16 Black -1.79 eV

(d) Figure 3.16 Cyan 0.01 eV

Figure 3.17: Wavefunction visualization: interband transition
Excitations from silver d-states to delocalized silver sp states. Wavefunctions output in k-space where the bands differ in energy by the transition energy of $\sim$ 1.4 eV.

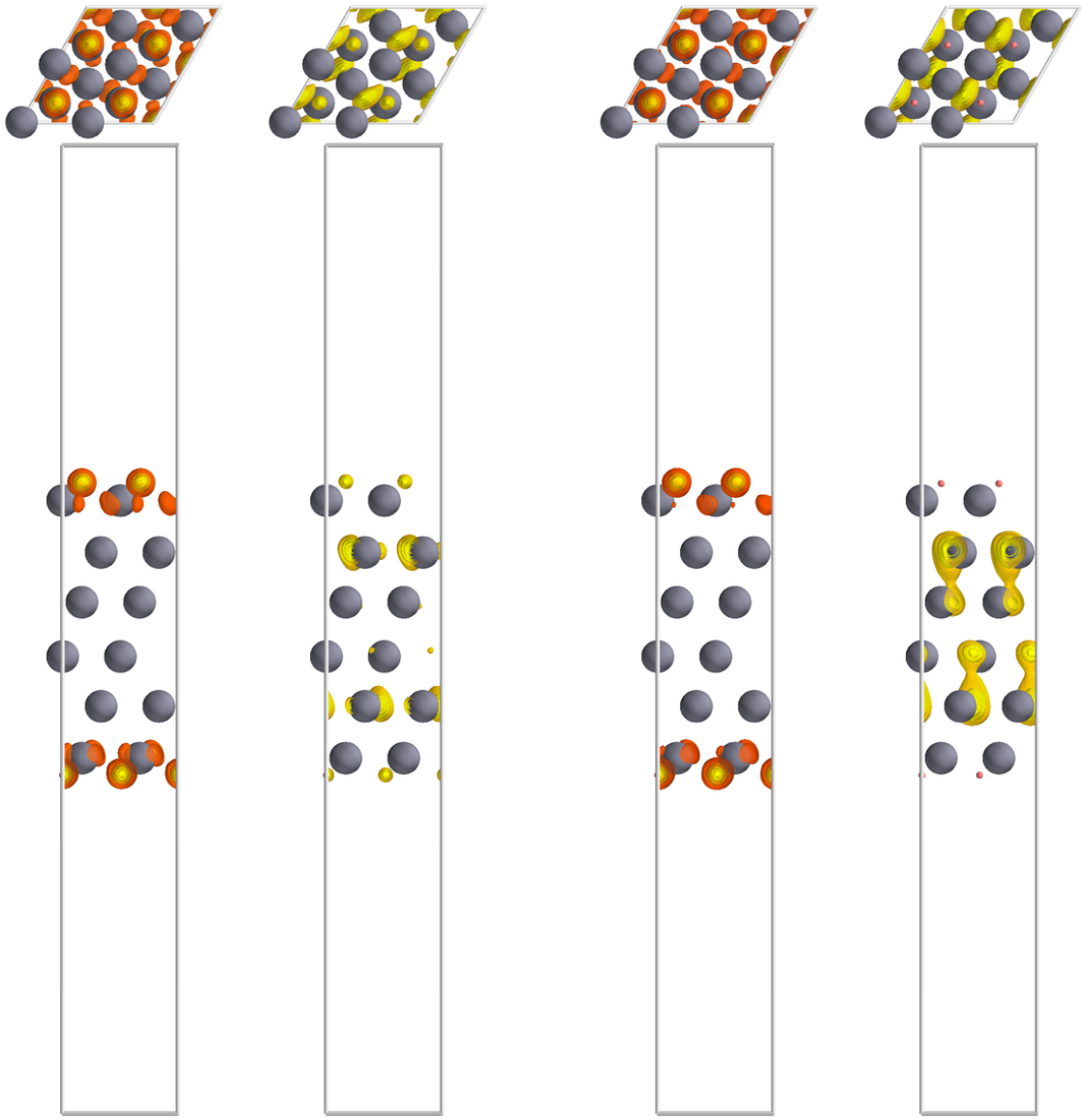

(a) Figure 3.16 Black -0.72 eV

(b) Figure 3.16 Green 1.43 eV

(c) Figure 3.16 Black -0.52 eV

(d) Figure 3.16 Green 1.63 eV

Figure 3.18: Wavefunction visualization: interband transition
Excitations from silver d-states to delocalized silver sp states. Wavefunctions output in k-space where the bands differ in energy by the transition energy of $\sim$ 2.2 eV.

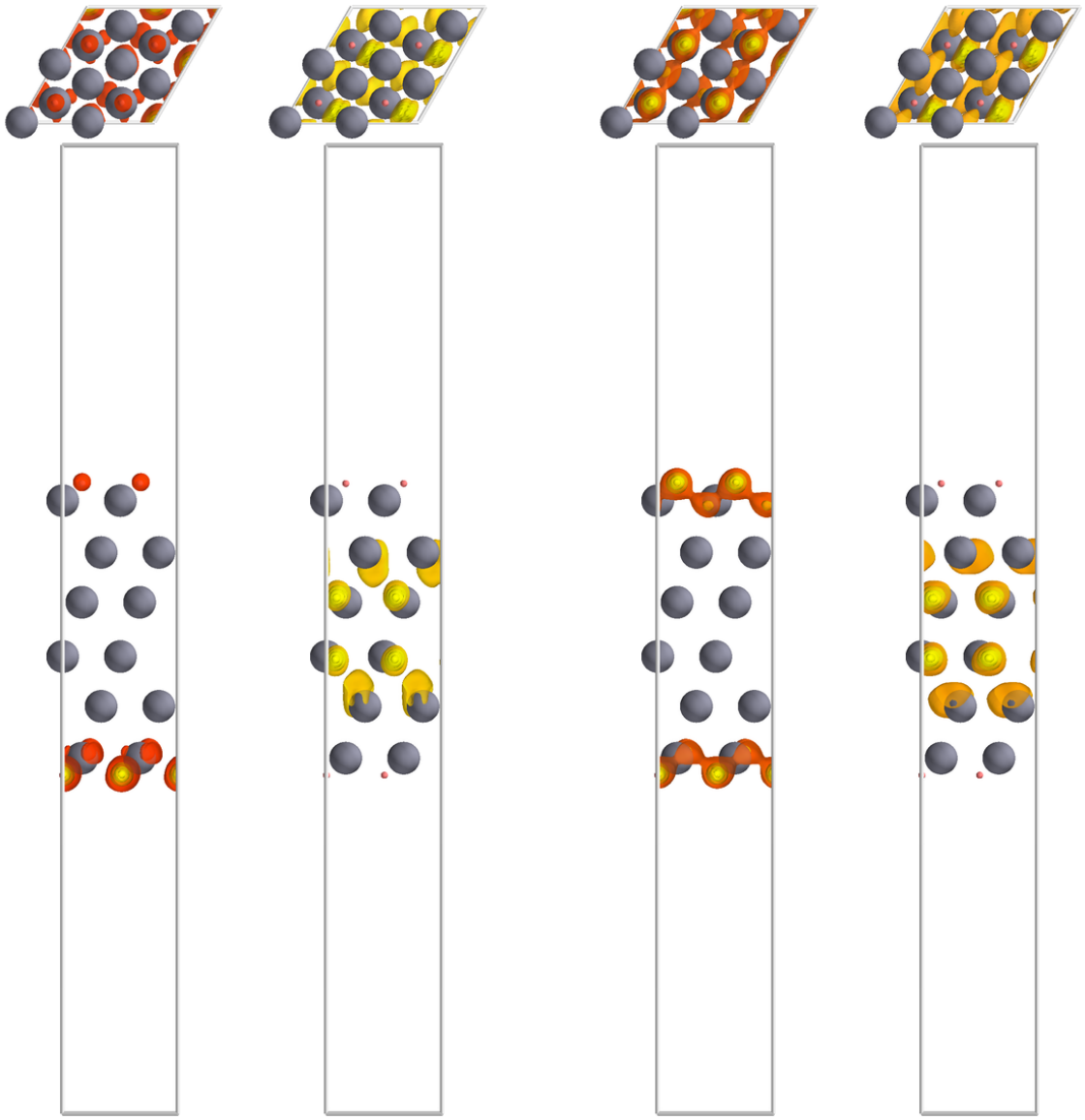

(a) Figure 3.16 Black -0.07 eV

(b) Figure 3.16 Red (lower) 2.70 eV

(c) Figure 3.16 Black -1.6 eV

(d) Figure 3.16 Red (lower) 1.17 eV

Figure 3.19: Wavefunction visualization: interband transition
Excitations from silver d-states to delocalized silver sp states. Wavefunctions output in k-space where the bands differ in energy by the transition energy of $\sim$ 2.8 eV.

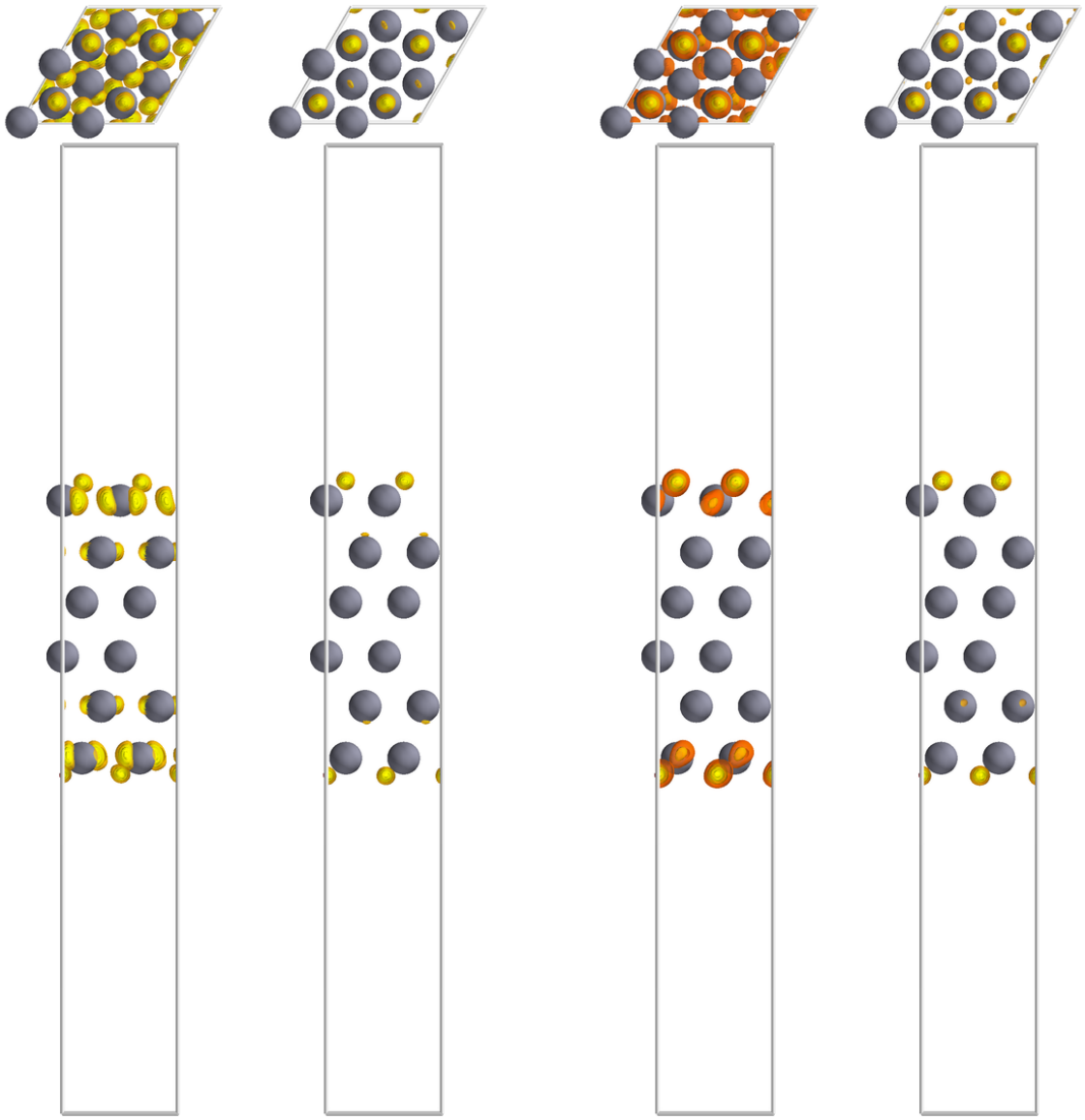

(a) Figure 3.16 Black -2.99 eV

(b) Figure 3.16 Red (upper) 0.49 eV

(c) Figure 3.16 Black -1.06 eV

(d) Figure 3.16 Red (upper) 2.41 eV

Figure 3.20: Wavefunction visualization: interband transition
Excitations from silver d-states to delocalized silver sp states. Wavefunctions output in k-space where the bands differ in energy by the transition energy of ~ 3.5 eV.

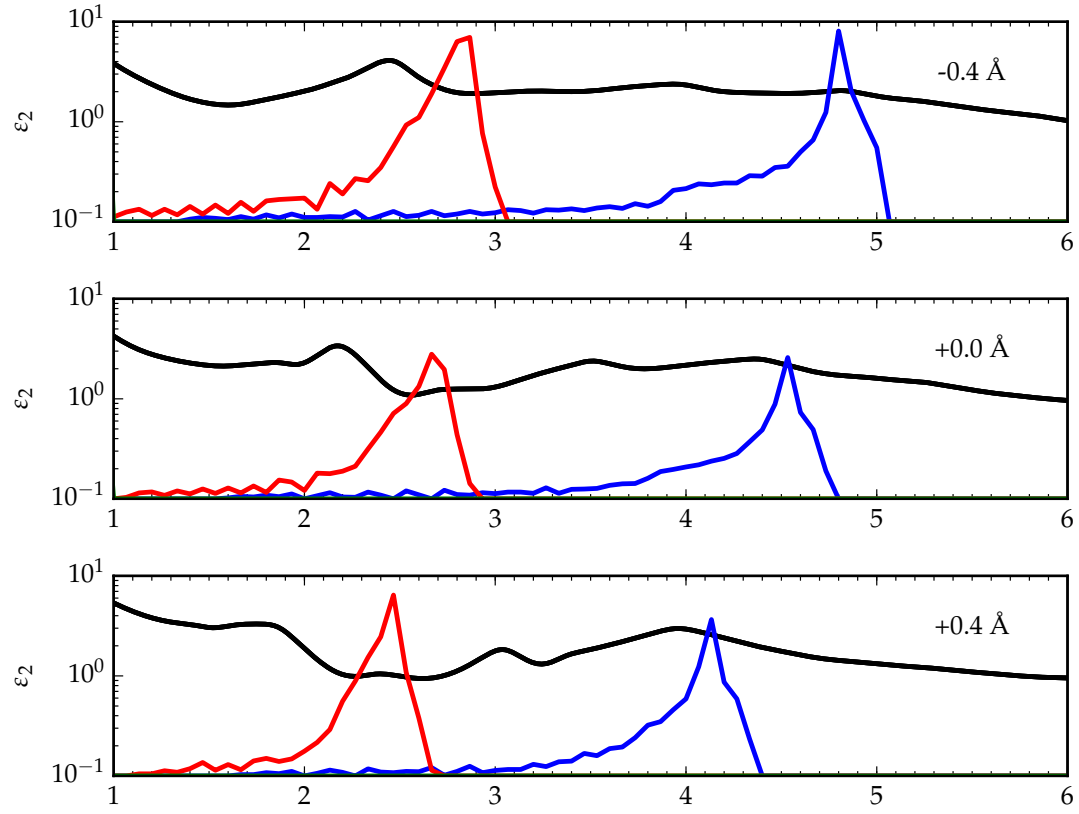

(a)

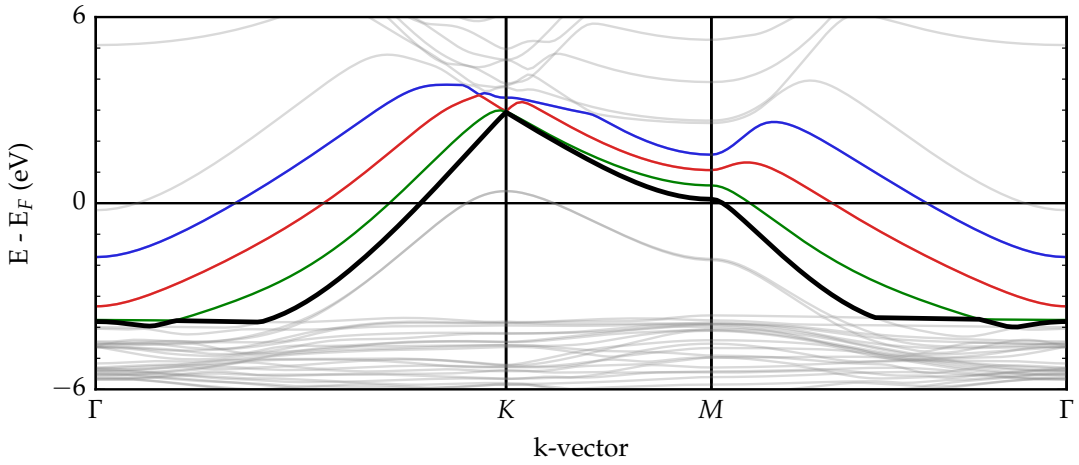

(b)

Figure 3.21: **a.** Transition plot showing this state can transition to a number of states above the Fermi level, associated with peaks in the extinction. **b.** Band structure showing this H-state (solid black line) and silver s,p states (colored lines) There are two degenerate hydrogen states; these results are functionally identical to the other band at the same energy.

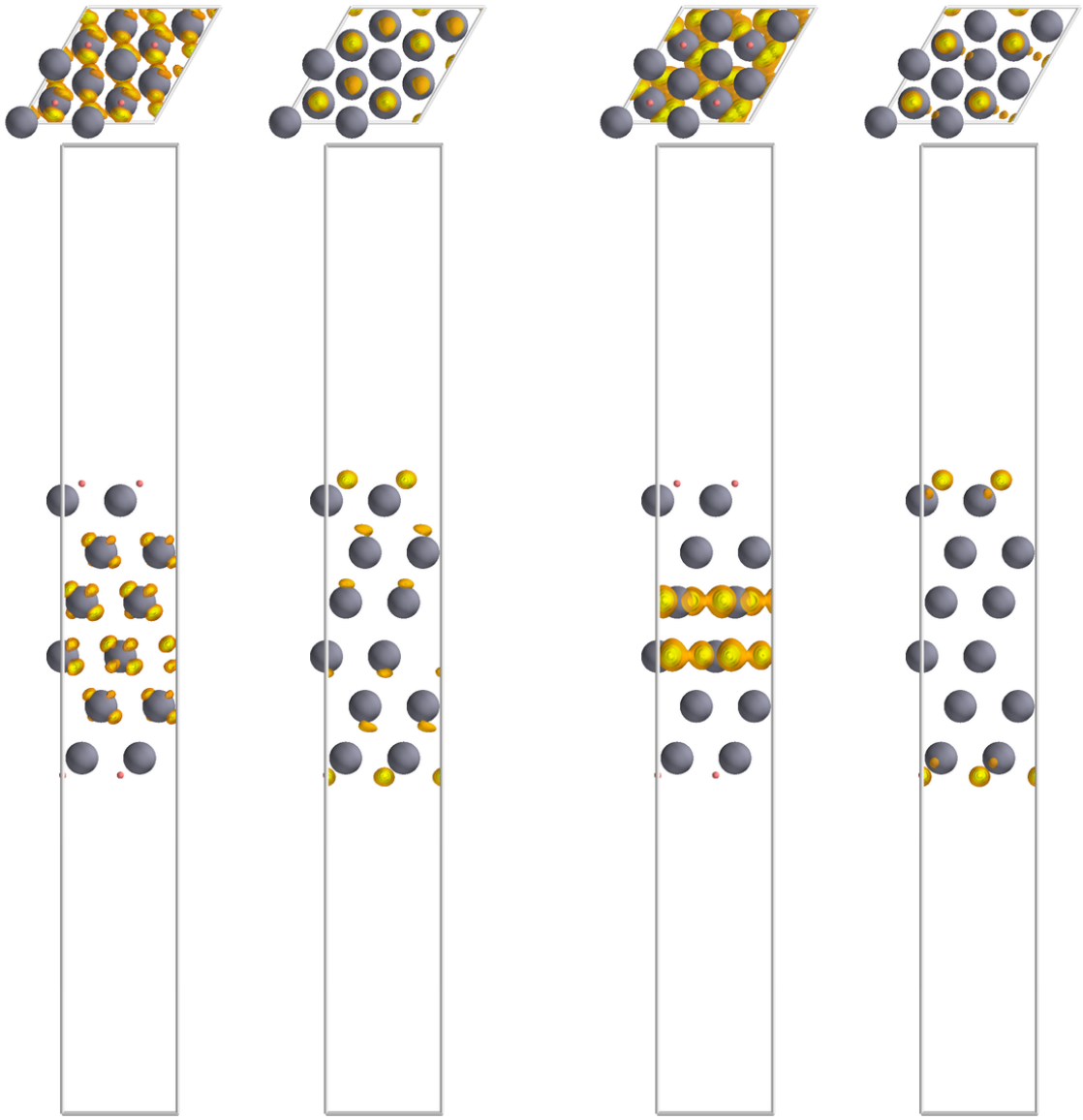

(a) Figure 3.21 Black -3.85 eV

(b) Figure 3.21 Blue 0.35 eV

(c) Figure 3.21 Black -1.52 eV

(d) Figure 3.21 Blue 2.68 eV

Figure 3.22: Wavefunction visualization: interband transition
Excitations from silver d-states to delocalized silver sp states. Wavefunctions output in k-space where the bands differ in energy by the transition energy of $\sim$ 4.0 eV.

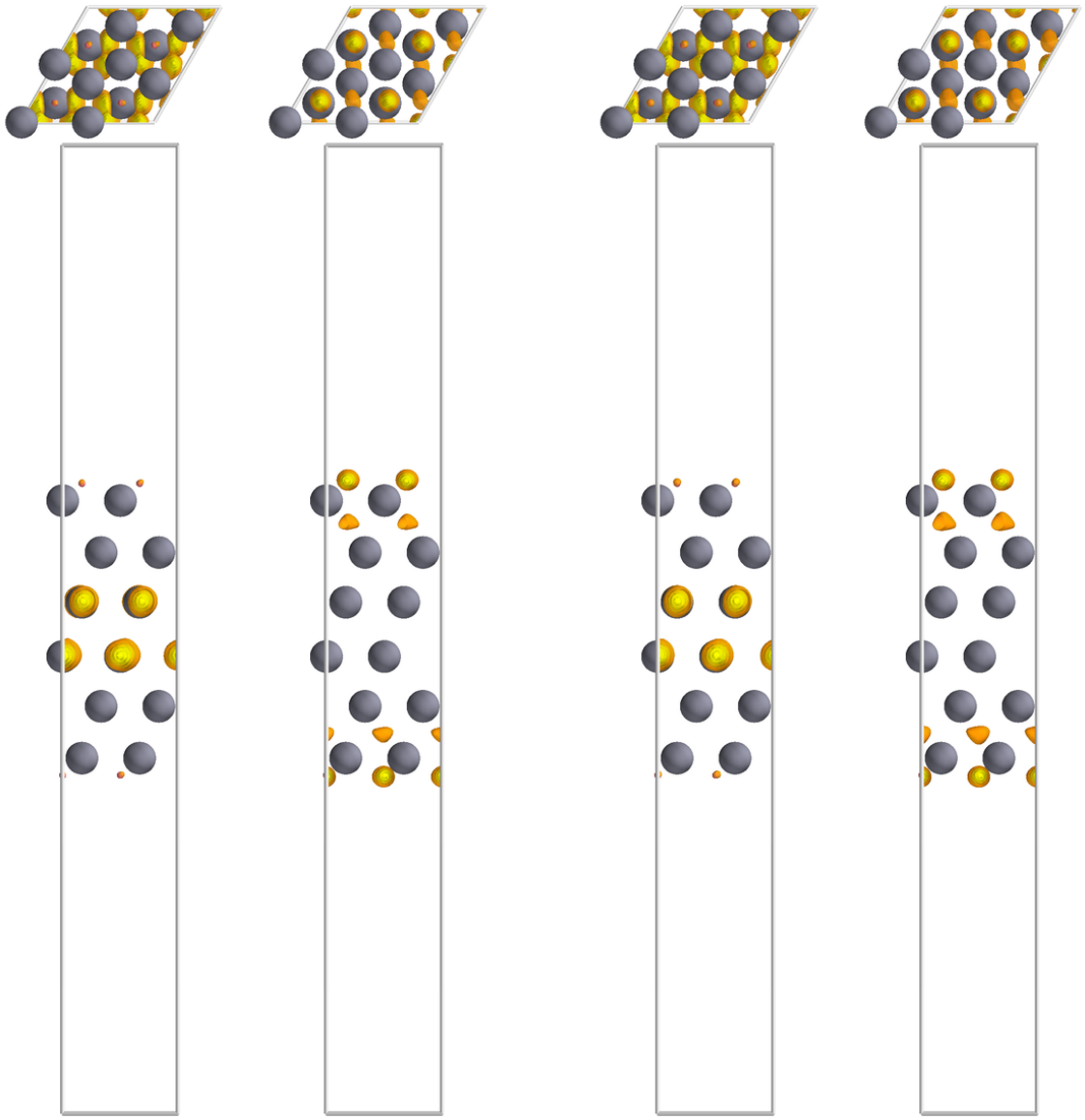

(a) Figure 3.21 Black -1.23 eV

(b) Figure 3.21 Blue 2.97 eV

(c) Figure 3.21 Black -1.07 eV

(d) Figure 3.21 Blue 3.13 eV

Figure 3.23: Wavefunction visualization: interband transition
Excitations from silver d-states to delocalized silver sp states. Wavefunctions output in k-space where the bands differ in energy by the transition energy of $\sim$ 4.0 eV.

negative adsorbate; this analysis suggests a positively charged adsorbate is also a possibility. The impact of such an adsorbate would have a similar effect to a negatively-charged adsorbate.

3.3.3 Affect of Strongly Interacting Adsorbate

The results in this section use the LDA exchange-correlation functional [113] due to some GPAW issues with the use of the GLLB-SC functional with spin-polarized systems. The quantitative predictions (such as the d band description and consequently the interband transition) are not as robust compared to the GLLB-SC approach but we review this case study to look at more overarching trends for a weakly-bound adsorbate (hydrogen) and a more strongly-bound adsorbate – oxygen.

Qualitatively the results for clean and H-covered surfaces agree well with those from the previous section, the addition of hydrogen to the surface increases the single-particle transitions over most of the energy range, with the change being largest for Ag – due to the low interband transition at low energies in the absence of adsorbates.

Simulated EELS spectra for clean Ag, Ag with a monolayer of H, and Ag with a monolayer of O are found in Figure 3.24. The suppression of surface plasmon resonance – the change in loss function for the clean slab compared to hydrogen-covered – is smaller here. The LDA exchange-correlation functional does not accurately locate the d-band – putting it at $\sim$2.5 eV instead of around 4 eV below the

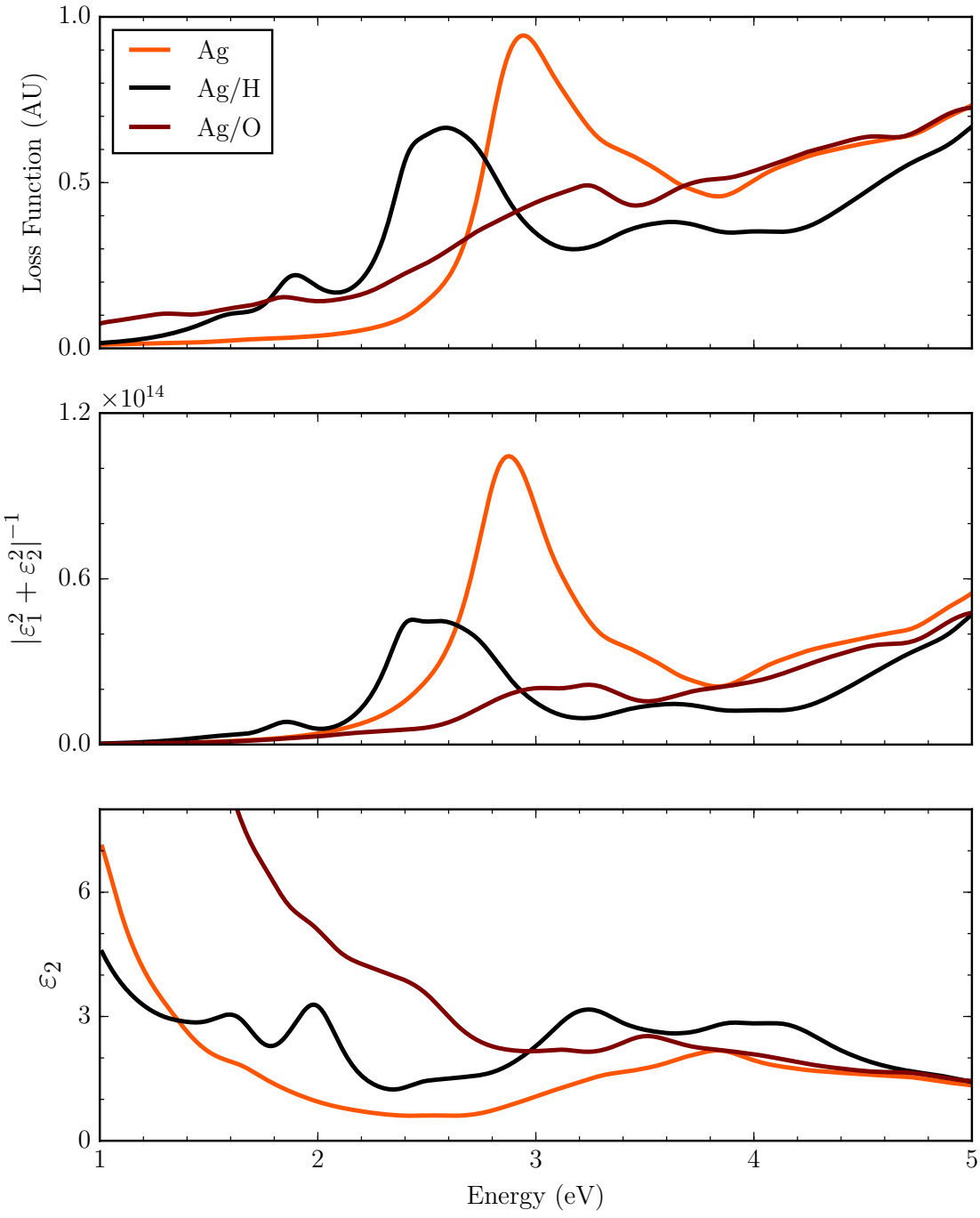

Figure 3.24: (Top) DFT-calculated EELS spectra for Ag (orange), Ag/H (black) and Ag/O (brown). (Middle) Electric field contribution to spectra. (Bottom) Single-particle contribution to spectra.

Fermi level (compare Figure 3.5 and Figure 3.25) – causing the interband transition to damp the plasmon. This shifts the plasmon peak to a lower energy ($\sim$3 eV) and to a lower value ($\sim$0.9) relative to GLLB-SC-predicted values ($\sim$3.7 eV and $\sim$1.5, respectively). The same five single-particle peaks emerge again for Ag/H – four responsible for transitions from H states to silver sp states and one interband transition from Ag d states to the sp band. Of note are the effects of the electric field on the two lowest-energy peaks in ε_2 at 1.6 eV and 2.0 eV; the value of ε_2 for both peaks is roughly the same, however the extinction at 2 eV is around 70% greater than for 1.6 eV – this shows the importance of the LSPR condition on increasing extinction associated with adsorbate states. Transitions from Hydrogen s and Ag sp band hybridized states to other Ag sp band states begins to take off above 2.5 eV.

Atomic oxygen was found to bind to the surface with a magnetic moment of 0.7 μ_B and a bond distance of 2.053 Å. The binding of oxygen increases the single-particle transitions for energies below 3 eV – the absorption spectrum more closely resembles a metal with a broad interband transition than Ag. This is likely due to the presence of a large number of strongly hybridized Oxygen p and Ag p, d states immediately below the Fermi level, shown in the rightmost pane of Figure 3.25.

Simulated EELS spectra for clean Cu, Cu with a single monolayer of H, and Cu with a single monolayer of O are found in Figure 3.26. The suppression of surface plasmon resonance – the change in loss function for the clean slab compared to hydrogen-covered – is smaller here. Similarly to Ag, the LDA exchange-correlation functional overestimates the energy of the d-band – putting it at $\sim$1.5 eV below the

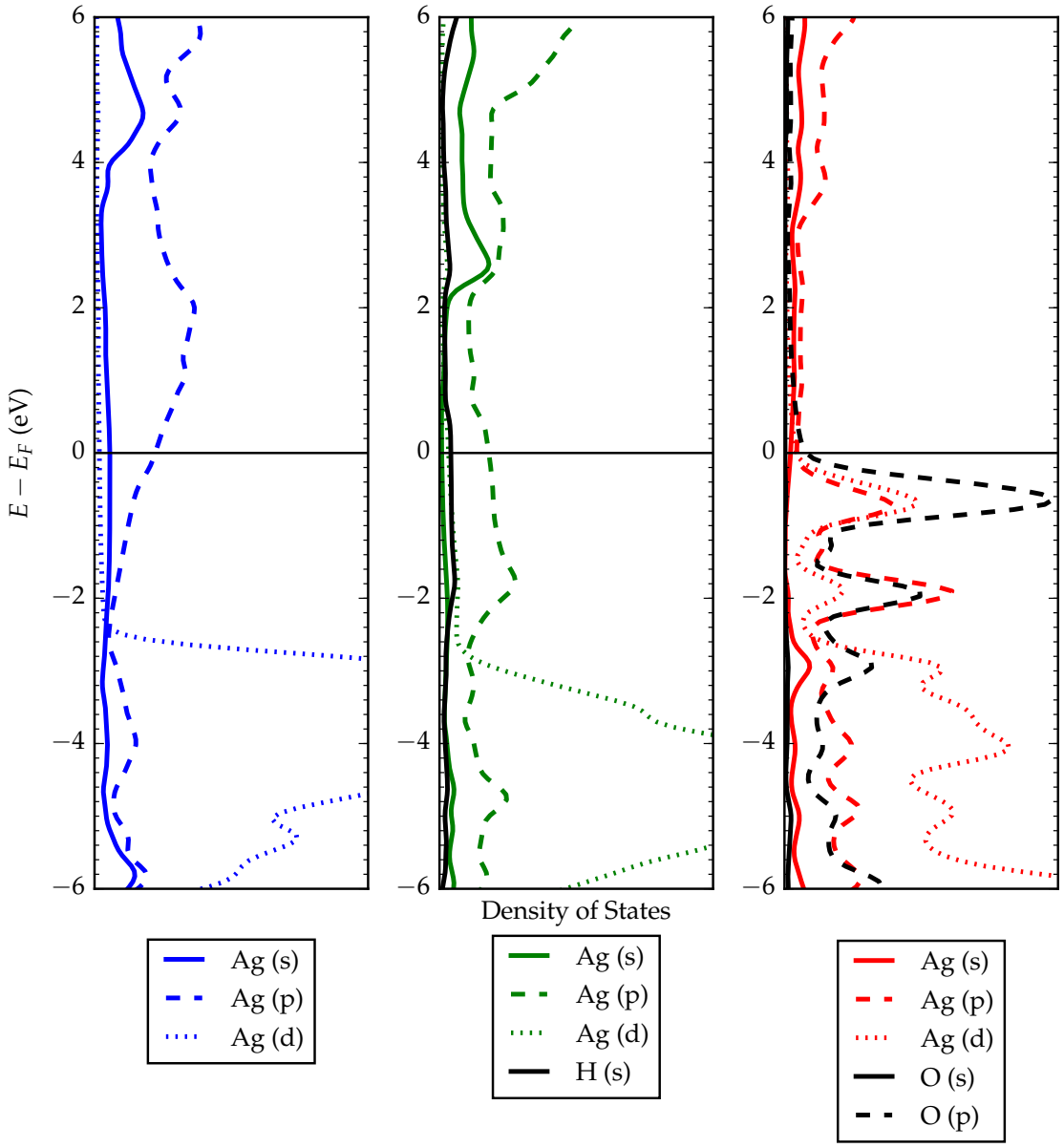

Figure 3.25: Projected Density of States (PDOS). (Left) Electronic density around a surface Ag atom in a clean slab projected onto s (solid), p (dashed) and d (dotted) orbitals. (Middle) PDOS for a surface Ag atom (green lines) and hydrogen (black line) in a slab with 1 monolayer of Hydrogen adsorbed. (Right) PDOS for a surface Ag atom (red lines) and oxygen s (solid black line) and p (dashed black line). Introduction of hydrogen shifts the edge of the sp band above the Fermi level down from 3.5 eV to just above 2.0 eV. Introduction of oxygen generates a large number of states just below the Fermi level.

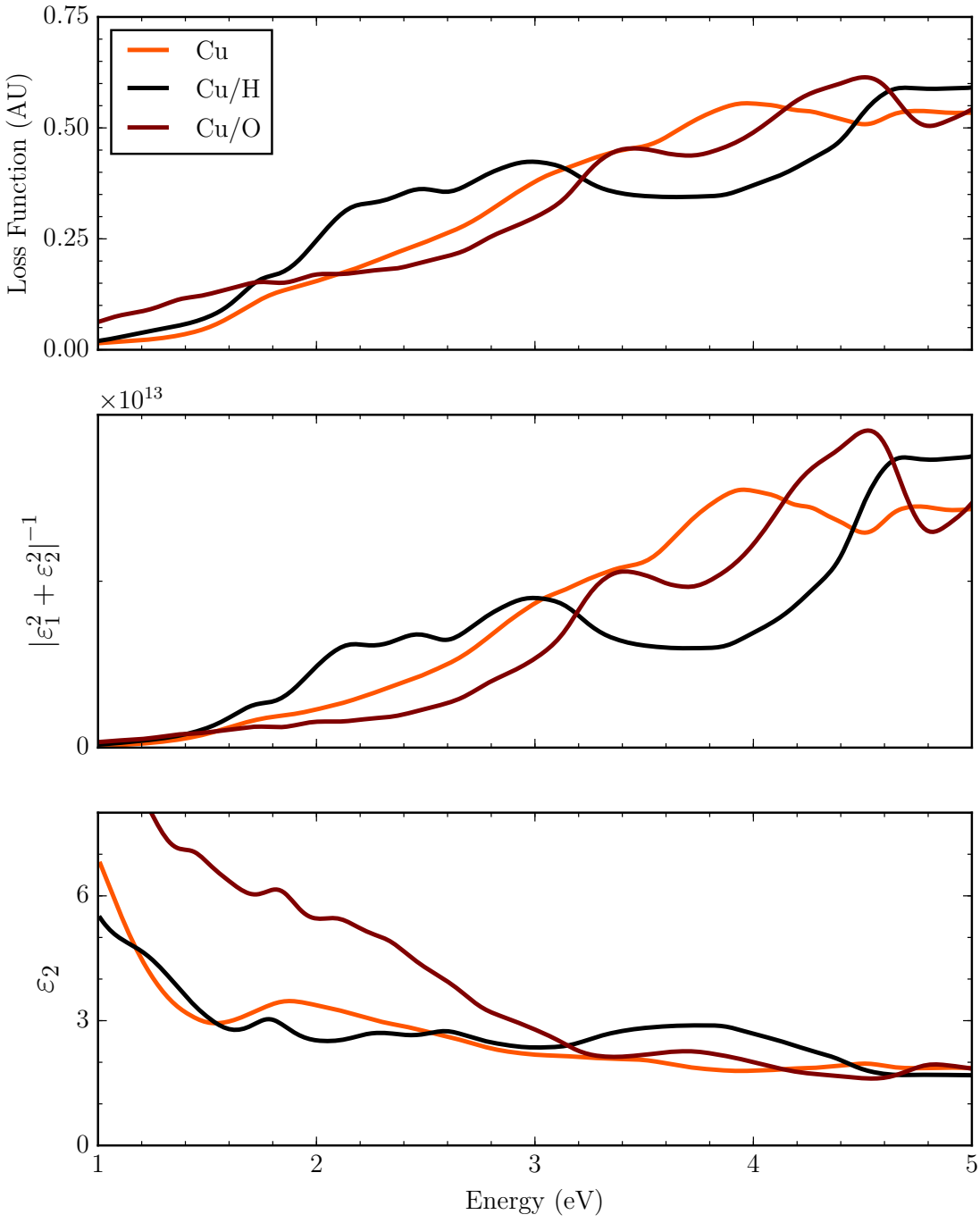

Figure 3.26: (Top) DFT-calculated EELS spectra for Cu (orange), Cu/H (black) and Cu/O (brown). (Middle) Electric field contribution to spectra. (Bottom) Single-particle contribution to spectra.

Fermi level instead of ∼2.5 eV – see Figure 3.5 and Figure 3.27.

The spectrum for Cu shows a weak plasmon peak (correlated to a peak in the electric field effect) at around 4 eV. The addition of hydrogen shows the presence of several peaks – these appear to be from hybridized O p/Cu p/Cu d states to similar states above the Fermi level. Atomic oxygen was found to bind to the surface with a magnetic moment of 0.51 μ_B and a bond distance of 1.859 Å. Similar to Ag, the oxygen-covered surface exhibits much higher single-particle transitions for energies below 3 eV. This correlates well with the O p/Cu p/Cu d states between 3 eV below the Fermi level and the Fermi level.

Simulated EELS spectra for Pt, Pt/H, and Pt/O are found in Figure 3.28. The d-band has some states above the Fermi level – this matches roughly the location for the GLLB-SC functional. Oxygen adsorbs to the Pt surface with a M-O bond distance of 1.996 Å.

The spectra for all three cases are largely similar; the low-energy interband transition washes out any plasmon peak – the introduction of adsorbates such as H and O leave the loss function largely similar.

The presence of empty metal (d and p) states (see Figure 3.29) just above the Fermi level mean that there is a wide energy range of filled states below the Fermi level from which electrons can be promoted.

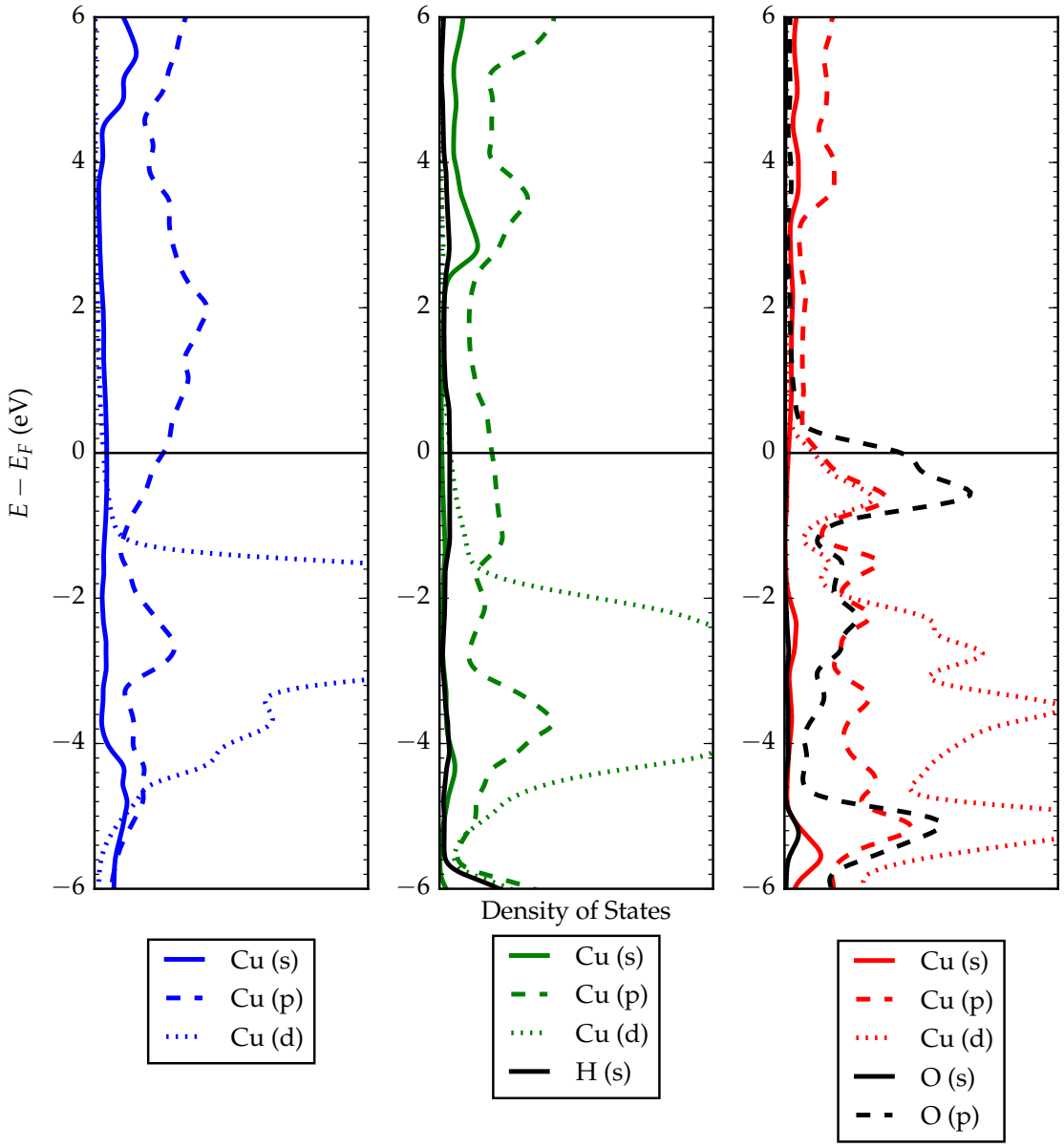

Figure 3.27: PDOS plots for Cu. (Left) Electronic density around a surface Cu atom in a clean slab projected onto s (solid), p (dashed) and d (dotted) orbitals. (Middle) PDOS for a surface Cu atom (green lines) and hydrogen (black line) in a slab with 1 monolayer of Hydrogen adsorbed. (Right) PDOS for a surface Cu atom (red lines) and oxygen s (solid black line) and p (dashed black line). Introduction of hydrogen shifts the edge of the sp band above the Fermi level down from around 4 eV to around 2.4 eV. Introduction of oxygen generates a large number of states just below and at the Fermi level.

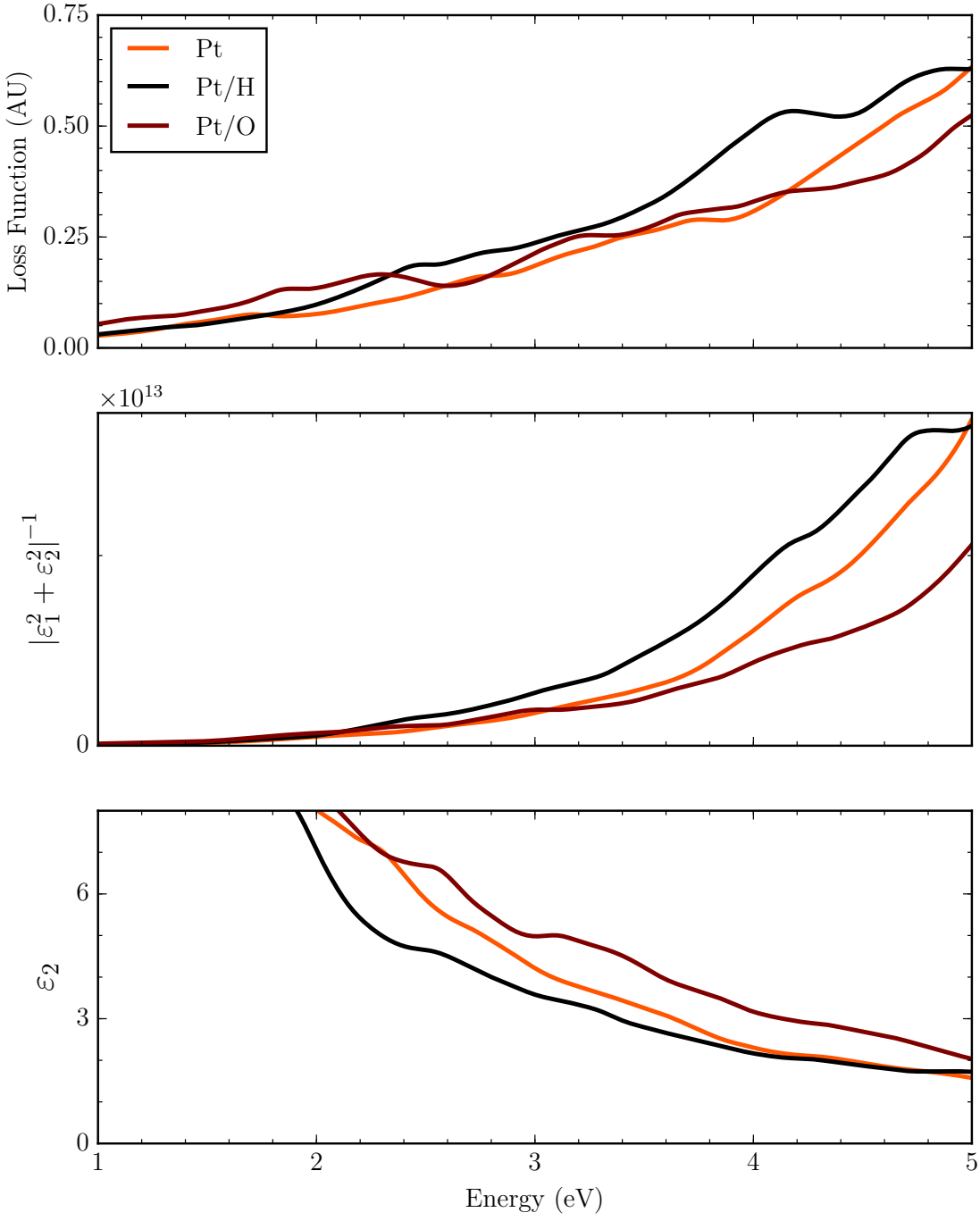

Figure 3.28: (Top) DFT-calculated EELS spectra for Pt (orange), Pt/H (black) and Pt/O (brown). (Middle) Electric field contribution to spectra. (Bottom) Single-particle contribution to spectra.

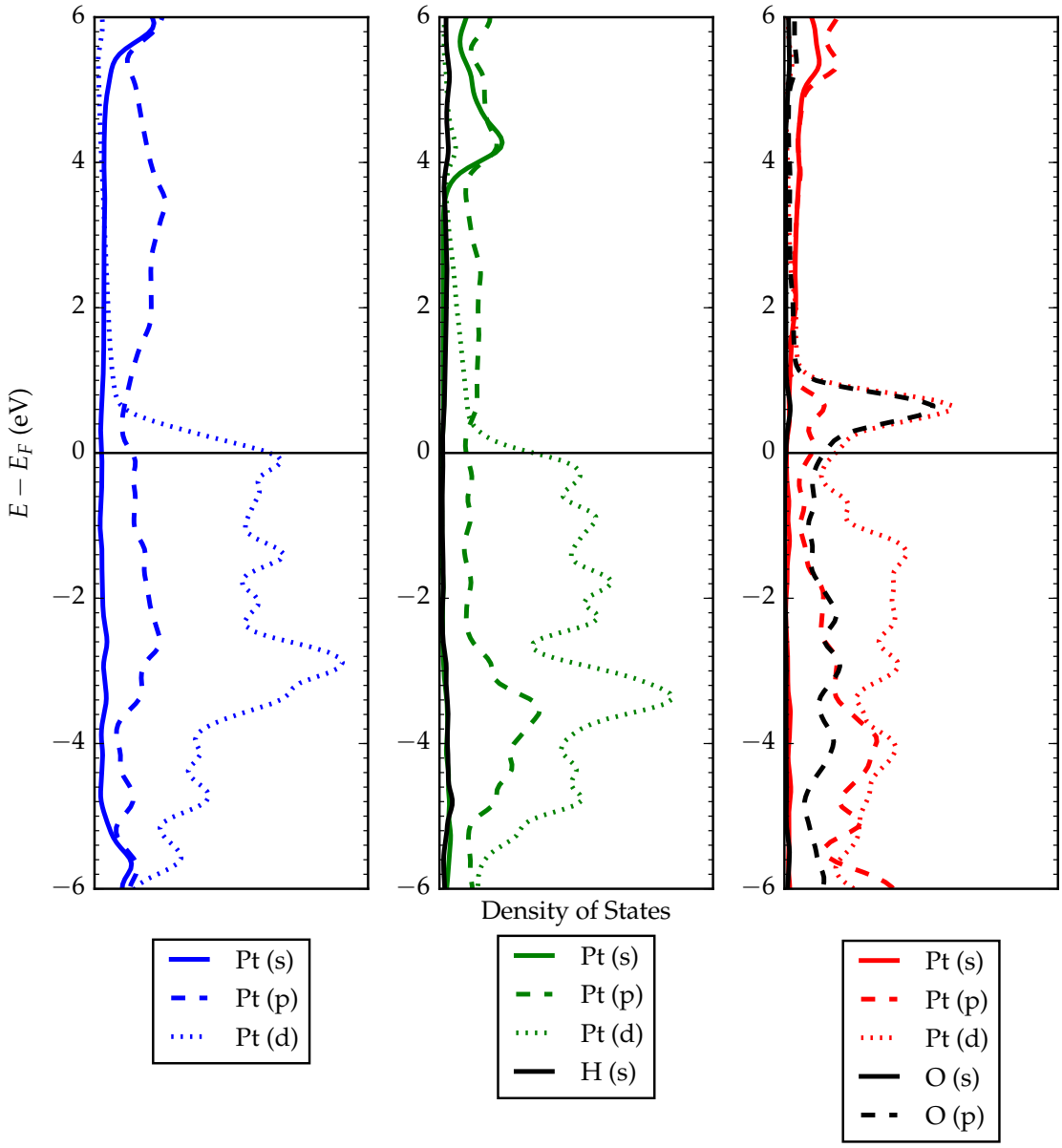

Figure 3.29: PDOS plots for Pt. (Left) Electronic density around a surface Pt atom in a clean slab projected onto s (solid), p (dashed) and d (dotted) orbitals. (Middle) PDOS for a surface Pt atom (green lines) and hydrogen (black line) in a slab with 1 monolayer of Hydrogen adsorbed. (Right) PDOS for a surface Pt atom (red lines) and oxygen s (solid black line) and p (dashed black line). Introduction of hydrogen shifts the edge of the sp band above the Fermi level down from above 5 eV to around 4 eV. In the presence of oxygen there are some new states introduced around and above the Fermi level.

3.4 Conclusions

In this chapter we've reviewed the effects of the composition of the metal surface, the effects of adding a simple adsorbate to the surface, and the effects of adding an adsorbate that changes the electronic structure of the surface by a much greater amount. The high-energy threshold of the interband transition of Ag lends to its strong LSPR compared to Cu with its similar electronic structure.

In order to react, reagents must adsorb to the catalytic surface; catalysts typically operate in conditions where the reacting species have a non-zero concentration. Under these conditions, the presence of adsorbates will substantially change the optical properties of the catalytic particles, likely decreasing the strength of the plasmon intensity.

CHAPTER 4

Energetic Charge-Carrier Lifetime and Decay

The surface plasmon combination of a photon and collective oscillation discussed in chapter 2 and chapter 3 decays to form a single hot electron through a process called Landau damping. In an unreactive environment, this hot electron collides off other electrons forming a thermalized distribution of electrons. The hot electron distribution cools over time by coupling to substrate phonon modes, increasing the thermal temperature of the substrate. The time scales of these processes are important to modeling interactions between energetic charge-carriers and adsorbates – whether it is the initial hot electron or the resulting thermal distribution triggering a chemical transformation. In this chapter we use the Fermi liquid model and Boltzmann transport equations to look at time scale of the initial thermalization – the formation of a large group of low-energy charge-carriers from a small number of high-energy charge-carriers – and the TTM to review the time scale of the lifetime of this resulting distribution.

4.1 LSPR-Mediated Heating of Substrate

Optical pump and probe experimental studies have been performed to shed light on the transfer of energy from a single excited charge-carrier to other electrons and substrate phonons through electron-electron and electron-phonon scattering [116, 117, 118]. The formation of a highly energetic charge carrier on a single nanoparticle (or multiple charge carriers for a collection of nanoparticles) comprises a highly athermal charge-carrier distribution; Fermi–Dirac statistics do not govern the energy distribution [119].

The initial hot electron collides with unexcited electrons, transferring the energy from a single charge carrier to a large number of lower-energy charge carriers over a few hundred femtoseconds; the resulting distribution follows Fermi–Dirac statistics at an effective electronic temperature above the thermal temperature of the substrate, $T_e > T_{ph}$ [45, 120, 121]. The maximum change in electronic temperature from pre-excitation ΔT_e^{me}, assuming heat transfer to the substrate is very slow, can be calculated as [87]:

$$\Delta T_e^{me} = \left[T_0^2 + 2\frac{N\hbar\omega}{aV_{np}} \right]^{\frac{1}{2}} - T_0 \tag{4.1}$$

where $\hbar\omega$ is the energy of the incoming photon, N is the number of photons, V_{np} is the volume of the nanoparticle, T_0 is the initial temperature, and a is a constant defining the electron heat capacity, $C_e = aT_e$ where a = 65 $\frac{J}{m^3K^2}$ for Ag. Ag nanocubes under illumination by 1, 2, or 3 photons (see Figure 4.1) with an ini-

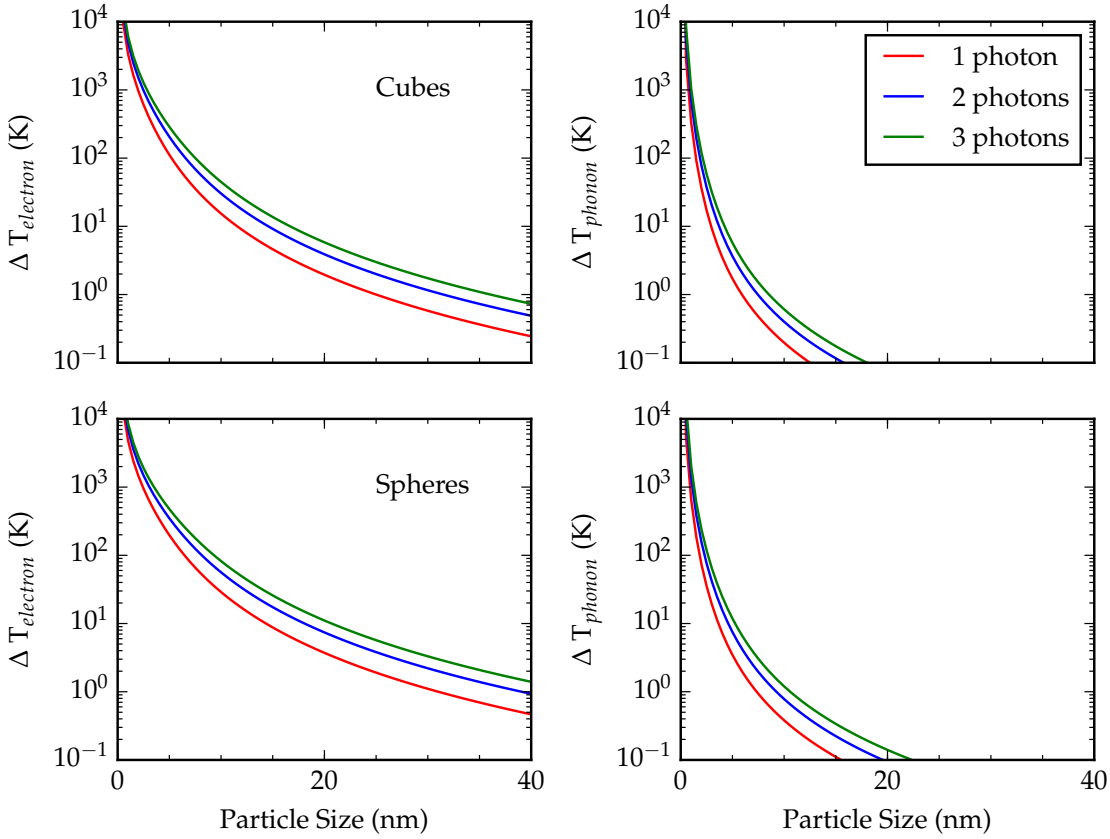

Figure 4.1: Maximum increase in temperature (T_e^{em}) for silver nanocubes (top) or nanospheres (bottom) illuminated with 1, 2, or 3 photons at 3 eV. Electronic temperature increase (left) for a single photon is $\sim$ 110 K for 5 nm cubes, $\sim$ 200 K for spheres. Maximum phonon temperature increase (right) for silver nanocubes. The temperature increase is $\sim$ 5 K at 5 nm.

tial temperature of 473 K, the electronic temperature change is negligible (i.e. $<$ 1 K) for particles over 20 nm. The temperature change exponentially increases as the particles decrease in size, small particles show a much larger increase in temperature ($>$ 1000 K for $\sim$ 2 nm particles). The excited charge carriers couple to substrate phonon modes around 1 – 10 ps [23]. On even longer time scales the heat is dissipated from the substrate to the surrounding medium [122, 123]. The characteristic timescale experiments and most of the methods discussed in this chapter

have traditionally been applied to single crystal studies; quantum confinement effects could cause the timescales to be slightly different for small nanoparticles.

Assuming all energy from the electrons goes into substrate phonons, the change in thermal electronic temperature can be calculated as [87]:

$$\Delta T_{ph}^{m} = \frac{\Delta T_{e}^{me} C_e}{C_L} \tag{4.2}$$

where C_L is the lattice heat capacity. As the data in Figure 4.1 show, the increase in phonon temperature is under 1 K down to below 10 nm nanocubes. Even at 3 nm, the increase is still on the order of 10 K. For spheres an increase of around 10 K is accomplished at a diameter of roughly 4 nm. For a commercial catalytic process, an increase of this amount ($\sim$ 10 K) approximately doubles the reaction rate [124]. Under some high-intensity situations, light-induced heating of the nanostructure can trigger chemical transformations [62, 125]. On the other hand, reactions can be triggered by transfer of optically excited energetic charge-carriers to surface-adsorbed molecules [13, 14, 50, 55, 126, 127]. It is hard to envision a scenario in which multiple electron-hole pairs are excited on any one particle in the low-intensity experiments (on the order of solar intensity, $\sim$1000 mW cm^{-2}). Therefore it is highly unlikely these low-intensity photon-driven processes on particles in excess of 3 nm are triggered through plasmon-mediated thermal heating of the nanostructure.

Many hot electron dynamics models such as the two-temperature model rely on an equivalent electronic temperature whereby the electrons follow a thermal-

ized Fermi–Dirac distribution giving the fraction of filled electronic states (f) as a function of state energy (E) [128, 129, 130]:

$$f_{F-D}(E) = \frac{1}{e^{\frac{E-E_F}{kT_{el}}} + 1} \tag{4.3}$$

where k is the Boltzmann constant, E_F is the Fermi energy, and T_{el} is the electronic temperature. When a single surface plasmon decays through Landau damping to form a single high-energy electron, or a number of high-energy electrons for a collection of nanoparticle, the resulting distribution is highly athermal – that is, it does not have a well-defined electronic temperature [131]. This electron will scatter off other electrons, transferring energy to the entire sea of electrons and ultimately forming a hot thermalized electron distribution. The time scale for this electron thermalization is the time scale of electron-electron coupling ($\sim$ 100 fs) which is fairly low compared to the time to couple to surface phonons ($\sim$ 1 ps); we will treat these two processes separately using the Boltzmann transport equations (§ 4.2) and the TTM (§ 4.3).

4.2 Thermalization of Electron Gas: Fermi Liquid

One result from the model of an electron gas as a non-interacting sea is that the lifetimes of excited electrons should be infinite in the absence of electron-electron interactions; the presence of these interactions with other electrons results in finite lifetimes of excited states. Fermi Liquid theory accounts for interactions be-

tween quasi-particles (elementary excitations) and a collection of surrounding particles [132]. The state of the interacting system in Fermi Liquid Theory is governed by the explicit distribution function, $f(\mathbf{k})$ where $\mathbf{k}$ comprises different wavenumbers.

4.2.1 Electronic Lifetimes

From Fermi Liquid theory we can get a rough estimate of the lifetimes of the high-energy excited states formed from the plasmon decay, assuming a Fermi–Dirac distribution at zero temperature (a step function where all states below E_F are filled and all states above are empty). An expression for the finite approximate electron lifetime due to to electron-electron scattering, is Equation 4.4 [133, 45]:

$$\frac{1}{\tau_{e-e}(E)} = \frac{m_e e^4 (E - E_F)^2}{64\pi^3\hbar^3 (\varepsilon_0\varepsilon_b)^2 E_S^{3/2}\sqrt{E_F}} \times \left[\frac{2\sqrt{E_F E_S}}{4E_F + E_S} + \arctan\sqrt{\frac{4E_F}{E_S}}\right] \tag{4.4}$$

where τ_{e-e} is the lifetime, m_e is the effective mass of an electron, e is the charge of an electron, $\hbar$ is the Planck constant, ε_0 is the permittivity of free space, ε_b is the interband contribution, E_S is the screening energy (associated with the screening length, q_S with $E_S = \frac{\hbar^2 q_S^2}{2m}$), E_F is the Fermi Energy. For the values of parameters used, please refer to Table 4.1.

The screening length describes the damping of electric fields caused by movement of the quasi-particles. Electrons tend to repel one another; around each electron there is a slightly electron-deficient area corresponding to a slight positive charge. This tends to compensate the negative charge of the electron; a larger

screening hole – i.e. longer screening length – reduces electron-electron repulsion over a larger area, enhancing electron-electron collisions. The Thomas-Fermi approximation for screening length neglects the contribution of the d-electrons to the screening, overestimating the actual screening length.

To bring the results more in line with experimental results, an adjustable parameter is used to calculate the screening length such that $q_s = \beta q_{TF}$ where $\beta = 0.73$ for Ag. This gives a screening length of 0.56, Å [45] in agreement with estimations from the literature at 0.6 Å [134]. This length corresponds to a screening energy (E_S) of ∼12.1 eV. For high temperatures (Maxwell-Boltzmann distribution), a Debye screening model could also be used to self-consistently calculate the screening length for an excited electron distribution [45, 135, 136, 137]. We assume that the overall electron distribution is not hot enough to follow Maxwell-Boltzmann statistics and we use the static screening approach.

Calculated lifetimes for a range of screening lengths are shown in Figure 4.2. For a screening length of 0.056 Å the lifetime of electrons around 1.5 eV above the Fermi level is around 200 fs; electrons around 3 eV above the Fermi level have a lifetime of around 100 fs. The Thomas–Fermi screening length underestimates the lifetime of excited states by roughly a factor of 2. These lifetimes suggest that the energy will begin to propagate through the electron gas on time scales well below 1 picosecond.

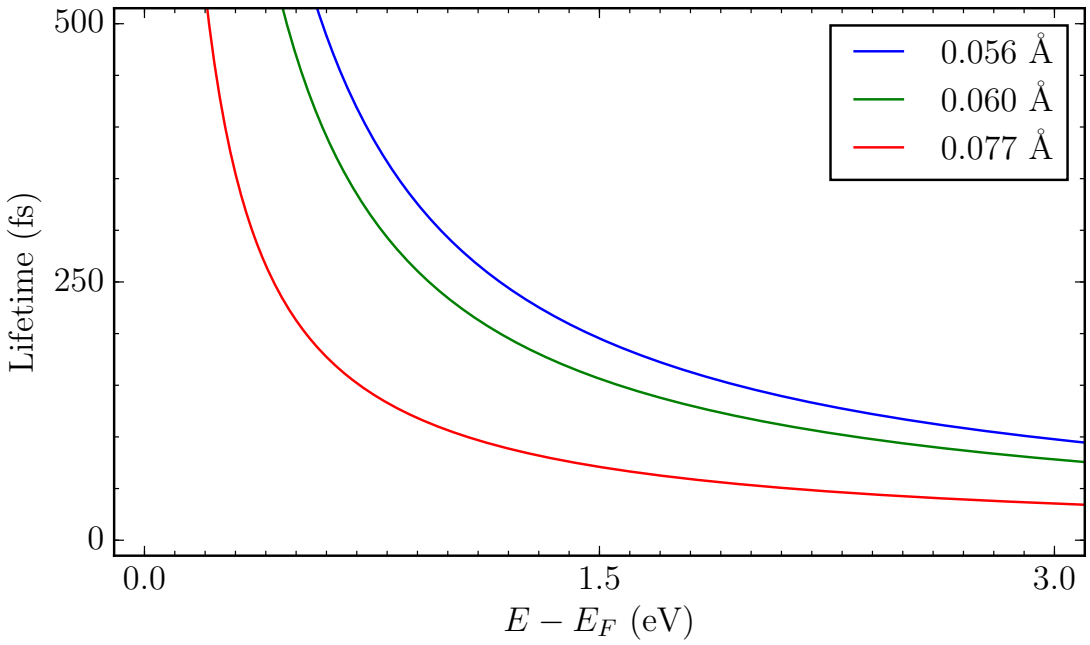

Figure 4.2: Lifetimes of excited electrons as a function of energy. Thomas–Fermi (red) underestimates the lifetimes.

4.2.2 Athermal Electron Dynamics: Boltzmann Equation

The formation and decay of highly athermal high-energy charge-carriers requires treatment of the electronic distribution explicitly through time – high energy and low energy electrons behave differently. The Boltzmann transport equations are a system of differential equations through time that describes changes in the electronic distribution function due to collisions with other electrons and phonons. We treat the electron distribution functions explicitly as a function of energy using the Boltzmann equation, where the hot electrons can gain/lose energy through a number of processes [136]:

$$\frac{\partial f(k)}{\partial t} = \left.\frac{\partial f(k)}{\partial t}\right|_{el-el} + \left.\frac{\partial f(k)}{\partial t}\right|_{el-ph} + \left.\frac{\partial f(k)}{\partial t}\right|_{el-exc} \tag{4.5}$$

Assuming an isotropic conduction band (i.e. $f(k) = f(E(k))$)[136, 87]:

$$\frac{\partial f(E)}{\partial t} = \frac{\partial f(E)}{\partial t}\bigg|_{el-el} + \frac{\partial f(E)}{\partial t}\bigg|_{el-ph} + \frac{\partial f(E)}{\partial t}\bigg|_{el-exc} \tag{4.6}$$

where $el - el$ is the electron-electron collision integral (i.e. scattering probability), $el - ph$ is the electron-phonon collision integral, and $el - exc$ is optical excitation. There are other more complicated processes such as electron-phonon-excitation, impact ionization, and multiphoton ionization that are neglected in our analysis [45, 135, 136, 137, 138]. We are studying electron dynamics in the first few hundred femtoseconds after the initial excitation, electron distribution changes on the energy scale of a phonon only have a minor influence on the overall dynamics [87]. Electron thermalization takes place on time scales of $10^1 - 10^2$ fs whereas electron-phonon energy exchange takes place on time scales closer to $10^1 - 10^3$ fs. For studying the initial hot electron dynamics, we therefore neglect the second term account for electron-phonon interactions. We are studying low light intensity, single-photon excitations; the third term is also assumed negligible. We handle the electronic excitation through initial conditions, discussed in subsubsection 4.2.2.1. Equation 4.6 simplifies to:

$$\frac{\partial f(E)}{\partial t} = \frac{\partial f(E)}{\partial t}\bigg|_{el-el} \tag{4.7}$$

The electron-electron interaction is described using a screened Coulomb potential [121, 136, 139]. The form of the electron-electron collision integral containing

for electrons at energy E_1 and E_2 colliding to give electrons at energy E_3 and E_4 is calculated as [45]:

$$\left.\frac{\partial f\left(E_1\right)}{\partial t}\right|_{e-e}=\frac{m_e e^4}{32\pi^3\hbar^3\varepsilon_0^2 E_S\sqrt{E_1}}\times \iint F\left[\frac{\sqrt{\tilde{E}}}{\tilde{E}+E_S}+\frac{1}{\sqrt{E_S}}\arctan\sqrt{\frac{\tilde{E}}{E_S}}\right]_{\tilde{E}_{min}}^{\tilde{E}_{max}} dE_2 dE_3 \quad (4.8)$$

where m_e is the effective mass of an electron, e is the charge of an electron, $\hbar$ is the Planck constant, ε_0 is the permittivity of free space, ε_b is the interband contribution, E_S is the screening energy (associated with the screening length), $\tilde{E}_{min}$ and $\tilde{E}_{max}$ are limits fulfilling conservation of energy ($E_1+E_2=E_3+E_4$):

$$\tilde{E}_{max}=\inf\left\{\left(\sqrt{E_2}+\sqrt{E_4}\right)^2;\left(\sqrt{E_1}+\sqrt{E_3}\right)^2\right\} \quad (4.9)$$

$$\tilde{E}_{min}=\sup\left\{\left(\sqrt{E_2}+\sqrt{E_4}\right)^2;\left(\sqrt{E_1}+\sqrt{E_3}\right)^2\right\} \quad (4.10)$$

and F is the Pauli exclusion term:

$$F=\left[1-f\left(E_1\right)\right]\left[1-f\left(E_2\right)\right]f\left(E_3\right)f\left(E_4\right) - f\left(E_1\right)f\left(E_2\right)\left[1-f\left(E_3\right)\right]\left[1-f\left(E_4\right)\right] \quad (4.11)$$

This term accounts for the effect of filling on collision probability; electrons can only collide from filled states and scatter to empty states. Note the similarities between Equation 4.8 and Equation 4.4; electron-electron collisions are primarily

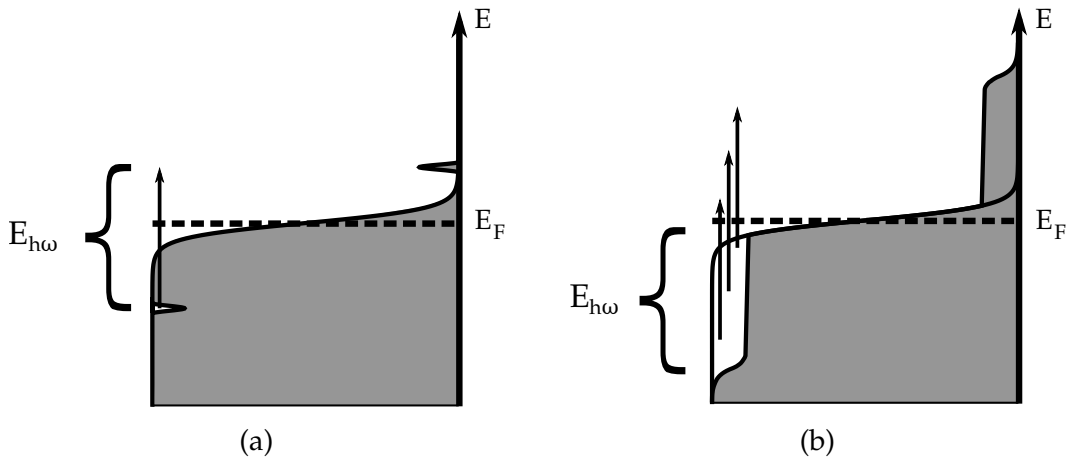

Figure 4.3: **a.** Formation of a single hot electron created by a single photon scattering event. **b.** Total collection of hot electrons formed over a population of nanoparticles.

responsible for excited electron decay. The parameters for this model are summarized in Table 4.1:

Table 4.1: Summary of Parameters for Boltzmann Transport Model

Effective electron mass, m_e	$1m_e$	
Interband permittivity, ε_0	3.7	
Fermi Energy, E_F	5.5	eV
Screening length, q_S^{-1}	0.056 Å	eV

4.2.2.1 Electronic Excitation

The decay of a plasmon (photon absorption) forms a single electron-hole pair in the substrate. The energy difference between the initial state of the electron and the final state is the incoming photon energy; $E = \hbar\omega$. This process can occur at any energy where there are both electrons and free states available at the correct energies, primarily for $E - \hbar\omega \leq E \leq E_F$, as shown in Figure 4.3a. For a collection of particles, a number of holes are created between E and $E - E_F$ and the hot elec-

trons are formed between E and $E + E_F$, as shown in Figure 4.3b. One treatment for the change in distribution is given assuming an isotropic parabolic conduction band and weak excitation limit [87]:

$$f(E) - f_0(E) = A\{\sqrt{E - \hbar\omega} f_0(E - \hbar\omega)[1 - f_0(E)] - \sqrt{E + \hbar\omega} f_0(E - \hbar\omega)[1 - f_0(E + \hbar\omega)]\} \quad (4.12)$$

This gives an average electron distribution over a collection of nanoparticles excited at a photon energy $\hbar\omega$.

4.2.2.2 Electron Distribution Function

Changes to the electron distribution function are tracked as $\Delta f = f(t) - f(t_0)$ as well as the linearization of the Fermi–Dirac distribution, termed Φ [138]:

$$\Phi(f(E)) = -\ln\left(\frac{1}{f(E)} - 1\right) \quad (4.13)$$

In thermal equilibrium Φ is linear with respect to energy with slope equal to $\frac{1}{k_B T_{el}}$. Linearity of the distribution describes adherence to Fermi–Dirac statistics and the slope is related to the electronic temperature; any deviation from linear behavior highlights deviations from a thermal distribution. An effective electronic temperature is determined by fitting a value to the simulation results using the least-squares method; minimizing the sum of the square residuals.

4.2.3 Results

The differential equation in Equation 4.6 is solved using Fortran 90 code with a 4th order Runge-Kutta method [140] with a step size of 1 fs. The first case we examine is shown in Figure 4.4 is a strong excitation (T_{el} ends at 3000 K) shown for relatively low energy photons of $\hbar\omega$ = 1.58 eV (785 nm wavelength). The initial electronic distribution at $T_{el} = 493K$ is a dashed red line; the excited distribution comprising a 'slice' of electrons moved from below the Fermi level to above is the solid red line in Figure 4.4. The small number of high-energy states transition to a large number of low-energy excited electrons just above the Fermi level; this is the peak developing above $E - E_F = 0$. Concurrently, a large number of corresponding holes is formed just below the Fermi level; this is the trough just below $E - E_F = 0$. The linearization function, Φ, shows that even at relatively low times of around 500 – 1000 femtoseconds, the function shows mostly linear behavior and can be approximated reasonably by an electronic temperature.

The bottom frame in Figure 4.4 shows the least-squares fitting of the distribution to an electronic temperature. Early on the distribution as a whole acts as if it were at a lower temperature; as the energy propagates through the electron distribution the effective electronic temperature increases up to around 3000 K. Simultaneously, as the distribution thermalizes, the sum of square residuals found by fitting the distribution to a Fermi–Dirac distribution rises to a maximum and then decreases. Within the first picosecond the distribution has largely thermalized.

Very similar results are seen for photons of 2.33 eV (Figure 4.5) and 3.00 eV

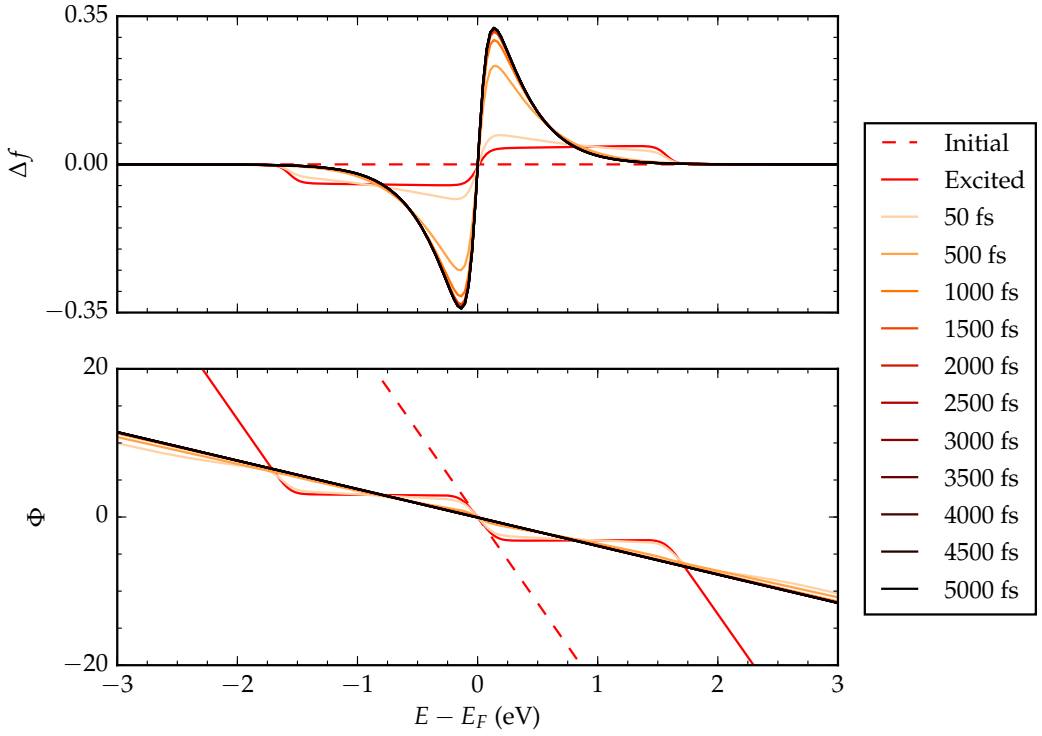

(a)

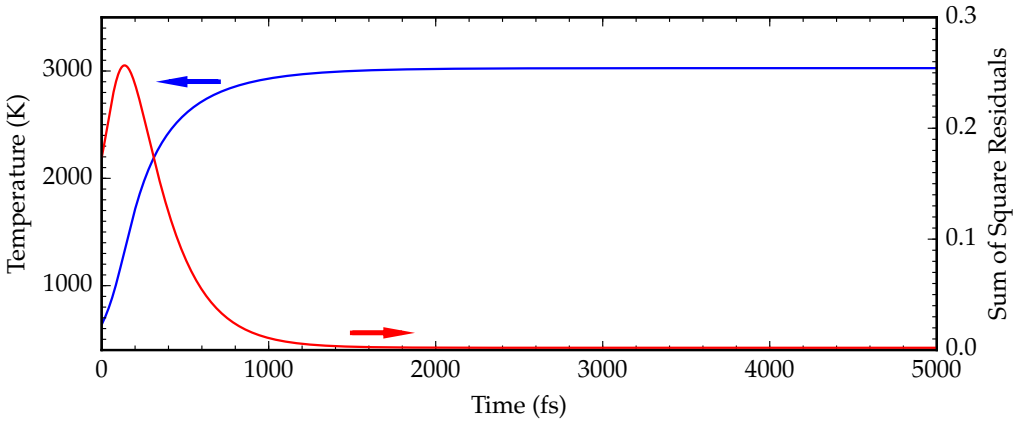

(b)

Figure 4.4: **a.** Change in electron distribution function and Φ (see Equation 4.13) with respect to energy for a high-intensity laser excitation of photons at 1.58 eV (785 nm). Virtually all change occurs over the first 1000 fs. **b.** The fitted electronic temperature (blue) increases as a function of time, asymptotically approaching 3000 K. The sum of square residuals for the fit (red) give a measure of thermalization and show most deviation disappears on the order of 500 fs – 1 ps.

(Figure 4.6); the time scale for thermalization are on the order of a few hundred femtoseconds.

The second case we examine is the average distribution for a collection of 2 nm particles, each under illumination from a single photon. This is shown in Figure 4.7, Figure 4.8, and Figure 4.9 for single photons of 1.58 eV, 2.33 eV, and 3.00 eV, respectively. The time scale for this weaker event is longer, but still on the order of a single picosecond for thermalization; within a few hundred femtoseconds the electronic temperature is in excess of 1000 K.

These simulations tell us that – depending on the strength of the excitation – the time from initial plasmon decay to the formation of a large number of low-energy electrons is on the order of a few hundred femtoseconds, while true thermalization takes longer – on the order of one picosecond.

4.3 Cooling of Electron Gas: Two-temperature Model

The next process the electrons participate in is coupling to substrate phonons, dissipating heat from the hot electrons. This typically occurs on time scales longer than thermalization – on the order of a few picoseconds. We probe the timescales of this process using the two-temperature model – treating the hot electrons through an electronic temperature, T_{el} – which handles dissipation of heat from this electron gas to substrate phonons (modeled by a phonon temperature, T_{ph}). Two coupled partial differential equations relate the transfer of heat, in Equation 4.14

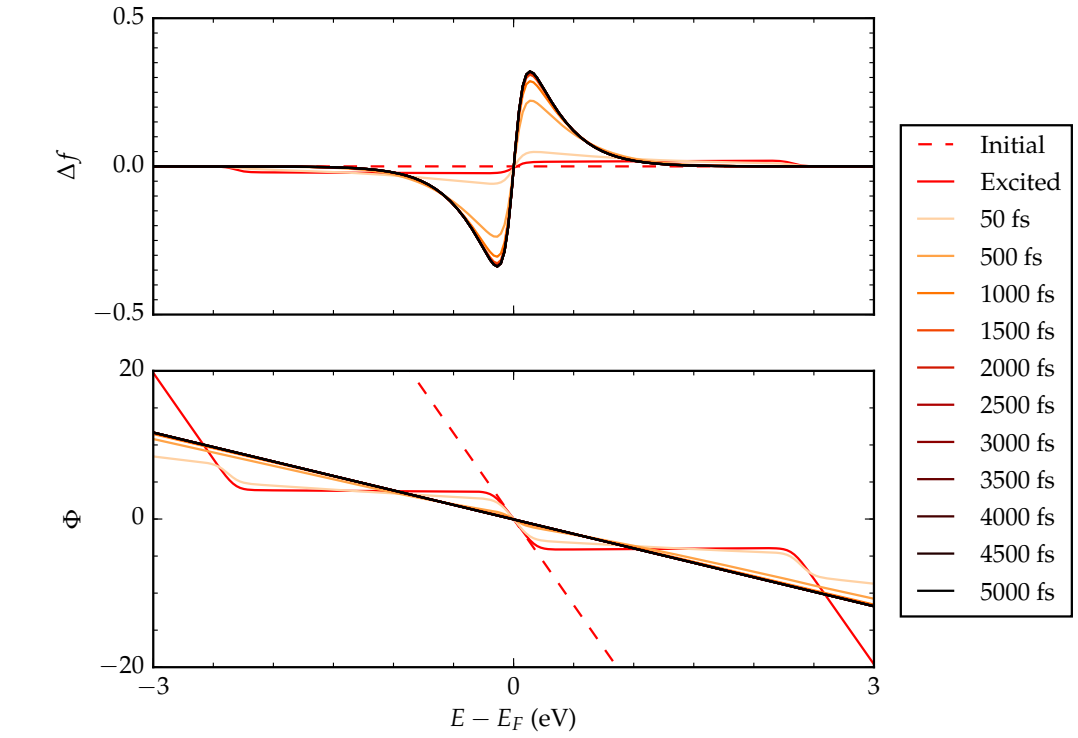

(a)

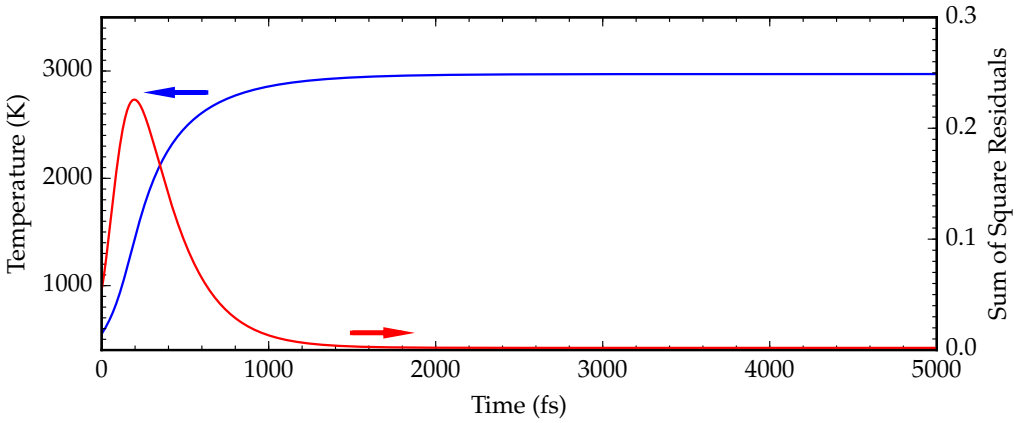

(b)

Figure 4.5: **a.** Change in electron distribution function and Φ (see Equation 4.13) with respect to energy for a high-intensity laser excitation of photons at 2.33 eV (532 nm). Virtually all change occurs over the first 1000 fs. **b.** The fitted electronic temperature (blue) increases as a function of time, asymptotically approaching 3000 K. The sum of square residuals for the fit (red) give a measure of thermalization and show most deviation disappears on the order of 500 fs – 1 ps.

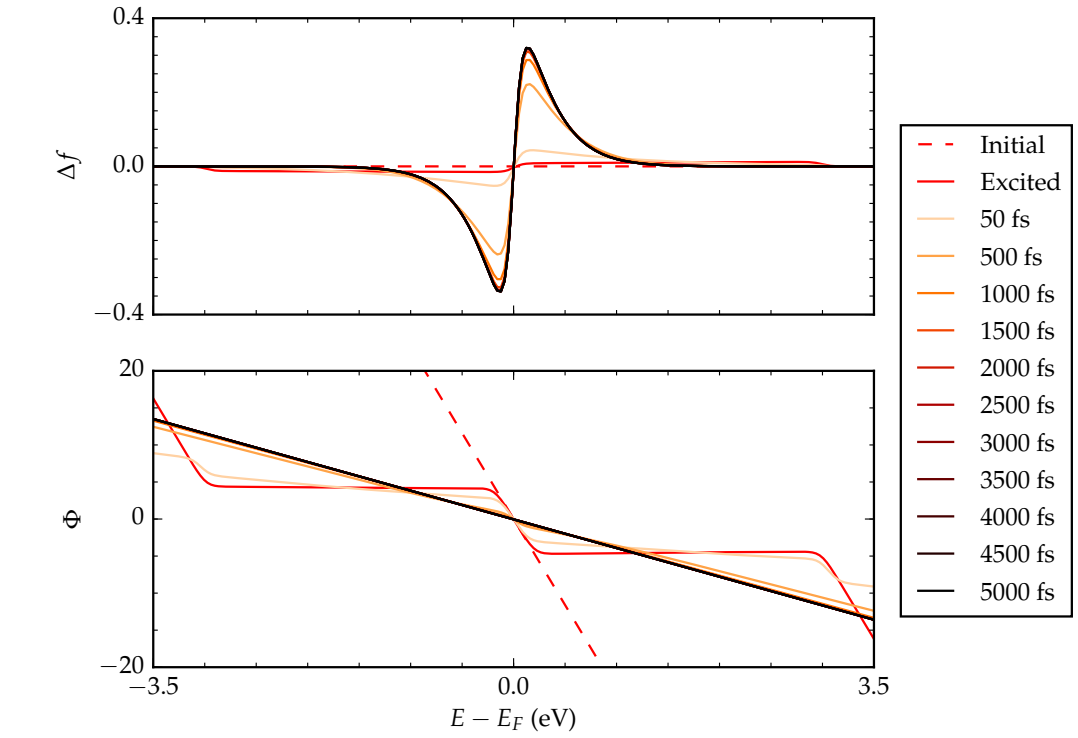

(a)

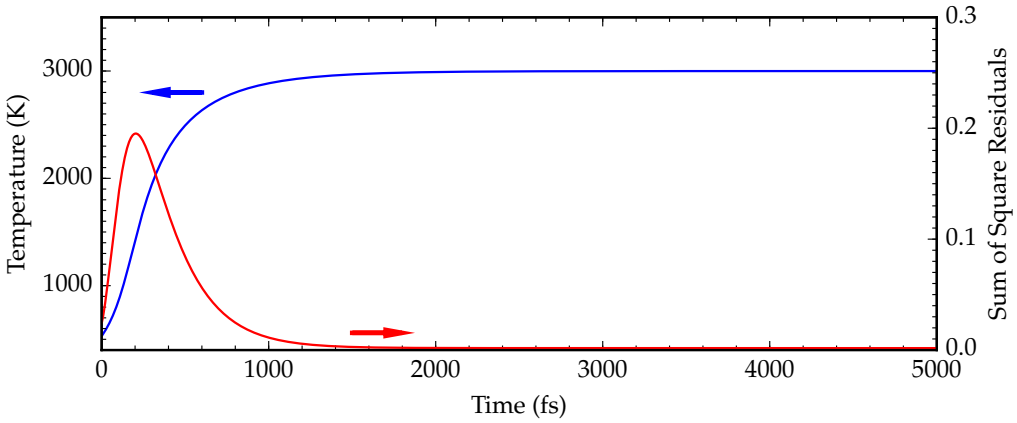

(b)

Figure 4.6: **a.** Change in electron distribution function and Φ (see Equation 4.13) with respect to energy for a high-intensity laser excitation of photons at 3.00 eV (413 nm). Virtually all change occurs over the first 1000 fs. **b.** The fitted electronic temperature (blue) increases as a function of time, asymptotically approaching 3000 K. The sum of square residuals for the fit (red) give a measure of thermalization and show most deviation disappears on the order of 500 fs – 1 ps.

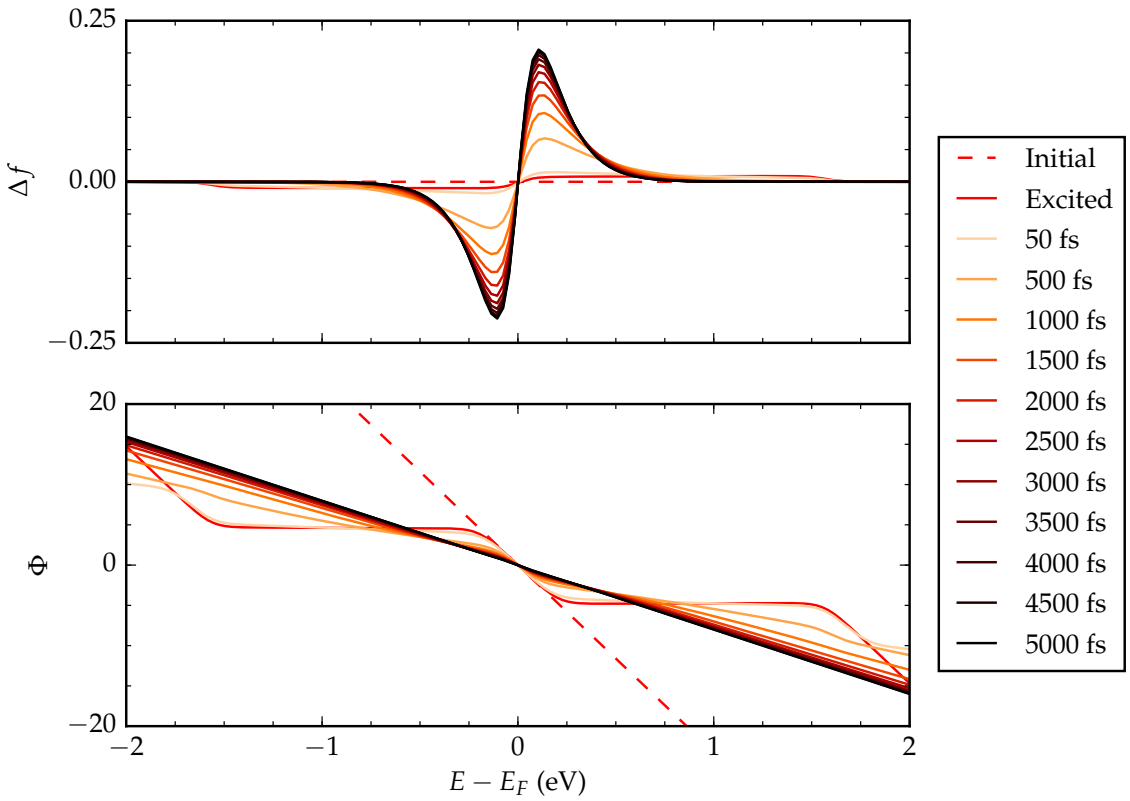

(a)

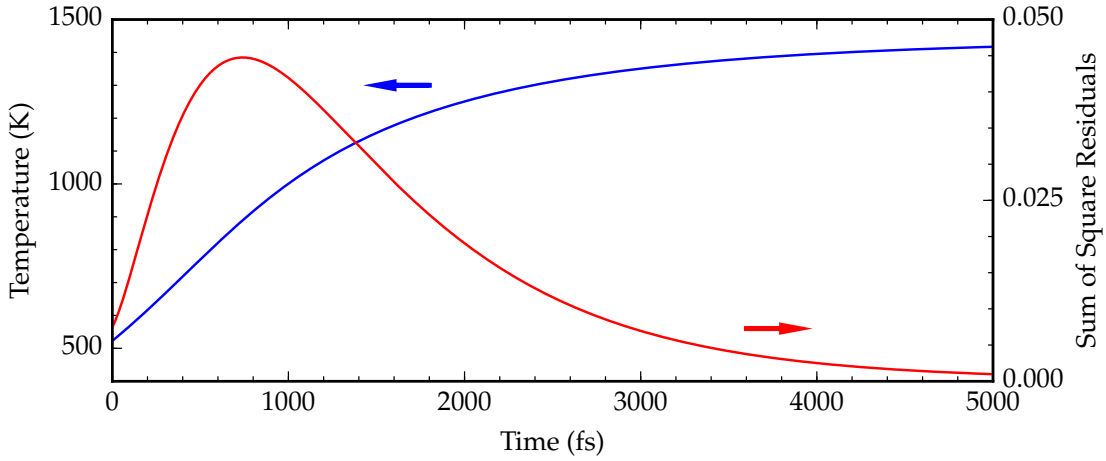

(b)

Figure 4.7: **a.** Change in electron distribution function and Φ (see Equation 4.13) with respect to energy for a collection of 2 nm particles each impacted by a single 1.58 eV photon. The time scale of thermalization is longer for the weaker excitation. **b.** The fitted electronic temperature (blue) increases as a function of time, asymptotically approaching ∼1400 K. The sum of square residuals for the fit (red) give a measure of thermalization and show most deviation disappears on a longer time scale; 1 – 4 ps.

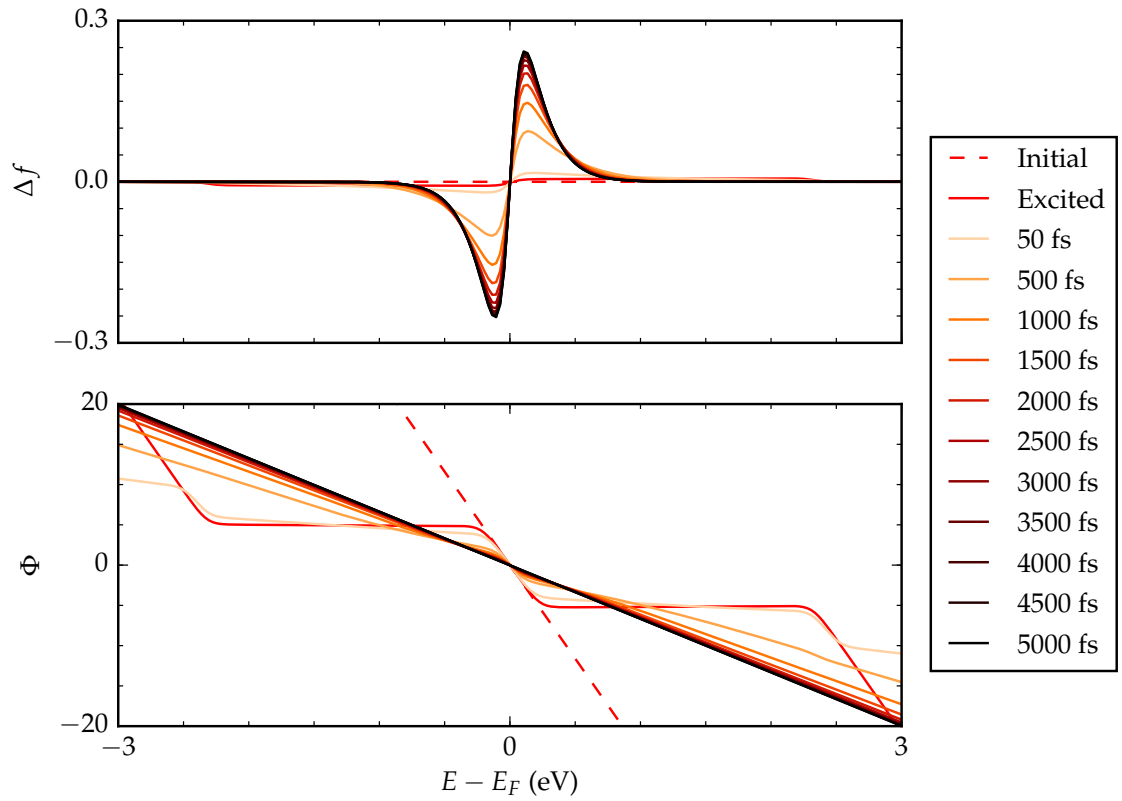

(a)

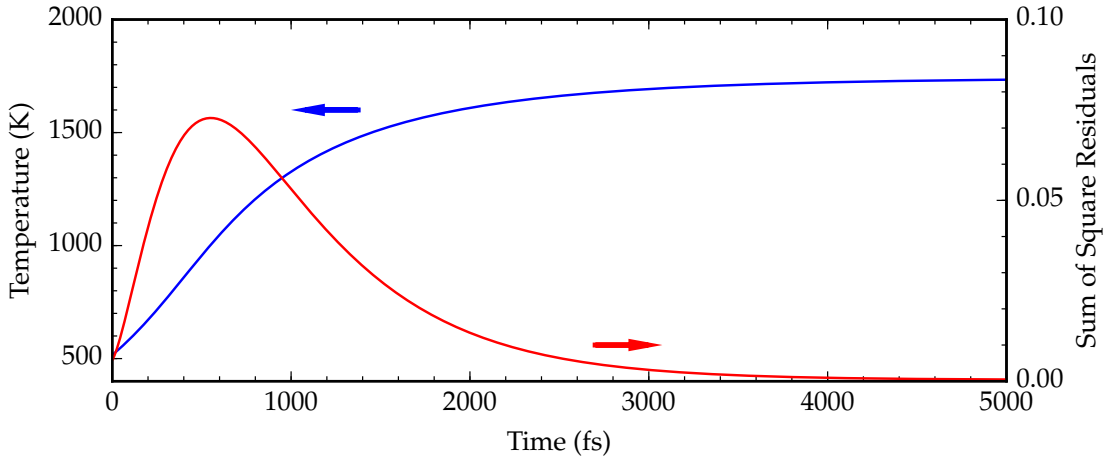

(b)

Figure 4.8: **a.** Change in electron distribution function and Φ (see Equation 4.13) with respect to energy for a collection of 2 nm particles each impacted by a single 2.33 eV photon. The time scale of thermalization is longer for the weaker excitation. **b.** The fitted electronic temperature (blue) increases as a function of time, asymptotically approaching ∼1400 K. The sum of square residuals for the fit (red) give a measure of thermalization and show most deviation disappears on a longer time scale; 1 – 4 ps.

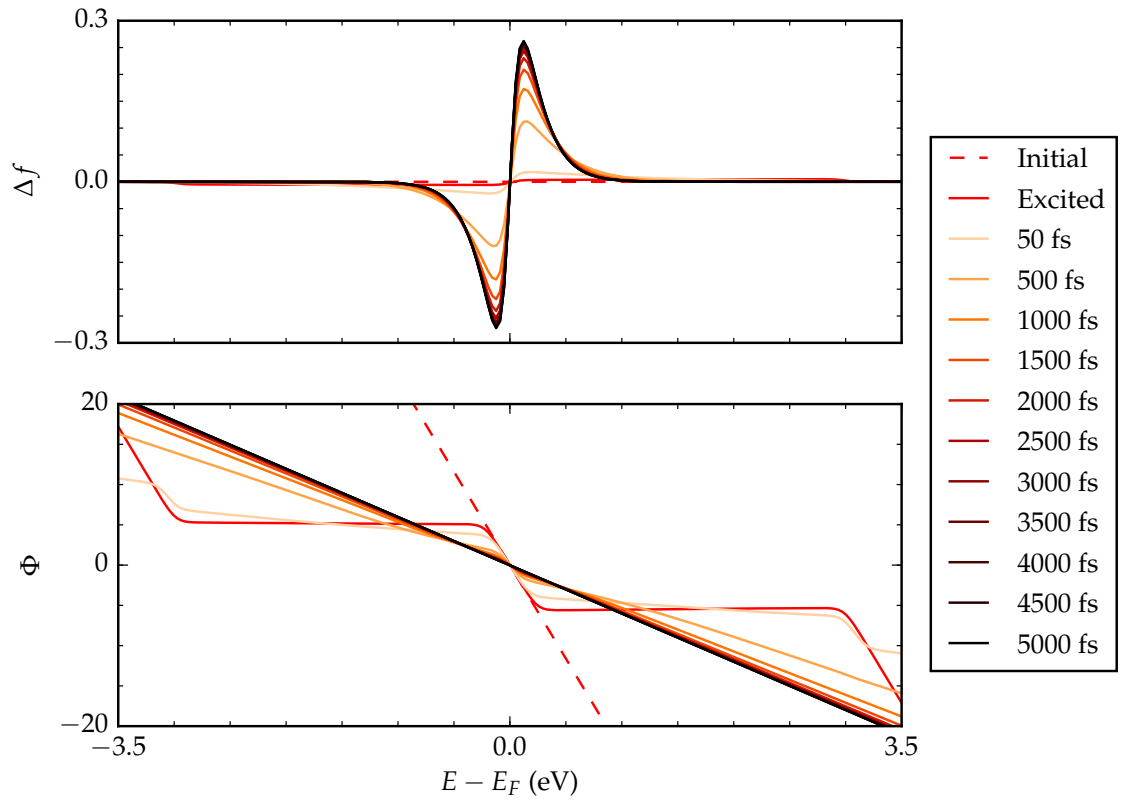

(a)

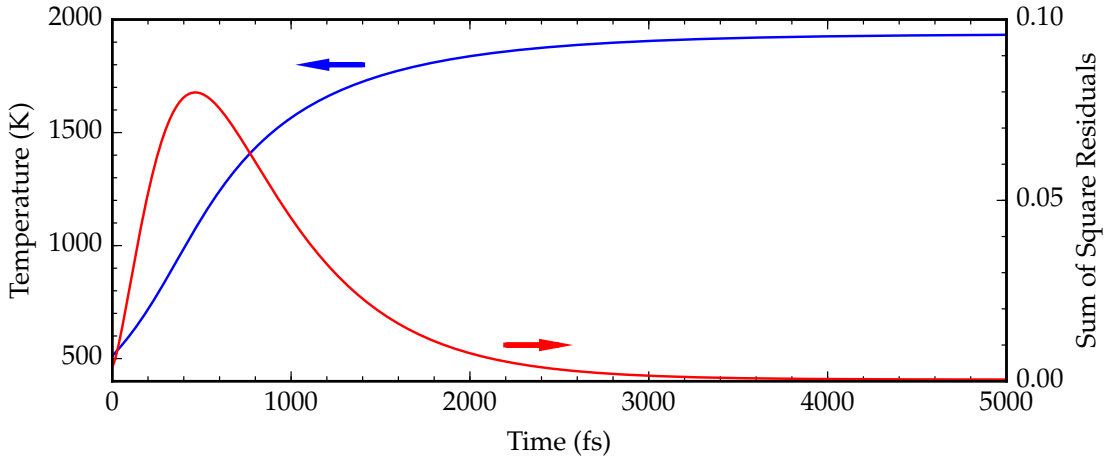

(b)

Figure 4.9: **a.** Change in electron distribution function and Φ (see Equation 4.13) with respect to energy for a collection of 2 nm particles each impacted by a single 3.00 eV photon. The time scale of thermalization is longer for the weaker excitation. **b.** The fitted electronic temperature (blue) increases as a function of time, asymptotically approaching ∼1400 K. The sum of square residuals for the fit (red) give a measure of thermalization and show most deviation disappears on a longer time scale; 2 – 4 ps.

Table 4.2: Summary of Parameters for Two-Temperature Model

Atom density, n	5.863×10^{28}	atoms/m^3
Coupling constant, g	3.50×10^{16}	W/m^3K
Electron Specific Heat, a	62.8	J/m^3K^2
Debye Temperature, Θ_D	215	K

and Equation 4.15 [129]:

$$C_{el}\frac{\partial}{\partial t}T_{el} = \nabla_z k \nabla_z T_{el} - g\left(T_{el} - T_{ph}\right) + S\left(z,t\right) \tag{4.14}$$

$$C_{ph}\frac{\partial}{\partial t}T_{ph} = g\left(T_{el} - T_{ph}\right) \tag{4.15}$$

where C_{el} and C_{ph} are the electron and phonon heat capacities, respectively, and S is a laser source term, modeling adsorption at the surface and the penetration of some light into the interior. The electron heat capacity, as described in § 4.1 varies as a constant with respect to the electronic temperature: $C_{el} = aT_{el}$ where $a = 65\frac{J}{m^3K^2}$ for Ag. The phonon heat capacity can be calculated with the Debye model [141]:

$$C_{ph} = 9nk_B\left(\frac{T_{ph}}{\Theta_D}\right)^3 \int_0^{\frac{\Theta_D}{T_{ph}}} \frac{x^4 e^x}{\left(e^x - 1\right)^2} dx \tag{4.16}$$

with atom density n, and Θ_D is the Debye temperature. We are looking at small particles under low intensity (on the order of single-photon excitations) and we assume the electron gas has already thermalized (i.e. there are no spatial gradients)

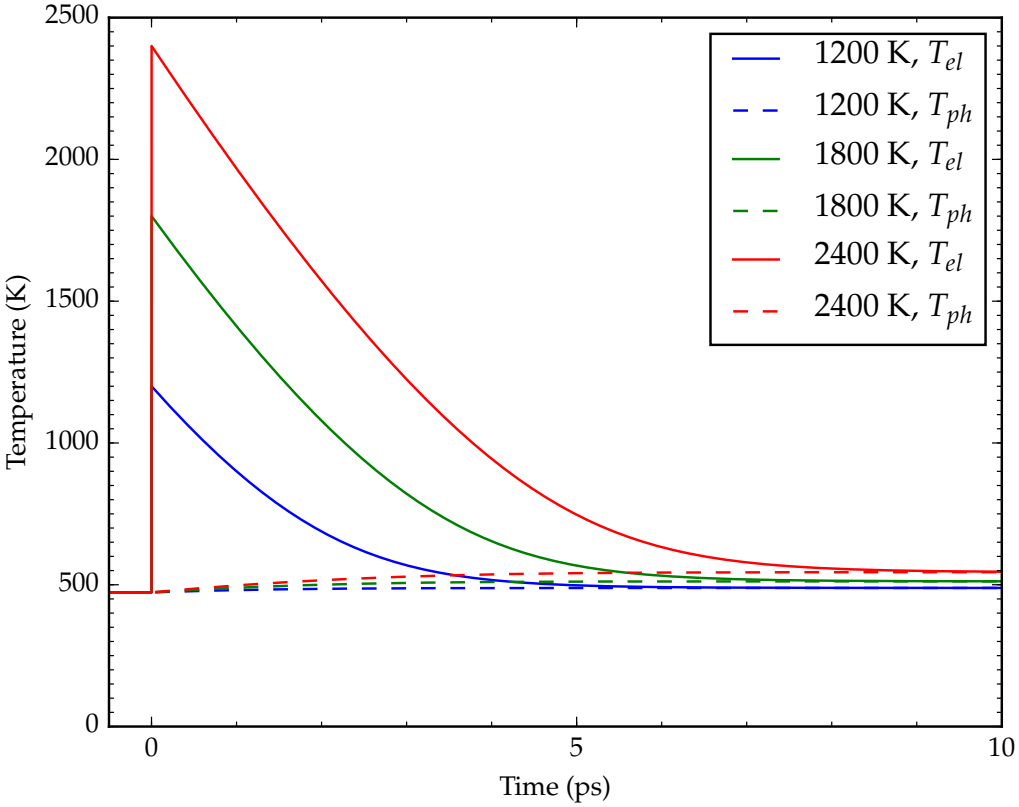

Figure 4.10: Cooling of hot electron cloud at 2400 K (red), 1800 K (green), and 1200 K (blue). Decay is on the order of 1 – 6 ps.

and the source term is zero. The resulting system of differential equations is:

$$C_{el}\frac{\partial}{\partial t}T_{el} = -g\left(T_{el} - T_{ph}\right) \tag{4.17}$$

$$C_{el}\frac{\partial}{\partial t}T_{ph} = g\left(T_{el} - T_{ph}\right) \tag{4.18}$$

The initial conditions for the electronic and phonon temperatures will depend on the temperature increase; for a single photon this corresponds to particle size. The results for a range of initial electronic temperatures are found in Figure 4.10. The characteristic time scales of the electron-phonon coupling are of around two orders

of magnitude greater than the electron-electron collisions discussed above; we assume that zero time for these simulations refers to the formation of a thermalized distribution at an excited temperature. The electronic temperatures of these particles remain excited for a few picoseconds after the initial excitation.

4.4 Conclusions

In this chapter we have modeled lifetimes of the initial athermal electron distribution, the time scales of formation of a large number of low-energy excited charge-carriers and the time scales of heat dissipation to substrate phonon modes for small Ag nanoparticles. These models are typically used for modeling high-intensity pulsed lasers; we are looking at lower-intensity events, down to single-photon. The time scales of the initial high-energy electrons is on the order of $1\times10^2 - 2\times10^2$ fs for electrons 1.5 eV to 3.0 eV above the Fermi level. Electron-electron scattering of these high-energy electrons with electrons around the Fermi level begin to form a large number of lower energy electrons around 2×10^2 fs – 1×10^3 fs. These low-energy excited electrons can scatter off of substrate phonons to cool on time scales around 1×10^3 fs – 5×10^3 fs.

At any point in this process there are possibilities for hot electrons to trigger chemical transformations in adsorbates present on the surface. The initial high-energy electrons can transiently occupy adsorbate antibonding states, exciting adsorbate vibrational modes over a single (or small number of) relatively high-energy event(s). The thermalized group of electrons can also scatter off adsorbate states

over a large number of low-energy scattering events. These two pathways are discussed in more detail in chapter 5.

CHAPTER 5

Electron-Mediated Chemical Transformation

Surface plasmon-mediated chemical transformations are reactions triggered by energetic charge-carriers generated on the surface by LSPR. We use the photon-driven dissociation of O_2 as a case study for probing mechanisms for charge-carrier driven molecular transformations [13, 14, 142]. These experiments are controlled carefully to operate under kinetic limitations. The reaction rate exhibits a four-fold increase under low intensity light illumination (see Figure 5.1a).

There are two experimental signatures distinguishing a charge-carrier driven reaction from a reaction driven by thermal heating [15]. The first is a transition from a linear to superlinear dependence of the reaction rate on photon flux (intensity) from low to high intensity (flux) – see Figure 5.1c. Under low intensity illumination the linear dependence implies that single-photon events trigger chemical transformations while at high intensities, multiple-photon events play a role [9, 15, 143, 144, 145]. The second experimental signature is an elevated kinetic isotope effect – the ratio between two reaction rates involving heavier and lighter isotopes – see Figure 5.1b. While not an exclusive signature of electron-driven reactions, the reaction also exhibited an exponential dependence of reaction rate

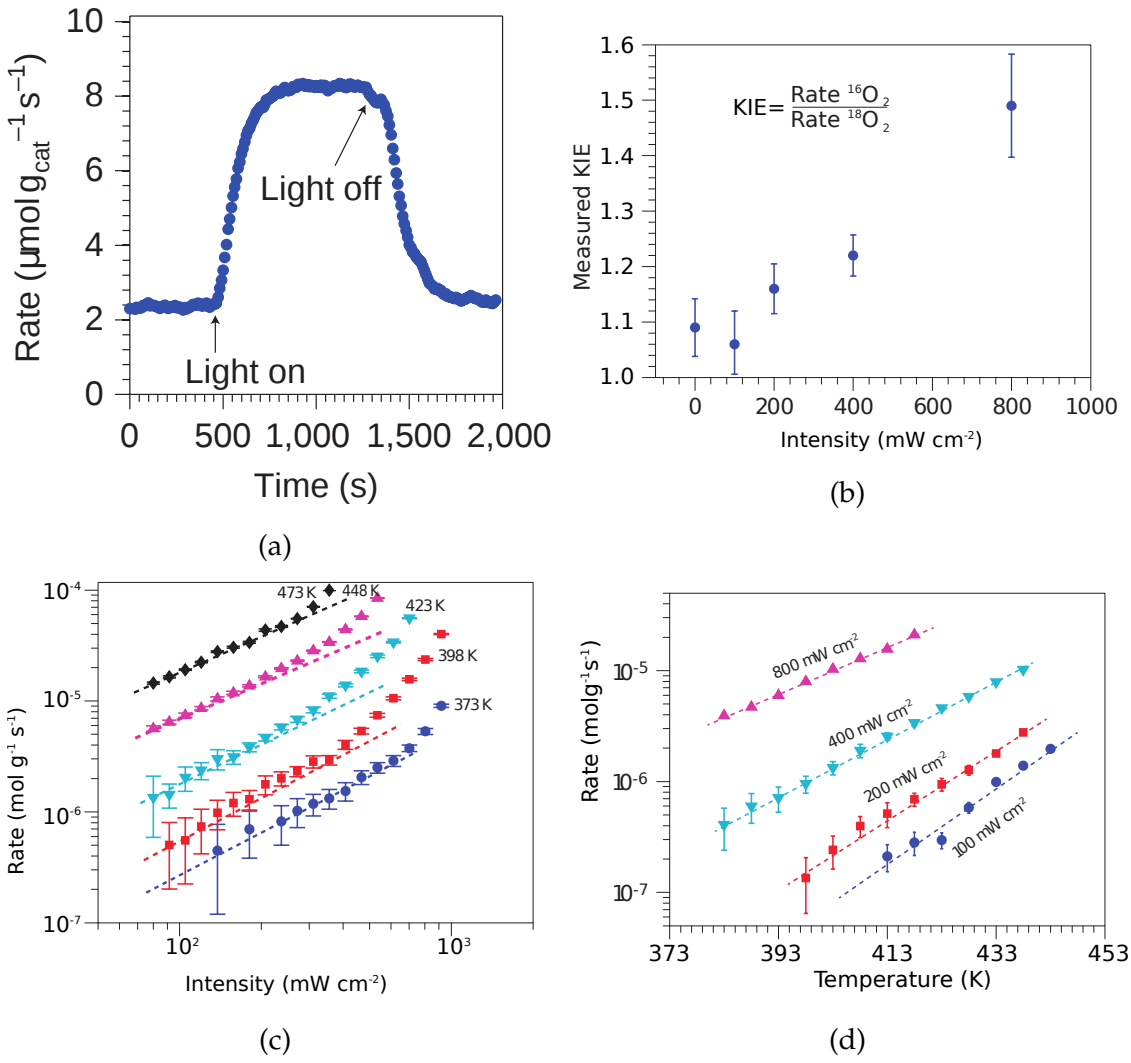

Figure 5.1: **a.** Light drives four-fold increase in O_2 dissociation rate. **b.** Photon-driven reaction shows elevated KIE relative to thermal rate, KIE_{therm} ~1.05 – 1.1. **c.** Reaction rate increases linearly as a function of light intensity up to a critical threshold where the rate transitions to a superlinear power-law dependence on intensity. **d.** Reaction rates increase exponentially with thermal temperature. All from [14].

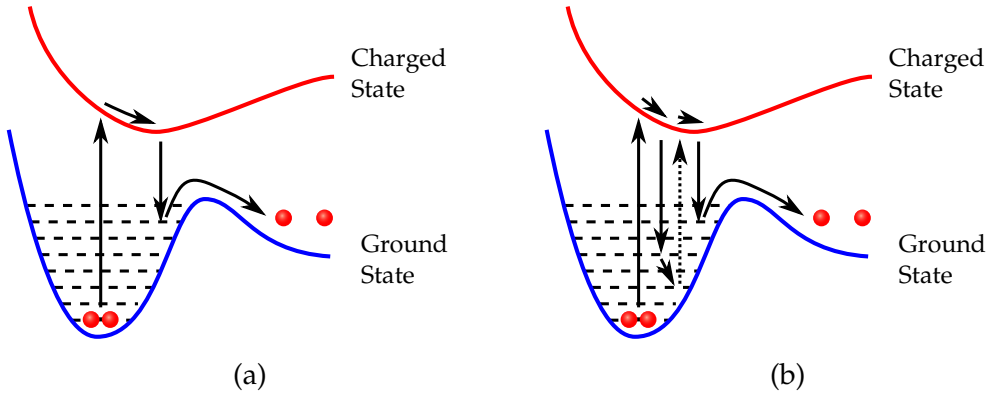

Figure 5.2: **a.** Schematic of electron-driven reaction where the adsorbate is pushed to a new potential energy surface and drops down at a higher vibrational mode. **b.** Above a critical intensity threshold multiple scattering events occur before the adsorbate decays in vibrational energy, leading to a superlinear reaction rate dependence on light intensity.

on thermal temperature (Figure 5.1d) – in contrast to the behavior of other photocatalysts such as semiconductors. Any model for hot-electron mediated reactions should be consistent with these experimental signatures.

Energetic electrons on the surface can transiently populate empty electronic states in the adsorbate-metal complex, inducing vibrational motion. The excitation of an energetic electron into antibonding states can excite the metal-adsorbate complex to a new excited PES; Figure 5.2a shows such an excitation. Electronic occupation of the antibonding orbital weakens the strength of the molecular bond – lengthening the equilibrium bond distance. In the case of a vibrating diatomic molecule this exerts a force along the reaction coordinate, inducing movement. The molecule moves along the excited PES until it decays down to the uncharged PES in an excited vibrational mode, re-emitting the electron at a lower energy. This inelastic scattering process transfers energy from the electron to the adsorbate vibrational modes. The vibrationally excited molecule is more likely to react than a

molecule in the ground state; if it does not react immediately it eventually returns to thermal equilibrium. This transfer in energy from a single electron scattering event to the adsorbate gives a linear dependence of reaction rate on light intensity, and is termed the Dissociation or Desorption Induced by Electronic Transitions (DIET) mechanism [146].

Under high photon flux, molecules will remain vibrationally excited for subsequent electronic scattering events (see Figure 5.2b) leading to an exponential power-law dependence of reaction rate on temperature. This regime is addressed with the Dissociation or Desorption Induced by Multiple Electronic Transitions (DIMET) model – consistent with the linear/superlinear transition exhibited by the Ag/O_2 experiments.

The ground state and excited state PES are independent of mass – the forces exerted on the molecule are independent of the atomic weights. Therefore, isotopes of differing weights will experience different accelerations; lighter atoms will experience more acceleration compared to heavier atoms [4, 147]. Modeling these processes requires treatment of both the ground and excited-state PES of these systems [148, 149, 150, 151]. The DIET/DIMET model results in both a linear to superlinear transition and an elevated KIE that is consistent with experimental results [13, 14].

This does not mean, however, that this mechanism is responsible under all conditions for all systems. Under certain conditions (e.g. high intensity, small particles) the interaction of a large number of low-energy electrons could scatter off of adsorbate states without the molecule being fully promoted to the excited PES.

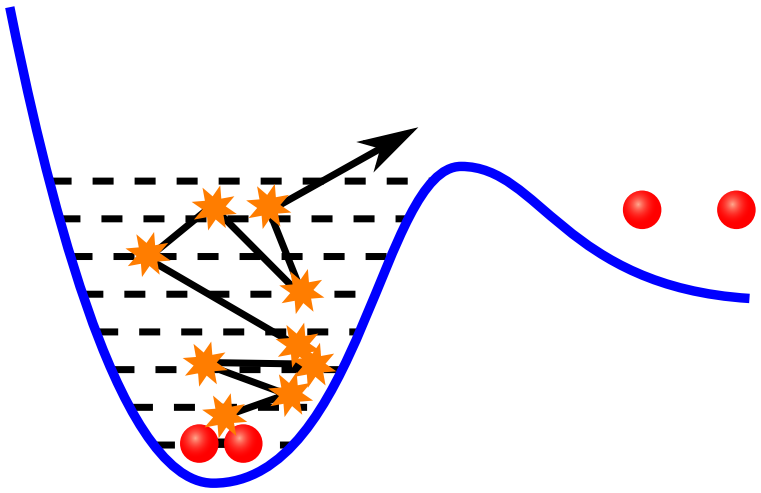

Figure 5.3: Many low-energy electron scattering events can push an adsorbate up the vibrational ladder.

As oxygen molecules vibrate over the metal surface, adsorbate states close to the Fermi energy will be filled periodically – the result of this is a drag force exerted on the molecule by the formation of (additional) low-energy electron-hole pairs. Additionally, low energy charge-carriers can inelastically scatter off the adsorbate, either gaining or losing energy. This second process is similar to Brownian motion: the adsorbate temperature will over time equilibrate with the electronic temperature [152]. A schematic diagram of this fluctuation-driven process is found in Figure 5.3.

5.1 Langevin Simulations

Using the low-intensity experiments involving O_2 dissociation on Ag (100) as a case study, we can suggest experimental signatures that we would expect to observe for an electronic friction-driven oxygen dissociation. Persson and Persson

developed a method for calculating vibrational lifetimes of adsorbates over metal surfaces; the physical basis of this model was the flow of energy between vibrating molecules above a metal surface and the metal surface itself [153]. As adsorbate molecules vibrate over the surface, the molecule remains on the ground state PES. Occasional filling of some adsorbate states is not enough to push the molecule up to an excited PES, in contrast to the DIET/DIMET model. The approach was originally developed for studying vibrational lifetimes (decay) over metal surfaces but was generalized to include charge carrier-induced excitations of adsorbates triggered by high-intensity lasers [154, 155, 156, 157, 158, 159].

5.2 Methods

Electronic friction can be used within molecular dynamics simulations through the Langevin equation to simulate the electron-adsorbate coupling. The Langevin equation is a force balance of all forces acting on the adsorbate. We use molecular oxygen as a case study to see what experimental signatures we would expect for a photocatalytic process driven by an electronic friction mechanism.

An adsorbate molecule vibrating over the surface encounters three forces. The first force is that of the molecular bond; thermal vibrations along the axis of the molecule are described well as a simple harmonic oscillator (see subsection 5.2.1). The second force is that of the friction force described above, that serves to sap energy from the adsorbate; this force is dependent on the electronic friction (i.e. the drag force exerted on the adsorbate through the formation of electron-hole pairs

in the substrate) and the velocity of the adsorbate along the molecular bond. Electronic friction is governed by Fermi's Golden Rule, that is, an electronic transition coupled to a vibrational transition (see subsection 5.2.2). It is strongly dependent on position, i.e. bond length, and the orbital overlap, i.e. electronic structure. The third force is a coupling between the adsorbate and the hot electron bath in the substrate at temperature; this force manifests as a random force governed by a gaussian distribution centered around 0 (see subsection 5.2.3). This third force is related to the second term: both are coupled electronic/vibrational transitions and both are governed by the electronic friction term.

The Langevin equation is [152]:

$$M\frac{d^2x}{dt^2} = -\frac{d}{dx}V_0\left(x\right) - \eta\left(x\right)\frac{dx}{dt} + \xi\left(t\right) \tag{5.1}$$

where x is the length of the molecular bond, V_0 is the molecular ground state PES, η is the position-dependent electronic friction, t is time, and ξ is the fluctuation force. The Langevin equation is solved numerically using the velocity Verlet algorithm [160, 161]:

$$V_{n+\frac{1}{2}} = V_n + \frac{\Delta t}{2}\frac{1}{M}\left(-\frac{d}{dx}V_0\left(x_n\right) - \eta\left(x_n\right)\frac{dx}{dt}_n + \xi\left(n\right)\right) \tag{5.2}$$

$$X_{n+\frac{1}{2}} = X_n + \Delta t V_{n+\frac{1}{2}} \tag{5.3}$$

$$V_{n+1} = V_{n+\frac{1}{2}} + \frac{\Delta t}{2}\frac{1}{M}\left(-\frac{d}{dx}V_0\left(x_{n+1}\right) - \eta\left(x_{n+1}\right)\frac{dx}{dt}_{n+1} + \xi\left(n+1\right)\right) \tag{5.4}$$

5.2.1 Ground State PES

The ground state PES was constructed using DFT calculations performed using the real-space grid-based projector augmented wavefunction code implemented in GPAW [111, 112]. Oxygen was placed on bridge sites on a 2x2x5 unit cell of an Ag (100) surface with the top three layers and adsorbate were allowed to relax until the forces on each atom were below 0.05 eV; the model system can be found in Figure 5.4a. After the system reached minimum energy, the oxygen bond distance was increased and decreased up to 0.5 Å to sample different bond lengths. A vacuum layer was 8 Å was inserted in the direction perpendicular to the surface. A 5x5x1 Monkhorst-Pack grid was used for sampling k-points in the Brillouin zone. The Revised Perdew Burke Ernzerhof (RPBE) functional was used to approximate exchange and correlation effects [101]. Fermi smearing was applied at an electronic temperature of 0.05 eV to aid convergence, and only occupied bands were converged. Real-space grid length of 0.18 Å was used.

The resulting PES is found in Figure 5.4b. A harmonic oscillator ($E = k \times x^2$) was fitted to the potential energy surface with a forcing constant k = 20.06 eV/Å and a fundamental vibrational energy ($\hbar\omega$) equal to 0.102 eV; this fit is compared to the DFT results in Figure 5.4b.

5.2.2 Electronic Friction

Electronic friction describes the transfer of energy between an adsorbate and a substrate. The electronic friction model has been used to describe electron-mediated

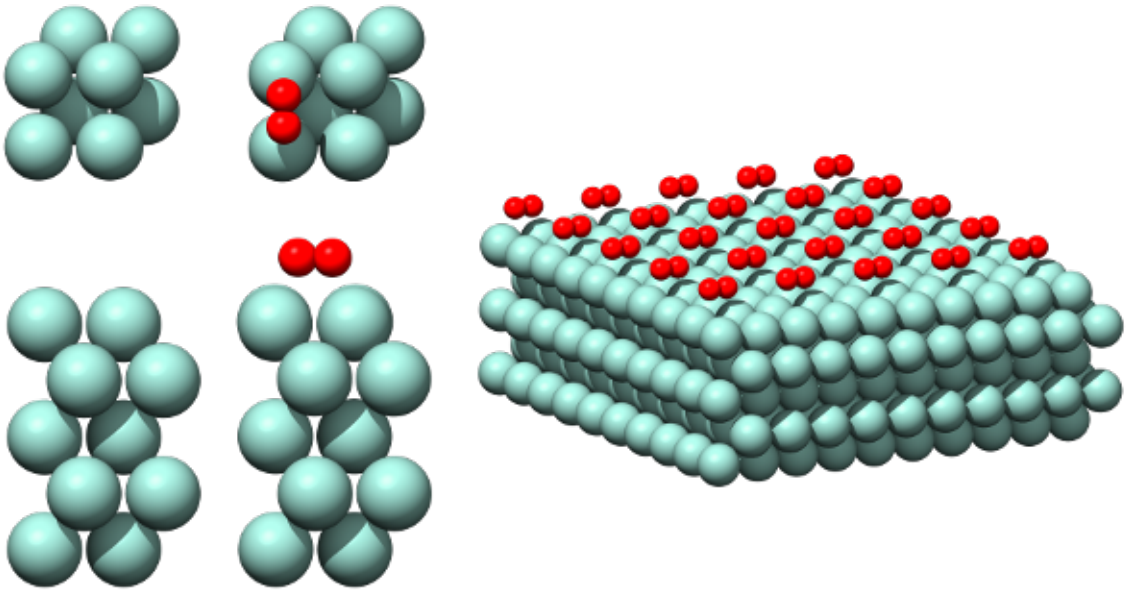

(a)

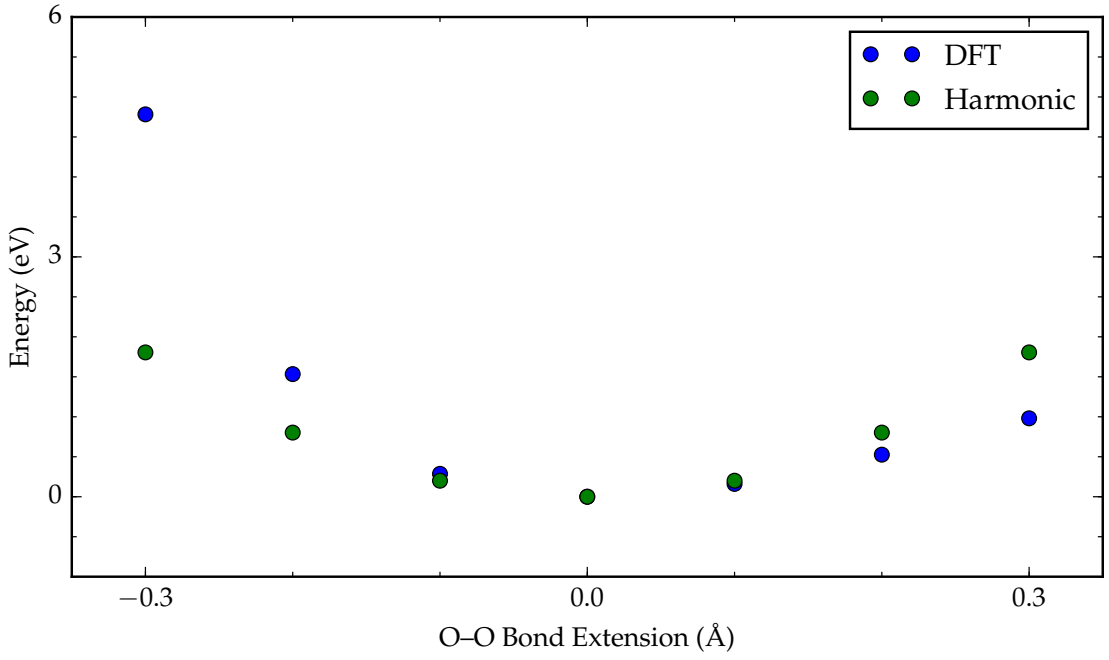

(b)

Figure 5.4: **a.** Top (top) and side (bottom) views of Ag slab (left) and Ag/O_2 (right). **b.** Potential energy surface for O_2 on Ag with harmonic fitting.PES

vibrational decay or excitation of adsorbates [152, 156, 158, 162, 163, 164, 165]. It accounts for coupling between admolecule degrees of freedom and the substrate sea of electrons. Contrasting the DIET model, the excited state potential energy surface does not play a role; the adsorbate remains on the uncharged ground-state potential energy surface [155]. The transition rate (Γ) resulting from coupling between a vibrational transition (u→v) and an electronic transition (i→f) is modeled using Fermi's golden rule [164, 166]:

$$\Gamma = \frac{4\pi}{\hbar} \sum_{fv} \left| V_{i,f,u,v} \right|^2 \delta \left(E_{iu} - E_{fv} \right) \tag{5.5}$$

where $V_{i,f,u,v}$ is the off-diagonal coupling between electronic and vibrational states, $E_{iu} - E_{fv}$ is the change in energy between initial and final electronic/vibrational energy. Assuming that the vibrational wave functions (i.e. the change in energy between vibrational states) can be approximated by a harmonic oscillator and that we are interested only in the rate of transition from the ground state to the first excited state (i.e. u = 0, v = 1) we can simplify Equation 5.5 to a sum over final electronic states:

$$\Gamma = \frac{2\pi\hbar}{M} \sum_{\beta} \hbar\omega \left| \left\langle \phi_R^i \left| \nabla_{\mathbf{R}} \right| \phi_R^f \right\rangle \right|^2 \delta \left(E_0 - E_f + \hbar\omega \right) \tag{5.6}$$

where ϕ are the many-electron wave functions, M is the reduced mass, and ω is the vibrational transition frequency. These are approximated by Kohn-Sham orbitals

(from DFT, see subsection 3.1.3), giving:

$$\Gamma = \frac{2\pi\hbar}{M} \sum_{kk'} (\varepsilon_k - \varepsilon_{k'}) \left| \langle \varphi_k \left| \nabla_{\mathbf{R}} \right| \varphi_{k'} \rangle \right|^2 \delta (\varepsilon_k - \varepsilon_{k'} + \hbar\omega) \tag{5.7}$$

A realistic solid gives a continuum of filled states, k and empty states, k'; using DFT gives a discrete set of states. Using a discrete set of states leaves very few or no sets of electronic transitions that satisfy the delta function. Krishna and Tully developed an averaging procedure that circumvents this limitation by using an energy window of varying width ε and calculating the value $\varepsilon^2 \times \Gamma$:

$$\Gamma\varepsilon^2 = \frac{2\pi}{M} \sum_{kk'} (\varepsilon_k - \varepsilon_{k'})^2 \left| \langle \varphi_k \left| \nabla_{\mathbf{R}} \right| \varphi_{k'} \rangle \right|^2 \tag{5.8}$$

Quadratic regression with respect to the energy window, ε, gives a result for the transition rate, Γ which is related to the electronic friction by the reduced mass [167, 168, 169, 170]:

$$\eta = M \times \Gamma \tag{5.9}$$

The electronic friction is determined by position – which modifies the orbital overlap – as well as electronic temperature – which changes the filling of states. The calculated electronic friction for O_2 on Ag (100) can be found in Figure 5.5. The fitting (for Equation 5.8) is shown in Figure 5.6 for equilibrium bond length and extended bond lengths from equilibrium (from -0.3Å– 0.5 Å)

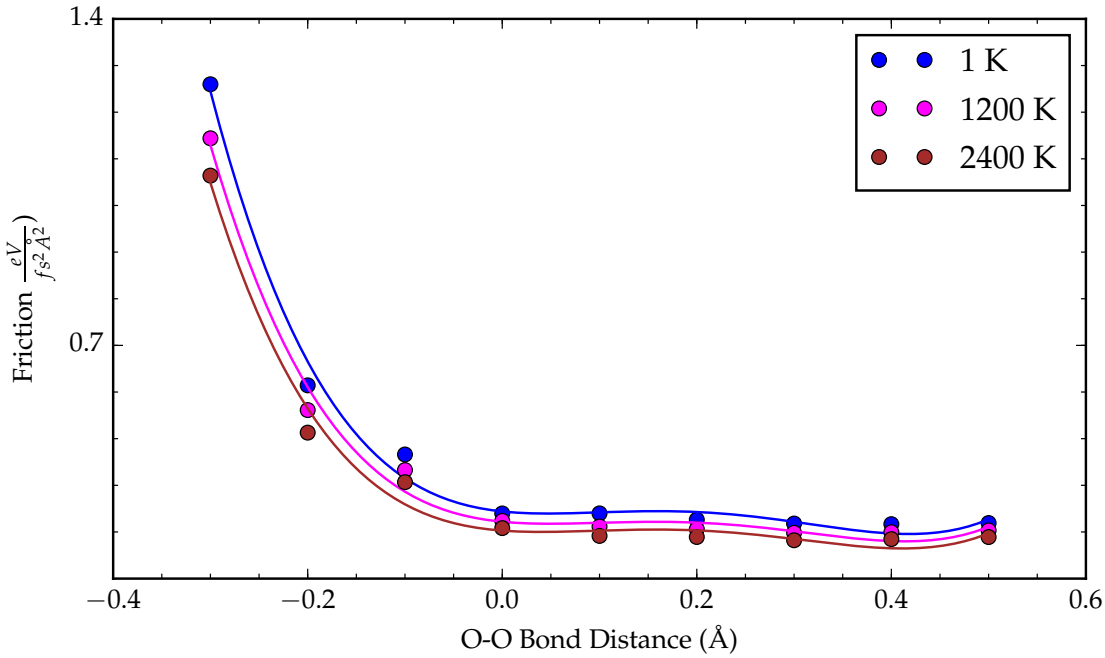

Figure 5.5: Position-dependent electronic friction and schematic diagram of hot electron bath-driven reaction. Electronic friction decreases as electronic temperature increases. Dots are calculated from DFT, lines are a fourth order polynomial fit used in dynamics simulations.

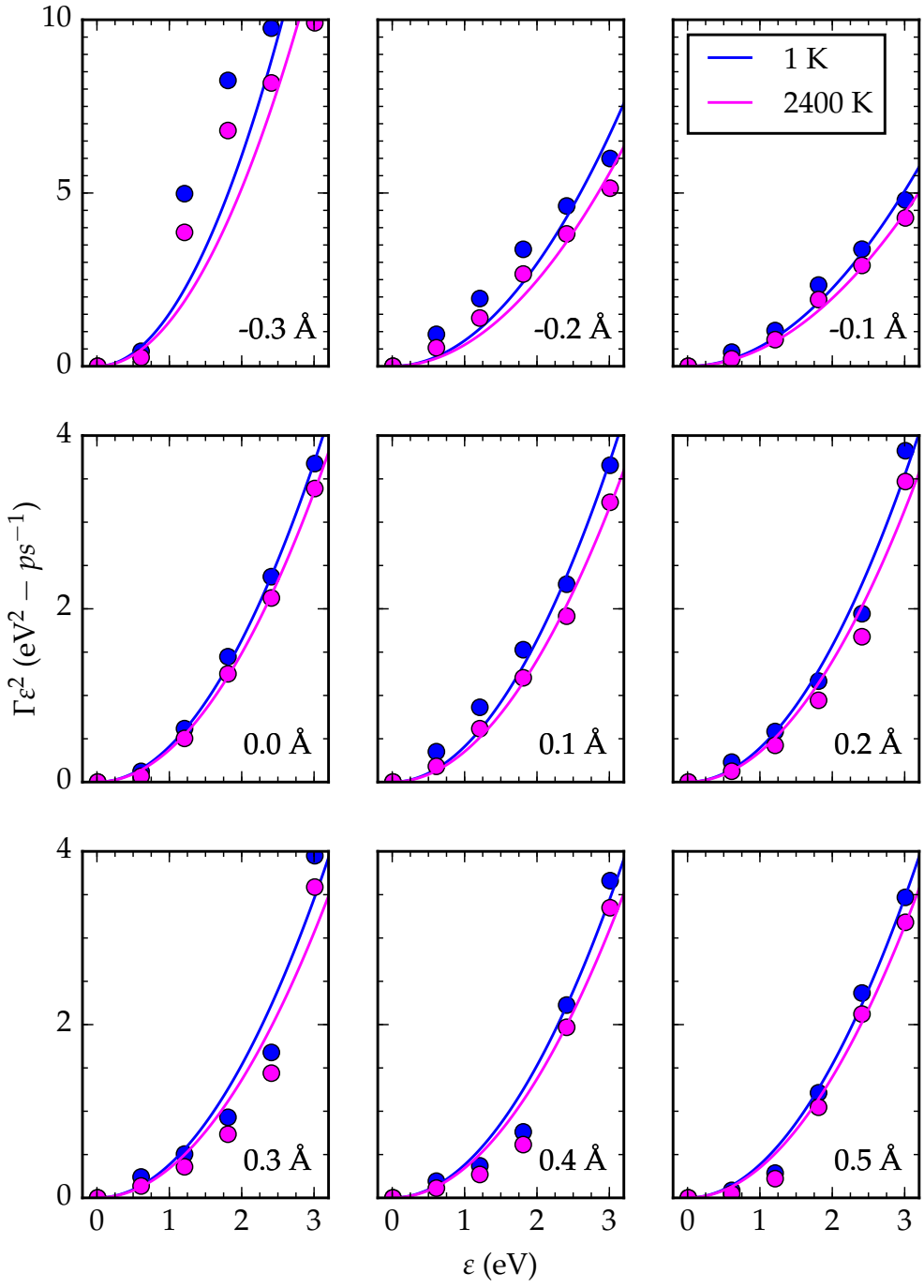

Figure 5.6: Quadratic fit of transition rate Γ, from $\Gamma\varepsilon^2$ as a function of ε. The assumption of a quadratic expression begins to break down with bond distances far from equilibrium.

5.2.3 Stochastic Fluctuation Force

The last force acting on the adsorbate is a random stochastic fluctuation force from the fluctuation-dissipation theorem; which assumes the adsorbate will equilibrate with the hot electron bath temperature, T_{el}. At its heart, this process is again an electronic transition coupled to a vibrational transition and is governed by the position-dependent electronic friction, $\eta(x)$. The force takes the form of a gaussian distribution with standard deviation [152]:

$$\sigma = \sqrt{2\eta(x) k_B T_{el}} \tag{5.10}$$

where η is again the electronic friction. In general, this fluctuation force will force adsorbate temperature (and energy) toward equilibration with the hot electron cloud, which will (in general) be well below the energy required to dissociate. The random nature of this force, however, means that it can push some molecules up the vibrational ladder if enough sequential fluctuation events occur to increase the energy of a particular adsorbate molecule.

A sampling of 10 trajectories can be found in Figure 5.7 for temperatures from 800 K to 2400 K. The same random seed was used in each set of simulations; only the magnitude of the fluctuation force (proportional to $\sqrt{T_{el}}$) is different. The data in this figure highlights the fluctuation force - the blue trajectory (the one ending at the highest energy) has gained between 0.10 eV and 0.2 eV, depending on the electronic temperature. Over thousands and millions of molecules, some will gain enough energy to dissociate; the dissociation yield will give us a reaction rate ana-

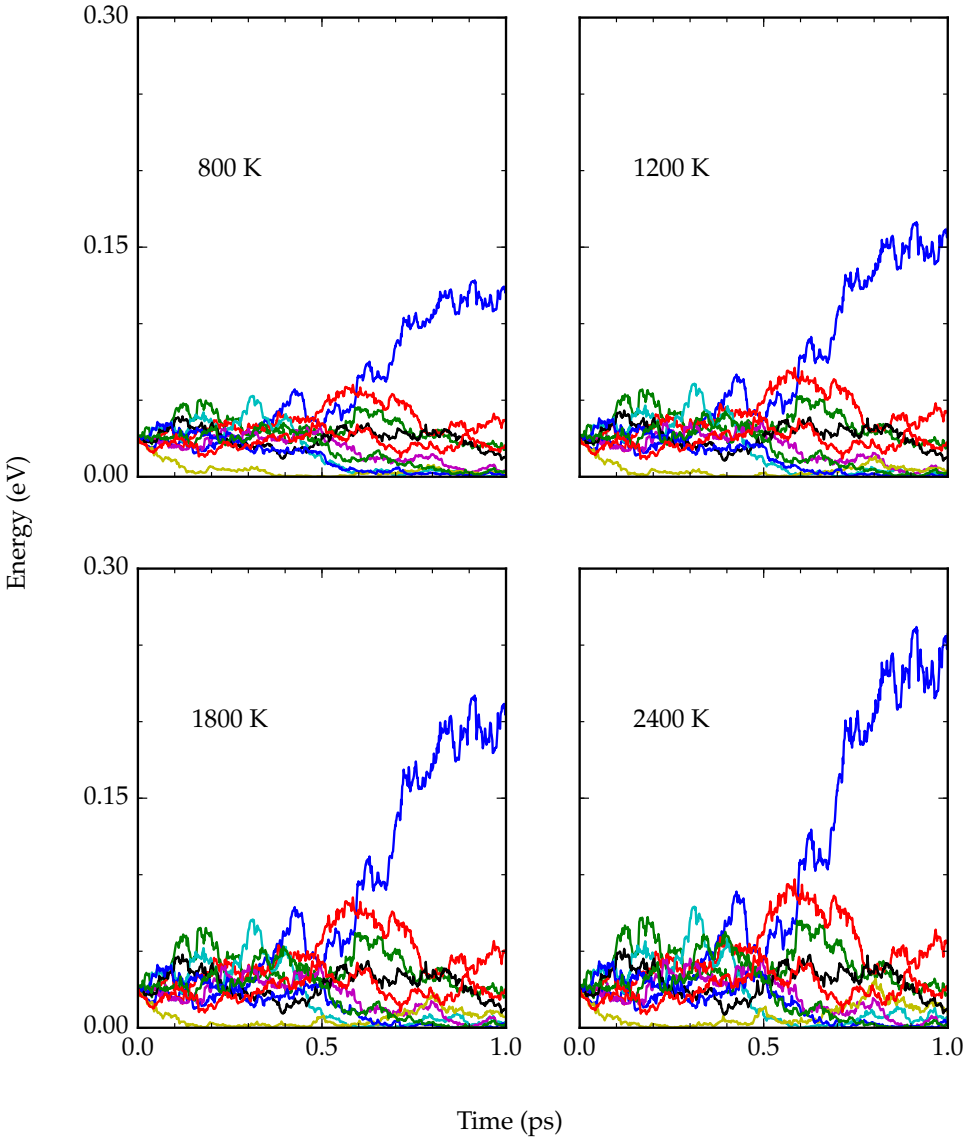

Figure 5.7: Sampling of molecular trajectories at different electronic temperatures with the same random number sequence for the fluctuation force. Lower electronic temperature is dominated by friction dissipation; higher electronic temperature leads to formation of more energetic oxygen molecules.

logue to determine which KIE and thermal temperature effects we expect to see.

5.2.4 Quantum-Corrected Initial Conditions

Molecules on the surface will comprise a large number of initial energies and populate both the vibrational ground state and vibrationally excited states. To sample these conditions, we used quantum initial conditions with classical simulations as they give better agreement with the quantum mechanical master equation compared to classical – all particles starting at $E = 0$ – or quasiclassical, where all particles starting in defined vibrational modes, n with $E = E_0\left(\frac{1}{2} + n\right)$ [158]. Isotope effects come into play in the initial conditions – different isotopes have different fundamental frequencies (ω), meaning the fundamental vibrational energy (E_0) is different. Temperature effects will change the initial populations of vibrationally excited states.

Each vibrational mode has a corresponding quantum wavefunction which follows the Wigner distribution as a function of energy (plotted in Figure 5.8):

$$\mathcal{P}_n = \frac{(-1)^n}{\pi\hbar} e^{-\frac{E}{E_0}} L_n\left(\frac{2E}{E_0}\right) \tag{5.11}$$

where L_n are the Laguerre polynomials [171, 172]. We employ quantum initial conditions over many initial positions (x) and momentum (p) to consistently sample energy space [158]. The selection method, involves sampling multiples of the quantum position ($x_Q = \sqrt{\hbar/m\omega} = 0.07$ Å) and momentum ($p_Q = \sqrt{\hbar m\omega} = 9.2$ eV-fs-A^{-1}). The sampling scheme involved a (8x8) grid from $0x_Q, 0p_Q$ to $3.5x_Q, 3.5p_Q$

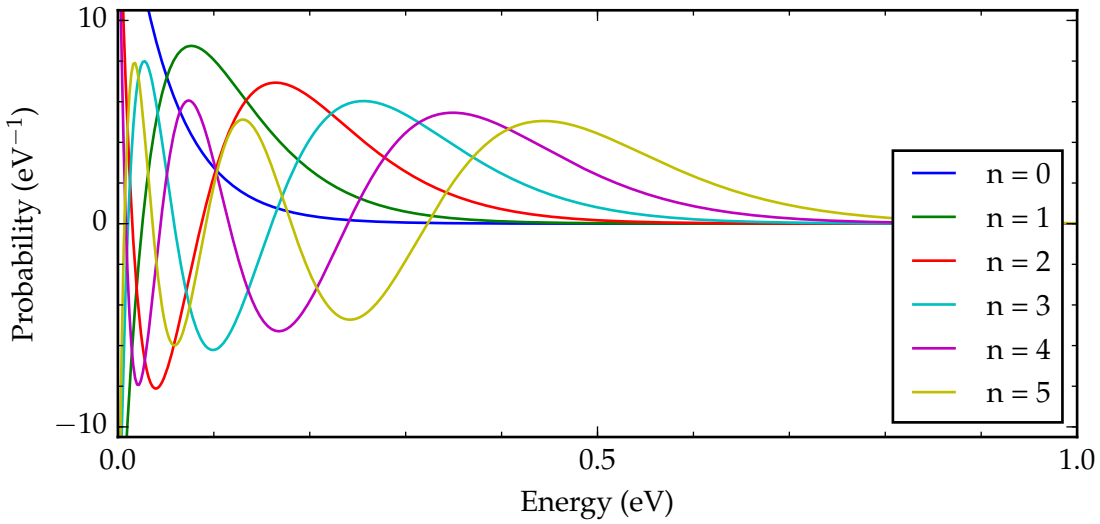

Figure 5.8: Probability distribution function for lowest five vibrational modes for quantum initial conditions.

in increments of $0.5x_Q$ and $0.5p_Q$.

At each initial point, 5×10^6 trajectories are simulated, giving a final probability distribution, $\frac{dP\left(E;x_0,p_0\right)}{dE}$. The final distribution is calculated for each vibrational initial state with each point weighted by the probability of that point in the vibrational mode:

$$\frac{dP_n\left(E\right)}{dE} = \int \mathcal{P}_n\left(x_0,p_0\right)\frac{dP\left(E;x_0,p_0\right)}{dE}dx_0dp_0 \tag{5.12}$$

A sample probability distribution function for ^{16}O and ^{18}O at 1 picosecond is shown in Figure 5.9a for the ground state and first five vibrationally excited states. We can calculate the final distribution for all vibrational states by weighing each vibrational mode from Equation 5.12 by the Bose–Einstein distribution:

$$\frac{dP\left(E\right)}{dE} = \sum_n \frac{dP_n}{dE}\frac{1}{e^{\frac{-E_n}{k_BT}}-1} \tag{5.13}$$

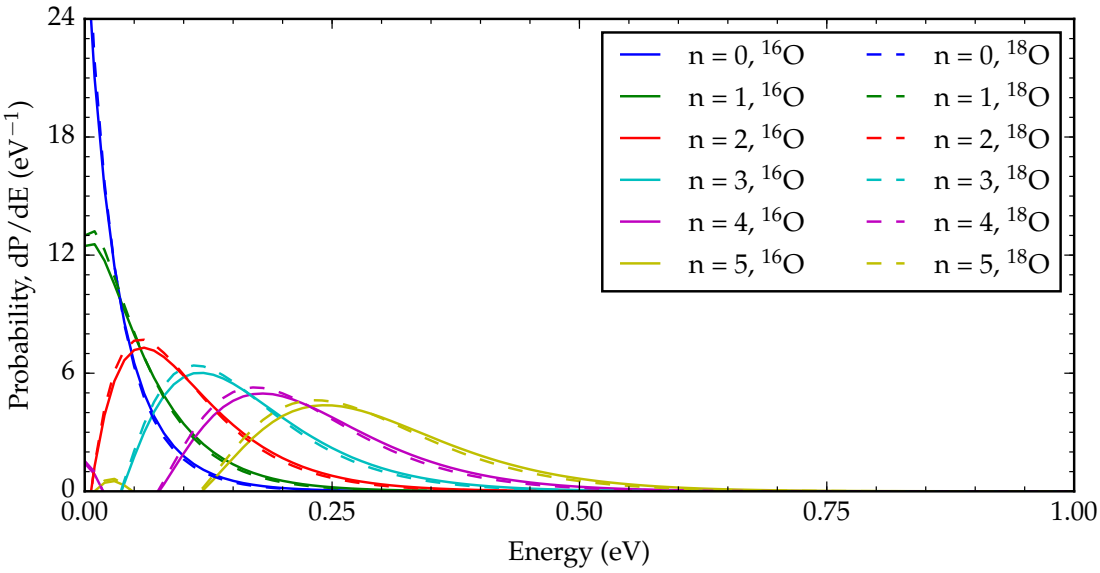

(a)

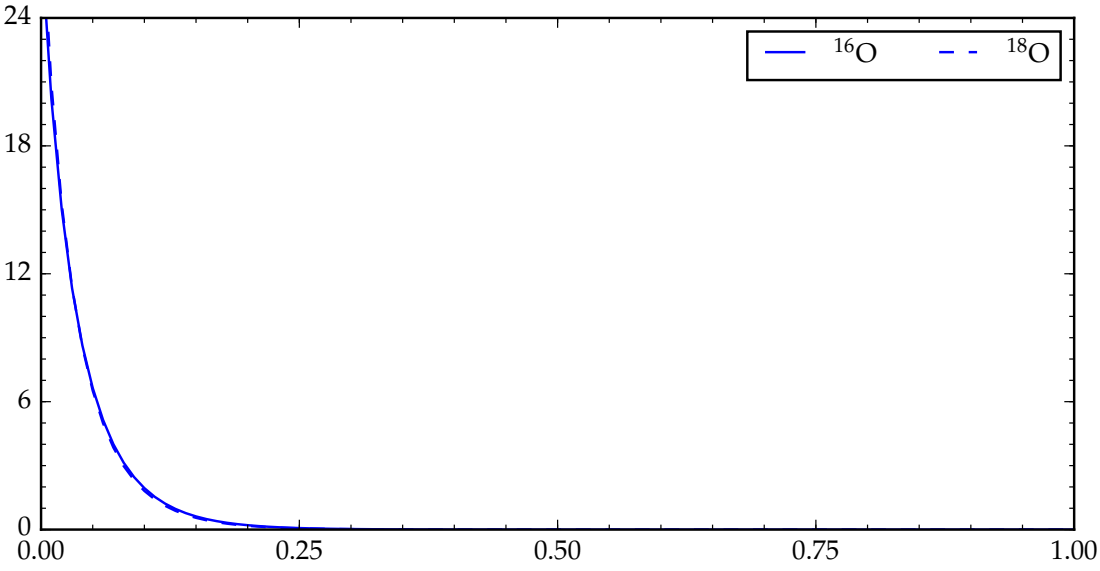

(b)

Figure 5.9: **a.** Probability distribution functions plotted as a function of energy for the lowest six vibrational modes. **b.** Overall distribution function at a thermal temperature of 373 K.

A sample final distribution for ^{16}O can be found in Figure 5.9b for an initial thermal temperature of 373 K. We assume that any molecules in this final distribution above the barrier energy have dissociated, as the vibrational lifetime of excited states ($\sim$1 ps) [173] is much larger than the timescale of an individiual vibration (on the order of a few femtoseconds [10]) [15]. Therefore, the reaction rate analogue used to observe trends for thermal temperature and isotope is the ratio of the probability of molecules above the barrier to the probability of molecules over all energies:

$$P_{diss} = \frac{\int_{E_{barrier}}^{\infty} \frac{dP(E)}{dE}}{\int_{0}^{\infty} \frac{dP(E)}{dE}} \tag{5.14}$$

5.3 Results and Discussion

We use the experimentally-determined dissociation barrier for oxygen on silver of 0.84 eV [174]; the trends were not sensitive to the reaction barrier (see Appendix C). Simulation time was 1 picosecond with timesteps of 5 fs. The simulation time was determined as the lifetime of vibrationally excited O_2 as well as the time scale for thermalized electrons to decay through coupling to substrate phonons. The time step was taken as the time scale for a single metal-adsorbate excitation, which can range from 0.8 to 5 fs [10, 13]. The time scale for metal-adsorbate excitation was 5 fs but the simulation time step (for the numerical method) was 0.5 fs to improve accuracy. Any of the time scales up to 5 fs give qualitatively similar results, as discussed in Appendix C. The friction model can capture the experimental sig-

natures of elevated KIE and exponential dependence of reaction rate on thermal temperature. The data in Figure 5.10a shows an elevated KIE for lower and higher electronic temperatures. These results qualitatively match very well with experimental results of 1.1 to 1.5 for more intense light; inherent simplifications in this model mean we would not expect full quantitative agreement.

The origin of the elevated kinetic isotope effect is twofold. The first factor is the nature of the electronic scattering events – an identical force on objects of two different masses will exert a larger acceleration on a smaller-massed object. The random electron scattering events will therefore exert a larger random force on ^{16}O relative to ^{18}O, leading to a larger dissociation rate. The second factor is a change in fundamental vibrational frequency of ^{16}O compared to ^{18}O. The PES of molecular oxygen is independent of the mass of the constituent atoms; the forcing constant is identical between the two cases. The zero-point energy – the energy in the vibrational ground state – is related to the fundamental frequency:

$$\omega = \sqrt{\frac{k}{m}} \tag{5.15}$$

The ratio of zero point energies is thus related by the square root of the ratio between the two masses; the fundamental energy (frequency) of molecular oxygen changes from is 0.102 eV (0.155 fs^{-1}) to 0.096 eV (0.146 fs^{-1}) moving from ^{16}O to ^{18}O. The energies of all excited states are slightly lower as well; ^{18}O must climb further out of the potential energy surface to reach the barrier energy.

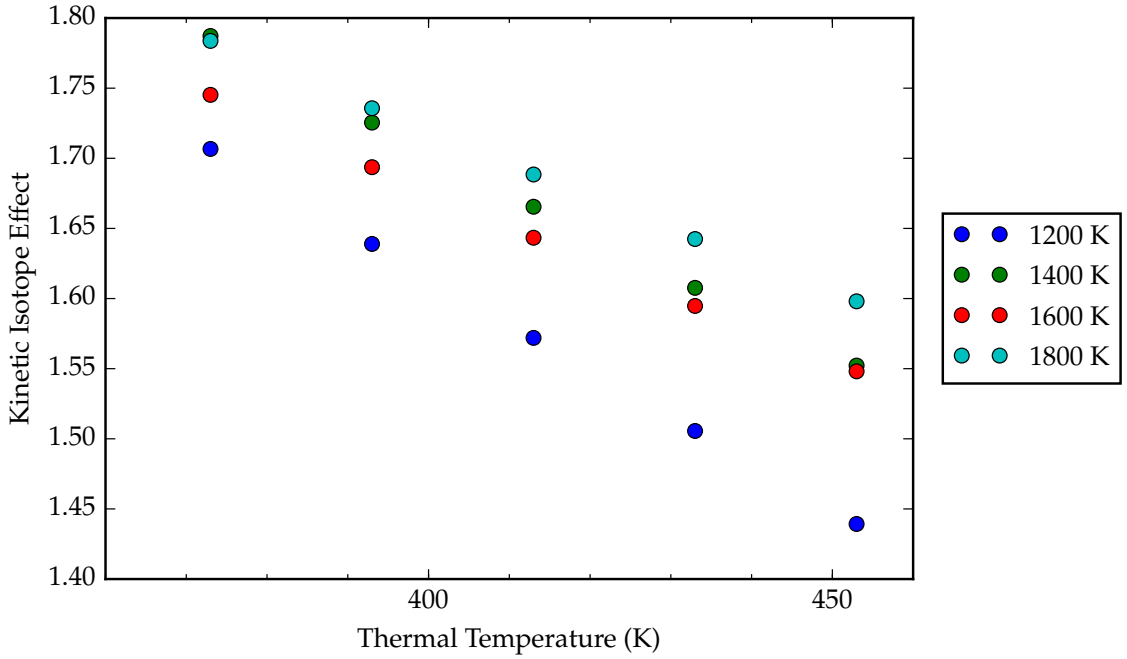

(a)

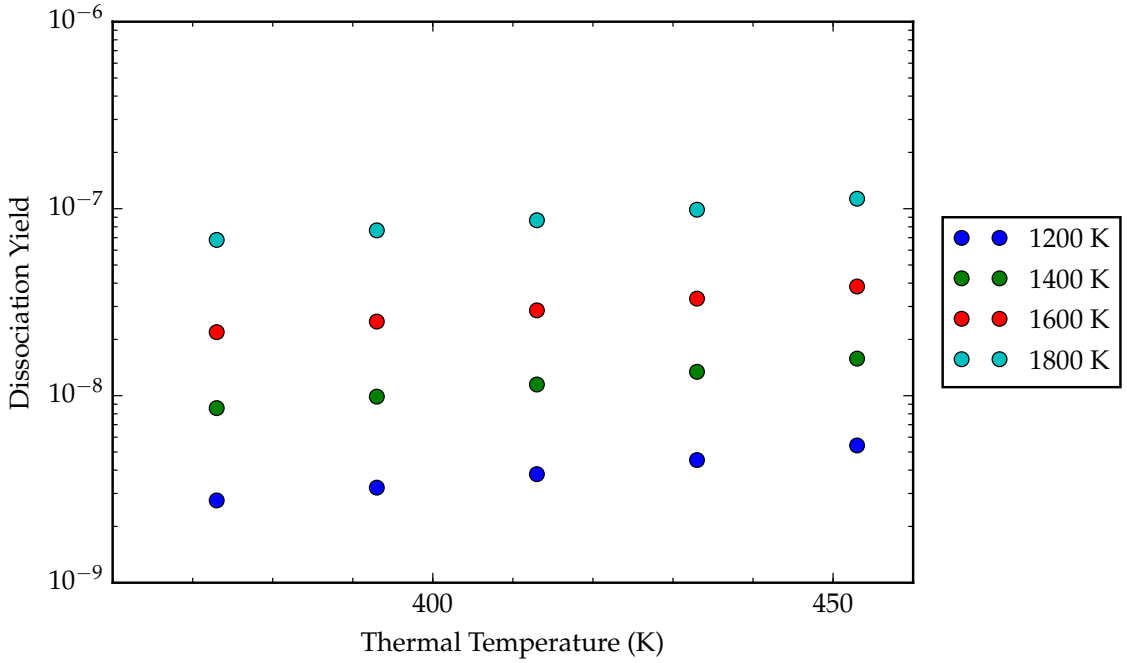

(b)

Figure 5.10: **a.** Predicted kinetic isotope effect is dependent on electronic temperature; light intensity under some conditions. **b.** Predicted reaction rate as a function of thermal temperature shows exponential behavior (note the y-axis scale is logarithmic).

5.4 Limitations and Future Directions

Some of the limitations of this model include its simplicity – a simple 1-D model does not quantitatively capture the complex physics associated with a molecule vibrating both within itself and over a surface [156]. Another current limitation is no implementation of the effects of light intensity except through electronic temperature. A linear intensity dependence is clearly consistent with the results herein – each 1 picosecond simulation predicts the response of adsorbates to a single hot electron bath – running two simulations would result in doubling the reaction rate. The high-intensity regime is much more complicated; in high-intensity situations multiple-photon excitations could cause a higher elevated electronic temperature – as seen in chapter 4 using the TTM, the cooling time is longer for a stronger electronic perturbation. A stronger electronic perturbation (i.e. higher electronic temperature) coupled to a longer cooling time could lead to a non-linear dependence in reaction rate on light intensity. Adding in such effects would require adding changing electronic temperature and electronic lifetimes and are a logical next step.

5.5 Conclusions

In this chapter, we investigated a case study for a plasmon-driven chemical transformation of oxygen on silver driven by a large number of low-energy charge carriers, outlining the experimental signatures expected for such a reaction. A localized

increase in electronic temperature (e.g. at the surface of the nanoparticles due to decay of a surface plasmon) could generate a large number of low-energy charge-carriers. We would expect oxygen dissociation driven by such a distribution – similar to a thermalized electron bath – to exhibit an elevated kinetic isotope effect and a reaction rate depending exponentially on thermal temperature. These energetic charge-carriers could trigger chemical transformations with experimental signatures similar to those seen for DIET/DIMET processes.

CHAPTER 6

Conclusions

Most of the previous work on photon-triggered reactions – of which an enormous amount exists – focuses on semiconductors and single-crystal metals. The former class of catalysts generate a smaller number of energetic electron-hole pairs in the bulk, which can migrate to the surface of the semiconductor and trigger chemical transformations. The latter is typically performed over single-crystal catalysts under high-intensity illumination, generating a large number of lower energy charge-carriers. In recent years, more work has focused on probing how a new class of nanostructured photocatalysts exhibiting LSPR can trigger chemical transformations, but understanding of the full process is not yet complete. In this dissertation, we have developed a framework for modeling aspects of the properties of LSPR and the subsequent production and decay of hot electrons.

We looked at the formation of energetic electrons directly formed in adsorbate states, which could trigger chemical transformations through a DIET-type mechanism. We modified a physically transparent quantum mechanical model, useful for predicting the optical properties of nanostructured catalysts, to study induced changes in the electronic and optical properties of the catalytic particles by adding

adsorbate states. We evaluated the changes to the optical extinction cross section – a measure of how well incoming light energy is pumped into the formation of electron-hole pairs – and showed that as the energy of an electronic transition within the adsorbate becomes closer to – without being on top of – the photon energy fulfilling the LSPR condition, a larger extinction peak due to that transition is observed. When the two energies are almost identical, the presence of adsorbate states suppresses the plasmon condition somewhat; but even so, we suggest that this would enhance electronic transitions within the adsorbate relative to the case with little or no LSPR.

We used the oscillator strengths from the quantum model to predict the steady-state generation rate of energetic charge-carriers in a silver nanocube, and showed that the number of charge-carriers produced is increased by tuning the adsorbate HOMO-LUMO gap to the photon energy which matches the photon energy that stimulates LSPR.

We used more rigorous first-principles quantum-chemical calculations to further probe how the addition of adsorbates changes the optical properties. We developed a method for identifying and visualizing electron-donating and electron-accepting states, and found that for metals such as Ag and Cu that bound weakly to H and have strong LSPR, the introduction of hydrogen generates multiple states that participate in electronic transitions, either by donating an electron for excitation or giving states that accept an energetic electron. The introduction of adsorbates to a metal such as Pt gives a much smaller influence on the extinction, as there is no strong LSPR at these lower energies to enhance the transitions.

Introduction of a more strongly-bound oxygen generated a large number of states near the Fermi level, generating a much larger number of transitions (higher ε_2, suppressing the LSPR of Ag even more. A stronger interaction between an adsorbate and a surface makes it harder to target a particular electronic excitation, suggesting that targeting specific excitations for chemical selectivity might be easier using substrates that interact weakly with adsorbates.

We also modeled the formation of a thermalized electron cloud created by the decay of a small number of energetic charge-carriers. The time scale of this thermalization is on the order of a few hundred femtoseconds up to $\sim$1-5 ps. We probed how this thermalized electron cloud could be triggering chemical transformations in the framework of electronic friction, a mechanism typically discussed in vibrational lifetime/decay. We found that this mechanism is consistent with experimental signatures for LSPR-mediated photocatalysis including the elevated KIE and exponential dependence of reaction rate on thermal temperature.

The theoretical framework outlined in this dissertation has improved understanding of the fundamental characteristics of LSPR-mediated photocatalysis using first-principles methods and molecular dynamics simulations to study aspects from the formation and characteristics of LSPR to formation and thermalization of energetic electrons to triggering of chemical transformations by these thermalized electrons.

APPENDIX A

Finite-Difference Time-Domain Simulations

FDTD simulations were performed by Robert Campana using the free software package MEEP [175, 176, 177]. Simulations were performed in a three-dimensional grid of length 344 nm on each side, with grid spacings of 1 nm, with the outermost 50 nm in each direction a perfectly matched layer. The two model systems were a single Ag nanocube (of side length 75 nm) in air and a dimer of Ag nanocubes (each of side length 75 nm) in air. The dielectric function for silver was calculated using data by Rakic et al. [178]. One cube in the dimer system was rotated 45 degrees around the axis parallel to light propagation with a separation between the two cubes of 1 nm. The light source propagated perpendicular to the interparticle axis using polarization both both perpendicular and parallel to the interparticle axis.E Light source wavelengths ranged from 300 nm to 1000 nm.

APPENDIX B

Density Functional Theory: Supplemental

B.1 Slab Thickness Convergence

Model systems for 10 layer slabs are found in Figure B.1a (6 layer slabs can be found in Figure 3.2a). DFT-calculated dielectric functions are found in Figure B.2 for 6 and 10 layer Ag and Ag with a monolayer of H. A 8x8x1 Monkhorst-Pack grid was used for sampling k-points in the Brillouin zone for relaxation. The LDA functional was used to approximate exchange and correlation effects [113]. Fermi smearing was applied at an electronic temperature of 0.05 eV to aid convergence, and only occupied bands were converged. In plane wave mode, wave functions were expanded in plane waves with a cutoff energy of 500 eV.

After geometry optimization, the vacuum distance between parallel slabs was increased to 30 Åand a 100x100x1 Monkhorst-Pack grid was used for sampling k-points in the Brillouin zone. For optical simulations we used the modified GLLB-SC functional for its improved treatment of Ag d bands [111, 114, 115]. Fermi smearing was applied at an electronic temperature of 0.05 eV. A diagonalization of the full Hamiltonian was not feasible on the 10 layer slabs; convergence was

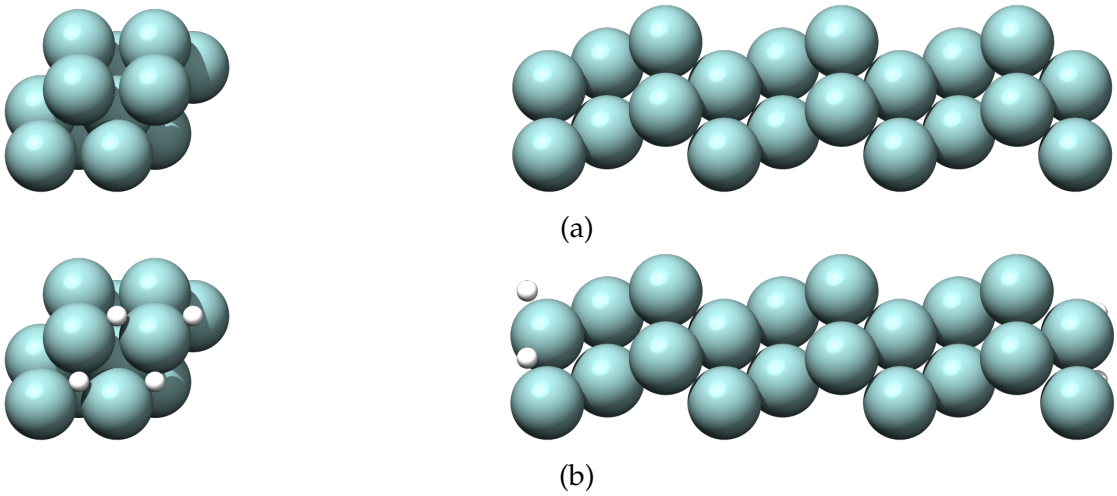

Figure B.1: **a.** 10 layer Ag slab. **b.** 10 layer Ag slab with a monolayer of H.

obtained by using either the conjugate-gradient or Davidson eigensolver in GPAW to converge all bands up to 10 eV above the Fermi level.

Optical response DFT calculations were performed with the LrTDDFT code for extended surfaces in GPAW [111]. The EELS loss spectra was calculated by GPAW with an initial frequency grid spacing (at $\omega = 0$) of 0.01 eV and a broadening factor of 0.10 eV. Moving from 6 to 10 layers brings the real part of the dielectric function up (see Figure B.2. The addition of hydrogen induces a much larger change to the 6 layer slab compared to the 10 layer slab; due to the higher number of surface states compared to bulk states. The features are largely the same with the silver peak at around 3.5 eV preserved for both 6 and 10 layer slabs. There is a slight qualitative change in some of the new peaks for Ag/H (in particular, the peak at around 2.1 – 2.2 eV) but the overall shape and features remain largely similar.

A comparison of the calculated EELS spectrum for a clean Ag slab is found in Figure B.3. The plasmon intensity of the smaller slab is stronger, reflecting a larger ratio of surface states to bulk states strengthening the surface plasmon reso-

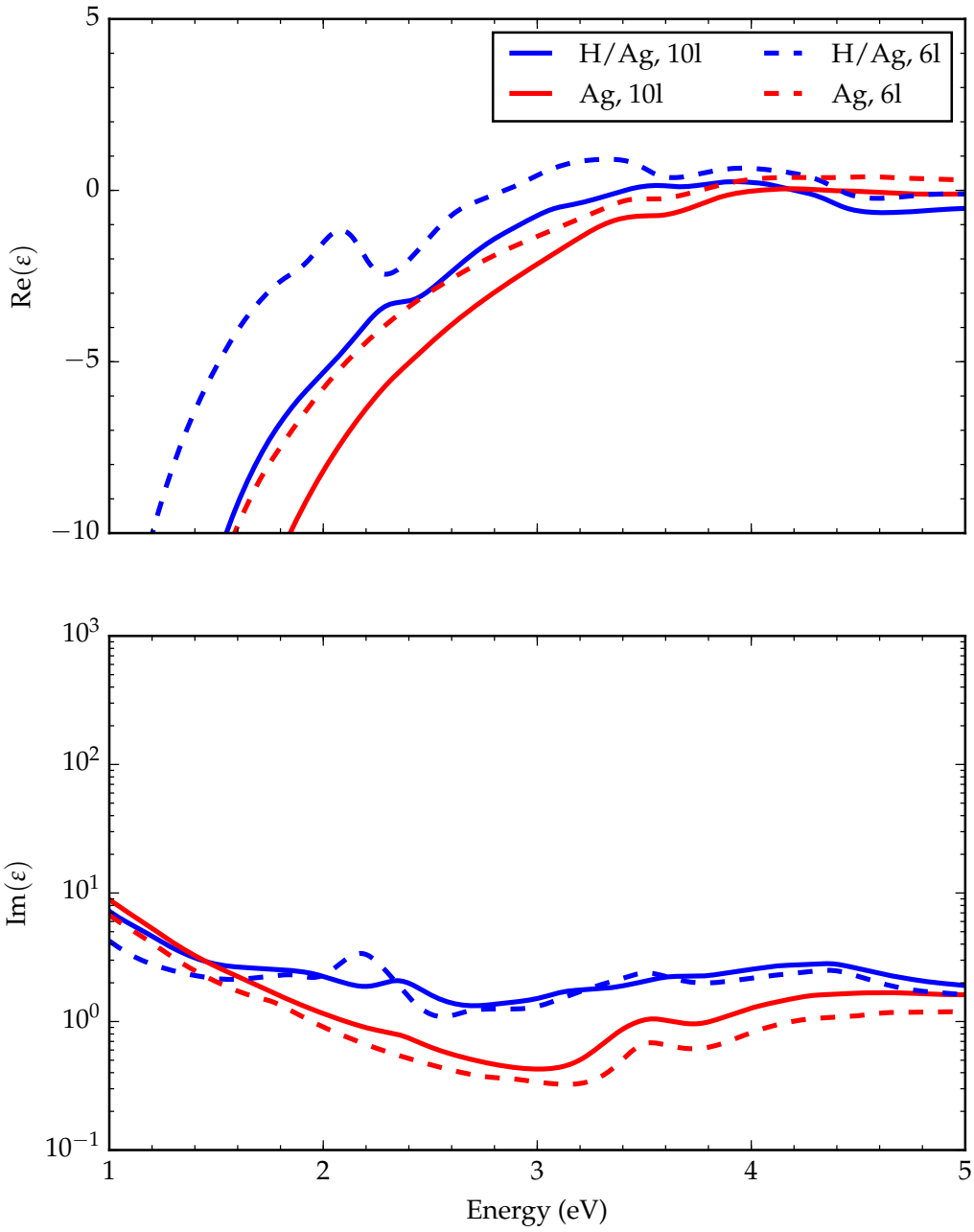

Figure B.2: DFT-calculated real (top) and imaginary (bottom) dielectric functions for 6 and 10 layer clean Ag slabs and H-covered Ag slabs. Peaks in the imaginary part of the dielectric at around 3.5 eV correspond to interband Ag transitions; Peaks around 2.3–2.4 eV for H-covered are transitions to or from adsorbate states.

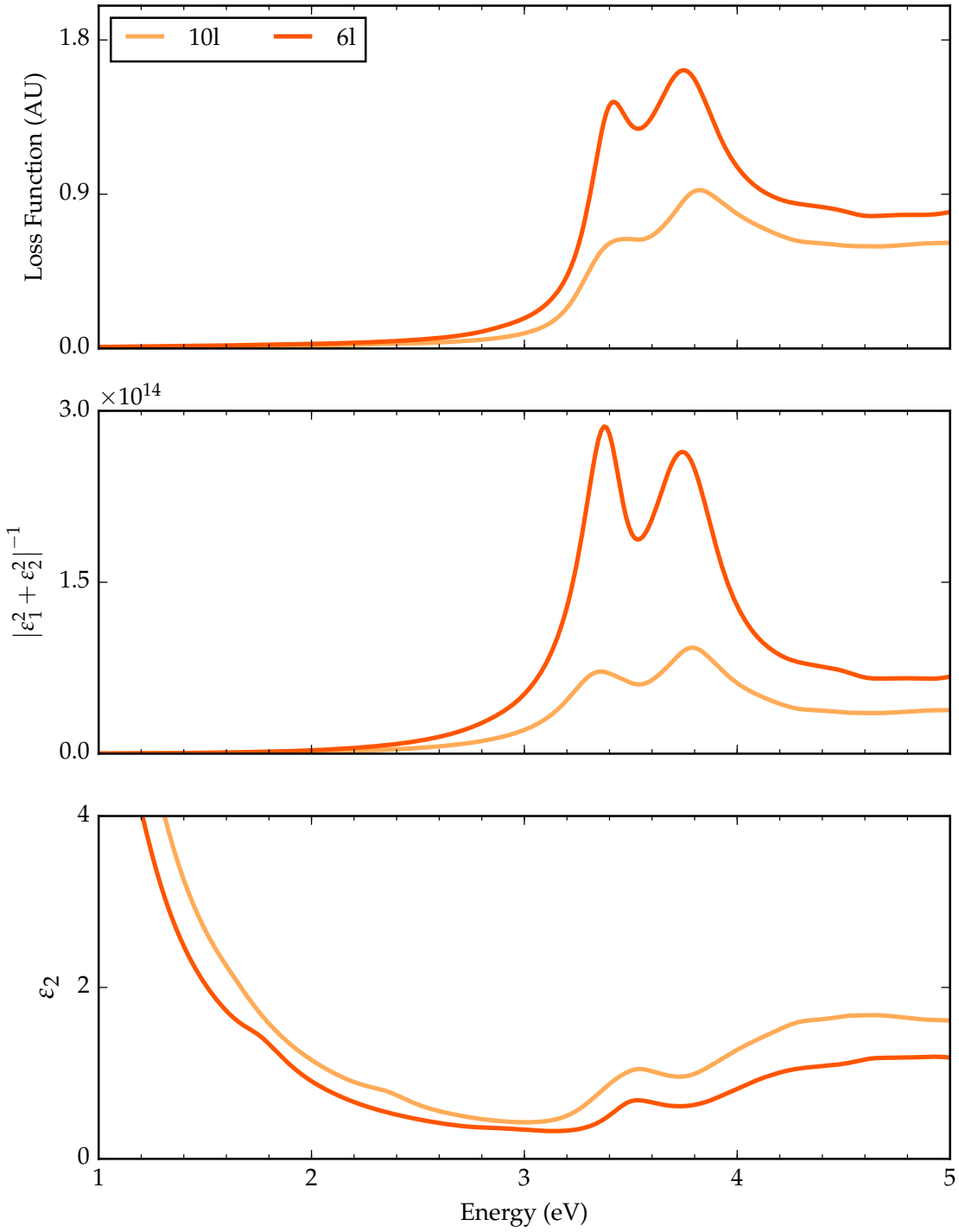

Figure B.3: DFT-calculated EELS spectra for 6 and 10 layer clean Ag slabs.

nance, but the features and plasmon peak location remain the same.

A comparison of the calculated EELS spectrum for a H-covered slab is found in Figure B.4. There is a much larger change in the extinction, notably a larger redshift for the 6 layer slab, with the plasmon peak changing from around 3.0 – 3.5 eV for a 10 layer slab down to around 2.5 eV for a 6 layer slab. Importantly, the formation of new transitions are apparent in both slabs (see bottom of Figure B.4) with the appearance of two peaks around 1.7 to 2.2 eV, another peak around 2.7 eV, and additional peaks above.

While the smaller system places more importance on the surface states, we use it for computational simplicity; any trends discussed here should apply to larger systems and it will be easier to identify electronic transitions that are modified with the addition of adsorbate molecules.

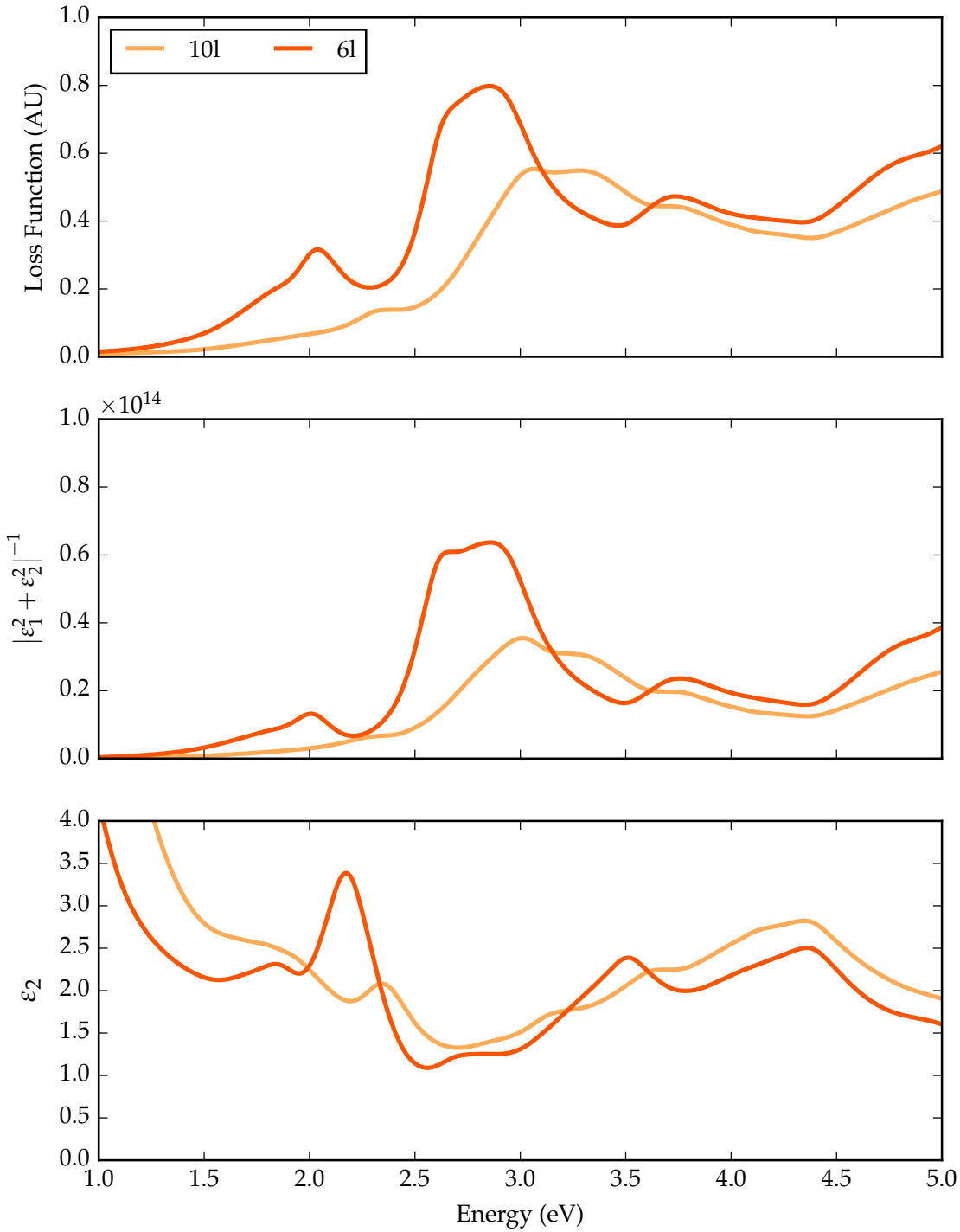

Figure B.4: DFT-calculated EELS spectra for 6 and 10 layer single monolayer H-covered Ag slabs

APPENDIX C

Langevin Dynamics

C.1 Effect of Barrier Height

The activation barrier for oxygen dissociation over an Ag surface has been experimentally determined to be 0.84 eV [174] and calculated by DFT for the Ag(100) facet to be 1.17 eV [14]. Langevin dynamics results for a sampling of barrier energies between these two values are found in Figure C.1. There are some quantitative differences between different barriers but the trends and qualitative behavior are consistent in all cases: an elevated KIE that trends toward higher values for higher electronic temperatures.

C.2 Effect of Step Size

In Langevin dynamics, the step size should be determined as the time scale of the fluctuation event – electron scattering. The electronic lifetime of the transient negative ion, O_2^- is around 5 – 10 fs. The step size used in the simulations in this dissertation was 5 fs, on the higher end of the time scale for electronic friction

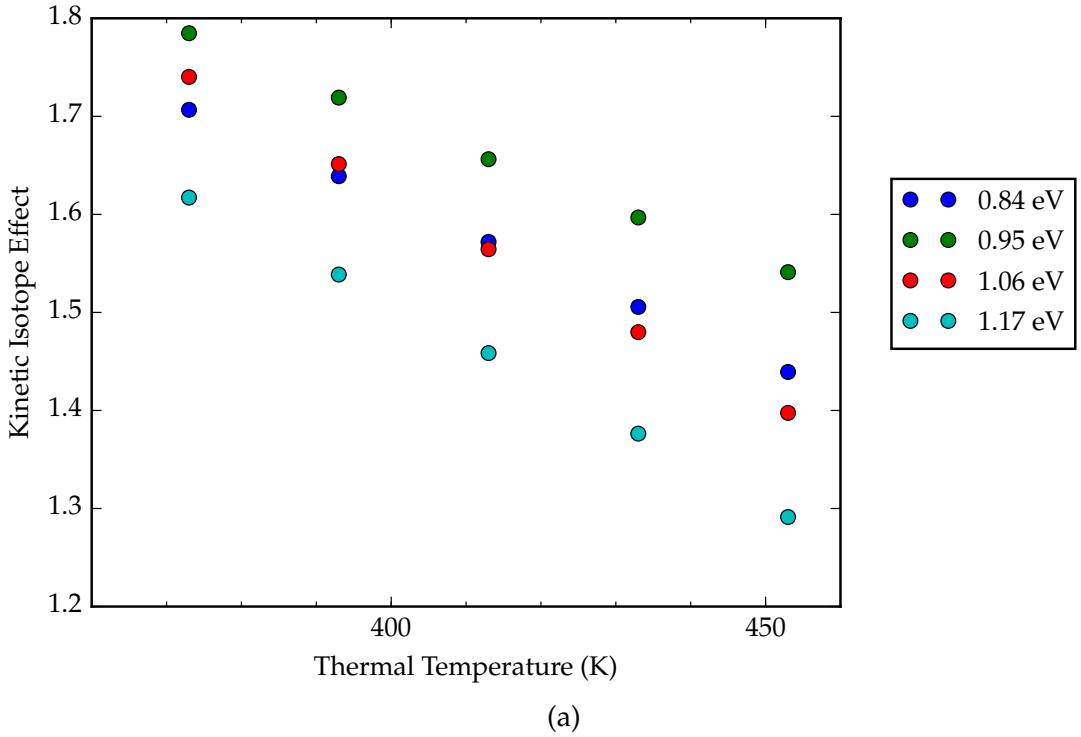

(a)

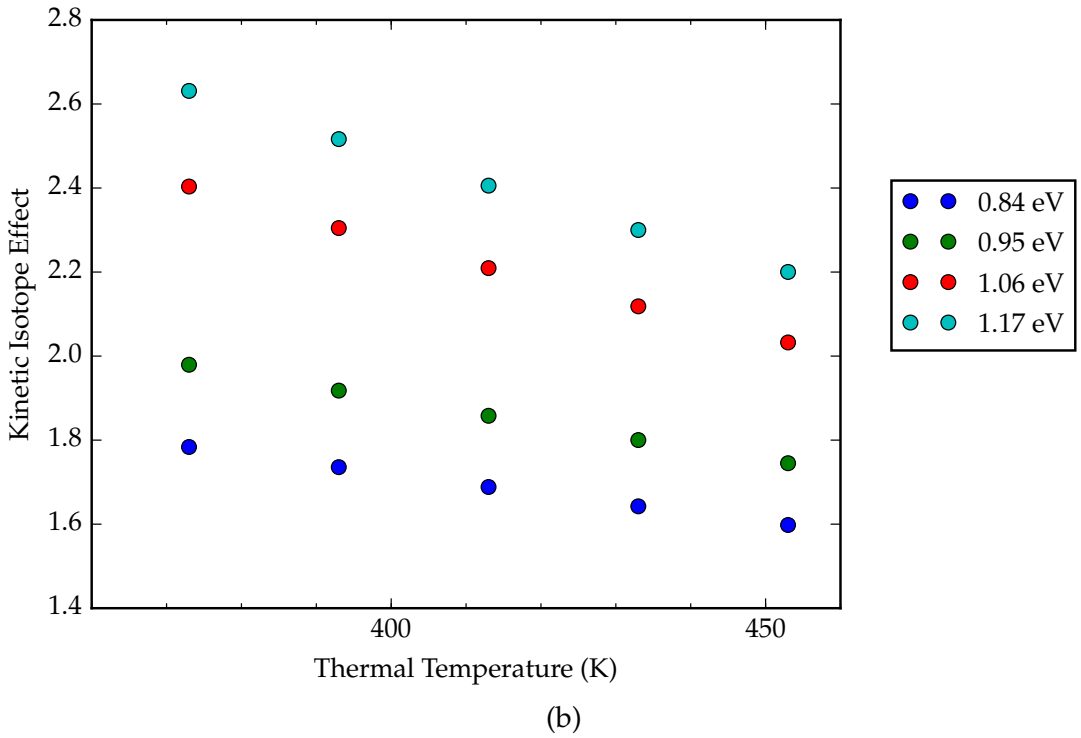

(b)

Figure C.1: Effect of barrier height on kinetic isotope effect. **a.** T_{el} = 1200 K. **b.** T_{el} = 1800 K. All show an elevated KIE above 1.3 with higher electronic temperature giving a larger KIE.

events.[10] This appendix shows the trends are preserved as the friction/fluctuation time scales are decreased to 2.5 fs and 0.5 fs. The integration timestep of 0.5 fs is used for all simulations; new friction and fluctuation forces are calculated every 1, 5, or 10 steps for each time scale. The results for both are consistent with the trends for 5 fs; an elevated KIE is expected and the reaction rate dependence on thermal temperature is still exponential, exhibiting a stronger dependence. Results for 5 fs are included again for comparison.

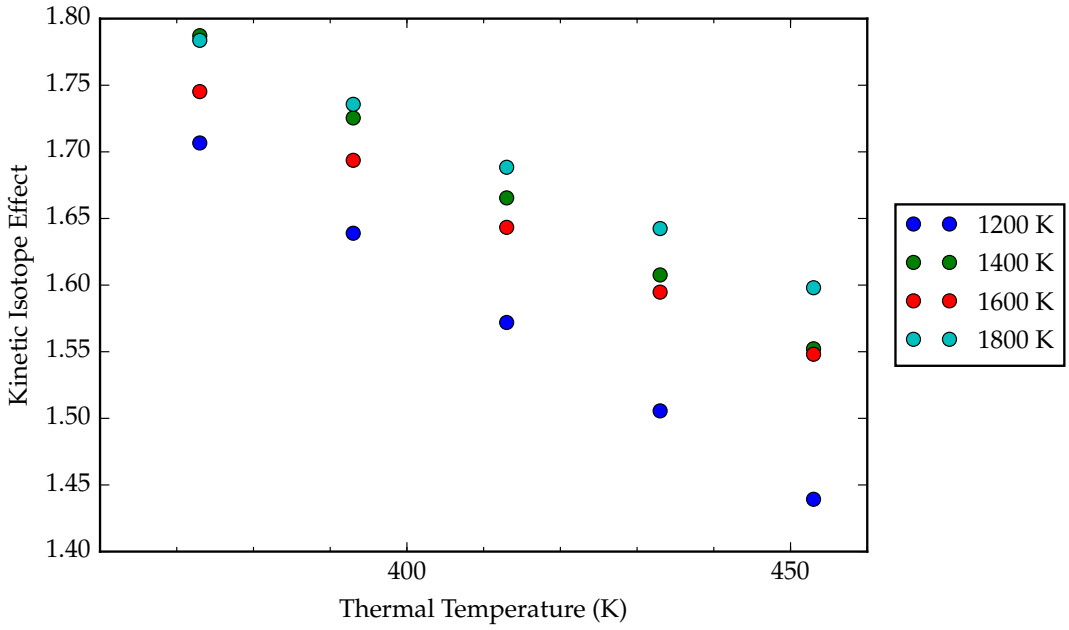

(a)

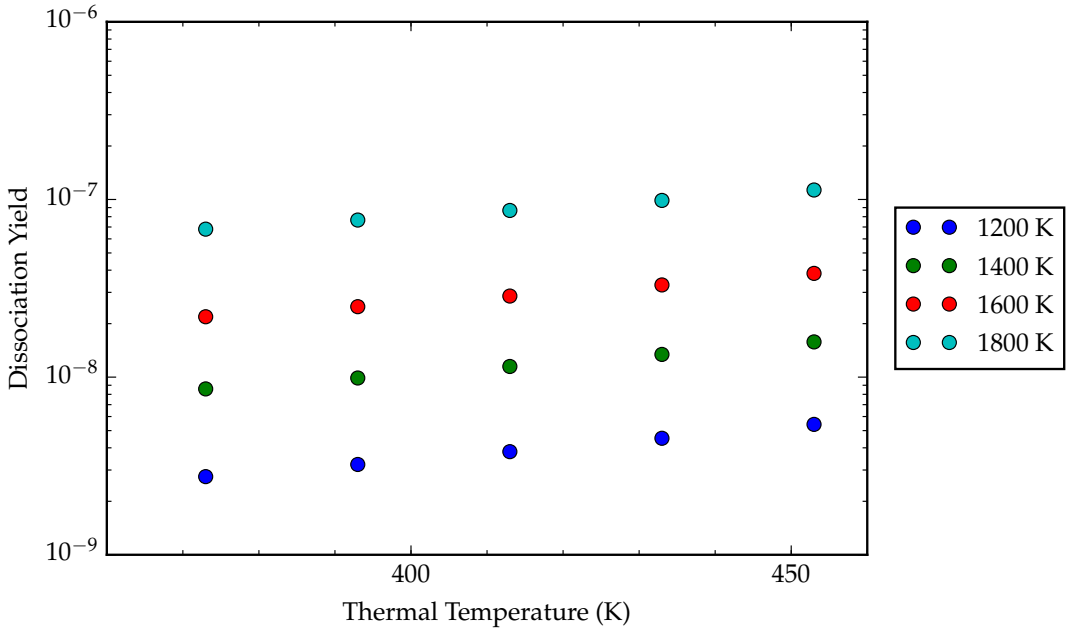

(b)

Figure C.2: Results for a step size of 0.5 fs. **a.** Predicted kinetic isotope effect shows elevated values between 1.4 and 1.8. **b.** Predicted reaction rate as a function of thermal temperature shows exponential behavior (note the y-axis scale is logarithmic).

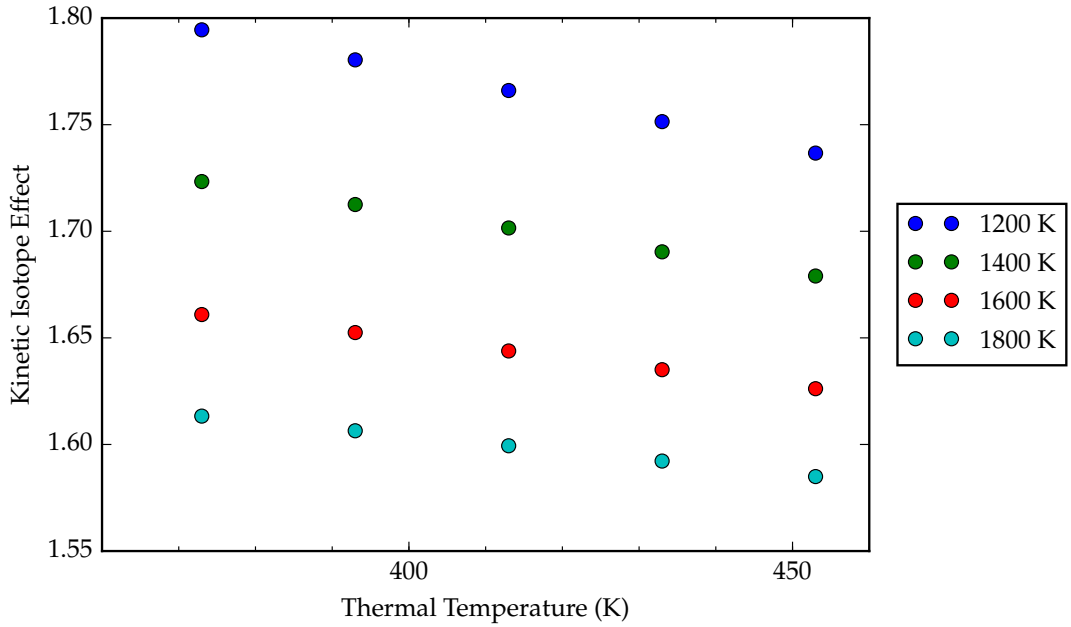

(a)

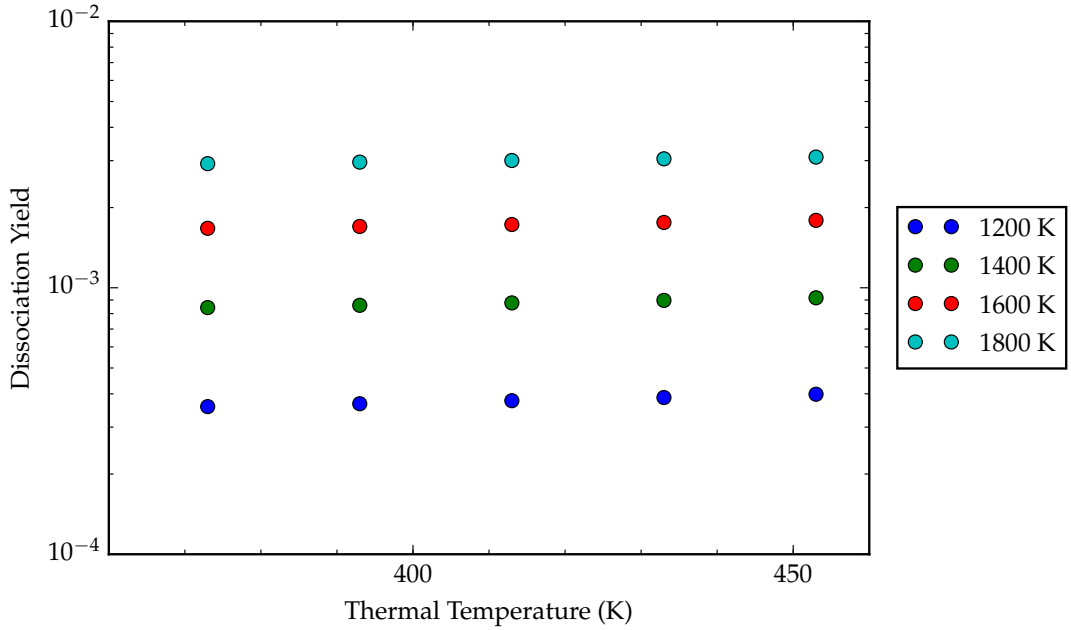

(b)

Figure C.3: Results for a step size of 2.5 fs. **a.** Predicted kinetic isotope effect is more weakly dependent on electronic temperature compared to 0.5 fs, exhibiting KIE values between 1.6 and 1.8. **b.** Predicted reaction rate as a function of thermal temperature shows exponential behavior (note the y-axis scale is logarithmic). Reaction rate dependence on temperature is weaker but still increases exponentially.

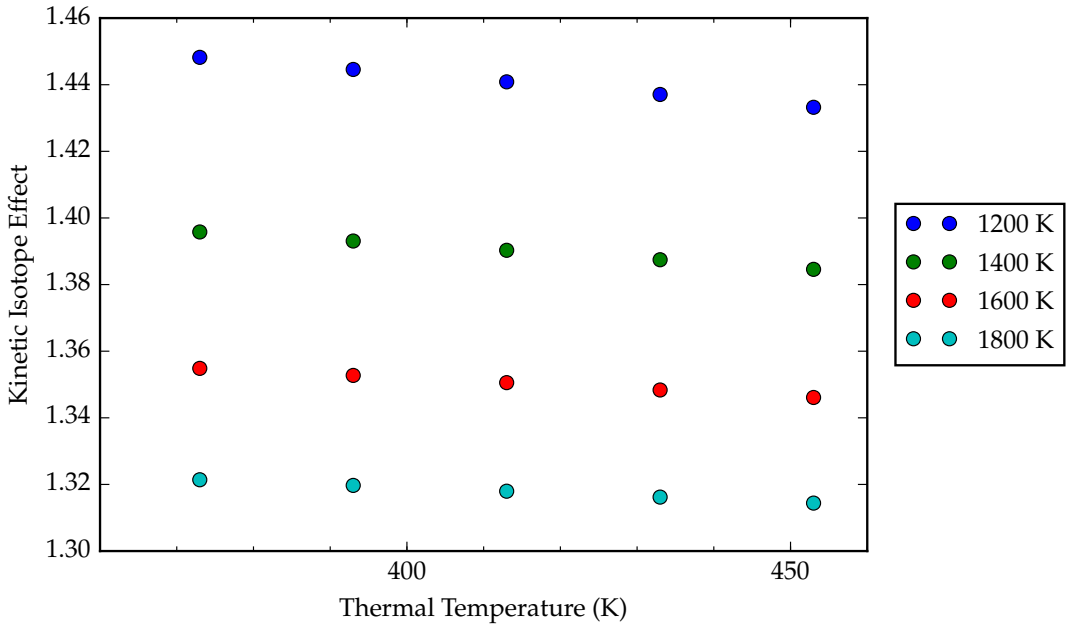

(a)

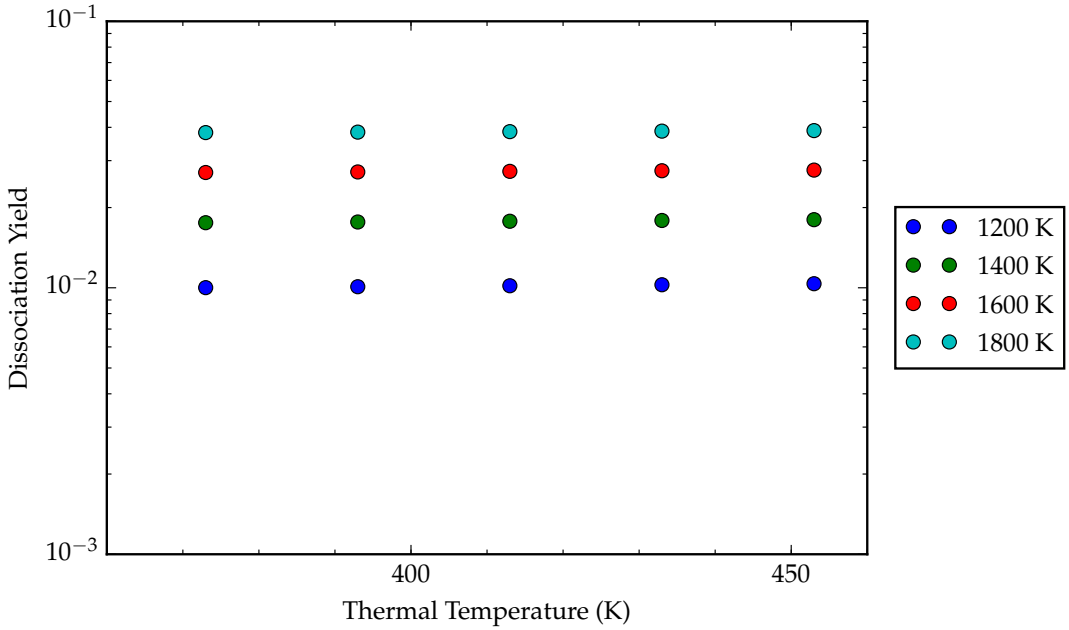

(b)

Figure C.4: Results for a step size of 5 fs. **a.** Predicted kinetic isotope effect is less dependent on electronic temperature compared to smaller time scales: between 1.3 and 1.5. **b.** Predicted reaction rate as a function of thermal temperature shows exponential behavior (note the y-axis scale is logarithmic). Reaction rate dependence is even weaker compared to 2.5 fs and 0.5 fs interaction times.

BIBLIOGRAPHY

[1] G. Ertl, H. Knözinger, and J. Weitkamp. *Handbook of Heterogeneous Catalysis*. Wiley-VCH Verlag GmbH, Weinheim, July 1997.

[2] J. W. Gadzuk. Vibrational excitation in molecule–surface collisions due to temporary negative molecular ion formation. *The Journal of Chemical Physics*, 79(12):6341, December 1983.

[3] S. Gao, B. I. Lundqvist, and W. Ho. Hot-electron-induced vibrational heating at surface: importance of a quantum-mechanical description. *Surface Science*, 341(3):L1031–L1036, November 1995.

[4] M. Bonn. Phonon- Versus Electron-Mediated Desorption and Oxidation of CO on Ru(0001). *Science*, 285(5430):1042–1045, August 1999.

[5] S. Linic, U. Aslam, C. Boerigter, and M. Morabito. Photochemical transformations on plasmonic metal nanoparticles. *Nature Materials*, 14(6):567–576, May 2015.

[6] J. A. Prybyla, T. F. Heinz, J. A. Misewich, M. M. T. Loy, and J. H. Glownia. Desorption induced by femtosecond laser pulses. *Physical Review Letters*, 64(13):1537–1540, March 1990.

[7] X.-L. Zhou, X.-Y. Zhu, and J.M. White. Photochemistry at adsorbate/metal interfaces. *Surface Science Reports*, 13(3-6):73–220, January 1991.

[8] J. A. Prybyla, H. W. K. Tom, and G. D. Aumiller. Femtosecond time-resolved surface reaction: Desorption of Co from Cu(111) in 325 fsec. *Physical Review Letters*, 68(4):503–506, January 1992.

[9] W. Ho. Reactions at Metal Surfaces Induced by Femtosecond Lasers, Tunneling Electrons, and Heating. *The Journal of Physical Chemistry*, 100(31):13050–13060, January 1996.

[10] L. Bartels, G. Meyer, K.-H. Rieder, D. Velic, E. Knoesel, A. Hotzel, M. Wolf, and G. Ertl. Dynamics of Electron-Induced Manipulation of Individual CO Molecules on Cu(111). *Physical Review Letters*, 80(9):2004–2007, March 1998.

[11] S. Funk, M. Bonn, D. N. Denzler, Ch. Hess, M. Wolf, and G. Ertl. Desorption of CO from Ru(001) induced by near-infrared femtosecond laser pulses. *The Journal of Chemical Physics*, 112(22):9888, June 2000.

[12] D. Denzler, C. Frischkorn, C. Hess, M. Wolf, and G. Ertl. Electronic Excitation and Dynamic Promotion of a Surface Reaction. *Physical Review Letters*, 91(22):226102, November 2003.

[13] P. Christopher, H. Xin, and S. Linic. Visible-light-enhanced catalytic oxidation reactions on plasmonic silver nanostructures. *Nature Chemistry*, 3(6):467–72, June 2011.

[14] P. Christopher, H. Xin, A. Marimuthu, and S. Linic. Singular characteristics and unique chemical bond activation mechanisms of photocatalytic reactions on plasmonic nanostructures. *Nature Materials*, 11(12):1044–50, December 2012.

[15] T. Olsen, J. Gavnholt, and J. Schiøtz. Hot-electron-mediated desorption rates calculated from excited-state potential energy surfaces. *Physical Review B*, 79(3):035403, January 2009.

[16] C. F. Bohren and D. R. Huffman. *Absorption and Scattering of Light by Small Particles*. 1998.

[17] K. A. Willets and R. P. Van Duyne. Localized surface plasmon resonance spectroscopy and sensing. *Annual Review of Physical Chemistry*, 58:267–97, January 2007.

[18] J. A. Scholl, A. L. Koh, and J. A. Dionne. Quantum plasmon resonances of individual metallic nanoparticles. *Nature*, 483(7390):421–7, March 2012.

[19] M. Moskovits, I. Srnova-Sloufova, and B. Vlckova. Bimetallic Ag–Au nanoparticles: Extracting meaningful optical constants from the surface-plasmon extinction spectrum. *The Journal of Chemical Physics*, 116(23):10435, May 2002.

[20] Y. Xia, Y. Xiong, B. Lim, and S. E. Skrabalak. Shape-controlled synthesis of metal nanocrystals: Simple chemistry meets complex physics? *Angewandte Chemie - International Edition*, 48(1):60–103, 2009.

[21] S. Linic, P. Christopher, and D. B. Ingram. Plasmonic-metal nanostructures for efficient conversion of solar to chemical energy. *Nature Materials*, 10(12):911–21, December 2011.

[22] M. Rycenga, C. M. Cobley, J. Zeng, W. Li, C. H. Moran, Q. Zhang, D. Qin, and Y. Xia. Controlling the Synthesis and Assembly of Silver Nanostructures for Plasmonic Applications. *Chemical Reviews*, 111(6):3669–3712, 2011.

[23] M. A. El-Sayed. Some interesting properties of metals confined in time and nanometer space of different shapes. *Accounts of Chemical Research*, 34(4):257–264, 2001.

[24] K. L. Kelly, E. Coronado, L. L. Zhao, and G. C. Schatz. The Optical Properties of Metal Nanoparticles: The Influence of Size, Shape, and Dielectric Environment. *The Journal of Physical Chemistry B*, 107(3):668–677, January 2003.

[25] C. Burda, X. Chen, R. Narayanan, and M. A. El-Sayed.

[26] L. Brus. Noble metal nanocrystals: plasmon electron transfer photochemistry and single-molecule Raman spectroscopy. *Accounts of Chemical Research*, 41(12):1742–9, December 2008.

[27] C. M. Cobley, S. E. Skrabalak, D. J. Campbell, and Y. Xia. Shape-Controlled Synthesis of Silver Nanoparticles for Plasmonic and Sensing Applications. *Plasmonics*, 4(2):171–179, March 2009.

[28] N. Grillet, D. Manchon, F. Bertorelle, C. Bonnet, M. Broyer, E. Cottancin, J. Lermé, M. Hillenkamp, and M. Pellarin. Plasmon coupling in silver nanocube dimers: Resonance splitting induced by edge rounding. *ACS Nano*, 5(12):9450–9462, 2011.

[29] K. Bosnick, M. Maillard, and L. Brus. Single Molecule Raman Spectroscopy at the Junctions of Large Ag Nanocrystals. *The Journal of Physical Chemistry B*, 107(37):9964–9972, September 2003.

[30] S. Nie. Probing Single Molecules and Single Nanoparticles by Surface-Enhanced Raman Scattering. *Science*, 275(5303):1102–1106, 1997.

[31] S. Kuhn, U. Hakanson, L. Rogobete, and V. Sandoghdar. Enhancement of single-molecule fluorescence using a gold nanoparticle as an optical nanoantenna. *Physical Review Letters*, 97(1), 2006.

[32] M. Moskovits. Surface-enhanced Raman spectroscopy: a brief retrospective. *Journal of Raman Spectroscopy*, 36(6-7):485–496, June 2005.

[33] P. K. Jain, X. Huang, I. H. El-Sayed, and M. A. El-Sayed. Noble metals on the nanoscale: optical and photothermal properties and some applications in imaging, sensing, biology, and medicine. *Accounts of Chemical Research*, 41(12):1578–86, December 2008.

[34] H. A. Atwater and A. Polman. Plasmonics for improved photovoltaic devices. *Nature Materials*, 9(3):205–213, 2010.

[35] E. M. Larsson, C. Langhammer, I. Zorić, and B. Kasemo. Nanoplasmonic probes of catalytic reactions. *Science*, 326(5956):1091–1094, 2009.

[36] J. A. Schuller, E. S. Barnard, W. Cai, Y. C. Jun, J. S. White, and Mark L Brongersma. Plasmonics for extreme light concentration and manipulation. *Nature Materials*, 9(3):193–204, March 2010.

[37] P. Kambhampati, C. M. Child, M. C. Foster, and A. Campion. On the chemical mechanism of surface enhanced Raman scattering: Experiment and theory. *The Journal of Chemical Physics*, 108(12):5013–5026, 1998.

[38] E. Hao and G. C. Schatz. Electromagnetic fields around silver nanoparticles and dimers. *The Journal of Chemical Physics*, 120(1):357–66, January 2004.

[39] L. Gunnarsson, T. Rindzevicius, J. Prikulis, B. Kasemo, M. Käll, S. Zou, and G. C. Schatz. Confined plasmons in nanofabricated single silver particle pairs: Experimental observations of strong interparticle interactions. *The Journal of Physical Chemistry B*, 109(3):1079–1087, 2005.

[40] J. Zhang, Y. Fu, M. H. Chowdhury, and J. R. Lakowicz. Metal-enhanced single-molecule fluorescence on silver particle monomer and dimer: coupling effect between metal particles. *Nano Letters*, 7(7):2101–7, July 2007.

[41] J. Zuloaga, E. Prodan, and P. Nordlander. Quantum description of the plasmon resonances of a nanoparticle dimer. *Nano Letters*, 9(2):887–891, 2009.

[42] S. F. Tan, L. Wu, J. K. W. Yang, P. Bai, M. Bosman, and C. A. Nijhuis. Quantum Plasmon Resonances Controlled by Molecular Tunnel Junctions. *Science*, 343(6178):1496–1499, March 2014.

[43] J. A. Scholl, A. García-Etxarri, A. L. Koh, and J. A. Dionne. Observation of quantum tunneling between two plasmonic nanoparticles. *Nano Letters*, 13(2):564–569, 2013.

[44] S. Link and M. A. El-Sayed. Spectral Properties and Relaxation Dynamics of Surface Plasmon Electronic Oscillations in Gold and Silver Nanodots and Nanorods. *The Journal of Physical Chemistry B*, 103(40):8410–8426, October 1999.

[45] N. Del Fatti, C. Voisin, M. Achermann, S. Tzortzakis, D. Christofilos, and F. Vallée. Nonequilibrium electron dynamics in noble metals. *Physical Review B*, 61(24):16956–16966, June 2000.

[46] J. Bosbach, C. Hendrich, F. Stietz, T. Vartanyan, and F. Träger. Ultrafast Dephasing of Surface Plasmon Excitation in Silver Nanoparticles: Influence of Particle Size, Shape, and Chemical Surrounding. *Physical Review Letters*, 89(25):257404, December 2002.

[47] D. D. Evanoff and G. Chumanov. Size-controlled synthesis of nanoparticles. 1. "silver-only" aqueous suspensions via hydrogen reduction. *The Journal of Physical Chemistry B*, 108(37):13948–13956, 2004.

[48] D. D. Evanoff and G. Chumanov. Synthesis and optical properties of silver nanoparticles and arrays. *ChemPhysChem*, 6(7):1221–1231, 2005.

[49] J. Dawson. On Landau Damping. *Physics of Fluids*, 4(7):869, December 1961.

[50] S. Mukherjee, F. Libisch, N. Large, O. Neumann, L. V. Brown, J. Cheng, J. B. Lassiter, E. A. Carter, P. Nordlander, and N. J. Halas. Hot electrons do the impossible: plasmon-induced dissociation of H2 on Au. *Nano Letters*, 13(1):240–7, January 2013.

[51] S. Mukherjee, L. Zhou, A. M. Goodman, N. Large, C. Ayala-Orozco, Y. Zhang, P. Nordlander, and N. J. Halas. Hot-electron-induced dissociation of H2 on gold nanoparticles supported on SiO2. *Journal of the American Chemical Society*, 136(1):64–7, January 2014.

[52] H. Zhu, X. Chen, Z. Zheng, X. Ke, E. Jaatinen, J. Zhao, C. Guo, T. Xie, and D. Wang. Mechanism of supported gold nanoparticles as photocatalysts under ultraviolet and visible light irradiation. *Chemical Communications*, (48):7524, 2009.

[53] K. Fuku, R. Hayashi, S. Takakura, T. Kamegawa, K. Mori, and H. Yamashita. The synthesis of size- and color-controlled silver nanoparticles by using microwave heating and their enhanced catalytic activity by localized surface plasmon resonance. *Angewandte Chemie (International ed. in English)*, 52(29):7446–50, July 2013.

[54] Y. Zhang, Q. Xiao, Y. Bao, Y. Zhang, S. Bottle, S. Sarina, B. Zhaorigetu, and H. Zhu. Direct Photocatalytic Conversion of Aldehydes to Esters Using Supported Gold Nanoparticles under Visible Light Irradiation at Room Temperature. *The Journal of Physical Chemistry C*, 118(33):19062–19069, August 2014.

[55] Z. Zheng, T. Tachikawa, and T. Majima. Single-particle study of Pt-modified Au nanorods for plasmon-enhanced hydrogen generation in visible to near-infrared region. *Journal of the American Chemical Society*, 136(19):6870–3, May 2014.

[56] F. Wang, C. Li, H. Chen, R. Jiang, L. D. Sun, Q. Li, J. Wang, J. C. Yu, and C. H. Yan. Plasmonic harvesting of light energy for suzuki coupling reactions. *Journal of the American Chemical Society*, 135(15):5588–5601, 2013.

[57] X. Huang, Y. Li, Y. Chen, H. Zhou, X. Duan, and Y. Huang. Plasmonic and catalytic AuPd nanowheels for the efficient conversion of light into chemical energy. *Angewandte Chemie - International Edition*, 52(23):6063–6067, 2013.

[58] Y. Sugano, Y. Shiraishi, D. Tsukamoto, S. Ichikawa, S. Tanaka, and T. Hirai. Supported Au-Cu bimetallic alloy nanoparticles: An aerobic oxidation catalyst with regenerable activity by visible-light irradiation. *Angewandte Chemie - International Edition*, 52(20):5295–5299, 2013.

[59] Q. Xiao, S. Sarina, A. Bo, J. Jia, H. Liu, D. P. Arnold, Y. Huang, H. Wu, and H. Zhu. Visible light-driven cross-coupling reactions at lower temperatures using a photocatalyst of palladium and gold alloy nanoparticles. *ACS Catalysis*, 4(6):1725–1734, 2014.

[60] Q. Xiao, S. Sarina, E. Jaatinen, Ji. Jia, D. P. Arnold, H. Liu, and H. Zhu. Efficient photocatalytic Suzuki cross-coupling reactions on Au–Pd alloy nanoparticles under visible light irradiation. *Green Chemistry*, 16(9):4272, June 2014.

[61] M. J. Kale, T. Avanesian, H. Xin, J. Yan, and P. Christopher. Controlling catalytic selectivity on metal nanoparticles by direct photoexcitation of adsorbate-metal bonds. *Nano Letters*, 14(9):5405–12, September 2014.

[62] J. R. Adleman, D. A. Boyd, D. G. Goodwin, and D. Psaltis. Heterogenous catalysis mediated by plasmon heating. *Nano Letters*, 9(12):4417–4423, 2009.

[63] C. Fasciani, C. J. Bueno Alejo, M. Grenier, J. C. Netto-Ferreira, and J. C. Scaiano. High-temperature organic reactions at room temperature using plasmon excitation: decomposition of dicumyl peroxide. *Organic Letters*, 13(2):204–207, January 2011.

[64] D. A. Boyd, L. Greengard, M. Brongersma, M. Y. El-Naggar, and D. G. Goodwin. Plasmon-assisted chemical vapor deposition. *Nano Letters*, 6(11):2592–2597, 2006.

[65] L. Cao, D. N. Barsic, A. R. Guichard, and M. L. Brongersma. Plasmon-assisted local temperature control to pattern individual semiconductor nanowires and carbon nanotubes. *Nano Letters*, 7(11):3523–3527, 2007.

[66] J. Qiu, Y. C. Wu, Y. C. Wang, M. H. Engelhard, L. McElwee-White, and W. D. Wei. Surface plasmon mediated chemical solution deposition of gold nanoparticles on a nanostructured silver surface at room temperature. *Journal of the American Chemical Society*, 135(1):38–41, 2013.

[67] N. J. Hogan, A. S. Urban, C. Ayala-Orozco, A. Pimpinelli, P. Nordlander, and N. J. Halas. Nanoparticles heat through light localization. *Nano Letters*, 14(8):4640–4645, 2014.

[68] Z. Fang, Y. R. Zhen, O. Neumann, A. Polman, F. J. García De Abajo, P. Nordlander, and N. J. Halas. Evolution of light-induced vapor generation at a liquid-immersed metallic nanoparticle. *Nano Letters*, 13(4):1736–1742, 2013.

[69] L. R. Hirsch, R. J. Stafford, J. A. Bankson, S. R. Sershen, B. Rivera, R. E. Price, J. D. Hazle, N. J. Halas, and J. L. West. Nanoshell-mediated near-infrared thermal therapy of tumors under magnetic resonance guidance. *Proceedings of the National Academy of Sciences of the United States of America*, 100(23):13549–54, November 2003.

[70] I. H. El-Sayed, X. Huang, and M. A. El-Sayed. Selective laser photo-thermal therapy of epithelial carcinoma using anti-EGFR antibody conjugated gold nanoparticles. *Cancer Letters*, 239(1):129–135, July 2006.

[71] L. B. Carpin, L. R. Bickford, G. Agollah, T.-K. Yu, R. Schiff, Y. Li, and R. A. Drezek. Immunoconjugated gold nanoshell-mediated photothermal ablation of trastuzumab-resistant breast cancer cells. *Breast Cancer Research and Treatment*, 125(1):27–34, January 2011.

[72] C. Loo, A. Lin, L. Hirsch, M.-H. Lee, J. Barton, N. Halas, J. West, and R. Drezek. Nanoshell-enabled photonics-based imaging and therapy of cancer. *Technology in Cancer Research & Treatment*, 3(1):33–40, 2004.

[73] X. Lu, M. Rycenga, S. E. Skrabalak, B. Wiley, and Y. Xia. Chemical synthesis of novel plasmonic nanoparticles. *Annual Review of Physical Chemistry*, 60:167–92, January 2009.

[74] R. Hoffmann. *Solids and Surfaces: A Chemist's View of Bonding in Extended Structures*, volume 168. 1990.

[75] R. L. DeKock and H. B. Gray. *Chemical Structure and Bonding*. University Science Books, 1989.

[76] G. Veronis and S. Fan. Overview of simulation techniques for plasmonic devices. *Springer Series in Optical Sciences*, 131:169, 2007.

[77] P. B. Johnson and R. W. Christy. Optical Constants of the Noble Metals. *Physical Review B*, 6(12):4370–4379, December 1972.

[78] W.-H. Yang, G. C. Schatz, and R. P. Van Duyne. Discrete dipole approximation for calculating extinction and Raman intensities for small particles with arbitrary shapes. *The Journal of Chemical Physics*, 103(3):869, July 1995.

[79] G. W. Ford and W. H. Weber. Electromagnetic interactions of molecules with metal surfaces. *Physics Reports*, 113(4):195–287, November 1984.

[80] R. X. Bian, R. C. Dunn, X. S. Xie, and P. T. Leung. Single Molecule Emission Characteristics in Near-Field Microscopy. *Physical Review Letters*, 75(26):4772–4775, December 1995.

[81] L. Novotny, R. X. Bian, and X. S. Xie. Theory of Nanometric Optical Tweezers. *Physical Review Letters*, 79(4):645–648, July 1997.

[82] A. Taflove and S. C. Hagness. *Computational Electrodynamics*. Artech House, 2005.

[83] C. Girard and A. Dereux. Near-field optics theories. *Reports on Progress in Physics*, 59(5):657–699, May 1996.

[84] T. Wriedt. A Review of Elastic Light Scattering Theories. *Particle & Particle Systems Characterization*, 15(2):67–74, April 1998.

[85] R. Kubo. Electronic Properties of Metallic Fine Particles. I. *Journal of the Physical Society of Japan*, 17(6):975–986, June 1962.

[86] A. Kawabata and R. Kubo. Electronic Properties of Fine Metallic Particles. II. Plasma Resonance Absorption. *Journal of the Physical Society of Japan*, 21(9):1765–1772, September 1966.

[87] K. T. Tsen. *Non-Equilibrium Dynamics of Semiconductors and Nanostructures*. Taylor & Francis, 2005.

[88] U. Kreibig and M. Vollmer. *Optical Properties of Metal Clusters*, volume 118. 1995.

[89] L. Genzel, T. P. Martin, and U. Kreibig. Dielectric function and plasma resonances of small metal particles. *Zeitschrift für Physik B Condensed Matter and Quanta*, 21(4):339–346, December 1975.

[90] A. O. Govorov, W. Zhang, T. Skeini, H. Richardson, J. Lee, and Nicholas A. Kotov. Gold nanoparticle ensembles as heaters and actuators: melting and collective plasmon resonances. *Nanoscale Research Letters*, 1(1):84–90, July 2006.

[91] A. O. Govorov, H. Zhang, and Y. K. Gun'ko. Theory of Photoinjection of Hot Plasmonic Carriers from Metal Nanostructures into Semiconductors and Surface Molecules. *The Journal of Physical Chemistry C*, 117(32):16616–16631, August 2013.

[92] A. Manjavacas, J. G. Liu, V. Kulkarni, and P. Nordlander. Plasmon-Induced Hot Carriers in Metallic Nanoparticles. *ACS nano*, July 2014.

[93] H. Zhang and A. O. Govorov. Optical Generation of Hot Plasmonic Carriers in Metal Nanocrystals: The Effects of Shape and Field Enhancement. *The Journal of Physical Chemistry C*, 118(14):7606–7614, April 2014.

[94] B.N.J. Persson. Polarizability of small spherical metal particles: influence of the matrix environment. *Surface Science*, 281(1):153–162, 1993.

[95] R. G. Parr and W. Yang. *Density-Functional Theory of Atoms and Molecules*, volume 16. 1989.

[96] P. Hohenberg and W. Kohn. Inhomogeneous Electron Gas. *Physical Review*, 136(3B):B864–B871, November 1964.

[97] Q. Zhao, M. Levy, and R. G. Parr. Applications of coordinate-scaling procedures to the exchange-correlation energy. *Physical Review A*, 47(2):918–922, February 1993.

[98] J. P. Perdew, K. A. Jackson, M. R. Pederson, D. J. Singh, and C. Fiolhais. Atoms, molecules, solids, and surfaces: Applications of the generalized gradient approximation for exchange and correlation. *Physical Review B*, 46(11):6671–6687, September 1992.

[99] J. P. Perdew, J. A. Chevary, S. H. Vosko, K. A. Jackson, M. R. Pederson, D. J. Singh, and C. Fiolhais. Erratum: Atoms, molecules, solids, and surfaces: Applications of the generalized gradient approximation for exchange and correlation. *Physical Review B*, 48(7):4978–4978, August 1993.

[100] J. P. Perdew, K. Burke, and M. Ernzerhof. Generalized Gradient Approximation Made Simple. *Physical Review Letters*, 77(18):3865–3868, October 1996.

[101] B. Hammer, L. Hansen, and J. Nørskov. Improved adsorption energetics within density-functional theory using revised Perdew-Burke-Ernzerhof functionals. *Physical Review B*, 59(11):7413–7421, March 1999.

[102] J. Wellendorff, K. T. Lundgaard, A. Møgelhøj, D. D. Landis, J. K. Nørskov, T. Bligaard, and K. W. Jacobsen. Density functionals for surface science: Exchange-correlation model development with Bayesian error estimation. *Physical Review B*, 85(23):235149, June 2012.

[103] K. Capelle. A Bird's-Eye View of Density-Functional Theory. *Brazilian Journal of Physics*, 36:1318–1343, 2006.

[104] D. Sholl and J. A. Steckel. *Density Functional Theory: A Practical Introduction*, volume 58. 2009.

[105] S. Adler. Quantum Theory of the Dielectric Constant in Real Solids. *Physical Review*, 126(2):413–420, April 1962.

[106] N. Wiser. Dielectric Constant with Local Field Effects Included. *Physical Review*, 129(1):62–69, January 1963.

[107] M. Hybertsen and S. Louie. Ab initio static dielectric matrices from the density-functional approach. II. Calculation of the screening response in diamond, Si, Ge, and LiCl. *Physical Review B*, 35(11):5602–5610, April 1987.

[108] M. Hybertsen and S. Louie. Ab initio static dielectric matrices from the density-functional approach. I. Formulation and application to semiconductors and insulators. *Physical Review B*, 35(11):5585–5601, April 1987.

[109] A. Marinopoulos, L. Reining, A. Rubio, and V. Olevano. Ab initio study of the optical absorption and wave-vector-dependent dielectric response of graphite. *Physical Review B*, 69(24):245419, June 2004.

[110] M. Gajdoš, K. Hummer, G. Kresse, J. Furthmüller, and F. Bechstedt. Linear optical properties in the projector-augmented wave methodology. *Physical Review B*, 73(4):045112, January 2006.

[111] J. Yan, K. W. Jacobsen, and K. S. Thygesen. First-principles study of surface plasmons on Ag(111) and H/Ag(111). *Physical Review B*, 84(23):235430, December 2011.

[112] J. Mortensen, L. Hansen, and K. Jacobsen. Real-space grid implementation of the projector augmented wave method. *Physical Review B*, 71(3):035109, January 2005.

[113] J. P. Perdew and Y. Wang. Accurate and simple analytic representation of the electron-gas correlation energy. *Physical Review B*, 45(23):13244–13249, June 1992.

[114] O. Gritsenko, R. van Leeuwen, E. van Lenthe, and E. J. Baerends. Self-consistent approximation to the Kohn-Sham exchange potential. *Physical Review A*, 51(3):1944–1954, March 1995.

[115] M. Kuisma, J. Ojanen, J. Enkovaara, and T. T. Rantala. Kohn-Sham potential with discontinuity for band gap materials. *Physical Review B*, 82(11):115106, September 2010.

[116] J. Y. Bigot, J. Y. Merle, O. Cregut, and A. Daunois. Electron dynamics in copper metallic nanoparticles probed with femtosecond optical pulses. *Physical Review Letters*, 75(25):4702–4705, 1995.

[117] T. Hertel, E. Knoesel, M. Wolf, and G. Ertl. Ultrafast Electron Dynamics at Cu(111): Response of an Electron Gas to Optical Excitation. *Physical Review Letters*, 76(3):535–538, 1996.

[118] C. Voisin, N. Del Fatti, D. Christofilos, and F. Vallée. Ultrafast Electron Dynamics and Optical Nonlinearities in Metal Nanoparticles. *Journal of Physical Chemistry B*, 105(12):2264–2280, 2001.

[119] G. Tas and H. Maris. Electron diffusion in metals studied by picosecond ultrasonics. *Physical Review B*, 49(21):15046–15054, June 1994.

[120] W. Fann, R. Storz, H. Tom, and J. Bokor. Electron thermalization in gold. *Physical Review B*, 46(20):13592–13595, November 1992.

[121] C.-K. Sun, F. Vallée, L. Acioli, E. Ippen, and J. Fujimoto. Femtosecond-tunable measurement of electron thermalization in gold. *Physical Review B*, 50(20):15337–15348, November 1994.

[122] G. Baffou and R. Quidant. Thermo-plasmonics: Using metallic nanostructures as nano-sources of heat. *Laser and Photonics Reviews*, 7(2):171–187, 2013.

[123] G. Baffou and R. Quidant. Nanoplasmonics for chemistry. *Chemical Society Reviews*, 43(11):3898–907, 2014.

[124] H. S. Fogler. *Elements of Chemical Reaction Engineering*, volume 42. 2006.

[125] J. Qiu and W. D. Wei. Surface Plasmon-Mediated Photothermal Chemistry. *The Journal of Physical Chemistry C*, 118(36):140703144218005, July 2014.

[126] D. H. Jeong, J. S. Suh, and M. Moskovits. Photochemical Reactions of Phenazine and Acridine Adsorbed on Silver Colloid Surfaces. *The Journal of Physical Chemistry B*, 104(31):7462–7467, 2000.

[127] D. H. Jeong, N. H. Jang, J. S. Suh, and M. Moskovits. Photodecomposition of Diazanaphthalenes Adsorbed on Silver Colloid Surfaces. *The Journal of Physical Chemistry B*, 104(15):3594–3600, 2000.

[128] S. I. Anisimov, B. L. Kapeliovich, and T. L. Perelman. Electron emission from metal surfaces exposed to ultrashort laser pulses. *Zhurnal Eksperimentalnoi I Teoreticheskoi Fiziki*, 66(2):375–377, 1974.

[129] S. I. Anisimov and B. Rethfeld. Theory of ultrashort laser pulse interaction with a metal. In Vitali I. Konov and Mikhail N. Libenson, editors, *Nonresonant Laser-Matter Interaction*, pages 192–203. International Society for Optics and Photonics, April 1997.

[130] Z. Lin, L. Zhigilei, and V. Celli. Electron-phonon coupling and electron heat capacity of metals under conditions of strong electron-phonon nonequilibrium. *Physical Review B*, 77(7):075133, February 2008.

[131] L. Landau. On The Vibrations of the Electronic Plasma. *Zhurnal Eksperimentalnoi I Teoreticheskoi Fiziki*, 16(7):574–586.

[132] L. D. Landau. The theory of a Fermi liquid. *Soviet Physics JETP-USSR*, 3(6):920–925, 1957.

[133] P. Nozières and D. Pines. *Theory Of Quantum Liquids: Normal Fermi Liquids*. Westview Press, 1994.

[134] J. G. Gordon and S. Ernst. Surface plasmons as a probe of the electrochemical interface. *Surface Science*, 101(1-3):499–506, December 1980.

[135] B. C. Rethfeld. *Mikroskopische Prozesse bei der Wechselwirkung von Festkörpern mit Laserpulsen im Subpikosekundenbereich*. PhD thesis, Technischen Universität Braunschweig, 1999.

[136] B. Rethfeld, A. Kaiser, M. Vicanek, and G. Simon. Femtosecond laser-induced heating of electron gas in aluminium. *Applied Physics A: Materials Science & Processing*, 69(S1):S109–S112, December 1999.

[137] A. Kaiser, B. Rethfeld, M. Vicanek, and G. Simon. Microscopic processes in dielectrics under irradiation by subpicosecond laser pulses. *Physical Review B*, 61(17):11437–11450, May 2000.

[138] B. Rethfeld, A. Kaiser, M. Vicanek, and G. Simon. Ultrafast dynamics of nonequilibrium electrons in metals under femtosecond laser irradiation. *Physical Review B*, 65(21):214303, May 2002.

[139] D. Snoke, W. Rühle, Y.-C. Lu, and E. Bauser. Nonthermalized distribution of electrons on picosecond time scale in GaAs. *Physical Review Letters*, 68(7):990–993, February 1992.

[140] W Kutta. Beitrag zur näherungweisen Integration totaler Differentialgleichungen. *Zeitschrift für Mathematik und Physik*, (46), 1901.

[141] M. Kaviany. *Heat Transfer Physics*. 2014.

[142] P. Christopher, D. B. Ingram, and S. Linic. Enhancing Photochemical Activity of Semiconductor Nanoparticles with Optically Active Ag Nanostructures: Photochemistry Mediated by Ag Surface Plasmons. *The Journal of Physical Chemistry C*, 114(19):9173–9177, May 2010.

[143] J. Misewich, T. Heinz, and D. Newns. Desorption induced by multiple electronic transitions. *Physical Review Letters*, 68(25):3737–3740, June 1992.

[144] D. G. Busch and W. Ho. Direct Observation of the Crossover from Single to Multiple Excitations in Femtosecond Surface Photochemistry. *Physical Review Letters*, 77(7):1338–1341, August 1996.

[145] T. Olsen and J. Schiøtz. Origin of Power Laws for Reactions at Metal Surfaces Mediated by Hot Electrons. *Physical Review Letters*, 103(23):238301, November 2009.

[146] H. L. Dai and W. Ho. *Laser Spectroscopy and Photochemistry on Metal Surfaces, Part 1*. World Scientific, 1995.

[147] C. Frischkorn. Microscopic understanding of an ultrafast photochemical surface reaction. *Surface Science*, 593(1-3):67–78, November 2005.

[148] P. W. Anderson. Localized Magnetic States in Metals. *Physical Review*, 124(1):41–53, October 1961.

[149] J. P. Muscat and D. M. Newns. Chemisorption on metals. *Progress in Surface Science*, 9(1):1–43, January 1978.

[150] J. Gavnholt, T. Olsen, M. Engelund, and J. Schiøtz. Δ self-consistent field method to obtain potential energy surfaces of excited molecules on surfaces. *Physical Review B*, 78(7):075441, August 2008.

[151] N. S. Wingreen, K. W. Jacobsen, and J. W. Wilkins. Inelastic scattering in resonant tunneling. *Physical Review B*, 40(17):11834–11850, December 1989.

[152] R. Kubo. The fluctuation-dissipation theorem. *Reports on Progress in Physics*, 29(1):255–284, January 1966.

[153] B. N. J. Persson and M. Persson. Vibrational lifetime for CO adsorbed on Cu(100). *Solid State Communications*, 36(2):175–179, October 1980.

[154] R. R. Cavanagh, D. S. King, J. C. Stephenson, and T. F. Heinz. Dynamics of nonthermal reactions: femtosecond surface chemistry. *The Journal of Physical Chemistry*, 97(4):786–798, January 1993.

[155] M. Brandbyge, P. Hedegård, T. F. Heinz, J. A. Misewich, and D. M. Newns. Electronically driven adsorbate excitation mechanism in femtosecond-pulse laser desorption. *Physical Review B*, 52:6042–6056, 1995.

[156] A. C. Luntz, M. Persson, S. Wagner, C. Frischkorn, and M. Wolf. Femtosecond laser induced associative desorption of H2 from Ru(0001): comparison of "first principles" theory with experiment. *The Journal of Chemical Physics*, 124(24):244702, June 2006.

[157] T. Olsen and J. Schiøtz. Memory effects in nonadiabatic molecular dynamics at metal surfaces. *The Journal of Chemical Physics*, 133(13):134109, October 2010.

[158] T. Olsen and J. Schiøtz. Quantum corrected Langevin dynamics for adsorbates on metal surfaces interacting with hot electrons. *The Journal of Chemical Physics*, 133(3):034115, July 2010.

[159] N. Shenvi, S. Roy, P. Parandekar, and J. Tully. Vibrational relaxation of NO on Au(111) via electron-hole pair generation. *The Journal of Chemical Physics*, 125(15):154703, October 2006.

[160] L. Verlet. Computer "Experiments" on Classical Fluids. I. Thermodynamical Properties of Lennard-Jones Molecules. *Physical Review*, 159(1):98–103, July 1967.

[161] W. C. Swope. A computer simulation method for the calculation of equilibrium constants for the formation of physical clusters of molecules: Application to small water clusters. *The Journal of Chemical Physics*, 76(1):637, January 1982.

[162] C. Springer, M. Head-Gordon, and J. C. Tully. Simulations of femtosecond laser-induced desorption of CO from Cu(100). *Surface Science*, 320(1):L57–L62, 1994.

[163] C. Springer and M. Head-Gordon. Simulations of the femtosecond laser-induced desorption of CO from Cu(100) at 0.5 ML coverage. *The Journal of Chemical Physics*, 205(1-2):73–89, April 1996.

[164] S. Monturet and P. Saalfrank. Role of electronic friction during the scattering of vibrationally excited nitric oxide molecules from Au(111). *Physical Review B*, 82(7):075404, August 2010.

[165] G. Füchsel, T. Klamroth, S. Monturet, and P. Saalfrank. Dissipative dynamics within the electronic friction approach: the femtosecond laser desorption of H2/D2 from Ru(0001). *Physical Chemistry Chemical Physics*, 13(19):8659–70, May 2011.

[166] V. Krishna and J. C. Tully. Vibrational lifetimes of molecular adsorbates on metal surfaces. *The Journal of Chemical Physics*, 125(5):054706, August 2006.

[167] M. Head-Gordon and J. C. Tully. Molecular-orbital calculations of the lifetimes of the vibrational modes of CO on Cu(100). *Physical Review B*, 46(3):1853–1856, July 1992.

[168] J. C. Tully, M. Gomez, and M. Head-Gordon. Electronic and phonon mechanisms of vibrational relaxation: CO on Cu(100). *Journal of Vacuum Science & Technology A: Vacuum, Surfaces, and Films*, 11(4):1914, July 1993.

[169] J. Trail, M. Graham, D. Bird, M. Persson, and S. Holloway. Energy Loss of Atoms at Metal Surfaces due to Electron-Hole Pair Excitations: First-Principles Theory of "Chemicurrents". *Physical Review Letters*, 88(16):166802, April 2002.

[170] J. R. Trail, D. M. Bird, M. Persson, and S. Holloway. Electron–hole pair creation by atoms incident on a metal surface. *The Journal of Chemical Physics*, 119(8):4539, August 2003.

[171] E. Laguerre. Sur le développement d'une fonction suivant les puissances corissantes d'un polynôme. *Journal für die reine und angewandte Mathematik*, 88:35–48, 1879.

[172] E. Laguerre and S. A. Levin. On the theory of numeric equations. *Journal de Mathématiques Pures et Appliquées*, 3, 1883.

[173] J. D. Beckerle, M. P. Casassa, R. R. Cavanagh, E. J. Heilweil, and J. C. Stephenson. Ultrafast infrared response of adsorbates on metal surfaces: Vibrational lifetime of CO/Pt(111). *Physical Review Letters*, 64(17):2090–2093, 1990.

[174] P. Christopher. *Design of Nanostructured Ag Catalysts for Selective Heterogeneous Catalytic and Photocatalytic Oxidation Reactions*. PhD thesis, The University of Michigan, 2011.

[175] M. J. Rycroft. Computational electrodynamics, the finite-difference time-domain method. *Journal of Atmospheric and Terrestrial Physics*, 58(15):1817–1818, 1996.

[176] V. A. Mandelshtam and H. S. Taylor. Harmonic inversion of time signals and its applications. *The Journal of Chemical Physics*, 107(17):6756–6769, 1997.

[177] A. F. Oskooi, D. Roundy, M. Ibanescu, P. Bermel, J. D. Joannopoulos, and S. G. Johnson. Meep: A flexible free-software package for electromagnetic simulations by the FDTD method. *Computer Physics Communications*, 181(3):687–702, 2010.

[178] A. D. Rakic, A. B. Djurisic, J. M. Elazar, and M. L. Majewski. Optical properties of metallic films for vertical-cavity optoelectronic devices. *Applied Optics*, 37(22):5271–5283, 1998.